

Laser-generated nanoparticle polymer composites for potential applications in tissue engineering

Dissertation
by

Yaya Li

for the degree of
Doctor of Natural Science
- Dr. rer. nat. -

Faculty of Chemistry
University of Duisburg-Essen
Germany

Essen, 2021

The present thesis was conducted from October 2017 to January 2021 at Technical Chemistry I of Prof. Dr.-Ing. Stephan Barcikowski, at Nanobiomaterials group of Dr. Christoph Rehbock in the Faculty of Chemistry of the University of Duisburg-Essen.

Disputation date: 29.11.2021

Referees: Prof. habil Dr.-Ing. Stephan Barcikowski

Universität Duisburg-Essen

Prof. Dr. Cornelia Lee-Thedieck

Leibniz Universität Hannover

Chairman: Prof. Dr. Alexander Probst

Universität Duisburg-Essen

DuEPublico

Duisburg-Essen Publications online

UNIVERSITÄT
DUISBURG
ESSEN

Offen im Denken

ub | universitäts
bibliothek

Diese Dissertation wird via DuEPublico, dem Dokumenten- und Publikationsserver der Universität Duisburg-Essen, zur Verfügung gestellt und liegt auch als Print-Version vor.

DOI: 10.17185/duepublico/75168

URN: urn:nbn:de:hbz:464-20211203-113231-9

Alle Rechte vorbehalten.

*Nothing in life is to be feared, it is only to be understood.
Now is the time to understand more, so that we may fear
less.*

Marie Curie (1867 - 1934)

Abstract

Nanocomposites have significantly contributed in medical device fabrication, 3D bioprinting, and tissue engineering applications. Various kinds of nanocomposites are increasingly investigated to control the nanoparticles (NP) dispersion in the polymer matrix and ion release kinetics from nanoparticles that are crucial prerequisites for the utilization of composites. Laser ablation in liquids (LAL) is a promising method for uniform *in situ* embedding of nanoparticles into polymers to fabricate composites free from chemical additives. Previous studies demonstrated its suitability; however, systematic studies on the scale-up of these materials and details on the working mechanism are not conducted. Particularly kinetics of ion release from nanoparticle-polymer composites matrices has not been fully understood yet. In addition, the role of nanoparticles in the gelation kinetics of collagen composites is not clear. Regarding other attractive biomaterial like nanoscopic bioactive glass, the mechanisms of fabrication by picosecond (ps) and nanosecond (ns) laser fragmentation have not been explained so far.

LAL of metal targets in macromolecular solutions was employed for synthesizing Au and Fe nanoparticle-loaded nanocomposites based on alginate, collagen, and thermoplastic polyurethane (TPU). In this regard, we investigated the influence of polymer solution parameters, such as polymer types, liquid viscosity, and pH on the nanoparticle productivities and particle size. Furthermore, confocal microscopy method revealed a good three-dimensional dispersion and differentiation in parallel of laser-generated nanoparticles in the polymer that was shown to be a suitable bioink for 3D printing. Moreover, the laser fragmentation method was successfully applied to downsize bioglass particles from micrometers (3.5-11 μm) to 20-50 nm, synergistically using iron salt as the fragmentation sensitizer for *in situ* doping.

Metal ion release from composites and protein adsorption capacity are hypothesized to be two key processes directing cell-scaffold interactions. Interestingly, a phenomenon of total Fe ion release concentration decreased with increasing mass loadings was only found in the Fe-alginate system under static conditions, neither in the Cu/Zn-alginate nor Fe-TPU control system. The attributed kinetics of special release behaviour of iron ions from alginate gels are probably not only the redox potential of metals and metal ions diffusion, but also the solubility of nano-metal oxides and affinity of metal ions with alginate. At the minute loadings with Fe nanoparticles down to 200 ppm, bovine serum albumin (BSA) and collagen-I protein adsorption on the surface of both the alginate and TPU composites was significantly increased compared

to unloaded control polymers, which could be correlated with Fe ion release and porous nature of alginate composites, but was independent of the global surface charge.

Notably, the embedded nanoparticles in polymer matrices showed significant influences on physicochemical and rheological properties. Results demonstrated that compared to alginate, the elastic modulus of nanoparticle-alginate gels was enhanced 1.5 times. Nanoparticles modified the surface charge of TPU to a more negative value. Moreover, nanoparticles enlarged the hydrogel network and increased the porosity but decreased the stiffness of alginate or alginate-fibrin blends. Meanwhile, synergetic effects of fibrin, FeNPs, and fetal bovine serum contributed to an enhanced endothelialization capacity of alginate hydrogels. These findings can pave way for the fabrication of various hydrogel-based biomaterials employed in tissue engineering.

Table of content

1 Introduction	1
2 Objectives.....	5
3 Theoretical Background	7
3.1 Tissue engineering.....	7
3.1.1 Protein adsorption on the surface of biomaterials for tissue engineering.....	8
3.1.2 Relationship between endothelial cells and surface of biomaterials	9
3.2 Nanoparticle polymer composites in tissue engineering	11
3.2.1 Properties of selected polymers for composites and polymer scaffold fabrication methods.....	11
3.2.2 Ion release from nanoparticle loaded polymer scaffolds	15
3.2.3 Impact of Au and Fe nanoparticles on properties of polymer composites	17
3.3 Bioactive glass in bone tissue engineering.....	18
3.4 Nanoparticles-polymer composites generated via laser synthesis in liquids.....	20
3.4.1 Laser ablation in liquids.....	20
3.4.2 Fabrication of nanocomposites based on laser ablation in liquids.....	22
3.5 Gelation of nanoparticles-polymer composites	25
3.6 Rheological property of nanoparticles-polymer composites	26
4 Materials and Methods	28
4.1 Chemicals and equipment.....	28
4.2 Laser synthesis of nanoparticles in liquids	31
4.2.1 Generation of nanoparticle-polymer composites via laser ablation in liquids.....	31
4.2.2 Nanoscopic bioactive glass prepared via laser fragmentation	33
4.3 Preparation of composite gels	36
4.4 Characterization and physicochemical determination of nanoparticle-polymer gels.....	37
4.5 Protein adsorption on composites.....	42
4.6 Demonstration of 3D printable nanoparticle-alginate hydrogel	43
4.7 Cell experiments	44
5 Results and Discussion.....	46
5.1 Productivity and scalability of laser processing for <i>in-situ</i> nanocomposite generation .	46
5.2 Particle characterization and distribution in the gel matrix.....	55

5.2.1 Effects of polymer solutions on particle size.....	55
5.2.2 Method development of confocal microscopy technique to identify nanoparticles in polymer matrices.....	60
5.3 Physicochemical properties of nanoparticle-polymer composites gels and the interaction with biological systems	65
5.3.1 Effect of embedded nanoparticles on the rheological property of hydrogels	65
5.3.2 Specific Fe ion release from alginate composites and their protein adsorption	68
5.3.3 Iron nanoparticles and fibrin blending promote serum-mediated endothelialization on alginate hydrogels	79
5.3.4 Influence of laser-generated Au nanoparticles on the physicochemical properties of collagen gels	89
5.3.5 Physicochemical properties of nanoparticle-TPU composites and their protein adsorption capacity	94
5.4 3D printability of alginate composites	98
5.5 Nanoscopic bioglass doped with iron produced by iron sputter-sensitized laser fragmentation	100
6 Summary	112
7 Outlook.....	115
8 References	116
9 Appendix	137
9.1 Supporting information	137
9.2 List of abbreviations and physical variables	154
9.3 List of Authored and Co-authored Publications	158
9.4 Curriculum Vitae	159
9.5 Declarations	160
9.6 Acknowledgment.....	163

1 Introduction

The goal of tissue engineering (TE) is to regenerate diseased or damaged tissue with functional scaffolds. Living cells successfully attaching to scaffolds are essential in tissue engineering, which can replace damaged tissue by recapitulating physiological cell responses and self-organizing into complex constructs based on the physicochemical microenvironment of matrices [1, 2]. Multiple biomaterials such as sodium alginate and collagen remain attractive candidates due to biocompatibility, tunable viscoelasticity, and easy manufacturing [3-6]. At the same time, thermoplastic polyurethane (TPU) is more interesting in respect to medical devices [7], and bioactive glass (BG) has remarkable performance in bone tissue engineering applications [8]. However, there are still a few major challenges in the application of these materials. They are non-cytocompatibility or poor mechanical properties associated with polymers. A concept to compensate for the drawback of polymers is the incorporation of nanoparticles to form nanocomposites. Here, embedded nanoparticles affect the physicochemical and mechanical properties of composites as well as cell proliferation and differentiation on the composites' surface [9, 10]. While therapeutic ions doped in BG to achieve multifunctional properties for cells and tissues is still an issue.

Synthesized nanoparticle methods consistently implement impurities from stabilizers and reducing agents, which require tedious purification procedures and can have unpredictable toxic effects on the surrounding cells [11]. Laser ablation in liquids (LAL) can be a promising approach to synthesize pure metal nanoparticles and incorporate them into a polymer matrix in a one-step process [12-15]. In our previous work, nanoparticle-TPU or -alginate composites were successfully prepared by LAL [12, 14, 15]. Moreover, it has been discussed that laser ablation based *in situ* preparation of composites method could overcome these limitations [16, 17], including scalability to high level of technology readiness [17]. Although bio-response is essential in the designed scaffolds, mechanical properties including stiffness and modulus as well as surface properties such as porosity, wettability, surface charge also have significant influences on cell transport and differentiation [18, 19]. So far, the mechanism of diffusion-based release and multi-element release has already been discussed; however, the effects of oxide solubility and the polymer matrix on Fe ion release have not been frequently considered. Moreover, little is known about the inter-relation between protein adsorption and ion release in polymer composites.

The most severe problem for TPU is surface-induced thrombosis occurring in polyurethane blood stents or other cardiovascular biomaterials [7]. The development of modifications of these polymers is a strategy to overcome the mentioned drawbacks. Inducing NPs modification which alters the physicochemical properties of polyurethane has been reported suitable for the immobilization of enzymes [20]. Hess *et al.* [15] embedded insoluble nanoparticles like Pt and Au into TPU using an *in situ* LAL approach and investigated the NP effects on endothelial cell adhesion and proliferation properties and found benign effects on cellular viability and proliferation at a low concentration of 0.1 wt%, which was up to three times higher than in the unmodified TPU. This pronounced effect was attributed to the incorporation of nanoparticles into TPU significantly elevating the hydrophilicity and polymer stiffness probed by AFM. However, nanoparticle productivity in TPU polymer solution and the ion release profiles from TPU matrix has not been considered.

Alginate is a natural water-soluble biopolymer that can be easily cross-linked in the presence of cations like Ca^{2+} , Cu^{2+} , and Zn^{2+} forming a stable gel network [21]. Thanks to biocompatibility, biodegradability, abundance and low cost, alginate hydrogels have been suggested to be applicable in wound healing [3], bone tissue engineering [22], and biological stent coatings [23]. Due to the absence of any adhesive sites and hydrophilic surfaces, alginate gels generate a so-called “non-fouling” effect [23, 24]. On one hand, such surfaces inhibit thrombocytes and bacterial adhesion and the prevention of biofilm formation [25]. On the other hand, the non-fouling effect also impairs interaction with cells as it avoids beneficial protein adsorption [24], which thus compromising the pre-endothelialization and anti-restenotic properties of alginate-coated stents. For this reason, two main strategies are currently proposed to modify alginate hydrogels to make them suitable for endothelial cell adhesion and proliferation. Iron nanoparticles combining with alginate hydrogel have been reported to achieve enhanced cell adhesion [12]. Furthermore, the fibrin interpenetrating into alginate networks seemed to exhibit tunable mechanical properties and adhesive behaviours at varying fibrin concentrations [26]. Given that biomaterials in the body immediately contact with surrounding proteins, protein adsorption may be an initial indicator of cytocompatibility. Inspired by these results, triple modification of alginate gels with FeNPs, fibrin, and serum protein coatings (SPCs) may provide synergetic effects to pave a way toward novel strategy for the coatings.

In contrast, triple-helical dominated collagen has abundant contacting sites such as hemidesmosomes and focal adhesions for the cell receptors. As collagen distributes in most of

the connective tissues, researchers make efforts to bio-fabricate collagen hydrogels or composite scaffolds and make them applicable in tissue engineering or regeneration [27]. However, the poor mechanical properties of collagen products cannot be ignored, as well as the problematic gelation kinetics [28, 29]. Even though glutaraldehyde is frequently used in the fabrication of collagen scaffolds, overdosage causing toxicity cannot be negligible [30]. Daood *et al.* [31] investigated how the different ratios of tiopronin-Au and 1-ethyl-3-(3-dimethylaminopropyl-carbodiimide hydrochloride (EDC) affected the collagen crosslinking and found a pronounced effect on improving biodegradation and mechanical properties. Recently, Vedhanayagam *et al.* [32] investigated the particle size effects on cell viability of cross-linked collagen with pectin and demonstrated small particles with 10 nm promoting collagen fibrillogenesis process as well as high cell viability rather than large particles with a size of 55 nm. Nevertheless, the effects of nanoparticles together with cross-linkers in gelation kinetics of collagen are still unclear.

Another attractive biomaterial, bioactive glass (BG), is a category of materials with bioactivity, osteoconductivity, and osteoinductivity which is suitable for bone tissue engineering [8, 33, 34]. BG can bind to bone tissue and stimulate bone regeneration by the release of Si^{4+} , Ca^{2+} , and PO_4^{3-} ions [35]. Among numerous BG compositions, 45S5-BG is capable of upregulating osteoblast proliferation by the controlled release of its ion dissolution products, thus leading to bone regeneration [36, 37]. To further enhance the dissolution, bioactivity, and protein-related bone therapeutics of bioglass, the addition of different elements has been proposed [38]. It should be also noted that osteogenesis can be induced through genetic pathway activation from the biochemically active ions and biophysical properties of constructed biomaterials as well. In this context, therapeutic inorganic ions such as iron (Fe), copper (Cu), zinc (Zn), strontium (Sr), Gallium (Ga), cerium (Ce) are considered to be doped in BG [39, 40]. For example, Fe ions play a key role in the enhancement of endothelial cell adhesion [12], erythroid differentiation [10], and the component of hemoglobin and structural stents [41]; while the Cu ions are considered to be antibacterial and an essential role in proangiogenic function [42]. Regarding the incorporation of inorganic ions, a direct mixture of metallic salt [38] or their oxide [43] and precursors of glass compositions is a common strategy.

Another concern associated with these obtained BG is their particle size. There is scientific evidence that nano-sized BG particles resulted in a significant increase in *in vitro* osteoblast cytocompatibility behaviour compared to similar micro-sized BG particles [44]. Moreover, a

smaller size with higher surface reactivity of BG can improve cell adhesion and speed up the ion release thus leading to accelerated degradation process of a silicate network [8]. Conventionally, sol-gel process based on the modified Stöber method has been frequently reported to synthesize nano BG [45-47]. However, producing BG particles in monodispersed submicrometer size with high dispersity is particularly challenging [35, 48], and sol-gel precipitation process usually requires a long reaction time and special chemical additives [48]. Recent studies proposed a laser-assisted method to prepare Fe-doped calcium phosphate spheres in submicrometer and micrometer [49]. Laser fragmentation in liquids (LFL) is frequently utilized to downsize particle diameter [50]. The size selectivity can be primarily achieved by LFL because the energy absorption cross-section of the product is usually smaller than that of the particulate educts [16]. It is known that BG has very weak absorption in the ultraviolet or visible wavelength range. Therefore, during the laser irradiation process, a light-absorbing agent is needed. Fe ions in solution have proved to be light absorbing agents [49, 51]. Hence, we proposed this technique to produce Fe or Cu ions doped 45S5-BG with controlled particle size, via *in-situ*-doping of BG during iron-sensitized LFL downsizing.

2 Objectives

In this work the knowledge on laser-fabricated nanocomposites is extended to different material systems with varying readiness levels. The NP productivity and generated efficiency in TPU and alginate polymer solution will be addressed. The most important is the ion release mechanism and protein adsorption, which are performed to deepen our understanding on their interactions with biological systems. The examination of two previously unexplored systems in context with LAL-generated nanoparticles in collagen solutions and laser fragmented nanoscopic bioactive glass will be conducted.

This work thereby aims to provide a systematic study addressing the aforementioned issues, to further develop and understand the nanoparticle-polymer- composites generation via chemically pure laser-based production methods. Particular emphasis is provided on how the physical, chemical and biological properties of these materials can be tuned based on: 1) nanoparticle material (iron, gold, doped bioactive glass), 2) the base polymer type (alginate, alginate-fibrin blends, TPU, Collagen) and 3) the nanoparticle/polymer mass ratio. Primary readout methods to document changes due to nanoparticle loading were A) mechanical properties (stiffness, oscillation modulus), B) chemical properties (surface charge, wettability, metal ion release) and C) interactions with biomolecules (protein adsorption) and endothelial cells. Furthermore, detailed investigations on the nanoparticle distribution in the polymer via confocal microscopy were conducted with particular emphasis on method development and differentiating nanoparticles from background scattering or aggregation-induced scattering (AIS) effect and detect co-localization of FeNPs and proteins at individual detective channels. Finally, experiments with partners were conducted to verify the 3D printability of the nanoparticle-polymer composites. The main research objectives of this thesis are illustrated in Figure 2-1.

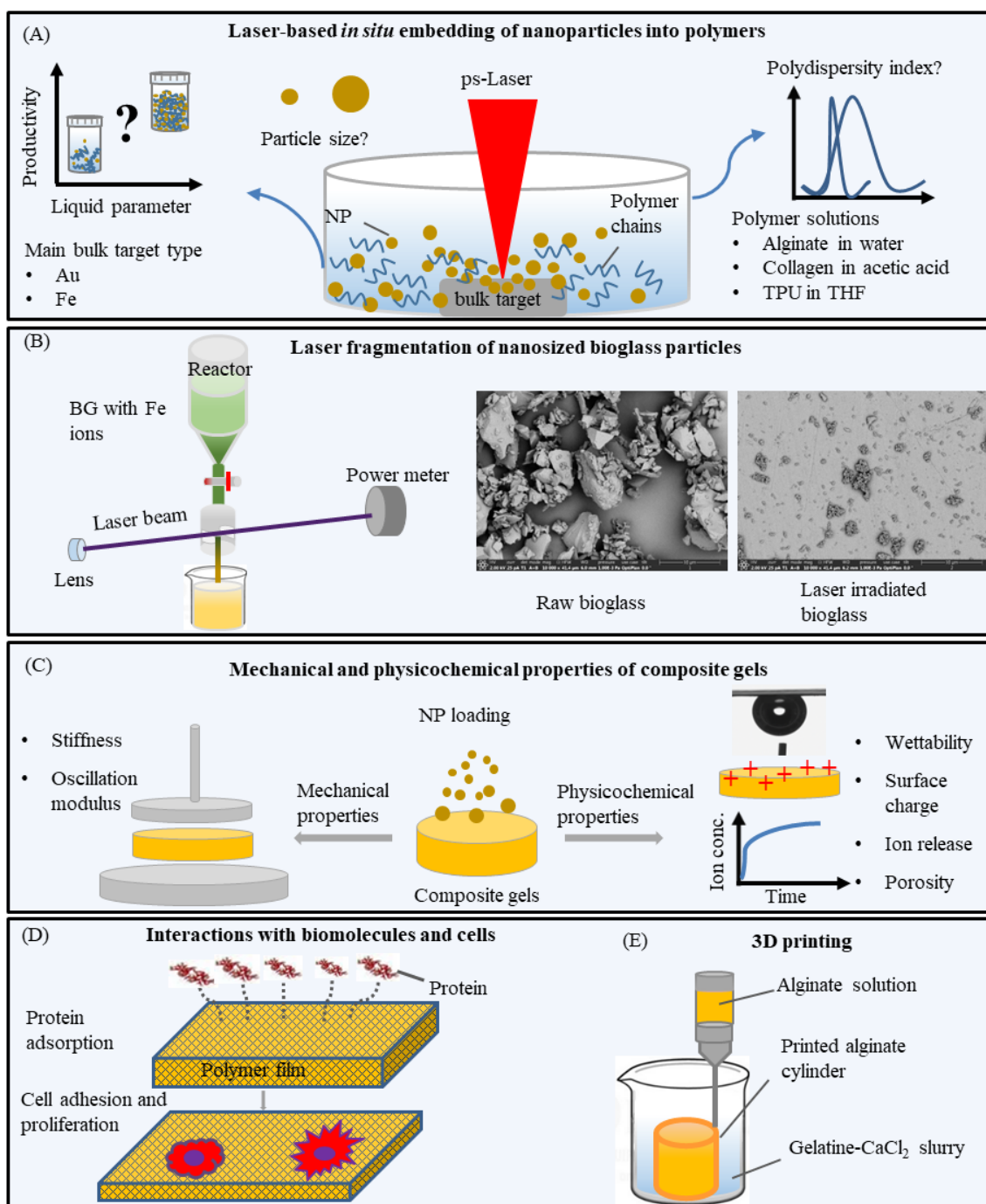


Figure 2-1: Illustrations of specific research objectives of this thesis: (A) nanoparticle-polymer composites synthesis via laser fabrication method, (B) laser fragmentation to downsize and *in-situ*-doped bioglass particles, (C) mechanical and chemical properties of composites gels, (D) interactions between composites gels and biomolecules and/or endothelial cells, (E) 3D printability of alginate composites. Laser ablation in polymer solutions leads to *in situ* generation of nanoparticle-polymer composites. The investigated special ion release, cellular response, mechanical and chemical properties, and 3D printability are promising for tissue engineering applications and medical device fabrication.

3 Theoretical Background

3.1 Tissue engineering

Tissue engineering (TE) is a multidisciplinary field of research about the human body, such as bone, skin, or organs as shown in Figure 3-1 [18]. Restoring damaged or diseased tissue to a functional and healthy state is the ultimate goal in TE via tissue repair or regeneration. For example, in wound healing, tissue repair can be defined as the coordinated mechanisms that restore tissue barriers and homeostasis. At the same time, regeneration is the tissue repair to nearly identical function and structure of uninjured tissue through proliferation and activation of resident stem cells or progenitor cells and production of new matrix [52]. The features of the extracellular matrix (ECM) have inspired the design example of scaffolds for TE, such as nanoscale topography, structure, optimized mechanical properties, and cellular bio-response [53].

Most TE strategies are based on three key elements: biological signals, cells, and scaffolds. In this process, scaffolds play an essential role in providing a framework where cells can attach, proliferate, migrate [12], and even directing erythropoiesis [10]. Generally, the design requirements of scaffolds are solid, cellular structure, and sufficient mechanical integrity. They can be prepared with ceramics, metals, and polymers. Polymer scaffolds have been increasingly studied due to their biocompatibility, biodegradability, and easy processability [18]. The term “biocompatibility” also means scaffolds are nontoxic to bare cells without any protective layer or causing any significant system reactions or inflammation related to the composition of scaffolds [6]. As exposed to the biological equilibrium, degradable scaffolds are able to undergo scission of chemical bonds or physical erosion, a feature termed biodegradability which results from (1) passive hydrolysis or active enzyme-catalyzed hydrolysis; (2) oxidation [54]. The raw polymer materials for preparing scaffolds are various and may be based on natural (alginate, chitosan, collagen, etc.) or synthetic polymers (poly (lactic-co-glycolic acid) [PLGA], poly(urethane) [PU], etc.). Their fabrication techniques include electrospinning [3], solvent casting/particulate leaching [55], and 3D printing [4, 56].

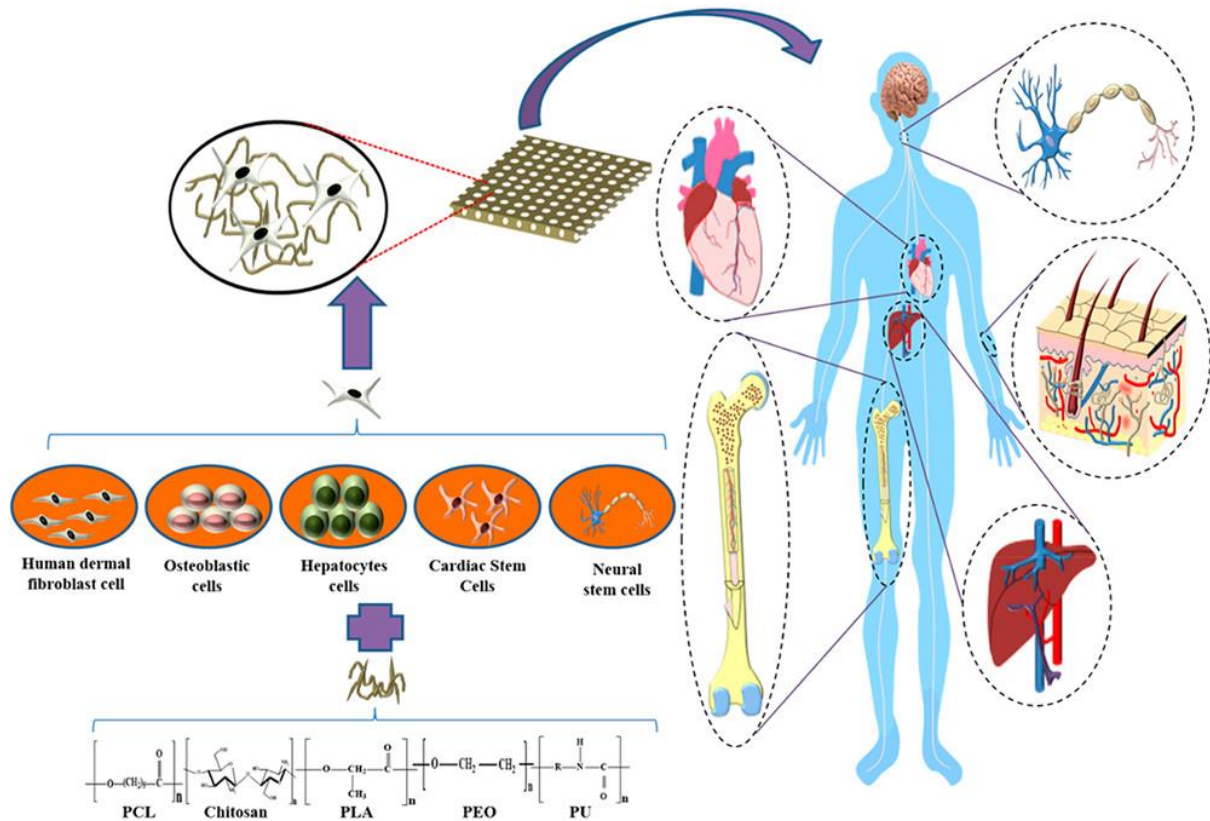


Figure 3-1: Illustration of the basic concept of tissue engineering. Cell-laden polymer scaffolds via 3D or 4D fabrication technologies were produced to repair and regenerate organs or tissues for human health [18].

Despite these advantages, lack of good mechanical properties, low stability in aqueous and physiological environments, and how to improve cell adhesion are still problems for polymer scaffolds [12, 57]. Researchers make efforts to deal with this issue through chemical or physical modifications, including the grafting of peptides or macromolecules [57], biopolymer blends [58], and nanoparticle complexes [3, 12, 56]. Among them, nanoparticle-polymer composites have been proved to be positive to improve mechanical properties and enhance cell adhesion and proliferation [12, 56].

3.1.1 Protein adsorption on the surface of biomaterials for tissue engineering

As a biomaterial is implanted into the body, it is immediately coated with proteins from the surrounding area, like blood plasma and serum. Hence, it is crucial to design new biocompatible materials and understand the mechanisms, kinetics, and thermodynamics between protein adsorption and solid surfaces. Why does protein adsorb? Firstly, free energy is minimized when proteins stick to surfaces compared to being surrounded by water molecules and the further

fundamentals and thermodynamics of protein adsorption on material surfaces have been interpreted in this review [59]. The interactions between proteins and surfaces are complex, including ionic or electrostatic interactions, hydrogen bonding, entropic interactions. Protein adsorption on a solid surface depends on the chemical and physical properties of surfaces and media, including wettability, surface charge, surface roughness, microstructure of the materials, pH, ionic strength of the media [60], and of course mechanisms can differ in protein characteristics including side chains of amino acids [61], and molecular weights [62]. Rusmini *et al.* [63] also described three different protein immobilization strategies through physical, covalent, and bioaffinity immobilization onto surfaces.

There are a number of previous studies about the protein adsorption process on the surface of biomaterials. Zhao *et al.* [64] focused on the adsorption of BSA on imprinted alginate/polyacrylamide hydrogel films, while Angar *et al.* [65] examined the adsorption-desorption mechanism of BSA on hydrogels. They all found that functional monomers combined into alginate hydrogels could favor protein adsorption due to enhanced mechanical properties and high swelling degrees. Yang *et al.* found that BSA displayed significant protein denaturation and spreading because of several available adsorption sites at high roughness surfaces, but in the case of myoglobin (MGB) and thyroglobulin (TGL) proteins adsorption followed a linear correlation with surface skewness [66]. Not surprisingly, the porous nature of materials was with a high protein adsorption capacity [67].

It is known that cells do not directly interact with the material surface but have specific receptors for proteins. Previous studies demonstrated that protein adsorption on the surface plays a vital role as the initial step for the interaction of cells with synthetic materials, often directly correlated with cellular adsorption [68, 69]. On a biomaterial scaffold surface, protein adsorption on the supramolecular level was proposed to affect vascularization via interacting with typical integrin expressed by cells [70]. Further, the adsorption of cellular proteins like collagen on catheters was reported to be a promising strategy for vascular regeneration [28]. Thus, protein adsorption may be an initial indicator of cytocompatibility and may be used as a biological readout to predict the cellular response of biomaterials.

3.1.2 Relationship between endothelial cells and surface of biomaterials

Endothelial cells (ECs) are major components of blood vessels and a forming layer between blood and extravascular cells. They can form a passive barrier between vessel and tissue and

involve several functional processes, such as blood vessel formation, coagulation, fibrinolysis, vascular tone regulation, and a role in the inflammatory response [71]. Pre-endothelialization is one of the solutions for stent therapy. Human umbilical vein endothelial cells (HUVECs) as best-characterized EC have been frequently used as an *in vitro* model system. HUVECs can respond to many physiological and pathophysiological stimuli and differentiate into 3D spheroids [72].

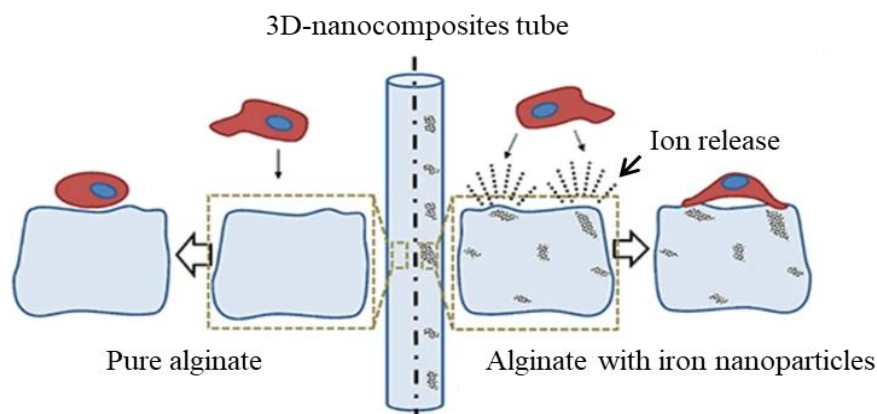


Figure 3-2: Assumed mechanism of ion release leading to significant improvement of cell adhesion on alginate hydrogel surface [12].

Cells and scaffolds are two indispensable components in TE. Many reactions are occurring as cells get in contact with biomaterials. As described before, protein adsorption is the first step during the contacting process, which involves surface wettability, roughness or charge [61]. Conversely, the surfaces show different effects on various cell types. The viability, morphology, and proliferation of cells are known to be affected by surface properties, such as roughness, stiffness, and wettability. As illustrated in Figure 3-2, Fe ion release was proposed to increase actin expression level, thus leading to cell adhesion cultured on iron-embedded alginate hydrogels [12]. Mi *et al.* [73] found high hydrophobicity of polymers with lower HUVEC cell adhesion. Still, they modified polymer by grafting dopamine, RGD, and heparin biomolecules into a more hydrophilic and rougher surface resulting in an enhancement of cell attachment. Chen *et al.* [74] investigated the effects of matrix stiffness on the adhesion of monocytes on endothelial cells and they concluded the stiffer matrix resulted in increased tension and permeability of the ECs monolayer. Hess *et al.* [15] found a dose-dependent effect of embedded noble metal (Au, Pt) nanoparticles into TPU on endothelialization without causing any inflammation or thrombosis. Precisely, significant endothelialization was already achieved at 100 ppm of NP loading in the polymer.

Regarding how endothelial cells respond to metal ions released from biomaterials, multiple studies have been carried out [12, 75]. It is known that Cu ion release from copper oxide nanoparticles smaller than 50 nm induces oxidative stress leading to cell death [76]. However, potential benign effects of therapeutic ion release are frequently reported in TE applications. For example, Fe ions release was also proposed to play a key role in HUVEC adhesion on alginate hydrogels [12] and triggering the erythropoiesis at a theoretical concentration of 1.63 $\mu\text{g/mL}$ of iron in poly(ethylene glycol) (PEG) [10]. Moreover, Mehrabi *et al.* [75] overviewed the critical role of various metal ion (Ca^{2+} , $\text{Fe}^{2+/3+}$, Ce^{3+} , Mg^{2+} , Sr^{2+}) release from glass networks in the proliferation and migration of fibroblasts, keratinocytes, and vascular endothelial cells and targeting different phases of the wound healing process.

3.2 Nanoparticle polymer composites in tissue engineering

Nanocomposites involve multiphase materials where at least one dimension of the constituent phases is less than 100 nm. Nanoparticle polymer composites intending to combine the advantages of nanoparticles and polymers are potentially applied in tissue engineering should be biocompatible, biodegradable, non-cytotoxic, and functional [6]. Nanoparticles can be derived from noble metals, ignoble metal/metal oxide, or ceramics. The morphology and size of nanoparticles can be adjusted, therefore, influence the stability, physicochemical properties, and interactions with the biological system (bio-distribution, cytotoxicity, and pharmacokinetics) [77, 78]. Furthermore, the embedding of nanoparticles alters the mechanical properties of the polymer matrix [64]. In this thesis, nanoparticles in different polymer matrices like alginate, TPU, and collagen are mainly discussed.

3.2.1 Properties of selected polymers for composites and polymer scaffold fabrication methods

Alginate

Alginate is a natural water-soluble biopolymer that easily forms a stable gel network in case cations like Ca^{2+} , Cu^{2+} and Zn^{2+} are present as cross-linkers [79] and is abundant, environment-friendly, and cheap. It is composed of a linear copolymer with homopolymeric blocks of (1-4)-linked β -D-mannuronate (M) and its C-5 epimer α -L-guluronate (G), respectively. The M or G blocks covalently linked together in different sequences or blocks, alternating M and G residues forming M, G, or MG blocks. Alginate hydrogels, due to their good cytocompatibility,

hydrophilicity, and low toxicity, have been broadly applied in TE [3, 4, 24, 80]. In addition, alginate-based composites offer many advantages including hemostatic capability and gel-forming ability upon absorption of wound exudates [81, 82]. Moreover, alginate films can mimic or be used as synthetic ECM, organizing cells into a three-dimensional architecture, providing mechanical integrity to the new tissue. They also provide hydration for the diffusion of nutrients and metabolites in and out of the cells, required for cell immobilization, transplantation, and tissue engineering [2, 83, 84]. However, cellular adhesion in the absence of additional functional ligands is limited. To compensate for the disadvantage of lacking cell adhesive ligands, alginate can be modified or blended with cell-adhesive materials or ligands to achieve desired cell behaviors [85]. Embedding Au or Fe nanoparticles into alginate is another option to achieve the expected positive results [12]. The general synthesis route of NP-alginate composites is firstly fabrication of nanoparticles and mechanical mixing with alginate. At present, the available techniques for nanoparticle synthesis are chemical [86, 87], gas phase [28], and laser ablation in liquids [12, 88, 89]. The mechanism and advantages of the laser-synthesis method are elaborated in section 3.4.

Fibrin

Fibrin is a polymerized product of fibrinogen and thrombin, forming long fibrin fibres involved in the clotting process. It is also a biodegradable, vasculogenic, anti-inflammatory protein and of high interest as a scaffold for tissue repair due to enhancing endothelial cell attachment and proliferation [26]. The endothelialization is an indicator for the vascular scaffolds, and fast endothelialization is helpful for quick recovery and reduces the chance of restenosis. The characteristics of fibrin scaffold in vascular tissue engineering have been described somewhere else, including the advantages and limitations of fibrin gels [90]. Fibrin-based scaffolds are biocompatible, easily processable, and have a high affinity to biological surfaces; however, a major challenge in applying fibrin gels is the rapid degradation and fibrinolysis causing inherent instability. Fibrin is rarely used alone due to its fast degradation in the dynamic physiological environment. Combining fibrin with other suitable materials is an effective strategy to overcome this drawback. Here, blending polymers such as polyglycolic acid (PGA) [90], collagen [91], and alginate [26] is an option. At the same time, integrating fibrin with nanoparticles is another possibility. Kirichenko *et al.* [92] investigated the effects of iron oxide nanoparticles on the gelation of fibrin gels and found the FeNPs incubation with thrombin resulted in enzyme activation and achieved a more distinct structural density of fibrin gels.

Moreover, silica nanoparticles were reported to enhance the mechanical properties of fibrin hydrogels without decreasing the fibrin proteins' ability to support cell proliferation and differentiation [93].

Collagen

Collagen is a critical component in connective tissues, which is considered a potential biomatrix in tissue engineering due to its excellent biocompatibility and involvement in various functional expressions of cells [94]. In comparison with other natural polymers, such as albumin and gelatin, collagen is not only a useful surface-active agent [95] but also exhibits biodegradability and weak antigenicity [96]. The structure of collagen Type I is based on a family of genetically distinct molecules having unique triple-helix configuration, made of three polypeptide subunits known as α -chains [97]. Nevertheless, the insufficient collagen-related mechanical property limited its growing medical applications. The researchers have already made efforts to improve this situation. It is suggested to cross-link collagen and consider it as a model for extracellular matrix, for example, combine collagen with synthetic or natural polymers or nanoparticles to overcome this problem. Recent studies have proved that AuNPs can crosslink well with collagen in the presence of EDC and Au-collagen materials have the potential to be applied in small molecule drug delivery as well as photothermal therapies, imaging, and cell targeting [98]. Xing *et al.* [99] prepared layered films of Au-collagen core-shell nanoconjugates and the obtained enhancement in mechanical properties is believed to influence cell response and promote cellular adhesion, growth, and proliferation. Hsieh *et al.* [28] found that AuNPs embedded in collagen could improve its biomechanical properties and thermal stability. The stromal-derived factor-1 α further promoted the migration of mesenchymal stem cells (MSCs) on the Au-collagen materials. Castaneda *et al.* [98] reported an approach to gelate collagen with tiopronin-modified AuNPs via EDC. In this process, tiopronin provided multiple carboxyl groups presented on the surface of AuNPs that can crosslink with collagen and couple with EDC. But tiopronin may present a variety of side effects and the role of AuNPs in the collagen gelation kinetics is still missing.

Thermoplastic polyurethane

Thermoplastic polyurethane (TPU) is suitable for application in different biomedical devices, like indwelling catheters [100], aortic balloons or mammary implants [101]. The biodegradability of modified polyester-based polyurethanes has been made possible for

scaffold fabrication [102, 103]. As successfully applied in soft tissue engineering, TPU is generally recognized to have desirable blood compatibility as well as great cellular affinity, cell adhesion, and proliferation rates. To improve the hemocompatibility and adhesive property of TPU for medical devices, attention could be focused on the nanoparticle embedded in TPU polymer. Metal nanoparticles, such as Au, Pt, Ag, and Cu, can modify the TPU surface by shifting the hydrophobic property towards an approaching hydrophilic state [14, 15]. Barcikowski group utilized laser ablation method to obtain well-dispersed nanocomposite TPU polymer films and found a fivefold improvement of endothelial colony-forming cells (ECFCs) proliferation [14, 15]. Attributed to the improved wettability negatively charged surface and higher mechanical stiffness in the vicinity of embedded nanoparticles, ECFCs were significantly adhering on the surface of TPU composites and remained in a nonthrombogenic and noninflammatory state [15].

The conventional methods used to fabricate porous polymer scaffolds are depicted in Figure 3-3 [18]. However, the drawbacks of these strategies cannot be ignored. It is believed that solvent casting has a high possibility to leave behind solvent residues in scaffolds [104]. Freeze drying and gas foaming have limitations in producing scaffolds with suitable pore size and mechanical properties [105]. The thermally induced phase separation procedures are time-intensive and complicated while electrospinning is also time-consuming and results in products with limited thickness. To overcome their drawbacks, advanced 3D bioprinting, which is believed to be the future of TE is developed to print biomaterials and living cells. The working principle of this technique can be categorized into extrusion, inkjet, and laser-assisted printing [106]. It can not only construct complex tissue models but also plot cells or other biological cues as desired [107]. Shear stress influenced by nozzle diameter, printing pressure, and viscosity of the dispersing medium should be considered during all printing. Controlling shear stress plays a key role in cell signalling and protein expression [108]. Bläser *et al.* [108] investigated shear stress of various concentrations of alginate ink and found moderate levels of shear stress (5-10 kPa) might stimulate cell proliferation. Alginate based hydrogels as printing inks have been reported but it presented a poor shape fidelity and resolution. However, this issue can be improved by incorporation of particles or fillers [4, 109]. 3D printability of LAL prepared Au/Fe polymer composites are yet to be demonstrated.

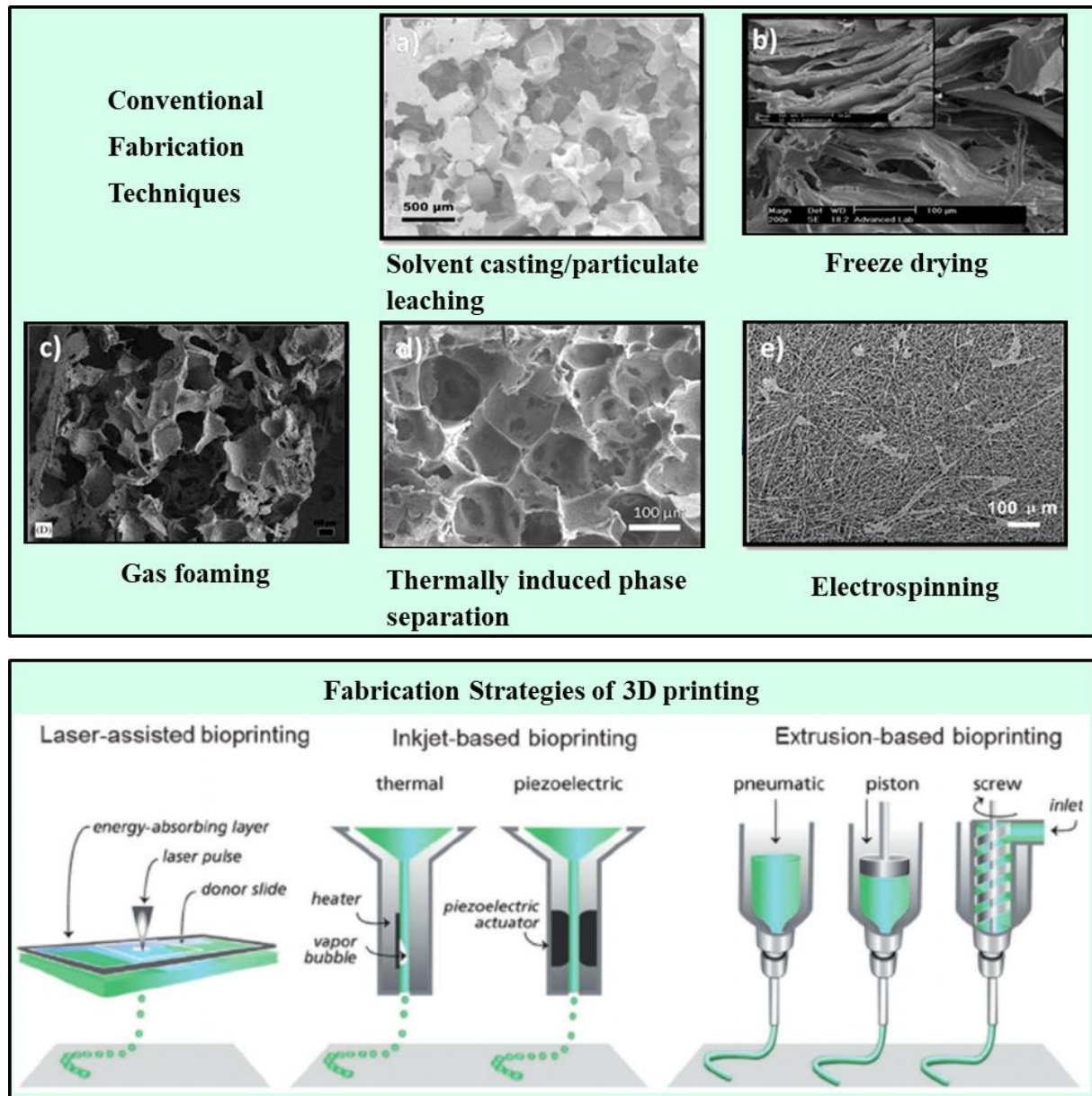


Figure 3-3: Conventional fabrication methods [18] and fabrication strategies of 3D printing [106] for polymer scaffolds.

3.2.2 Ion release from nanoparticle loaded polymer scaffolds

Metallic ion release plays a key role similar to a drug release system for tissue engineering applications. Patel *et al.* [110] suggested that Fe ion-releasing system of poly(ethylene glycol)-l-polyalanine (PEG-PA) thermogel significantly enhanced neurogenic differentiation. Fe ion release from phosphate-based glass fibres is believed beneficial to the initial cell attachment [111]. The studies have also revealed the importance of Fe ions in the regulation of the expression of vascular cell adhesion molecule (VCAM)-1 in microvascular endothelial cells [112].

In addition, it is important to control the ion release concentration in tissue engineering [113]. For example, a controlled ion release concentration is reported to promote osteogenesis, angiogenesis, and inhibition of bone resorption by osteoclasts, respectively [114]. An overdose could trigger adverse effects in the body [115]. It can be seen that the ion release concentration determines whether a substance is effective, ineffective or toxic. The so-called therapeutic window defines these areas (Figure 3-4), in which the respective substance shows desired effects. Below this concentration window of minimum effectiveness, no effect is observed; while above this window it is a toxic concentration, leading to adverse effects [113]. Moreover, the therapeutic response is also related to the onset time, offset time, and duration of the ion release process [116].

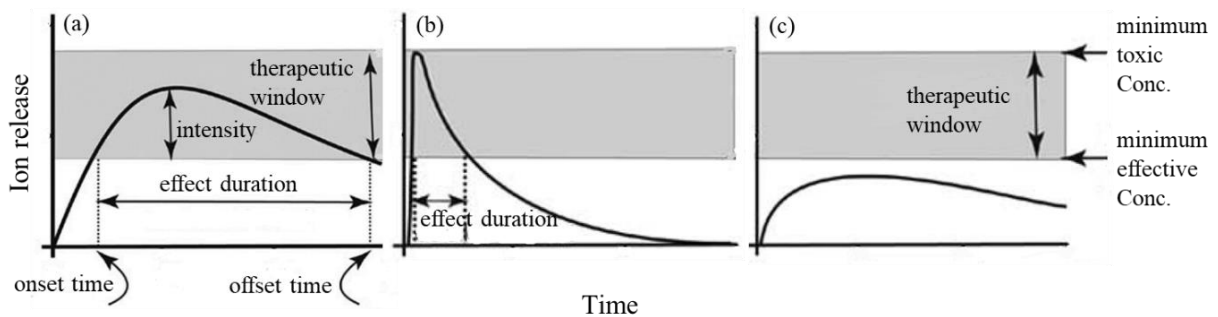


Figure 3-4: Schematic representation of the definition of the therapeutic window (modified from [116]). The grey band is indicating a therapeutic window for slower ion release formulations (a), more rapid ion release formulations (b), and formulations with prolonged ion release (c).

Generally, the ion release concentrations increase with increasing amount of nanoparticles amounts in the polymer matrix. And the release of ions from a nanoparticle-polymer composite is based on the principle of corrosion and diffusion. This takes place in three steps, oxidation (to erode the surface of nanoparticles), dissolution and diffusion (release of ions from the bulk nanoparticles). Different models can describe the kinetics of ion release, for example, the frequently used Korsmeyer-Peppas equation [117, 118]:

$$\frac{\partial c}{\partial t} = D_{eff} \frac{\partial^2 c}{\partial x^2} + k(C_s - C) \quad (1)$$

$$D_{eff} = D_{iw} \frac{\epsilon}{\tau} \quad (2)$$

C_s is the substance's solubility in the hydrophilic porous structure; k is the dissolution constant; In equation 2, the effective diffusivity D_{eff} in the pores can be expressed by substance's diffusivity in water D_{iw} , the porosity of system ε , and tortuosity of the diffusional path τ .

Korsmeyer-Peppas equation is termed from “swelling-controlled release from a polymeric system” depending on porous structure as well as the thermodynamic interaction between polymer and solute [118]. In the study of Hahn *et al.*, they determined Cu^{+2+} and Ag^+ ion release characteristics from silicone composites and proposed the two metal ions release profiles were described by a second-order exponential equation and pseudo-first order exponential equation, respectively [119]. And it should be noted that diffusion from the nanoparticle-polymer system is not following Fick's law [120]. When nanoparticles are embedded in polymers, the NP concentration and polymer matrix structures determine the diffusion. Moreover, several incubation factors are corresponding to the ion release mechanisms. The dissolution process of released ions diffusing out of the matrix into the surroundings can be influenced by the properties of solvents, such as pH [121, 122], concentration or ionic strength [123], the physicochemical property of polymer matrix [12], and the particle size [124]. Further, when the distance for diffusion increases, ions diffuse at a comparatively slow rate [125]. Recently, researchers found that modification using natural polymers like polysaccharides may slow their releasing rate into surroundings [87]. The diffusion-based release and multi-element release mechanisms have already been considered. It was acknowledged that Fe ion release was found to follow second-order kinetics [13]; however, the effects of oxide solubility and polymer matrix on Fe ion release have not been frequently studied.

3.2.3 Impact of Au and Fe nanoparticles on properties of polymer composites

Many outstanding publications dealt with improving the properties of polymer composites in the last few years. The characteristic physical properties of biomaterials including surface, physicochemical, mechanical properties are essential for cell growth and proliferation (Figure 3-5), which can be modulated by the incorporation of nanoparticles and polymeric networks [40]. For example, immobilization of AuNPs was demonstrated to stabilize enzyme molecules on polyurethane surfaces [20]. Mandapalli *et al.* [126] investigated six types of polymers including polyvinyl alcohol, hydroxypropyl methylcellulose, polycaprolactone, alginate, chitosan, and zein protein to study how AuNPs altered their physical properties. The results indicated that entrapment of AuNPs slightly decreased the porosity and swelling ratio but significantly increased the skin adhesion strength of all polymer films. However, contrasting

results were reported that the tensile modulus of nanoparticles-alginate composites was slightly lower than pure alginate ones, while the overall swelling ratio increased in the long-term [12].

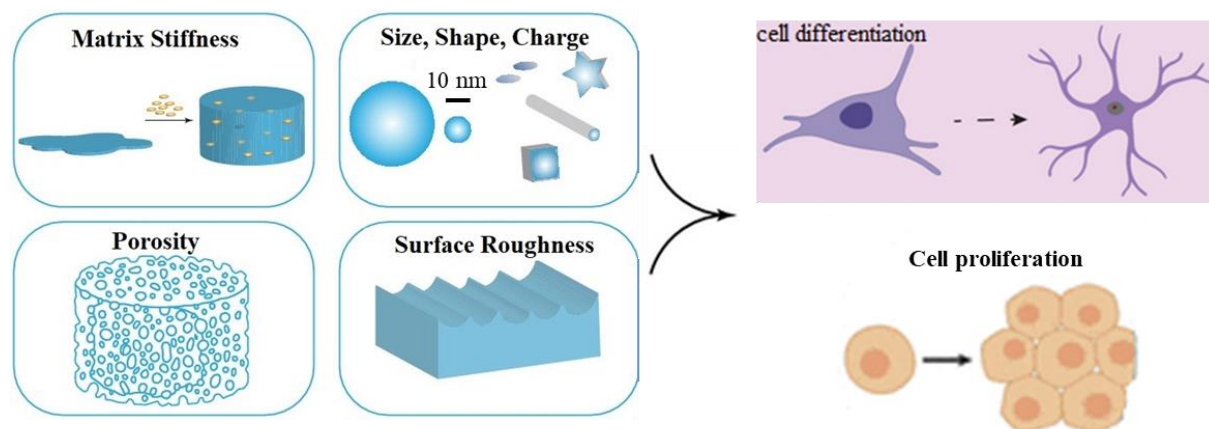


Figure 3-5: Characteristic physical properties of a biomaterial such as matrix stiffness, porosity, or roughness and effects on cell differentiation and proliferation (modified from [40]).

Except acting as an ion reservoir as described in section 3.2.2, ignoble metal nanoparticles influence the interface properties of polymer films. Fe/FeO NPs have been reported to lead to a more distinct structural density of fibrin gels in the presence of thrombin, which might be used for treating some hemostasis diseases [92]. Machida-Sano *et al.* [127] confirmed that Fe-alginate provided an appropriate surface for protein adsorption and cell attachment due to the less hydrophilic surface compared to pure alginate cross-linked by Ca^{2+} . Brändle *et al.* [10] have reported that the pore size of PEG hydrogels was around tens of micrometers and not affected by the embedded Fe nanoparticles. It is easy to measure the pore size of hydrogels with confocal microscopy or scanning electron microscopy after they are freeze dried. A rheological method is developed to investigate *in situ* dynamic polymerization reactions, mechanical properties, and even pore size of hydrogels [128, 129].

3.3 Bioactive glass in bone tissue engineering

Despite the remarkable self-healing properties of bone, the trauma or surgical resections provoking the emergence of relevant defects remains a critical issue in current clinical practice [130, 131]. When bone fails to heal properly, autograft or allograft is an attractive yet extremely challenging strategy [130, 132]. However, autografts are limited in supply since they require donor sites and also cause chronic pain at donor sites; while allografts are in a low rate of solid bony fusion due to lack of osteogenic and osteoinductive properties and have an increased risk

of immunologic mismatch and inflammatory reaction [132]. The utilization of synthetic scaffolds which support tissue regeneration could be an alternative to overcome these limitations. The “gold standard” for an ideal graft should be able to support osteointegration, osteoconduction, osteoinduction, and osteogenesis [133]. In recent years, numerous suitable bone graft substitutes have been developed. Venkatesan *et al.* [134] reviewed alginate-based composites to prepare artificial bones, including alginate-polymer, alginate-protein, and alginate-bioglass. These composites showed excellent biocompatibility, enhanced mechanical strength, and supported osteogenic differentiation.

Among these replacement materials, 45S5-BG with the compositions of 45 wt% SiO₂, 24.5 wt% CaO, 24.5 wt% Na₂O, and 6.0 wt% P₂O₅ initially synthesized by Hench [135] has advantages of controllable biodegradability, cell delivery, osteoconductivity and bioactivity [34, 133, 136]. As interaction with surrounding tissue or in the stimulated body fluid, the surface of 45S5-BG rapidly reacts inducing osteoconductive and osteoproduative effects [133]. Firstly, it is the exchange between Na⁺, Ca²⁺ cations and H⁺ or H₃O⁺, followed by soluble silica and calcium dissolution. The generated Si(OH)₄ can immediately re-polymerize and form a SiO₂-base layer on the surface. Due to the accumulation of Ca²⁺ and (PO₄)³⁻, CaO-P₂O₅ rich layer grows on top of the SiO₂-base layer. CaO-P₂O₅ rich layers continue to crystalize in the presence of OH⁻ or (CO₃)²⁻ from the surroundings and form a biologically active apatite layer that is believed to bond with the host tissue [45].

The evolution and grand challenges of bioactive glasses were well-documented in this review [114]. On the present commercial market, the trade melt-derived 45S5 BG particles are far larger than 1 μm [114]. Nanosized BG particles bear a larger specific surface area range of 28-70 m²/g and were reported to exhibit enhanced bioactivity [136]. Flame spray synthesis is another method to produce BG nanopowders with a 20-40 nm size distribution at a high temperature (1450 °C) [136]. Sol-gel technology is a conventional way to prepare solid or hollow spherical BG materials in nanoscale, but with uncontrolled compositions and failed doping of metallic ions [35]. It is still a challenge to achieve doped ions and nanosized BG particles simultaneously.

Laser fragmentation is a method to downsize microparticle or even nanoparticle colloids by transferring the energy of high-intensity light irradiation into the process [16, 137]. Siebeneicher *et al.* [50] reported a reduced bismuth ferrite particle size from 450 nm to below 10 nm using an elliptical liquid jet. The thermal mechanism of such flow jet setup was discussed

by Waag *et al.* with Mie theory and divided the cross-section into three main symmetry parts: non-irradiation, non-thermal mechanism, and thermal melting [137]. Not only for metals, but laser fragmentation was also reported to successfully reduce and narrow the particle size distribution (< 3 nm) of Yttrium Iron garnet without changing its stoichiometry [138]. Lau *et al.* [139] provided insights into the laser fragmentation mechanism downsizing zinc oxide and boron carbide particles. Charipar *et al.* [140] suggested photothermal evaporation and Coulomb explosion occurring to ZnO nanoparticle formation via laser fragmentation and perhaps accompanied with simultaneous laser melting. Recently, Nakamura and co-workers successfully prepared calcium phosphate glass spheres in submicrometer and micrometer sizes with a laser system at the wavelength of 355 nm, in the presence of metal salts as the light-absorbing agent [49]. Inspired by these results, laser fragmentation may be suitable for generating nanoscopic BG particles with doping metal ions.

3.4 Nanoparticles-polymer composites generated via laser synthesis in liquids

To prepare nanocomposites, mixing nanoparticles with polymer solutions is a common way. AuNPs can be chemically synthesized with raw material HAuCl_4 in the presence of reducing agents. Similarly, iron or iron oxide nanoparticles are generated through thermal decomposition and chemical reduction with various iron salts and reducing agents [11]. How to get rid of extra additives is one of the problems in the chemical synthesis of nanoparticles, which is vital to the following biological applications. In addition, the surface properties of polymer matrices are sensitive to particle dispersion. The laser ablation in liquid (LAL) method was demonstrated to obtain uniformly distributed nanocomposites [16, 141].

3.4.1 Laser ablation in liquids

The processes of LAL have been well discussed, which can be classified into three stages: the plasma phase, the cavitation, and dispersed nanoparticles interacting with liquid molecules after bubble collapse [16]. These physical processes are distinctly different from pulse duration (millisecond, nanosecond, picosecond) [142]. Since we utilized a picosecond laser in this work for ablation, we mainly discussed the mechanism of ps laser ablation in liquids. As shown in Figure 3-6a, plasma, composed of highly ionized or atomic matters, is generated on the target surface when a laser reaches the target through a liquid. A complex nanoparticle formation process will last from tens of ns to a few μs [142]. Laser-induced shock wave occurs in tens

of ns and moves away in hundreds of ns. A sharp quasi-hemispherical cavitation bubble forms in the liquid microseconds later. The ablated species (ions, atoms, and atom clusters) may interact with the surrounding liquid and trigger chemical reactions [142-144]. These cavitation bubbles undergo expansion and collapse after hundreds of microseconds. Several laser parameters such as laser intensity, fluence, repetition rate, and laser pulse duration, as well as liquid properties can affect the final obtained nanoparticles [16].

The primary particles (< 10 nm) form the plume expansions during the first ns and at the early stage of first bubble expansion and is possible to be ejected from the target. The initial plume expansion may cause injection of vaporized atoms into surrounding liquid thus leading to the particle formation outside the cavitation bubble. In this initial phase of LAL < 3 ns, a trimodal size distribution consists of atom clusters (1-2 nm), nanoparticles (< 10 nm) and large droplets (tens of nm) (Figure 3-6c) [145]. Major primary particles gather near the bottom of the bubble and density decays toward the top of the bubble [145]. The formation of secondary particles (≥ 50 nm) is suggested due to the agglomeration of primary particles during the bubble collapse. Figure 3-6b shows the evolution of phase states. The authors predict that smaller particles form in the liquid–gas region (orange zone) while larger particles originate from the metastable liquid (l) zone (yellow) [143].

3 Theoretical Background

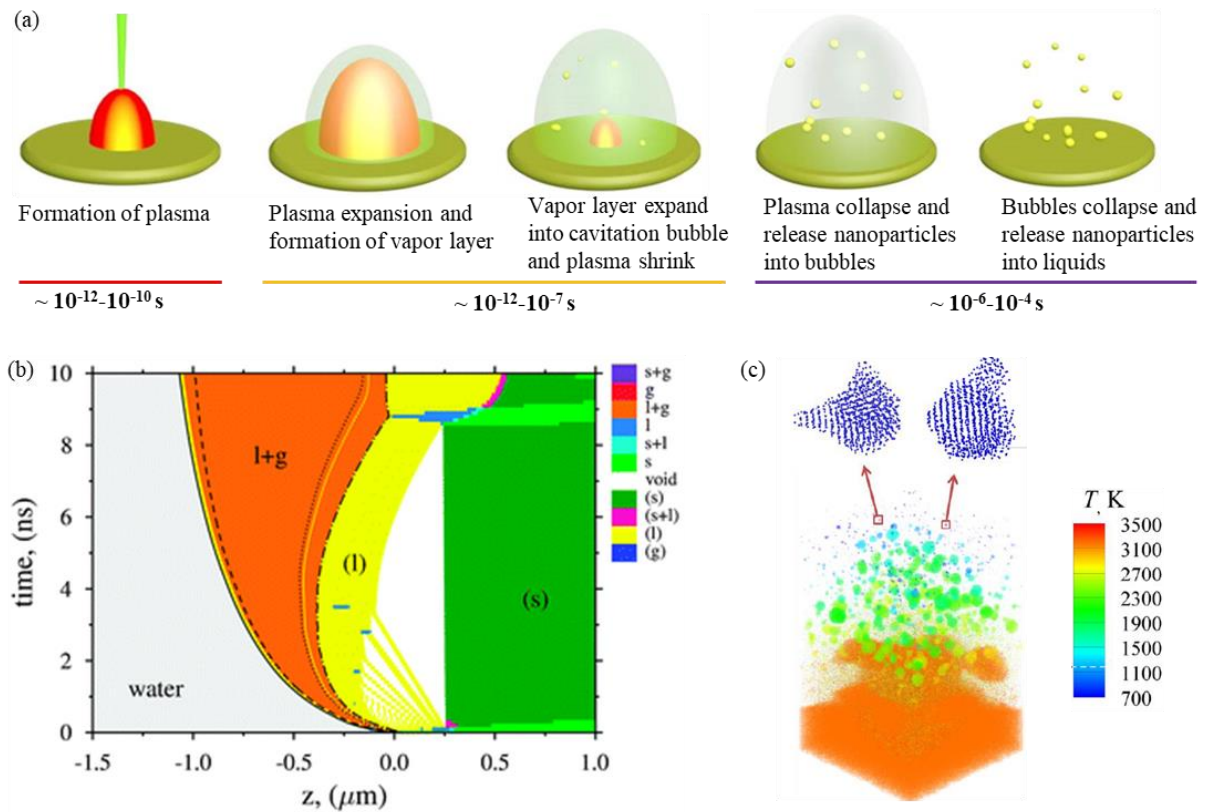


Figure 3-6: (a) Mechanism for laser ablation in liquids [142], (b) time-space phase diagram for femtosecond laser ablation of gold in water in simulations performed at the fluence of 0.55 J/cm^2 [143], (c) snapshot of the atomic structure colored by local temperature in simulations performed for 3 ns after the laser pulse at the fluence of 0.04 J/cm^2 and enlarged view of two crystalline nanoparticles located in the upper part of the bubble [145].

3.4.2 Fabrication of nanocomposites based on laser ablation in liquids

Previous findings demonstrate LAL is flexible, chemical clean, and open for the fabrication of other innovative nanoparticle-polymer composites. Zhang *et al.* [16] gave out similar explanation about the synthesis of nanoparticle-polymer composites through *in situ* LAL. The size quenching function of macromolecules in the LAL process, probably outside of the bubble, was frequently discussed [16, 88]. The liquids in the process of LAL can generally be water as well as in organic liquids such as ethyl acetate, ethanol, acetone [144], *N*-methyl-2-pyrrolidone (NMP) [146], monomer solution [147] or even oils [148]; while the targets can be any solids, such as noble or ignoble metals and ceramics. These liquids can be suitable solvents for the chosen polymers to get polymer solutions at desired concentrations. Three main strategies based

on LAL method to fabricate nanocomposites are discussed in reference [149], as shown in Figure 3-7:

(1) The bulk targets are laser-ablated in a solution of typical solvents with small amounts of polymer for *in situ* generation of nanocomposites. With this strategy, nanoparticles can be functionalized and stabilized. Moreover, through the evaporation of solvents or addition of more polymers, nanocomposites at the desired concentrations can be achieved.

(2) The bulk targets are laser-ablated in the monomers. Nanocomposites are formed as the initiators added for polymerization.

(3) The NP colloidal solution is firstly generated by LAL. Then the as-prepared solution or dry nanopowder is directly mixed with the polymer. However, the stability of obtained composites should be further improved.

A variety of nanoparticle-polymer composites have been produced through LAL, such as nanoparticle-TPU [14, 15], -alginate [12], -*N*-Vinylcaprolactam (VCL) and poly(ϵ -caprolactone) (PCL) [147], -PEG [17], -poly(methyl methacrylate) (PMMA) [150], -chitosan and starch [151]. Zhang and Gökce well documented the perspectives corresponding to nanoparticle-polymer composites' characterization, downstream processing methods, and potential applications [16]. In these studies, control over NP size and distribution are often discussed. Compared to other ligand-free method, for example gas-phase method, LAL has advantage of small particles uniform dispersion in polymer matrix [149]. However, compared to conventional chemical reduction synthesis, the drawback of limited NP productivity of LAL cannot be ignored. Million *et al.* [147] revealed a repetition rate in the range of 10-30 kHz and VCL monomer concentration below 0.02 M to gain a high laser efficiency of *in situ* embedding of Zn, Fe, Au NPs in polymer solutions, and the monomer turbidity could significantly reduce laser ablation efficiency. It is usually achieved high NP productivity at low polymer concentration. In this regard, uniform particle dispersion cannot be guaranteed. At an optimal polymer concentration, one can achieve well-dispersed nanocomposites, while using a polymer concentration lower or higher than this value will result in particle agglomeration or aggregates in the polymer matrices [14].

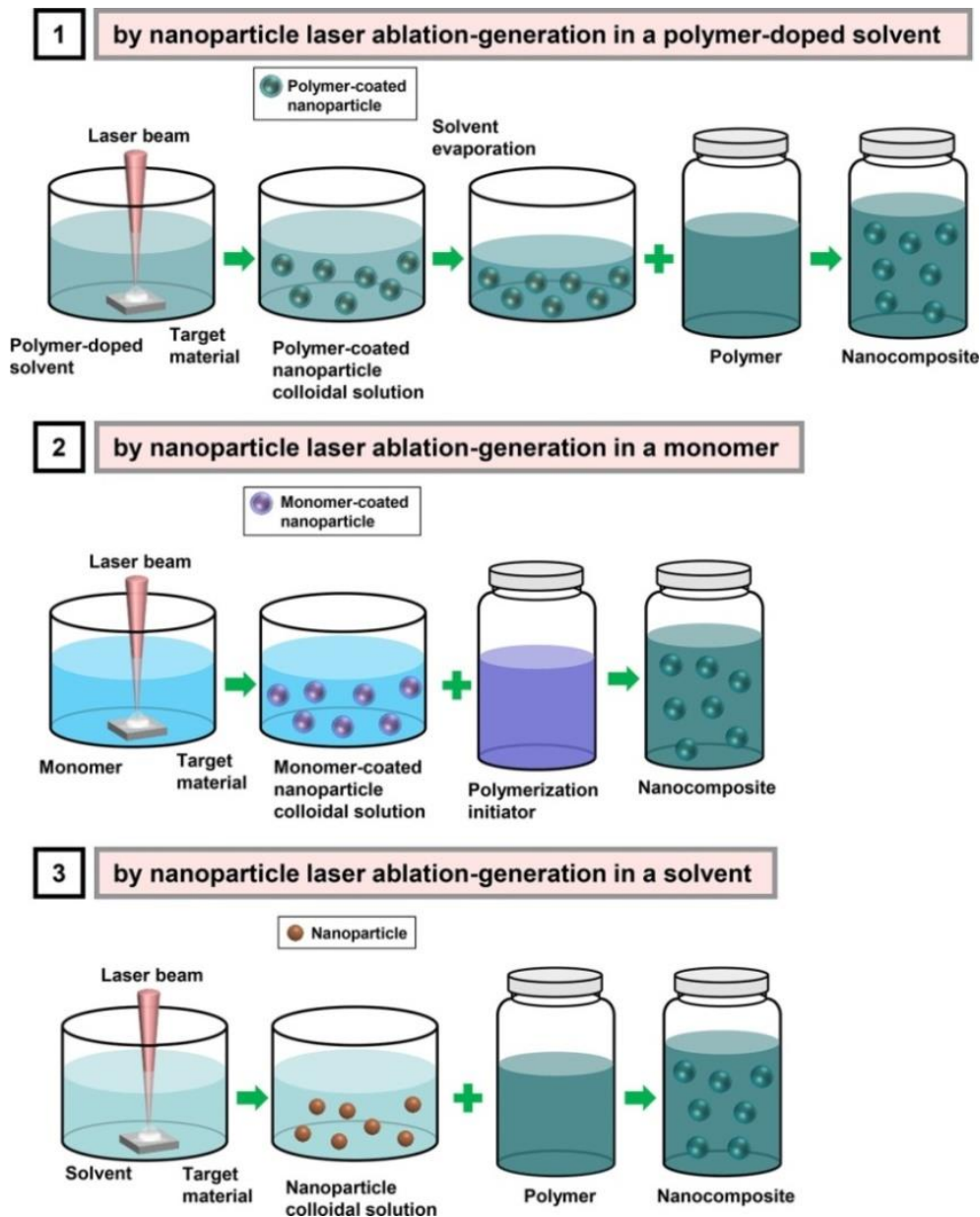


Figure 3-7: Strategies for the fabrication of nanoparticle-polymer composites based on the laser ablation in liquids method [149].

It is known that the laser ablation efficiency and productivity depend on the aforementioned laser parameters and liquids properties. Usually, the laser ablation rate is higher in water than in organic liquid [144]. It is evidenced that there are gas mixtures, such as H_2 and O_2 in water and H_2 , O_2 , CO , CO_2 , CH_4 , etc. in organic liquids, providing the shielding effect on the incoming laser. The slow ascending speed and extended dwell time of persistent bubbles will decrease the nanoparticle productivity [144]. However, with respect to polymer solutions, one should not only consider inorganic or organic solvents and polymer chains but also characteristics of polymer solutions, including viscosity, turbidity, density, and even pH values. Hence, work in

this thesis will focus on the effects of as-stated characters of polymer solutions on NP productivity, size distribution, dispersion in the polymer solutions and even gelated hydrogels or casting polymer films.

3.5 Gelation of nanoparticles-polymer composites

Gelation has no clear definition and it remains to be well understood. The transition from a system with soluble branched polymer or macromolecular chains to infinite molecules can be also called “gelation” and the critical point where gel first appears is called the “gel point” [152]. Gelation can also be defined as the formation of a three-dimensional network by chemical or physical cross-linking [153]. Physically crosslinking gels are usually weaker than the chemical ones because of the strong chemical bonds between polymer chains. Redaelli *et al.* [152] summarized the gelation mechanism of hydrogels for medical applications, as shown in Figure 3-8. They also described that cross-linking nature affects the properties of hydrogels in terms of mass transport, degradation, swelling behaviours, rheological and mechanical properties. Kojima *et al.* [154] added the ovalbumin secretory signal peptide in collagen gels could enhance collagen hydrogels’ stiffness and storage modulus and increase the contact angles. The formation of oxime cross-linked alginate hydrogels at the variation of pH and temperature can change their stiffness and stress relaxation, which has an ideal short-term cytocompatibility with the encapsulated cells [55]. Wu *et al.* [155] studied the mechanism and effects of polyphenol derivatives gelated with collagen and found that alkaline-oxidation conditions favoured cross-linking strength via covalent bonding.

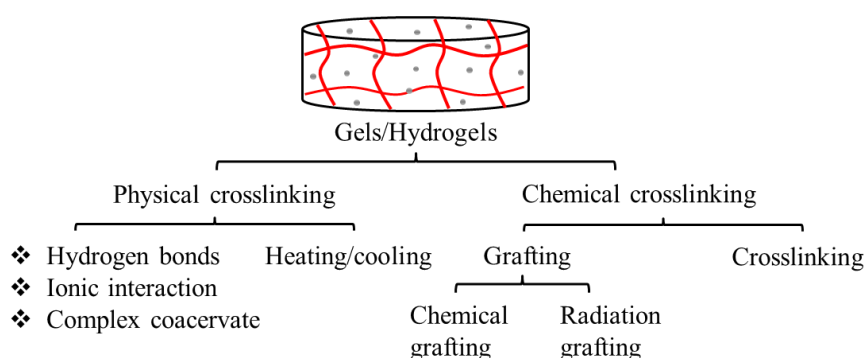


Figure 3-8: Classification of gelation mechanism (modified from [152]).

The hydrophilic, porous nature of cross-linked hydrogels contains four different states of water: free water, weak bound, semibound and strong bound water to the polymer network [156]. In turn, water organization is related to the swelling ratio, matter diffusion, release behaviours in

hydrogels. Swelling ability is determined by the interactive forces between polymer chains and water in an equilibrium state, which is also related to the pore size. For example, microporous alginate contains primarily water, and the swelling mechanism is related to molecular diffusion and convection in the water-filled pores [152].

3.6 Rheological property of nanoparticles-polymer composites

Rheological measurement is a primary experimental method to explore the physical, tunable mechanical, and viscoelastic properties of hydrogels related to their biological applications [157, 158]. For example, the mechanical stiffness of gels is essential to support itself as a scaffold to promote cell adhesion and growth [99]. To measure mechanical property quantitatively, shear rheology experiments are usually performed on the cell-embedded hydrogels [159]. Suitable flow properties would make hydrogels to be excellent candidates for injectable therapeutic delivery vehicles if they shear-thin upon the application of allowable shear stress and rapidly self-heal into solids once the stress is removed [160]. The outcome of the study showed that the viscosity of polymer solutions is a key parameter for 3D printing rather than the concentration or molecular weight [161].

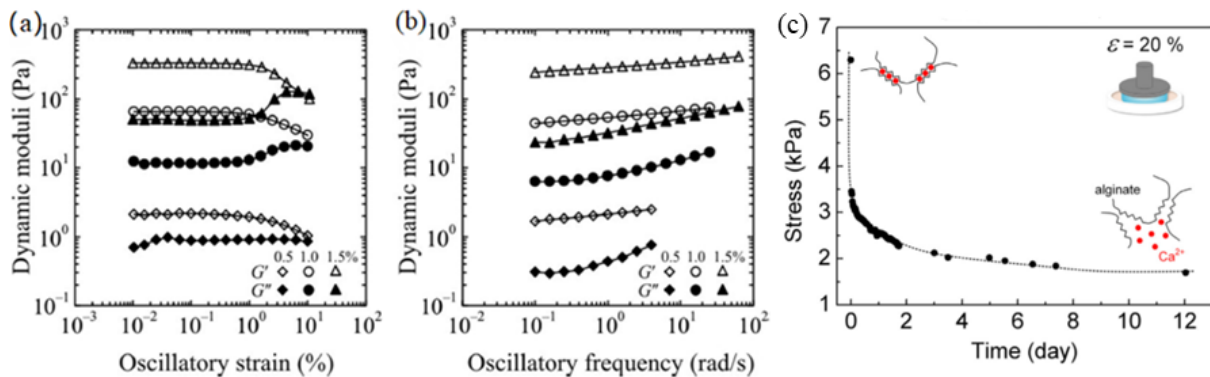


Figure 3-9: Storage and loss moduli as a function of (a) oscillatory strain and (b) oscillatory frequency for cellulose nanofibrils suspensions at different concentrations (0.5–1.5 wt%), measured using Couette geometry [162]. Stress relaxation of the Ca-alginate hydrogel (c) [163].

The field of rheology, theoretical and experimental, is well introduced in Thomas G. Mezger's book [164]. Yan and Pochan conducted the rheological characterization of polypeptide-based hydrogels, including bulk mechanical properties, gelation mechanisms, and the behaviour of hydrogels during and after flow [158]. For hydrogel samples, shear storage modulus (G'), loss modulus (G''), and loss factor ($\tan\delta$) parameters are critically monitored against frequency,

strain, and time, which can be measured with small amplitude oscillatory shear method (Figure 3-9). Usually, G' and G'' are characterized for morphological evolution [165]. The mechanical parameter, for example, elastic moduli (E) of hydrogels can also be determined from the storage modulus (G') using:

$$E = 2 \times G' (1 + \nu) \quad (3)$$

where ν = Poisson's ratio (0.5 for hydrogels [159]).

Moreover, the shear-thinning behaviour for non-Newtonian fluids whose viscosity decreases under shear strain and sometimes considered synonymous for pseudoplastic behaviour, can be defined as excluding time-dependent effects, for example, thixotropy reflected through complex viscosity against the shear rate [160, 161].

4 Materials and Methods

4.1 Chemicals and equipment

The used chemicals and devices in this work were listed in Table 4-1 and Table 4-2, respectively.

Table 4-1: Chemicals and materials used.

Chemical and materials	Producer	Specifications
Targets		
Au target	Allgemeine Gold- und Silberscheideanstalt AG	Purity \geq 99.99 %, 0.5 mm thickness
Cu target	Sigma-Aldrich, Goodfellow	Purity \geq 99.95 %, 0.5 mm thickness
Fe target	Sigma-Aldrich	Purity \geq 99.99 %, 0.25 mm thickness
Zn target	Sigma-Aldrich, Goodfellow	Purity \geq 99.95 %, 0.1 mm thickness
Macromolecules		
Agarose	Carl Roth GmbH	
Bovine serum albumin	Sigma-Aldrich	Purity \geq 96%
Collagen Type I	Sigma-Aldrich	
Sodium alginate	Sigma	61% β -D-mannuronic acid and 39% α -L-guluronic acid
TPU	Elastogran	Elastollan1190A, Shore A=90
TRITC-coupled albumin	Thermo Fisher	
Chemicals		
45S5 Bioglass	SCHOTT AG	
Calcium chloride	AppliChem	Purity \geq 97%
Coomassie Blue G-250	Sigma-Aldrich	
EDTA	Sigma	98.5 % purity
Ethanol	Sigma-Aldrich	Purity \geq 99.8%
Glacial acetic acid	J.T.Baker	Purity \geq 99 %
Glutaraldehyde	Alfa Aesar	50% w/w, aq-sol
Iron dichloride tetrahydrate	Alfa Aesar	98 % purity

Chemical and materials	Producer	Specifications
Chemicals		
Nitric acid	Merck Millipore	60%, suprapur
N-hydroxysuccinimide	Sigma-Aldrich	Purity \geq 98 %
Piperazin-N,N'-bis(2-ethansulfonsäure)	Sigma-Aldrich	pH 7.4
Phosphoric acid	AppliChem	85%
Sodium chloride	Sigma-Aldrich	Purity \geq 99 %
Thulium standard	Merck	Concentration: 1g/L
Tetrahydrofuran	Sigma-Aldrich	Purity \geq 99.9 %
Yttrium standard	Merck	Concentration: 1g/L
Zinc standard	Merck	Concentration: 1g/L
1-ethyl-3-(3-dimethylaminopropyl) carbodiimide	Sigma-Aldrich	Purity \geq 98 %
24-well plate	Eppendorf AG	

Table 4-2: Used equipment or devices in the experiments and analytics.

Equipment	Model	Producer	Used settings and specifications
Laser system			
Laser system	Atlantic 1064/532	Ekspla	Picosecond Wavelength: 1064 nm Pulse duration: <10 ps Pulse energy (at 100 kHz): > 160 μ J
	TERMOTEK	Edgewave	Picosecond Wavelength: 355 nm pulse energy (at 100 kHz): > 47 μ J
Scanner	Scancube 10 Software: Laser desk 1.0.3.31189	Scanlab	Scan speed: 6.0 m / s
Pulse generator	TGP 110	Aim&Thurlby Thandar Instruments	Frequency range: 0.1 Hz 10 MHz

Equipment	Model	Producer	Used settings and specifications
ADC	DC24000 UHR	CPS Instruments	405 nm laser
AFM	AFM 5100	Agilent Technologies	
Analytical balance	Precisa 300-9234/H	PESAWaagen	Readability: 0.01 mg
Contact angle	OCA-15	Dataphysics	Software: SCA20-F
DLS	380 DLS	PSS NICOMP	Measuring range: 0.3nm-10 μ m Accuracy: \pm 2%
Electrokinetic analyzer	SurPASS	Anton Paar	Software: VisoLab
FTIR	FT/IR-430	Jasco	
ICP-MS	ELAN 6000	Perkin-Elmer	Detection range: 1-270 u
LSCM	TCS SP8	Leica	White light laser (WLL), 1.5 mW, 470-670 nm
Micro-viscometer	Lovis 2000M	Anton Paar	
pH meter	PCE-PHD 1	PCE Instruments	Measuring range: 0-14 pH Accuracy: \pm 0.02 pH Resolution: 0.01 pH
Rheometer	Physica MCR 301	Anton Paar	
Power meter	Field Max II TOP	Coherent	
SEM	XL 30	Philips	
	Apreo S LoVac,	Thermo Scientific	
TEM	CM 12	Philips	acceleration voltage 20-120 kV Pressure: 10^{-6} mbar

Equipment	Model	Producer	Used settings and specifications
UV-Vis	Evolution 201	Thermo Scientific	Xenon lamp Measuring range: 190-1100nm Accuracy: ± 0.8 nm
XRD	DB	Bruker	Copper α radiation
3D-bioprinter	SuperFill – Robo	Black Drop	

Used equipment not listed here will be considered as standard laboratory equipment. The following computer programs were used for data evaluation: (1) OriginPro, version 2018, (2) ImageJ, version 1.45s, (3) Gwyddion.

4.2 Laser synthesis of nanoparticles in liquids

4.2.1 Generation of nanoparticle-polymer composites via laser ablation in liquids

Polymers were firstly dissolved in suitable solvents to get different concentrations. Alginate solutions were prepared by dissolving sodium alginate powder in deionized water. Thermoplastic polyurethane (TPU) was kindly provided by BASF company, Germany. TPU was dissolved in tetrahydrofuran (THF) while collagen type I was dissolved in diluted glacial acetic acid under stirring. The concentration of collagen was 0, 1, 2, 4 mg/mL. The acetic acid concentration was varied from 5 to 200 mM and pH values were recorded with a pH-meter and a microelectrode (Sartorius) at room temperature. The polymer viscosity was measured using a microviscometer. The picosecond pulsed laser beam was focused into a Polytetrafluoroethylene (PTFE) batch chamber containing the bulk target and 30 mL of the polymer solution. The laser parameters are listed in Table 4-3. During the ablation process, the liquid was stirred with a motor. The control samples of alginate solutions and TPU were laser-processed in the absence of an ablation target. The nanoparticle concentration was determined by the weight difference of the targets before and after laser ablation using an analytical balance. All the standard deviations in this work were from three-fold samples.

Table 4-3: Laser and process parameters used for the fabrication of nanoparticle-polymer composites.

Parameter	
Wavelength	1064 nm
Pulse duration	<10 ps
Pulse energy	88 μ J
Nominal laser fluence	1.26 mJ/cm ²
Repetition rate	100 kHz
Spiral	6 mm
Working distance (scanner lens to target)	110 mm
Water column	3 mm
Liquid volume	30 mL

Characterization of nanoparticle-polymer composites

Transmission electron microscopy (TEM) was employed to analyze the colloidal dispersion of polymer-coated nanoparticles. In case of high concentration of polymers hindering the investigation, deionized water was used to dilute them. The statistical analysis of the particle size was carried out using the ImageJ software. To determine the number-weighted particle size distributions, Feret diameters of at least 400 nanoparticles per sample were counted for statistical analysis. The data was plotted as histograms and fitted using a log-normal function to obtain the average particle size. The polydispersity index (PDI) was calculated from the following equations [166]:

$$PDI = \frac{Var(x)}{x_c^2} \quad (4)$$

$$Var(x) = e^{2 \ln(x_c) + w^2} (e^{w^2} - 1) \quad (5)$$

where x_c and w^2 from the Log-normal model representing median value and standard deviation, respectively.

To compare with the particle size from TEM, the number-weight value was used. Meanwhile, dynamic light scattering (DLS) and analytical disc centrifugation (ADC) analysis was also used to measure the size of particles. DLS measurements were carried out at 25 °C using a disposable

U-shaped capillary cell with a sample volume of 750 μL . The obtained hydrodynamic particle size can be calculated from Stokes-Einstein equation [167]:

$$D = \frac{k_B T}{6\pi\eta r} \quad (6)$$

k_B is Boltzmann constant ($1.38 \cdot 10^{-23}$ J/K); T is the kelvin temperature and η is the liquid's dynamic viscosity.

ADC measurements employed a saccharose density gradient (24 wt%, 22 wt%, 20 wt%, 18 wt%, 16 wt%, 14 wt%, 12 wt%, 10 wt%, 8 wt%, each 1.6 mL), a known size and density of standard particle solution to achieve particle size distribution based on the principle of detected sedimentation time and the absorbance of light. 0.1 mL of sample was injected after the size calibration at a centrifugation speed of 24,000 rpm with a lower detection limit set to 5 nm.

Ultraviolet-visible spectroscopy (UV-Vis) measurements were carried out to detect the specific absorbance of the analytes in a 750 μL quartz cuvette with 1 cm of light path length. The measuring spectral range was from 190 nm to 900 nm with an interval of 1 nm. Fourier-transform infrared spectroscopy (FTIR) was employed to characterize the chemical groups before and after laser ablation. As 1 mg of dry powder samples directly contact an optically dense crystal, the IR beam is internally reflected and recorded as an interferogram signal that can be transferred to an IR spectrum. 32 scans were set for each spectrum at the resolution of 4 cm^{-1} in the mid-infrared region of 4000-500 cm^{-1} . X-ray powder diffraction (XRD) was used to determine the iron phase of laser generated FeNPs in polymer solutions or in water. The freeze-dried powder was homogeneously spread on a silicon single crystal to minimize scattering. The scan was in a 2θ range of 10–90° with a 0.02° step^{-1} at 4° min^{-1} .

4.2.2 Nanoscopic bioactive glass prepared via laser fragmentation

Laser fragmentation of the reaction mixture

The raw bioglass (BG) powder was purchased from Schott AG with a diameter in the range of 3.5-4 μm . 89 mM Fe-EDTA solution was prepared with 1.78g $\text{FeCl}_2 \cdot 4\text{H}_2\text{O}$, 2.62g EDTA, 1.14g NaOH, and 400 μL HCl, as reported before [168]. 0.04 g alginate powder was dissolved in 20 mL Fe-EDTA solution. Prior to laser fragmentation, 5 wt% bioactive glass powder was

dispersed in the solutions. The laser fragmentation process was performed on the third harmonic (355 nm) of Nd:YAG laser system, details listed in Table 4-4.

The number of pulses per volume was calculated with the equation [169]:

$$N_p = \frac{h \cdot R_r}{V_L} \quad (7)$$

h indicates laser beam diameter; R_r is the repetition rate and V_L is the velocity of the liquid.

The employed setup is a flow jet controlled by a valve and the laser beam passing through the flowing liquid as previously described by Lau *et al.* [139]. The flow reactor was coupled with a power meter to balance laser power during the process (Figure 5-37a). The volumetric flow rate \dot{V} was measured with a timer and graduated cylinder, and the velocity of the liquid was calculated using \dot{V}/A (A indicates laser irradiated cross-sectional area). In this process, the working distance was 100 mm focal length of the lens so that 86.2 % of the liquid volume was illuminated by the laser [137]. 30 irradiation passages were used to obtain the final product. To separate small bioglass particles, laser fragmented product was centrifuged at 34 g for 5 min. Both supernatant and sediments were separately dried at 60 °C for 48 h and weighed with a precision balance to calculate the yield of small particles. All standard deviations are from triplicates.

Table 4-4: Laser parameters used for fragmentation of bioactive glass with a flow jet.

Laser parameters	Nanosecond LFL	Picosecond LFL
power (W)	9.2-10.4	4.6-6.8
wavelength (nm)	355	355
pulse duration	< 40 ns	10 ps
mean volume flow rate (mL/s)	0.54	0.54
pulse energy (μJ)	231-260	47-70
repetition rate (kHz)	40	98
laser fluence (mJ/cm ²)	56-63	3-4.5

Characterization of the bioglass products

The absorption spectra of the educts and product dispersion were obtained using UV-Vis spectrophotometry. Fourier-Transform Infrared Spectroscopy (FT-IR) was used to identify the changes of chemical groups or bonds of bioglass through laser fragmentation. X-ray powder diffraction (XRD) was used with a Bruker D8 Advance diffractometer (Cu K α radiation, $\lambda = 1.54 \text{ \AA}$; 40 kV, 40 mA) to determine the crystal structure of BG particles and contained Fe. The scan was in a 2θ range of $10\text{--}90^\circ$ with a $0.02^\circ \text{ step}^{-1}$ at 4° min^{-1} . The freeze-dried powder was homogeneously distributed on a single silicon crystal to minimize scattering.

The morphologies and particle sizes were measured by scanning electron microscopy (SEM) equipped with energy-dispersive X-ray spectroscopy (EDX). The hydrodynamic particle size of 0.1 mL samples was measured with an analytical disk centrifuge (ADC) at 12 000 rpm for 10 min. To further determine the distribution of the elements and iron phases, the prepared ultra-thin samples were analyzed using an analytical TEM system operated at 200 kV equipped with an energy dispersive X-ray spectrometer. It should be mentioned that the samples measured with ADC and TEM were firstly centrifuged at 537 g for 5 min. To detect elements in BG samples, the removal of extra ferrous ions was further conducted by centrifugation washing three times with MilliQ water at 537g for 10 min and dispersed again in MilliQ water.

***In vitro* ion dissolution study**

50 mM Tris buffer (Trizma base, Sigma-Aldrich) solution was used as the incubation medium adjusted to pH 7.0 with 1M HCl. Before ion dissolution study, bioglass powder was washed with MilliQ water to remove extra Fe-EDTA solution. 45 mg bioglass powders were added in 30 mL buffer solution and incubated at 37°C under static conditions. At different time points (1h, 4h, 8h, 24h, 48h, 72h), 1 mL solution was taken out of the system and pH was measured. The calcium ion concentration was determined with UV-Vis spectroscopy at the wavelength of 275 nm [170]. Firstly, the calibration line was obtained by combining a series of Ca^{2+} concentrations (25-800 mg/L) with EDTA forming Ca-EDTA complex, shown in Figure S24.

4.3 Preparation of composite gels

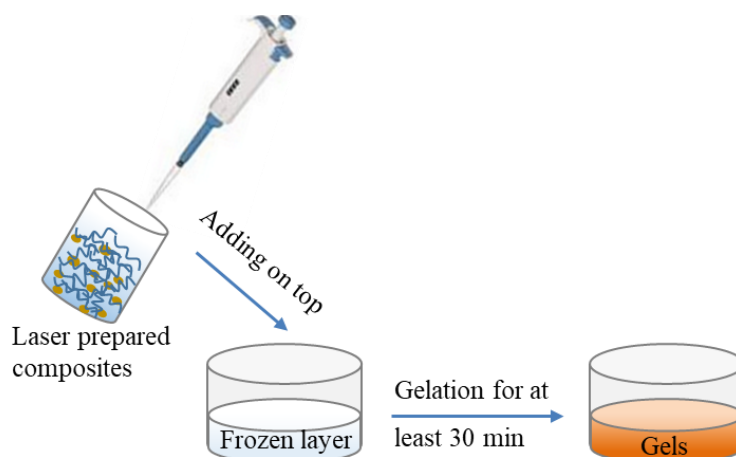


Figure 4-1: Illustration of hydrogel discs' preparation.

Alginate hydrogels were prepared with calcium chloride (CaCl_2), as displayed in Figure 4-1. Briefly, 500 μL of 25 mg/mL CaCl_2 were cast into a 24-well plate and frozen at -20°C to form a base layer. 500 μL of 1.5 % (m/v) alginate solution (pure alginate, nanoparticles-alginate) were added on top of this base layer. For complete gelation, the solutions were kept at room temperature for 40 min. These gels were immersed in PBS buffer overnight and washed 3 times.

Various collagen gels were prepared with cross-linkers, glutaraldehyde (GTA) and EDC/NHS as listed in Table 4-5. The GTA solutions were prepared by heating slightly and stirring for 15 min, while the EDC/NHS solutions were prepared by first mixing the EDC and NHS solids and then dissolving in water. The pH of collagen and Au-collagen solutions were adjusted with 0.1 M NaOH. The ionic strength was adjusted using sodium chloride and defined by modulating the salt concentration. Collagen gelation was prepared in a two-step procedure. Initially, 500 μL of the cross-linker solution was poured into a 24-well plate and placed in the fridge to form a solid base layer. Subsequently, 500 μL of Au-collagen (or pure collagen) solution was cast on top of the base layer. This process lasted for at least 1 hour. The amount of non-cross-linked amino groups can be calculated with the Bradford method [171]. The variable protein concentrations were used to make the calibration lines as showed in Figure S1. Finally, the crosslinking degree can be calculated via the absorbance value before and after cross-linking.

Table 4-5: Experimental parameters for the preparation of collagen gels. Samples were prepared to combine each level of the three factors: pH, ionic strength, cross-linkers, and Au nanoparticle concentration. The levels of ionic strength were defined by modulating the salt concentration.

Factor	Level					
pH	5.5	7.4	10			
Salt Conc. (mM)	0	45	83	166	206	
EDC/NHS	NHS	1	2	3	4	EDC
Glutaraldehyde (v/v)	0.1%	0.5%	1%	2%	4%	
Au Conc.(wt%)	0	0.01	0.02	0.04	0.06	

4.4 Characterization and physicochemical determination of nanoparticle-polymer gels

Laser scanning confocal microscopy (LSCM) for the detection of nanoparticle dispersion in polymer matrices

Laser scanning confocal microscopy (LSCM) is not only a powerful tool to investigate cells, but also a high-throughput technique for examining organic-inorganic composites [172, 173] and investigating metallic nanoparticles [12, 174-176]. Since 1990, the application of confocal microscopy was firstly reported by Knöster and Brakenhoff, studying the microstructure of glass fiber reinforced composites [177]. This technique gets popular in observing solid materials. Figure 4-2 illustrated the visualization of spatial particle distribution in the polymer matrix by LSCM. The LSCM is based on a conventional optical microscope but with a laser beam instead of a lamp. The light passing through a semi-transparent mirror is reflected away and toward the pinhole aperture, which allows only a small central portion of light through to the detection system. With emission/excitation filters, it is also possible to analyze multicolor immunofluorescence staining. The filters are used to separate fluorescent light reflected from the sample being examined.

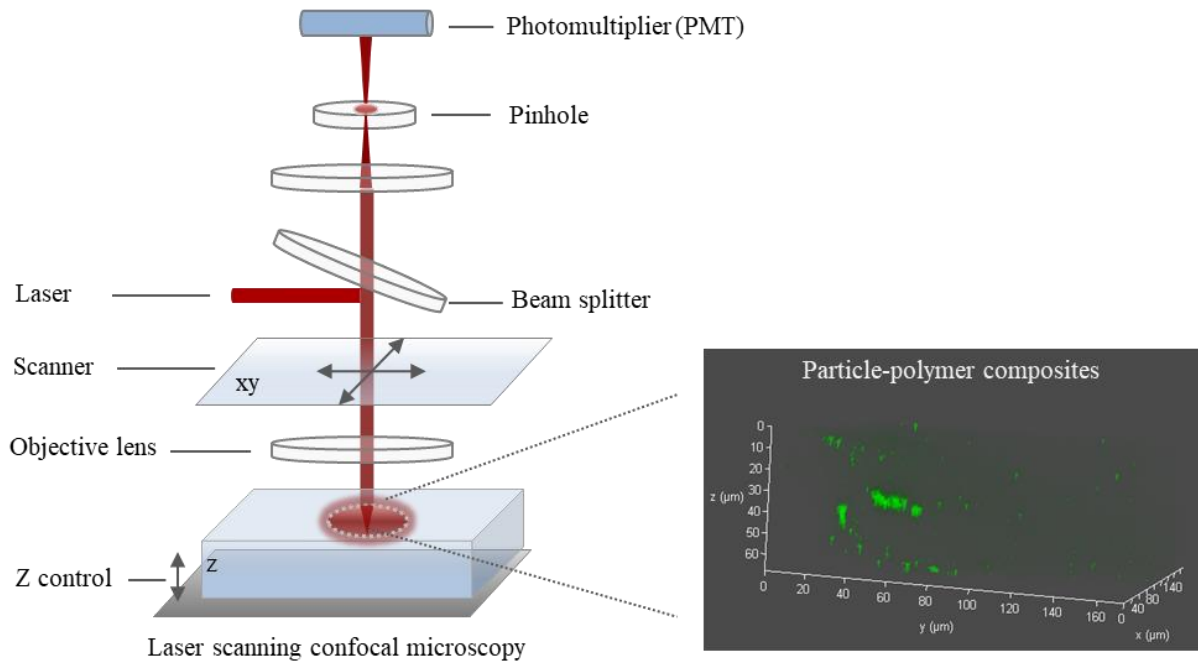


Figure 4-2: Illustration of spatial particle distribution in the polymer matrices visualized by LSCM.

There are two different modes in LSCM: reflection mode and fluorescence mode. Generally, the former is suitable for dry samples containing filler particles, while the latter usually requires samples to be stained with fluorescent dyes. All available laser light is used in the reflection mode, which is employed in addition to fluorescence imaging. Moreover, images detected from reflection mode can show identical features to images captured from fluorescence mode [172, 178].

Confocal microscopy is sensitive to the geometry and polarizability of particles while scattering patterns of metal nanoparticles are acquired. Due to the surface plasmon resonance (SPR) enhanced scattering, confocal microscopy can be used for the visualization of Au nanoparticles [12, 175]. Furthermore, single spots could also be observed in the polymer. Klein *et al.* [175] found that LSCM had a detection limit of gold nanoparticles with an equivalent diameter of 60 nm. It is well-known that azimuthally and radially polarized doughnut modes render different patterns: the signal of particles smaller than the resolution will be observed either as a ring or a spot with a weak surrounding ring of contrast, as proved by T. Züchner *et al.* [174]. Guan *et al.* [173] proposed an aggregation-induced scattering (AIS)-active effect to visualize the macrodispersion of inorganic fillers in polymer composites. The polymer matrix can be also

easily detected in the bright field mode when transmittance light detector (TLD) mode is chosen, and enable the transmitted light through a photomultiplier tube (PMT).

To investigate the distribution of nanoparticles in TPU, cross-linked alginate, and alginate-fibrin composites, the excitation wavelength was set at 532 nm for Au nanoparticle composites. The emission wavelength was in the range of 538-590 nm. For FeNPs, the excitation wavelength was at 470 nm while the emission wavelength in the range of 478-528 nm [12]. To visualize the protein coating, tetramethylrhodamine (TRITC)-coupled albumin was diluted 1:500 with FBS and incubated on the gels prepared as aforementioned. After washing two times with PBS the gels were analyzed in LSCM. The detected excitation wavelength was 555 nm and the emission wavelength was in the range of 563-620 nm. The obtained confocal microscopy images were processed with ImageJ software.

Atomic force microscopy (AFM)

Atomic force microscopy (AFM) was used to observe the morphology and relative stiffness of alginate, alginate-fibrin or alginate-fibrin-FeNPs hydrogel patches. For the investigation, these patches were cut into thin and flat membranes and stuck on a glass slide. It was then placed on the sample stage of AFM and AFM experiments were immediately performed. The pyramidal silicon nitride probe (Nanoworld AG, Neuchatel, Switzerland) with a nominal spring constant of 0.01-1.87 N/m was used for imaging. Images of the gel surface were scan in the tapping mode at the scale of $5 \mu\text{m} \times 5 \mu\text{m}$, and processed using Gwyddion software.

The analyzed surface roughness of the membranes was reflected by the mean roughness (R_a), the root mean square roughness (R_q), maximum distance from peak to valley (R_t). These parameters giving a great insight into the hydrogel surface properties, which can be defined based on the mean plane Z_j or standard deviation of Z values and N is the number of values, as shown below [179]:

$$R_a = \frac{1}{N} \sum_{j=1}^N |Z_j| \quad (8)$$

$$R_q = \sqrt{\frac{\sum(Z_i)^2}{N}} \quad (9)$$

Meanwhile, the force-distance curves were recorded to compare the relative stiffness of hydrogels [19].

Swelling and porosity determination

To determine the hydrogel swelling ratio, the dry (W_0) and wet (W_t) weights of gels were obtained from the drying samples and immersed in deionized water for 24 h. Here, the dry and wet weights were analyzed by analytical balance. The swelling ratio (S) of different samples was calculated using the following equations [180]:

$$S = \frac{W_t - W_0}{W_0} \quad (10)$$

The porosity (P) of the prepared discs of composites was determined using a method established in the literature [181]. Briefly, the discs were immersed in ethanol, a solvent that easily penetrated the pores without causing shrinkage or swelling [181], as displacement liquid until the discs were saturated. The samples were weighed before and after the immersion in alcohol. The porosity was calculated using the formula:

$$P = \frac{W_1 - W_2}{\rho V_1} \quad (11)$$

where W_1 and W_2 indicate the weight of discs before and after immersion in ethanol, respectively. V_1 is the volume before immersion in ethanol; ρ is the alcohol density.

Contact angle measurement

Nanocomposite films were prepared as described above. For labeling samples, alginate was abbreviated into Alg. Contact angles of the samples were measured by a Dataphysics OCA-15 instrument equipped with a video camera at room temperature by the captive bubble method. The contact angles of a captive air bubble and water were measured with a substrate fixed with composites films, facing downward in a square transparent glass vessel filled with deionized water. Once the air bubble was released from the J-shaped needle using a microsyringe beneath the glass substrate, images were captured within 30 seconds and contact angles were recorded by the software SCA20-F.

Surface zeta potential measurement

To obtain suitable films for measuring the surface zeta potential of TPU composites, TPU composite solution was cast into a glass petri dish. After drying, circular samples with 14 mm diameter and 0.2 mm of thickness were obtained by punching the thin films of the nanocomposites. All measurements were performed at various pH values between 4.5 and 8.5,

adjusted by adding 0.1 M KOH to the sample in the volume increment of 0.02 mL. A streaming potential was measured by the device SurPASS Electrokinetic Analyzer. According to the given measured streaming current, the surface zeta potential of the nanocomposites was calculated automatically by the software VisoLab.

Ion release measurement

For the ion release measurements, alginate discs and TPU nanocomposite films were placed in 50 mL tubes of polystyrene, which were previously cleaned by rinsing them in HNO₃ (2%) and deionized water. Subsequently, 8 mL of 2 mM PIPES buffer, adjusted to pH 7.4, was added. The samples were incubated at room temperature. Samples of the supernatant (700 µL) were taken at different time points (0.15-100 h) without refilling a fresh buffer medium, and nitric acid (1 vol%) was added for the stabilization of ions. The samples were stored at room temperature before measurement. The concentrations of metal ions in the sampled aliquots were analyzed with inductively coupled plasma mass spectrometry (ICP-MS) operating at 1,000 W plasma power, 14 L/min plasma gas flow, and 0.9 L/min nebulizer gas flow. Before the analysis, the samples were diluted ten times with 1% HNO₃ containing 10 µg·L⁻¹ of yttrium (Y) and thulium (Tm) as internal standards. The washing time between measurements was set to 10 s with 1% suprapur HNO₃ to avoid contamination and memory effects. A series of 11 dilutions in the range of 0.1–100 µg/L standard solution (ICP Multi-element-standard solution) were used for the calibration. Metal ion concentrations (µg/L) were calculated according to the corresponding calibration lines (correlation factor ≥ 0.99).

Rheology measurement

The rheological properties of the hydrogels were measured by using a rotational Rheometer. A 15 mm parallel plate with a specific measurement gap (4 mm for alginate and 1 mm for collagen hydrogels) was used. First of all, strain sweeps in the range of 0.1%-100% at the frequencies of 0.1-2.0 Hz were carried out to determine the linear viscoelastic range of the samples. The following three rheological experiments at 20 °C were adopted to explore the rheological properties of samples. The frequency sweep tests over an angular frequency were in the range of 0.01–100 rad/s at a constant strain of 1%. The steady-state flow tests were carried out in a range of shear rates of 0.5–500 s⁻¹, and the recovery tests were under a low shear rate. The pore size of alginate or collagen gels can be calculated using the following equation [182, 183]:

$$D = \left(\frac{RT}{G'N_A}\right)^{1/3} \quad (12)$$

where R is the gas constant (8.314 J/K·mol), T is the temperature in Kelvin, G' is the plateau value of storage modulus and N_A is Avogadro's constant ($6.022 \times 10^{23} \text{ mol}^{-1}$).

4.5 Protein adsorption on composites

Laboratory protein determination can be performed with the Bradford assay [171]. This protein assay can eliminate most of the interference elements and relatively insensitive biuret reactions. It is based on the observation that Coomassie Brilliant Blue G-250 (CBB) exists in two different color forms: red and blue. The red form is converted to the blue form upon binding with protein, which is a high sensitive measurement, as shown in Figure 4-3. The binding of the dye to protein is a rapid process (approximately 2 min), and the protein-dye complex remains dispersed in the solution for a relatively longer time (about 1 hour), thus making the procedure reliable and yet not time consuming. Typically, as the dye binds with the protein, the reaction occurring to form a protein-dye complex will cause a shift in the maximum absorbance from 465 nm to 595 nm and intensely absorbing light at 595 nm [171, 184, 185].



Figure 4-3: Formation of a complex between protein and Coomassie brilliant blue G-250 dye [184].

The adsorption of bovine serum albumin (BSA) on the alginate and TPU composites was carried out using the reported method [64, 186]. The surface water on alginate discs or TPU films was absorbed with clean filter paper to get the wet weight. Subsequently, samples were placed into 24 well plates containing 1 mL of 0.5 mg/mL BSA protein aqueous solution to evaluate the dynamic protein adsorption. The whole protein adsorption process last for 1 h, and the equilibrium adsorption capacity Q_e (mg/g) of each sample was calculated according to the following equation [64, 186]:

$$Q_e = (C_0 - C_e) V/m \quad (13)$$

where m (g) describes the mass of the wet hydrogel or the composites, V (mL) refers to the volume of the protein solution, and C_0 (mg/mL) and C_e (mg/mL) are the protein concentrations of the initial solution and the supernatant solution at equilibrium, respectively. The protein concentrations of the supernatant solution at equilibrium were determined by the Bradford method [171]. The calibration curves were built from the absorbance at 595 nm measured with a UV-Vis spectrometer after mixing standard BSA protein with protein reagent for 2 min in 3 mL plastic cuvettes. The protein concentration was plotted to determine the protein concentration in unknown samples, as shown in Supplemental Figure S2.

4.6 Demonstration of 3D printable nanoparticle-alginate hydrogel

The experiment in this part was performed by Jacqueline Stamm and Andreas Bläser, and the results have been published in *Nanotechnology*, 2020, 31, 405703.

A modified approach of the previously published submerged printing strategy was applied [108, 187, 188]. Briefly, a 10 mL glass beaker was filled with 10 mL of cross-linker containing gelatin slurry. A stock of 10 % (w/v) gelatin (gelatin type A, G2500, Sigma, St Louis, MO, USA) dissolved in 5 % (w/v) calcium-chloride solution (CaCl_2) was prepared. The gelatin was left to soak for 10 minutes at 24 °C until it formed swollen slurry. The printing cartridge was carefully rinsed with ethanol and flushed with distilled water before it was loaded with either 1 mL of 1.5 % (w/v) native alginate (i), iron-nanoparticle containing alginate (ii), or gold-nanoparticle containing alginate (iii). The beaker filled with the cross-linker containing, swollen gelatin slurry was placed on the printing platform. The printing cartridge was loaded into the printer and the tip of the needle was leveled to the bottom of the glass beaker. For the printing process the model of a cylinder was sliced into 0.2 mm thick layers (SuperFill - Slicer, Black Drop Biodrucker GmbH, Aachen, Germany). According to the previously created data set, the needle was moved layer by layer submerged in the gelatin-filled beaker. During the printing process, uniform alginate strands were deposited under a pressure of 0.2 bar. In contact with the CaCl_2 containing gelatin, the printed alginate formed a solid gel after a short time. Following the printing process, the gelatin slurry was melted at 38 °C. After approximately 25 minutes, the printed structures floated towards the surface and could be removed from the beaker with tweezers. Three specimens of each native, iron-, as well as gold-laden alginate were printed.

4.7 Cell experiments

The experiment in this part was performed by Alena Richter and the results have been published in *Adv. Mater. Interfaces*, 2021, 2002015.

Alginate or alginate-fibrin enriched with two different concentrations, 102 $\mu\text{g}/\text{mL}$ and 204 $\mu\text{g}/\text{mL}$ (referred to as 100 and 200 $\mu\text{g}/\text{mL}$) was used for hydrogel fabrication. 5 mg/mL or 10 mg/mL fibrinogen (n=6 each) and 0.5 I.U thrombin (CSL Behring GmbH, Marburg, Germany) per 10 mg fibrinogen were added to alginate solutions. Fibrinogen was isolated from human plasma obtained from donors after informed consent by cryo-precipitation as described previously [189]. Prior to polymerization, alginate solutions with or without iron nanoparticles were autoclaved for 30 min. Cell culture tested low melting agarose (1.5% (w/v)) and CaCl_2 (2.5% (w/v)) were dissolved, autoclaved and filled into 96-well-plates (75 μL) or 24-well-plates (500 μL) serving as a base-layer delivering the cross-linking Ca^{2+} . The base-layer was allowed to polymerize for 30 min before the addition of alginate solution (75 μL in 96-well-plates; n=6 for each group, 500 μL in 24-well-plates; n=2 for each group). After 45 min of gelation, the hydrogels were covered with ultrapure water until cell seeding.

Alginate hydrogels were used either directly in cell culture experiments or stored before seeding to promote formation of degenerative pores. For this, hydrogels covered with ultrapure water were kept at 4°C for 8 days. For coating with serum proteins, hydrogels were covered with fetal bovine serum (FBS; 100 μL in 96-well-plates, 300 μL in 24-well-plates) for 3 h at 37 °C after gelation. Unbound proteins were removed by washing the hydrogels with ultrapure water.

For cell seeding, unmodified and modified alginate hydrogels were separated from the base-layer of agarose/ CaCl_2 and transferred into new tissue culture plates. Human umbilical cord vein endothelial cells (HUVEC) (PELOBIOTECH GmbH, Planegg, Germany) of passage 2-7 were cultured in EBM-2 medium (Lonza, Köln, Germany) and seeded to the hydrogels in 96-well-plates (7500 HUVEC in 200 μL medium) or in 24-well-plates (47.070 HUVEC in 500 μL medium). The medium was changed after 48 h. To quantify the viability of HUVEC on the different hydrogels a WST-8-assay (Colorimetric Cell Viability Kit (PromoCell GmbH, Heidelberg, Germany) was performed after 72 h in 96-well-plates (n = 9 for each group). Cell culture medium was reduced to 100 μL , 10 μL of the dye were added and the well-plates were incubated at 37 °C and 5% CO_2 for 2 h. 100 μL of the supernatant was then transferred to a micro-test plate and absorption at 450 nm was measured at a microtiter plate reader.

Live/Dead staining was performed after 72 h in 24-well-plates. For this, the cell culture medium was removed and the hydrogels were washed twice with PBS. Hydrogels were incubated with 300 μ L calcein/ethidium-homodimer solution (Life Technologies, Darmstadt, Germany) for 45 min under light protection. After the staining solution has been removed, hydrogels were washed with PBS as before. Hydrogels were transferred to object slides and viability and morphology was evaluated by fluorescence microscopy imaging live cells green (calcein) and dead cells red (ethidium-homodimer). Graphical editing was conducted with Image J (Image J, Maryland, USA). Statistical calculations were performed by Graphpad Prism 5 (GraphPad Software, San Diego, California). Statistical calculations were performed by Graphpad Prism 5 (GraphPad Software, San Diego, California). The mean and standard deviation or standard errors of the mean were calculated for all values obtained in this study as indicated. Multiple comparisons between groups were performed by one-way ANOVA and Sidak's post-test. Differences were considered significant at $p < 0.05$. Significance levels were given as follows: * $p < 0.05$ and ** $p < 0.01$.

5 Results and Discussion

The following part of results and their discussion are presented in five subchapters. Firstly, the effects of liquid properties on laser generated nanoparticle-polymer composites are given. Here, the effects of polymer solutions such as concentrations, pH, and viscosity on the nanoparticle productivities via laser ablation are investigated and their obtained nanoparticle morphology, size, and stability are characterized. The polymer degradation during laser ablation is also considered. Secondly, the obtained nanoparticle morphology and size are characterized. Additionally, the method of confocal microscopy is developed to characterize particle distribution in polymer matrices. Nanoparticles altering the physicochemical properties of composites are evaluated, including their swelling ratio, porosity, surface roughness, surface charge, and elastic modulus. Thirdly, the special Fe ion release behaviour from the alginate system is discussed and a mechanism is suggested. The related protein adsorption was assessed and the evaluation of viability and endothelial cell proliferation on alginate, FeNPs-alginate, alginate-fibrin-FeNPs hydrogels were performed. In the fourth section, the rheological properties of nanoparticle-polymer composites are measured. In addition, 3D printability of laser prepared nanoparticle-alginate composites is proven. At last, nanoscopic bioglass was produced via laser fragmentation and their particle size and yield were determined.

5.1 Productivity and scalability of laser processing for *in-situ* nanocomposite generation

During the ablation, experimental parameters such as viscosity and the optical density of the liquid highly influenced the particle size and ablation efficiency [16, 17, 144]. The productivity of AuNPs obtained was 1100 ± 44 mg/h with the nanosecond laser [140]. Kohsakowski *et al.* [190] compared the nanoparticle productivities with ps and ns-laser and found noble metal NP productivity is higher than ignoble metal nanoparticles. Streubel *et al.* [191] obtained high productivity of 4 g/h for platinum and gold nanoparticles. Dittrich *et al.* [192] found that higher AuNP productivity was obtained at higher fluence, but laser efficiency decreased above the threshold fluence value. Million *et al.* [147] discussed the influence of repetition rate on ZnNPs, FeNPs, and AuNPs in an aqueous micro-gel system and found ablation efficiency decreased with increasing repetition rate but ablated nanoparticle mass initially increased and then slightly reduced. Recently, Waag *et al.* [193] observed the ablation rate of platinum, Au₉₀Pt₁₀, and gold to be 47 mg/(h·W), 44 mg/(h·W), and 21 mg/(h·W), respectively, using polygon-wheel beam

guidance. However, significantly reduced values are commonly found in organic solvents [144] and few works reported the NP productivity in polymer solutions [147, 150].

As shown in Figure 5-1 (lower row), a clear trend of reduced productivity with increasing polymer concentration was found. This was in line with the viscosity change of the studied polymer solutions, which was highly pronounced within the parameter matrix studied in this work (Figure 5-1, upper row). For example, the viscosity of a 1.5% w/v alginate in deionized water is 18.8 mPa·s, while a 3.0% w/v stock solution had a seven times higher viscosity of 136.1 mPa·s. At 1.5% w/v alginate concentration, the NP productivity (53 mg Au/h) was around two times higher than that in 3.0% w/v solution. And the highest specific nanoparticle productivity can be calculated at 5.5 ± 0.4 mg/(h·W) of Au and 2.1 ± 0.2 mg/(h·W) of Fe. Nonetheless, the correlation between viscosity and productivity is not universal, as verified by a direct comparison between the alginate and TPU system. Although the viscosity of TPU/THF solution is 1.33 mPa·s at the concentration of 1 wt%, the productivity of Au and Fe is around 8 mg/h, which is approximately 10 times lower than in an aqueous alginate system. In this context, the solvent (water vs. THF) seems to have a significantly more pronounced impact on productivity than the viscosity alone.

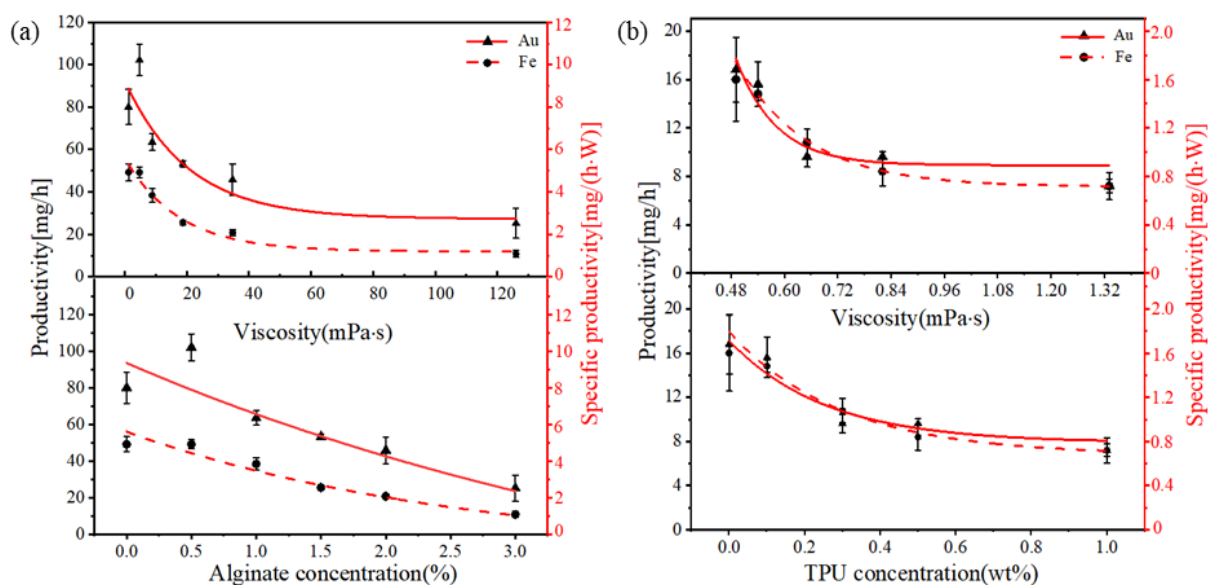


Figure 5-1: Influence of the concentration of alginate dissolved in water (a) and TPU in THF (b) on productivity during laser ablation using gold and iron targets.

The relationship between pH and viscosity of collagen solutions and the AuNPs specific productivity are plotted in Figure 5-2. Higher productivity was observed at a higher pH value

(Figure 5-2a). At pH 3.5, e.g. collagen in 5 mM acetic acid, the average Au productivity was around 6 mg/(h·W), which is two times more than at pH 2.7. At the lower pH, there are more CH_3COO^- and H^+ in the collagen solution. It is reported that the H^+ or OH^- in the solution interact with the surfaces of the crystalline solids and control their growth, which affects the final average size of the NPs [194]. Thereto, the larger particles at lower pH have a higher absorption cross-section that will decrease the particle productivity [144]. On the other hand, a higher concentration of organic solvent like acetic acid generates more gas of CH_4 and CO_2 and this could shield the incoming laser beam producing gas bubbles lowering productivity [144]. Similar to the case of NPs in alginate, AuNPs productivity significantly decreased with increasing viscosity and concentration of collagen solutions (Figure 5-2b). Due to larger persistent bubbles formed in highly viscous liquid, their longer dwelling time has a pronounced shielding effect [144]. Another interesting feature of collagen solution is opalescent/turbid appearance which can scatter light attributed to collagen chains indicating aggregation and therefore affecting the transmittance of the laser [195].

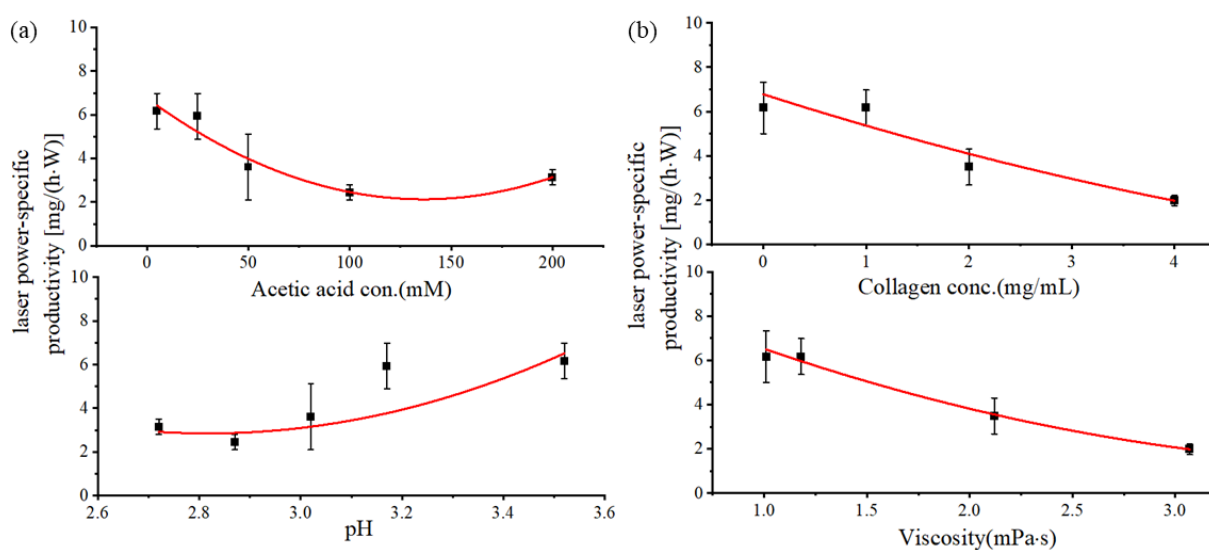


Figure 5-2: Influences of solution pH with 1 mg/mL collagen concentration (a) and collagen concentration in 5 mM acetic acid (b) on laser-ablated AuNPs specific productivity.

According to previous works in laser-produced nanoparticle-polymer composites, laser ablation time should not be less than 4 min to make the laser system to warm up and stabilize [13]. Generally, long ablation time contributes to a high nanoparticle concentration but not a high laser efficiency. For example, as shown in Figure 5-3b, power-specific productivity derived from collagen or TPU significantly decreased with increasing time. Also, in the alginate solution, the power-specific productivity of AuNPs decreased after 15 min (Figure 5-3a), while

it slightly decreased in the case of Fe nanoparticles. This phenomenon could be attributed to a high concentration of NPs in front of the targets generating laser-nanoparticle interactions consuming more laser power and eventually hampering subsequent laser pulses reaching the target with limited energy. However, the laser efficiency of ablated AuNPs and FeNPs seemed stable in TPU polymer solutions (Figure 5-3c,d).

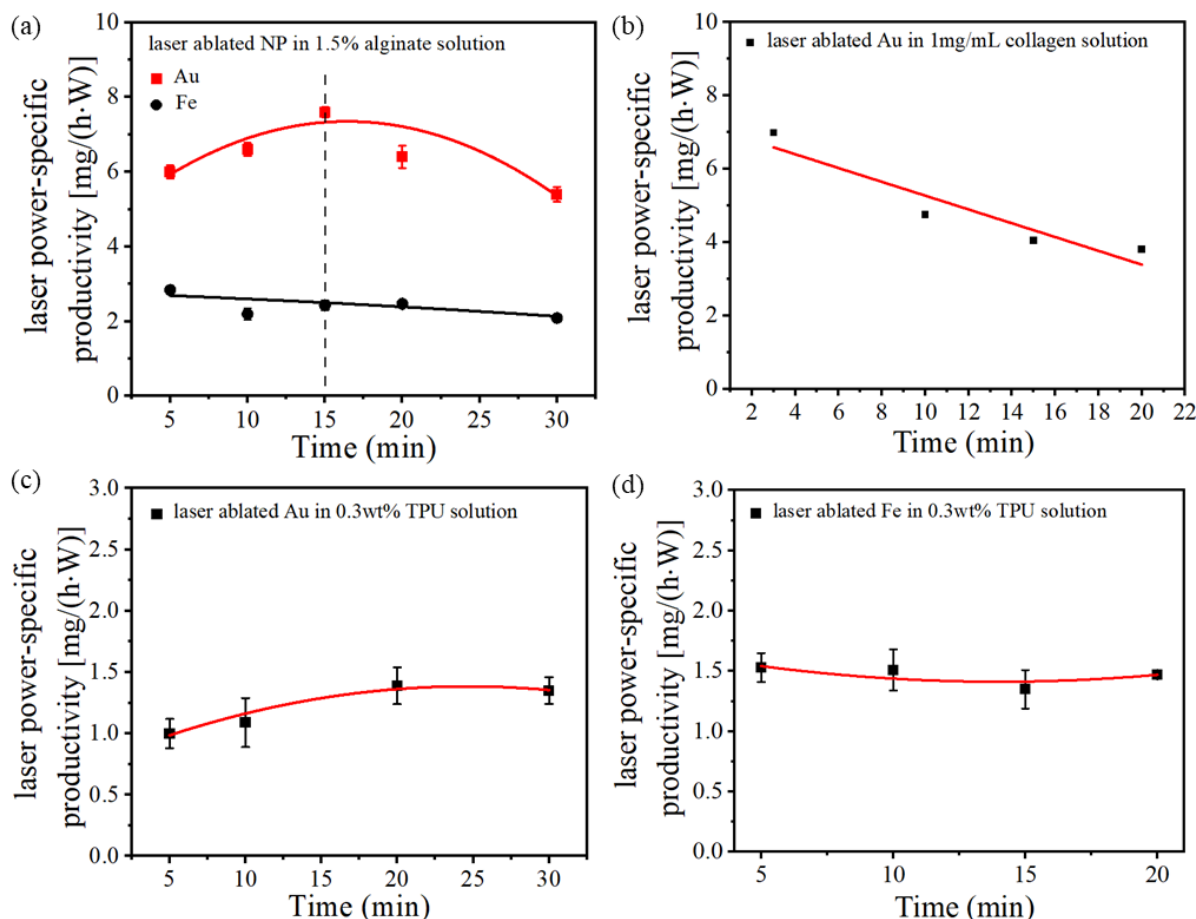


Figure 5-3: Laser power-specific ablation efficiency of nanoparticles at varying time points in different polymer solutions.

We compared power-specific productivities in alginate, TPU, collagen polymer solutions (Figure 5-4). The results clearly show that laser efficiency is the highest in alginate, around 3.5 times higher than in TPU, followed by collagen solutions. Concerning the different materials, Au mass productivity is usually higher than Fe in aqueous solution, a fact most likely attributed to different densities of Au and Fe. Considering this density effect, the ablated volume of Fe in our study is around 1.5 times higher than Au in this situation. Upon calculating the molar mass, the ablated Fe atoms is around $0.038 N_A$, 2.2 times more than Au in 1.5% w/v alginate solution, whereas in 1 wt% TPU solution, this value is $0.01 N_A$ that is about 3.3 times more than ablated

Au atoms. In the work of Waag *et al.*, they compared the specific ablation rate of platinum [47 mg/(h·W)], Au₉₀Pt₁₀ [44 mg/(h·W)], and gold [21 mg/(h·W)] and explained from the aspects of pulse overlapping and inferences of the metal's electronic structure causing energy coupling and heat conductivity, which seemed to have strong influences in NP productivity [193]. The absorption by electrons could transfer energy to the metal lattice, thus affecting the ablation behaviour. It indicates that the absorption of laser light depends on the optical properties of materials. In this case, the absorption of Au is more efficient than Fe [196]. However, this effect was less pronounced in organic liquids.

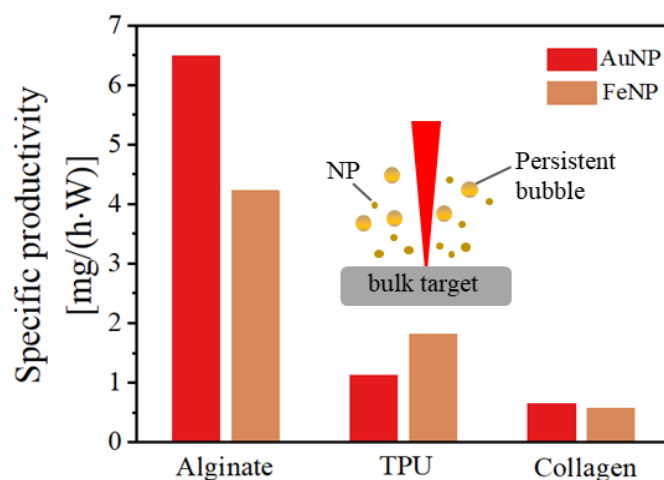


Figure 5-4: Power-specific productivities obtained for 1 wt% Au and Fe nanoparticles in polymer solutions.

Overall, the low viscous liquid usually results in high nanoparticle productivity in water compared to the organic solvents. Because low viscosity and low critical energy barrier are beneficial to the formation of a large number of nuclei. Significantly reduced productivities are commonly found in organic solvents [144]. The fact that nanoparticles synthesized in THF (> 60 nm) or aqueous acetic acid with a mean diameter of 68.9 nm as shown in section 5.2.1 are larger and hence have higher absorption cross-section, which might explain why the productivity of THF or aqueous acetic acid aqueous is lower compared to that of water, as Kalus *et al.* [144] described. They assumed that laser light is absorbed or scattered by the colloid. Thereto, the energy can no longer be efficiently transferred to the target. In their work, the authors also observed that the ascent speed of persistent gas bubbles in water is much faster, and the bubbles' dwell time is shorter than in organic liquid. This observation also results in less shielding of incoming light and, consequently, higher NP productivity in water. Another important aspect is the dissolved or dispersed state of polymer chains. For example, as Table

5-1 listed, the silk fibroin or collagen contains undissolved substances that largely shield incoming laser, leading to lower NP productivity.

Table 5-1: Summary of laser-ablated efficiency of Au or FeNPs in different polymer solutions. The laser parameters were kept the same during ablation.

Solvent	Polymer	Properties of polymer solutions				Obtained highest specific productivity (mg/h·W)	
		Viscosity (mPa·s)	Density (g/cm ³)	Turbidity (NTU ¹)	Ref.	Au	Fe
Water	Alginate	5.4	1.0	0.5	This work	12.0 ± 0.9	5.8 ± 0.5
	Fibroin	100	-	100	[197]	0.3	0.1
THF	TPU	0.5	0.9	20	This work	2.0 ± 0.3	1.9 ± 0.4
Acetic acid	Collagen	1.2	1.0	10	This work	6.2 ± 0.8	5.4 ± 1.3
	Chitosan	16.2	1.2	15	[198]	3.0 ± 1.2	4.8 ± 1.2
Acetone	PLGA	0.3	0.8	0.5	This work	14.0	-

¹Nephelometric Turbidity unit (NTU) is the unit used to measure the turbidity of a fluid or the presence of suspended particles in water, which can be measured with turbidity meters.

Table 5-1 summarized the highest power-specific productivity of Au or Fe nanoparticles in various polymers or biomolecule solutions. The representative digital photos of generated products were displayed in Figure S3. It indicates that laser ablation is a versatile method *in situ* preparing nanoparticle-polymer composite. Several factors were listed in this table. Regarding the effects of solvents like water or organic liquids as well as the viscosity of polymer solutions, we have discussed hereinabove. Further, polymer solutions' turbidity also played an essential role in NP productivity rather than density. No doubt high turbidity of the solution

shields incoming light and unsurprisingly, the lowest turbidity of water and acetone in 0.5 achieved the highest NP productivity.

The UV-Vis spectra of NPs in alginate or TPU were displayed in Figure S3. One can see SPR peaks of AuNPs featured at around 520 nm, while FeNPs show no typical SPR peaks. Instead, the absorption peak of FeNPs solutions was reported at approximately 275 nm, according to the calculation with the Mie model [199]. In our case, the absorption peaks were too broad to be assigned to pure metal Fe nanoparticles. As stated before, Au has more light absorption efficiency than Fe, leading to a higher NP productivity.

A potential limitation of the *in situ* fabrication method of nanoparticle-polymer composites by lasers is the frequently discussed aspect of polymer degradation, particularly if femtosecond laser pulses are applied. This is because of filamentation, liquid ionization, or strong nanosecond pulses (heating) [27]. Here, picosecond laser pulse durations may provide a good compromise to minimize colloid excitation effects while minimizing target heating. Therefore, the heat transfer from the target to the liquid remains low.

To verify potential degradation or damage of the alginate monomer by laser ablation, we examined blank alginate precursor solutions prior to and after laser irradiation via FTIR and UV-Vis spectroscopy (Figure 5-5a,b), indicating that degradation was minimal. Compared to pure alginate, the absorption spectra of laser-ablated metal particles in alginate significantly changed and AuNPs show a typical SPR peak at the wavelength of 520 nm (Figure 5-5b). There were presence of functional groups regarding hydroxyl, ether, and carboxylic in the FTIR spectra. It showed a wide peak at 3466 cm^{-1} which is a characteristic peak for stretching vibration of the OH group, and a peak at 2917 cm^{-1} corresponding to the stretching vibration of the CH_2 group. The band at 1610 cm^{-1} presented in the IR spectrum of sodium alginate is assigned to the stretching peak of carboxylate groups. Additionally, the bands around 1404 cm^{-1} (C–H bending), 1294 cm^{-1} (C–O stretching), and 1029 cm^{-1} (C–O–C stretching) are attributed to its saccharide structure [200]. There was a new peak at 2353 cm^{-1} that may be attributed to the embedding of AuNPs in alginate.

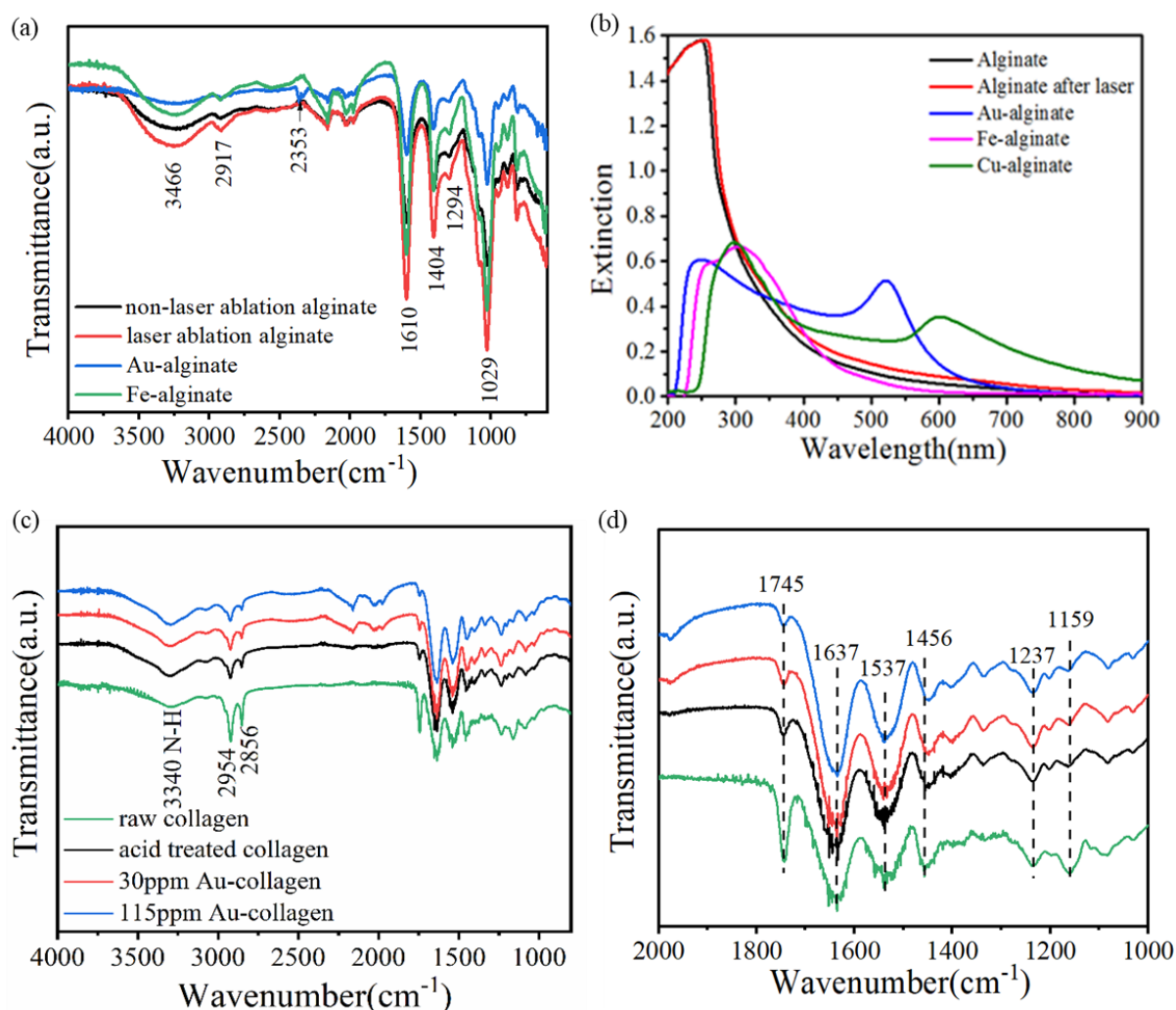


Figure 5-5: Fourier-transform infrared spectroscopy (FTIR) spectra (a) and UV-Vis spectra (b) of laser or non-laser ablation alginate, nanoparticles-alginate composites; FTIR spectra of raw collagen, acid treated collagen and Au-collagen composites (c), and enlarged spectra from 2000 to 1000 cm^{-1} (d).

Figure 5-5c,d display the interactions between Au and collagen macromolecules that were characterized by FTIR spectroscopy. It is known that some spectral regions refer to typical bands, such as 3050-2800 cm^{-1} (lipids, fatty, acyl chains), 1750-900 cm^{-1} (proteins) and 1200-900 cm^{-1} (saccharides) [201]. The characteristic peaks of raw collagen, acetic acid treated collagen and laser generated Au-collagen composites were found to be shifted or appeared new. The peak at 3340 cm^{-1} was due to the N-H stretching of collagen. 2954 cm^{-1} was the peak of CH_3 stretching. The enlarged spectra were showed to precisely recognize peaks changing in the range of 1000-2000 cm^{-1} . The peaks at 1637 cm^{-1} and 1537 cm^{-1} correspond to the amide I and amide II bands [28, 201], while the peak at 1237 cm^{-1} attributed to the C-N bond, amide III, and

N-H in plane bending [202]. There is a slight peak shift from 1456 cm^{-1} (raw collagen) to 1447 cm^{-1} , suggesting the interactions with acetic acid or AuNPs. Also, the peak intensities decreased along with band broadening. The collagen degeneration was not obvious during the laser processing, but the Au nanoparticles were successfully incorporated into collagen.

5.2 Particle characterization and distribution in the gel matrix

5.2.1 Effects of polymer solutions on particle size

Particle size is critical for understanding the products' physicochemical properties [78]. The LAL-synthesized primary particle sizes could be controlled with the assistance of salt quenching, polar organic molecules, biomolecules, or polymer capsulation [14, 16]. As Wagener *et al.* reported, in the presence of polymer chains (0.5 wt%), 50 nm aggregates of the unstabilized Ag nanoparticles were significantly reduced to 7 nm [14]. And at the optimal stabilization concentration of 0.3 wt% TPU, good particle distribution in the polymer matrix was achieved. Similarly, the size quenching effect of polymer chains was also observed in this work, as shown in Figure S4 and Figure S5a.

The obtained nanoparticle size was characterized using ADC or TEM (Figure 5-6). In this work, Au and Fe particle size prepared in water was shown in Figure 5-6a. By adding 0.15% (w/v) alginate molecules, there was no size reduction of Au particle (Figure 5-6b) due to the limited molecule size quenching effect. The average nanoparticle size was in the range of 6.3-7.5 nm. While Fe particle size was minorly reduced from 10.6 nm to 9.9 nm. In the 1.5% (w/v) alginate solution, Au and Fe particle size both were largely reduced. AuNPs derived from alginate solutions showed an average diameter of 3.3 ± 0.4 nm, whereas FeNPs had an average diameter of 8.0 ± 0.1 nm (Figure 5-6c). In previous studies on the synthesis of AuNPs in alginate using chemical reduction, the obtained particles were 5 ± 2 nm in diameter [203]. For comparison, our nanoparticles generated by the laser ablation method are smaller and uniformly dispersed, without any chemical additives. Nanoparticles generated in THF in the absence of TPU polymers turn out to have an average size of more than 60 nm, as shown in Figure 5-7a. Considering the work of Amendola *et al.*, they reported average size of Au and Fe nanoparticles in THF via laser ablation was 4.5 nm [204] and 20 nm [199]. It should be noted that aggregations and large particles around 50 nm can also be observed in their TEM images. However, with addition of TPU polymers, the obtained Au nanoparticles had average diameters of 5.3 ± 0.4 nm, while the average size of FeNPs was 12 ± 2.9 nm (Figure 5-7b). The results were comparable with the work of Lentz *et al.* [205], they used chemical reduction method to produce AuNPs with a size in the range of 5-20 nm, and then infused the AuNPs into TPU. In the unsteady state infusion process, different particle size distribution on the TPU surface was observed, which was not found in our work.

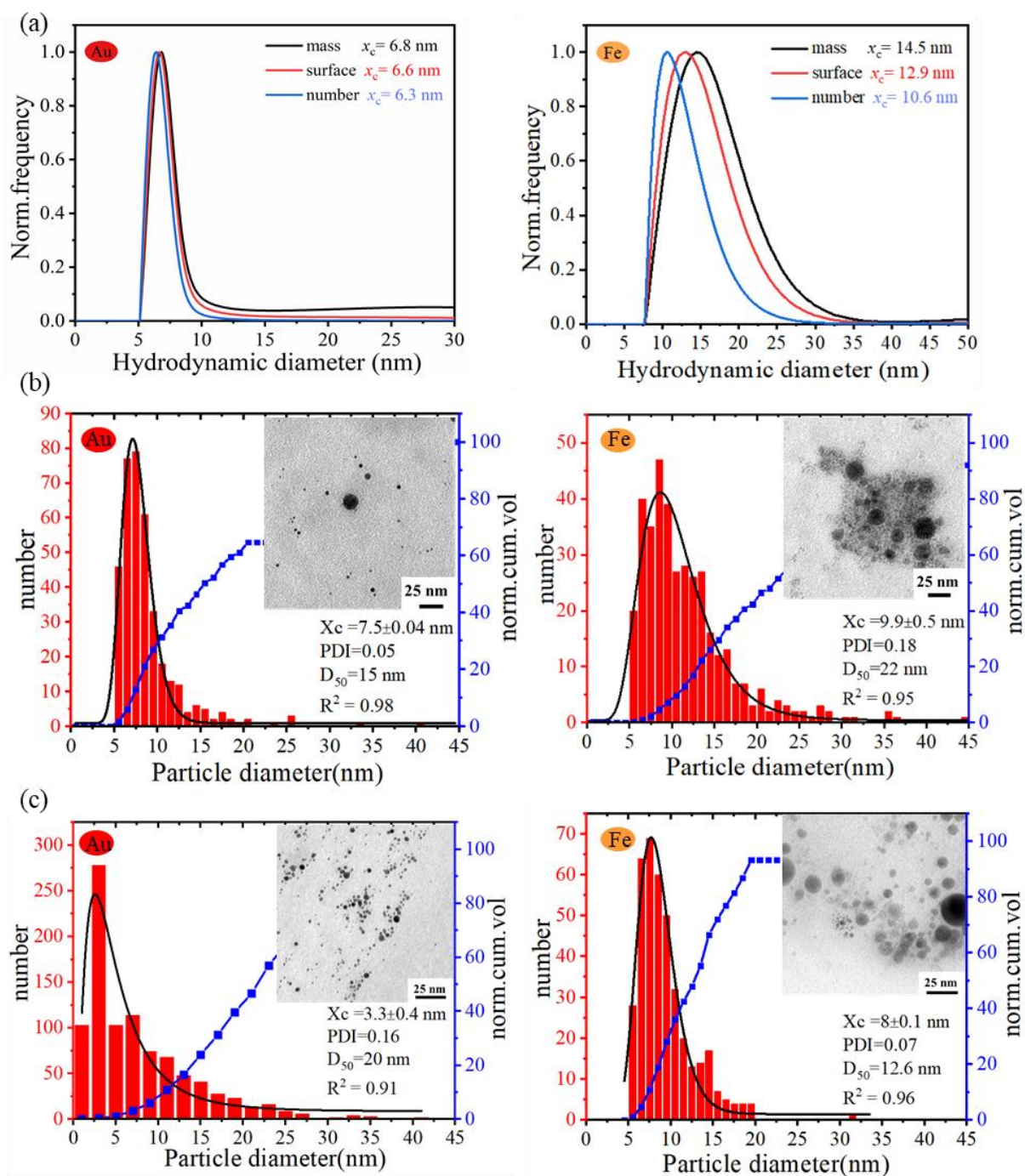


Figure 5-6: Analytical disc centrifugation (ADC) analysis of laser-generated Au and Fe in water (a). The calculated mass, number, and surface-weighted size distributions are shown. Particle size distributions and representative TEM images of Au and Fe nanoparticles generated in 0.15% (w/v) (b) and 1.5 % (w/v) (c) alginate aqueous solution. Parameters of the log-normal fitting and the calculated PDI are given in the diagrams.

The smaller particle size of Au compared to Fe may result from the laser ablation process. As stated in the nanoparticle productivity part, more ablated Fe atoms may have facilitated the

particle growth before it was quenched by the stabilizing polymer chains. Furthermore, stronger interactions between the polymer chains and the gold nanoparticles are conceivable in contrast to iron, which induces a more efficient size quenching.

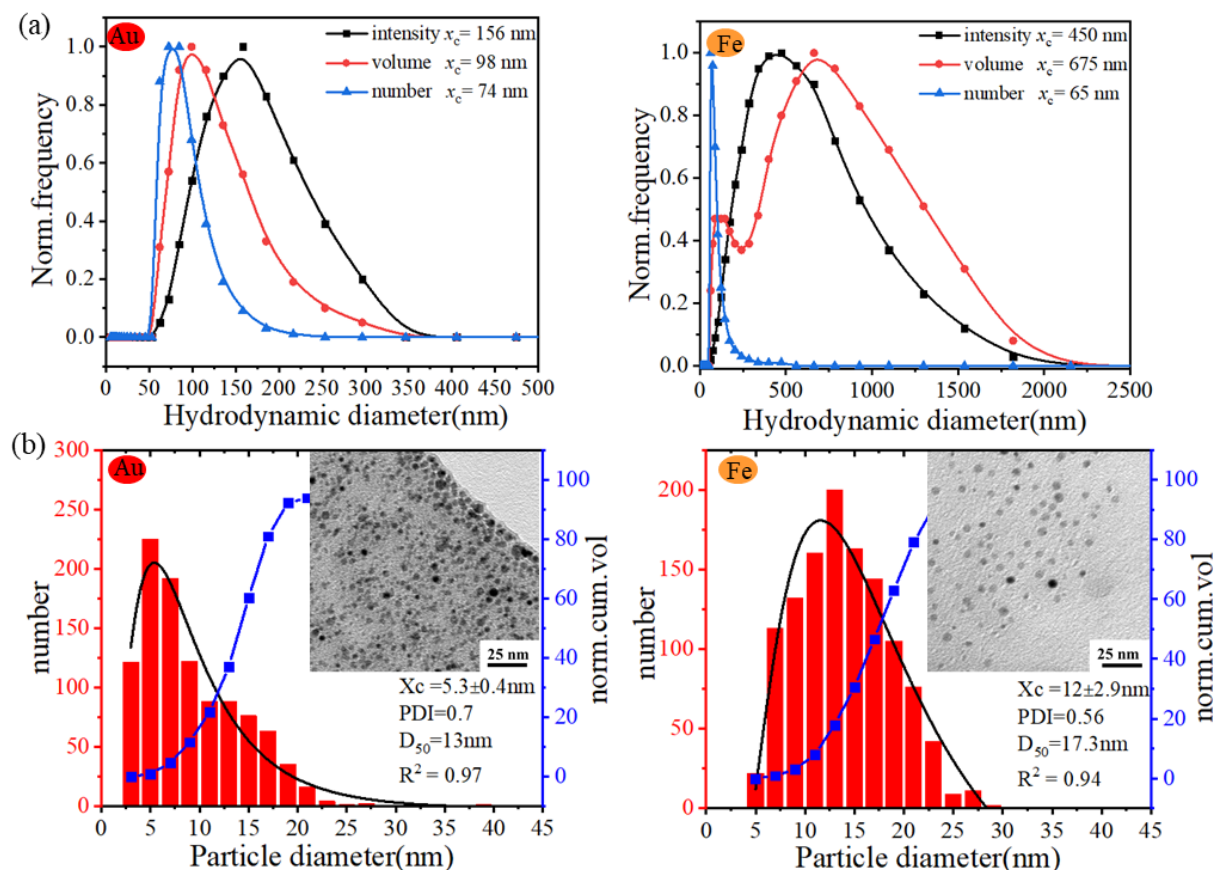


Figure 5-7: (a) DLS analysis of nanoparticles in THF; (b) Particle size distributions and representative TEM images of nanoparticles generated by the laser ablation of metal plates in 0.5 wt% TPU polymer solutions. Parameters of the log-normal fitting and the calculated PDI are given in the diagrams.

Furthermore, metal nanoparticles revealed a uniform spherical morphology without the formation of aggregates, even though particle agglomeration can be frequently found [12]. The PDI describes the width of the particle size distribution. A narrow size distribution had a PDI of 0.1-0.2, while polydisperse size distribution exceeded a PDI of 0.5 [166]. The PDI value of nanoparticles in alginate was 0.05 (Au) and 0.18 (Fe) in 0.15% (w/v) alginate, while it was 0.16 (Au) and 0.07 (Fe) in 1.5% (w/v) alginate. The PDI value of nanoparticles in TPU was 0.7 (Au) and 0.56 (Fe), respectively.

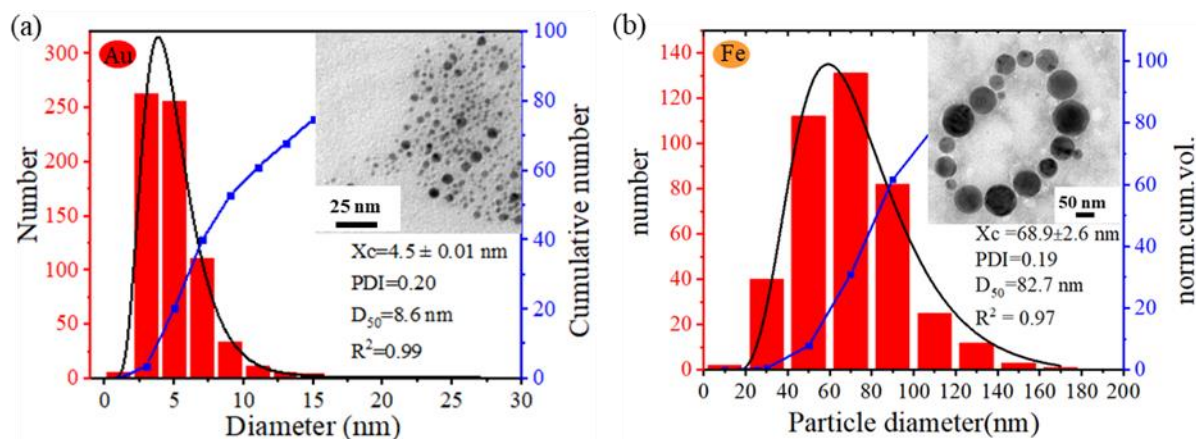


Figure 5-8: Preparation of Au, Fe-collagen composites by the laser ablation of bulk targets in 2 mg/mL collagen solutions in 5 mM acetic acid and their related particle size distributions and representative TEM image. Parameters of the log-normal fits are given in the diagrams.

AuNPs generated in other organic liquid like acetic acid was investigated as well. As shown in Figure 5-8a, AuNPs derived from 2 mg/mL collagen solutions in 5 mM acetic acid showed an average diameter of 4.5 ± 0.01 nm and revealed a uniform spherical morphology. The PDI value of Au nanoparticles in collagen was 0.2, which indicates a narrow size distribution. In the digital photos of Au-collagen composites (Figure S3e), we can see AuNPs concentrations increase with the decreasing collagen concentrations, which could be further reflected by the UV-Vis spectra indicating a decreasing intensity of AuNP SPR peaks (Figure S6c,d).

Laser-ablated Fe nanoparticles in the presence of collagen solution were characterized by TEM along with derived size distributions displayed in Figure 5-8b. Fe nanoparticles also revealed a uniform spherical morphology as in polyethylene glycol (PEG) [10], alginate, and TPU polymer. However, the corresponding average particle size in collagen is $68.9 \text{ nm} \pm 2.6 \text{ nm}$ far larger than previously stated polymers (alginate, TPU). It seems that the polymer chain size quenching effect disappeared in this case. The laser-ablated Fe species such as ions, atoms or atom clusters interact with the surrounding media including acetic acid solvent (pH in the range of 3.0-3.6) and collagen protein. The primary particles remaining in the plasma continue reacting with liquid media and grow into large particles. In the TEM images, one can clearly identify that FeNPs were arranged in rows or rings (Figure 5-8b and Figure S6b). FeNPs self-assembled structures may due to the magnetic nature of Fe oxides particles, which is a dominated by the arrangement of dipolar couplings [206]. As depicted in Figure S6a, there is a broad absorption band in the wavelength range of 350-380 nm in the UV-Vis spectra of the Fe-

collagen sample. It is believed that obtain detailed information is concerning the formation of magnetite Fe_3O_4 nanoparticles.

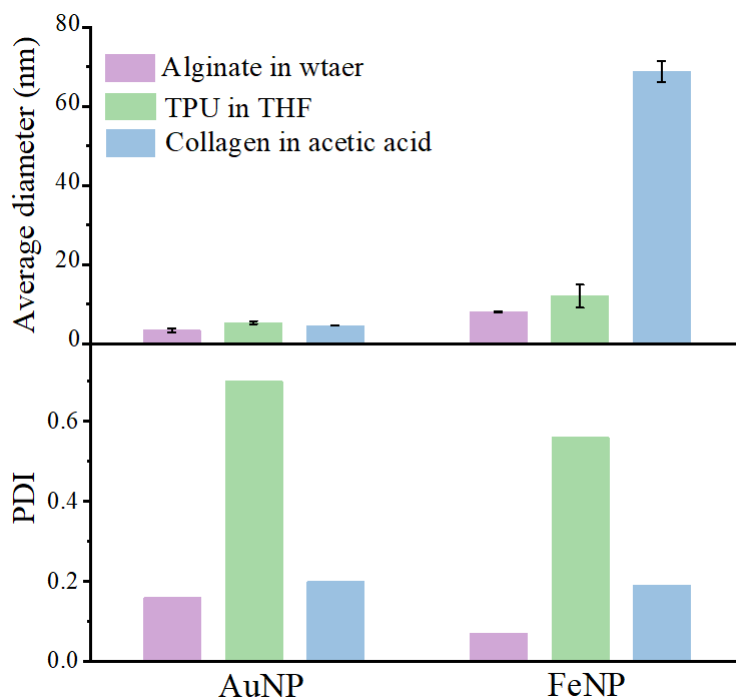


Figure 5-9: Summarized average diameters and PDI for Au and Fe nanoparticles in 1.5 % (w/v) alginate, 0.5 wt% TPU and 2 mg/mL collagen.

Figure 5-9 summarizes various particle sizes and related PDI derived from different samples. Overall, average size of AuNPs is slightly smaller than FeNPs, and largest average size of FeNPs are generated in the solvent of acetic acid. As described in section 3.4.1, nanoparticle formation is a complex process. Theoretically, particle formation mechanism may be attributed to condensation of clusters from the target material vapor [89]. Smaller AuNPs mainly originate from their primary particles during LAL while the larger FeNPs (> 60 nm) come from secondary particles.

It is also known that the AuNPs have a surface plasmon resonance effect. This may in turn lead to a photofragmentation process. The photon energy is readily converted to heat into the internal modes of some larger NPs inducing their fragmentation [207], even though the energy absorption by AuNPs is very weak. This interaction between AuNPs and photons can still be achieved in white light broad supercontinuum spectrum (400-1,200 nm) [194]. We have shown molecules or polymer chains that have a size quenching effect on NP in the laser ablation process. However, this quenching effect seemed vanished as FeNPs generated in the acetic acid

and the particle size could be larger than 100 nm (Figure 5-8b). Their average hydrodynamic particle size is around 7 times larger than that in water or THF. This result may be explained by the acidic pH destabilized nanoparticles formed on Fe target in 5 mM acetic acid. Narrow size distributions and smaller PDI value of Au, FeNPs can be found in water rather than in THF or acetic acid. That is to say, heterogeneous nucleation may form in THF or acetic acid solvents and they also have different growth rates. Nucleation and growth of nanoparticles are two inseparable processes but occurring at different speeds. The subsequent growth processes may result in broad size distribution and the phenomenon frequently occurs in lower supersaturation liquids [208]. Such a circumstance may occur in the equilibrium system that a low concentration of NPs was laser-generated in THF or acetic acid solvents.

5.2.2 Method development of confocal microscopy technique to identify nanoparticles in polymer matrices

Embedding metal nanoparticles into a polymer matrix may alter the roughness of the surface [28] and change their physicochemical properties [15], which may in turn influence protein interaction and cellular proliferation. Therefore, it is necessary to investigate the nanoparticle distribution in the polymer matrix. The nanoparticle-polymer composites were rotated in the z-axis to acquire “live” images to verify the nanoparticle distribution in the whole volume. During the laser ablation of a metal target in a polymer solution, the generated nanoparticles are immobilized by macromolecules and embedded *in situ* embedded into the polymers.

As shown in Figure 5-10 (c-f), the 3D images confirmed this point. The results showed that most nanoparticles were homogeneously distributed in alginate and TPU. However, small particle agglomeration also took place, which was in agreement with previous findings [12]. As stated in 5.2.1, there were also large particles (> 60 nm); hence, these detected spots cannot be differentiated from aggregates or large particles.

The laser-generated FeNPs alginate composites blending with fibrin fibres were also investigated with LSCM (Figure 5-11). In the bright field mode, fibrin fibres were observed. Moreover, FeNPs were distributed in both alginate and fibrin fibres as the overlay image displayed (Figure 5-11). It should be also pointed out that there are nanoparticle agglomerates in the hydrogel matrix after the gelation process. As section 4.4 described, this agglomeration or aggregation may be the reason that induced scattering active effect to visualize inorganic particle dispersion in polymer composites.

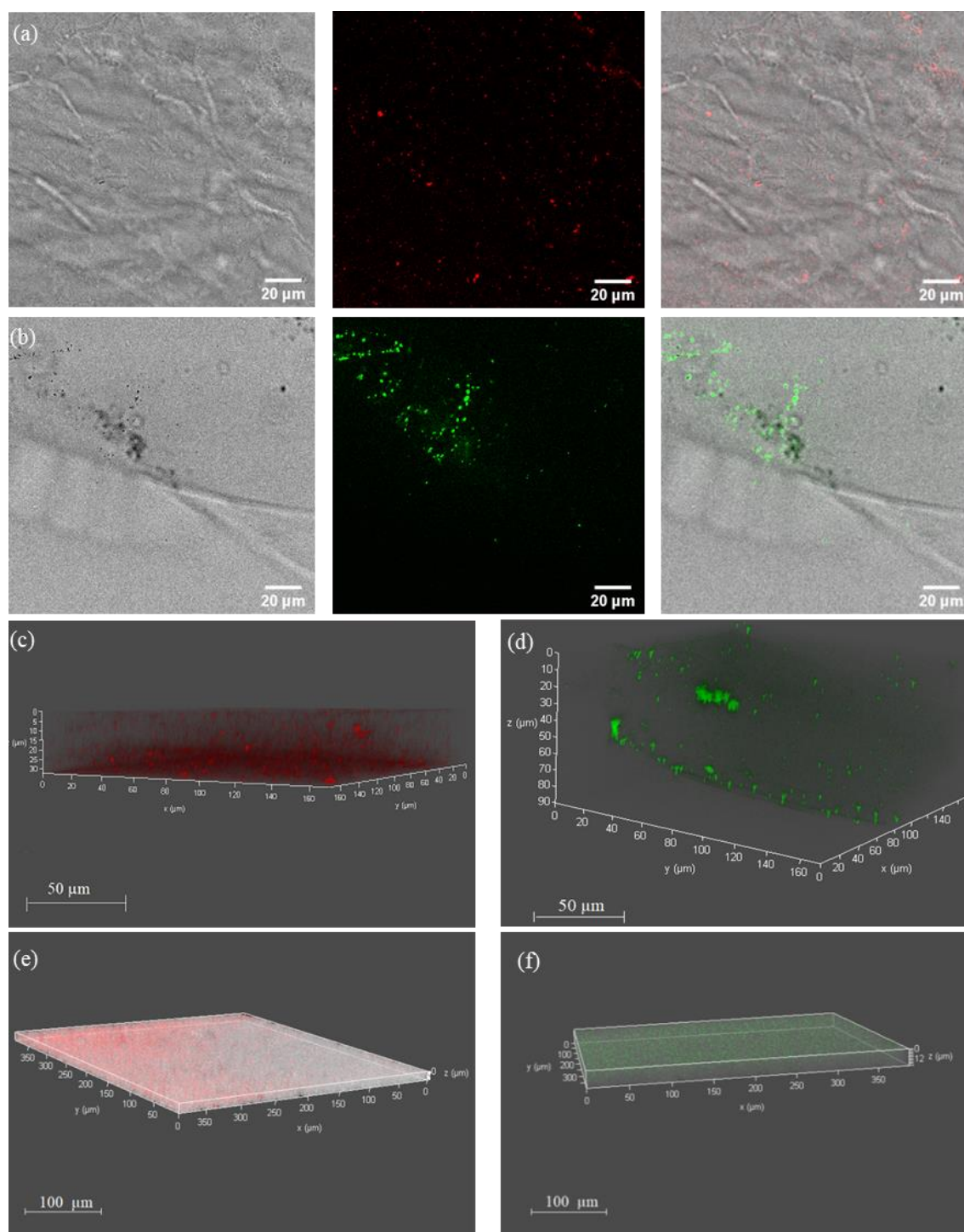


Figure 5-10: Laser scanning confocal microscopy images of gelled alginate and TPU filled with nanoparticles. Image reveals the particle distribution within the polymer matrix. Au nanoparticles (0.043 wt.%) in alginate (a), Fe nanoparticles (0.03 wt.%) in alginate (b) are shown. And left images represent the polymer matrix, middle means the nanoparticles and right is the overlays of nanoparticles and matrix. 3D images of gelled Au alginate composites (c), Fe-alginate composites (d), Au-TPU (0.069 wt.%) (e), and Fe-TPU (0.085 wt.%) (f) are shown.

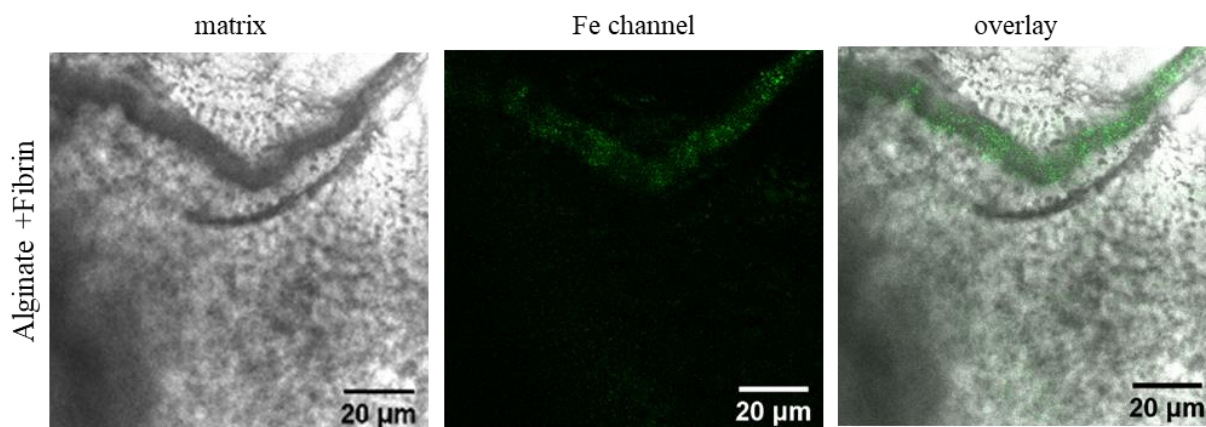


Figure 5-11: Surface characterization of alginate-based hydrogels by confocal laser scanning microscopy: additional blending with $10 \text{ mg}\cdot\text{mL}^{-1}$ fibrin showing the matrix structure (left), Fe-NP scattering at the wavelength of 488 nm (middle), and the overlay of both channels (right).

As alginate modified with fibrin fibres, FBS serum, and FeNPs, is there a correlation between NPs and protein? Are they co-localized? We hypothesized that the albumin labeled TRITC fluorophore preferred staining on the regions particularly where FeNPs were distributed. As shown in Figure 5-12, we can see the fibrin fibres and the signal of FeNPs and fluorescence of TRITC fluorophore-labeled serum proteins were detected under different observation channels. Meanwhile, we detected the overlay of the signals from Fe particles and TRITC fluorophore on the matrix and fibrin fibres. Therefore, we assumed that FeNPs have influence on the protein adsorption process.

There is an issue of whether these signals are the reflection from the alginate-fibrin matrix or not. To rule out this suspicion, a series of controls were measured with confocal microscopy as well. As displayed in Figure 5-13, we cannot detect any signals at the Fe channel. However, there are weak reflections in the TRITC channel, which may also result from the matrix of alginate as the detectable wavelength is overlapping [12]. Therefore, we can conclude that the abovementioned signals are from the particles or fluorophore.

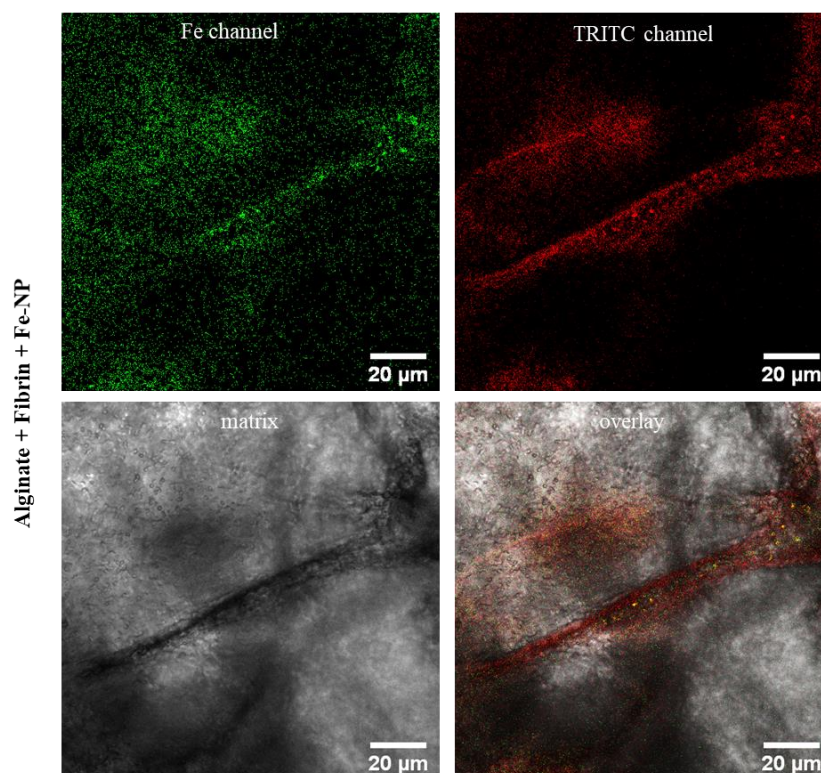


Figure 5-12: Serum protein deposition on alginate hydrogels. Confocal microscopy images of alginate hydrogels blended with $10 \text{ mg}\cdot\text{mL}^{-1}$ fibrin and enriched with $200 \text{ mg}\cdot\text{mL}^{-1}$ iron nanoparticles (Fe-NP) after incubation with TRITC fluorophore-labelled albumin in FBS solution: detected Fe-NP at 488 nm, detected albumin at 555 nm, matrix, and overlay picture.

In conclusion, we can identify various signals with different channels of LSCM. Due to aggregation scattering effect, it is possible to detect the dispersion of nanoparticles in the polymer matrix. Furthermore, nanoparticles can absorb proteins if they are labelled with typical fluorophores at suitable concentration, nanoparticles can be detected at the wavelength of this fluorophore and found them to be co-localized. According to this finding, if we fluorophore-labelled nanoparticles, this kind of particles may be detected at two channels: one is at the wavelength of aggregation scattering; another one is at the wavelength of fluorophore. Or, we can differentiate various types of nanoparticles.

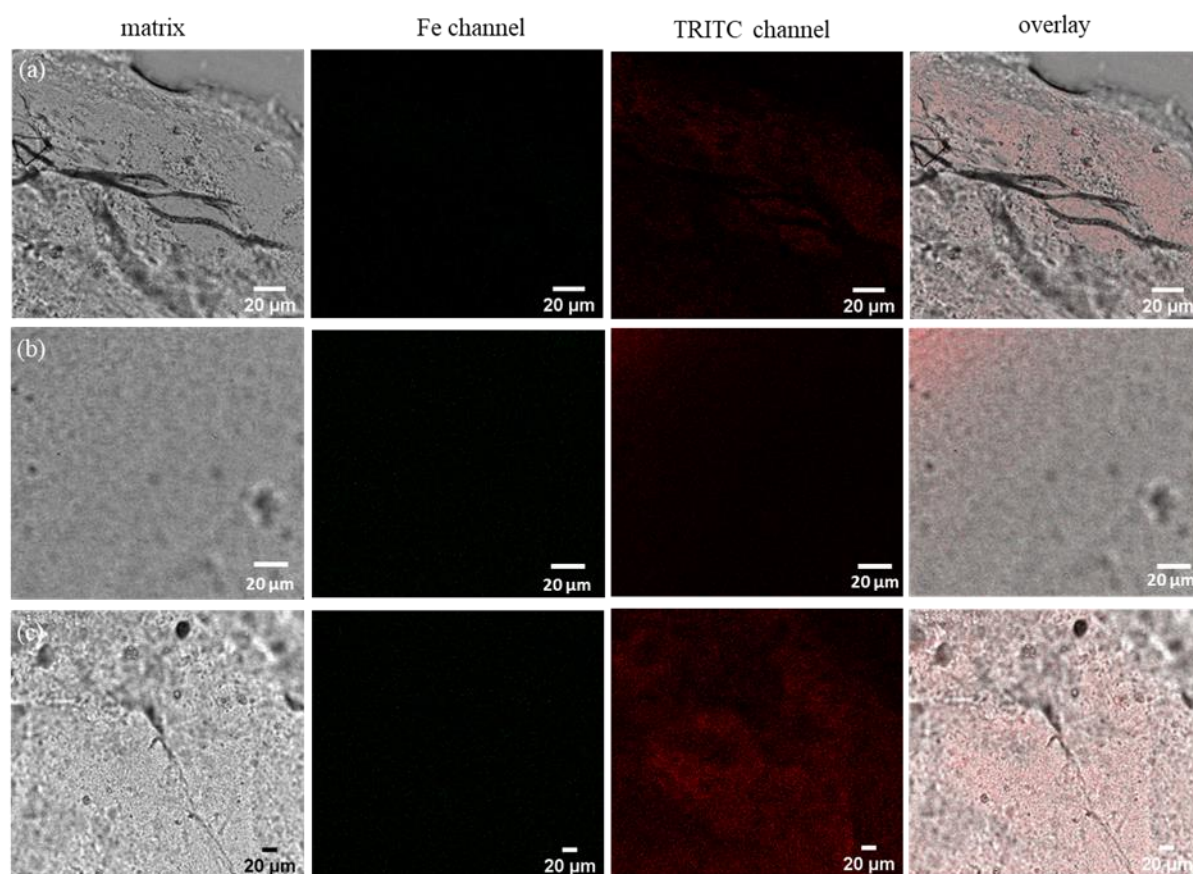


Figure 5-13: Serum protein deposition on alginate hydrogels. Confocal microscopy images of alginate hydrogels blended without (a) or with (b) 10 mg·mL⁻¹ fibrin after incubation with TRITC fluorophore-labeled albumin in the FBS solution. (c) Control for autofluorescence of alginate-fibrin gels plus fetal bovine serum without fluorophore. Shown are matrix images, detected albumin at 555 nm, and overlaid pictures.

5.3 Physicochemical properties of nanoparticle-polymer composites gels and the interaction with biological systems

5.3.1 Effect of embedded nanoparticles on the rheological property of hydrogels

The rheological and mechanical properties of the hydrogel are important for the application of tissue engineering [160]. The rheological evaluation should be also taken into account before 3D printing [109]. Li *et al.* [128] conducted rheological measurements to select the ratio of alginate and graphene materials for 3D printing. Since the incorporation of metal nanoparticles with hydrogel may enhance the mechanical properties [157], which we expected this to occur in the alginate composites as well. Furthermore, the laser-generated alginate composites are suitable bioinks for 3D printing.

Two main rheological parameters, storage or elastic modulus (G') and loss or viscous modulus (G''), not only provide the general information regarding the progress of polymerization reactions, but they also show correlations between reaction kinetics and resulting mechanical properties [182]. Oscillatory rheological measurements can be performed by recording the moduli G' and G'' within a wide range of angular frequencies. The modulus and stiffness were often reported to increase with increasing embedded nanoparticle concentrations until gels break down at a critical strain [209].

Figure 5-14 displayed the dependence of storage modulus G' and loss modulus G'' on angular frequency for the gelled alginate and nanoparticles alginate composites. It should be noted that G' is larger than G'' , indicating a characteristic of a solid-like material. That is, damping factor $\tan\delta$, e.g. the proportion of G'' and G' , should be below 1 (Figure S8). G' and G'' of nanoparticle-alginate gels were significantly greater than pure alginate as displayed (Figure 5-14a-d). Overall, the storage modulus and loss modulus was dependent on the nanoparticle loading amounts in alginate. At minimum nanoparticle concentration of 0.01 wt%, the enhancement of rheological property was significant. But at concentrations above 0.5 wt%, the enhancement was not continued. This phenomenon may relate to the different binding ways of Au or FeNPs with alginate chains. As elaborated in the section 5.3.2, the polymer showed shrinkage and turned to a tight structure due to the increasing bondage of Fe ions with alginate. Another explanation may go to the water content.

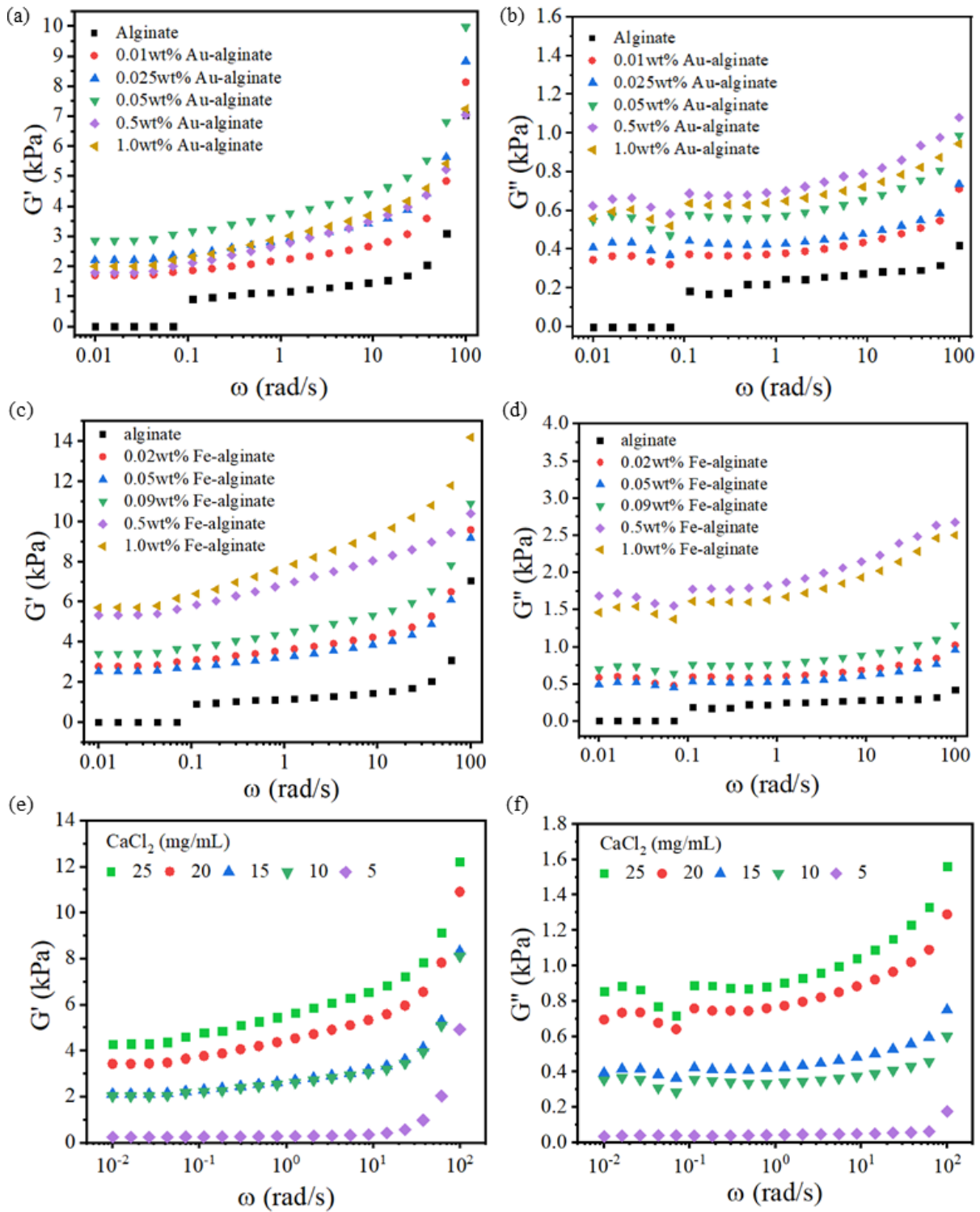


Figure 5-14: Dependence of G' (a, c, e) and G'' (b, d, f) on angular frequency for pure alginate, nanoparticle-alginate composites, Fe-alginate hydrogels cross-linked with various concentrations of CaCl_2 solution.

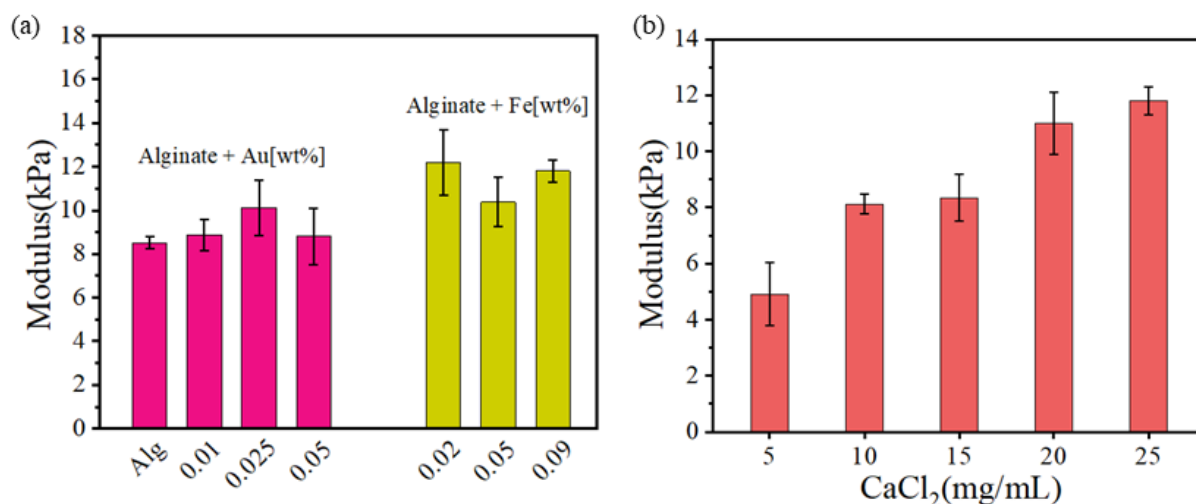


Figure 5-15: Calculated shear modulus of alginate, Au-alginate, Fe-alginate (a) and Fe-alginate cross-linked by various concentrations of CaCl₂ solution (b) at different angular frequencies in 100 rad/s.

To investigate the gel transition process, five different CaCl₂ concentrations were added to crosslink 1.5% (w/v) alginate. With increasing CaCl₂ concentrations, G' and G'' of gels increased and increased along with the frequency (Figure 5-14e,f). The results were confirmed from the findings of Li *et al.* [128]. There was an apparent gap between the curves between 5 mg/mL and 10 mg/mL CaCl₂. At 5 mg/mL concentration, G' and G'' were of the same value indicating insufficiency to accomplish the gelation process. But at the 10 mg/mL concentration, G' is much higher than G'', meaning the gelation process was complete. These results indicated all the laser prepared alginate-nanoparticle composites are anticipated to be printable in CaCl₂ solutions with a concentration of more than 10 mg/mL.

According to equation 3, the calculated shear modulus of alginate gels with/without Au and Fe nanoparticles was compared in Figure 5-15. With embedded nanoparticles, the modulus was slightly enhanced. For the Fe-alginate hydrogels, the effects were more pronounced. The highest modulus was around 12.4 kPa. Moreover, a pronounced modulus increase was also found with the increasing CaCl₂ concentrations. The results indicate a rising stiffness of alginate hydrogels. Matrix stiffness can affect the cell morphology, mechanotransduction and behaviours. For example, monocyte adhesion to endothelial cells on stiff matrix (~ 20 kPa) is less than on soft surface (~ 8 kPa) [74]. Alginate based composites with tunable stiffness and elastic modulus can be suitable biomaterials for the vascular grafts.

5.3.2 Specific Fe ion release from alginate composites and their protein adsorption

This part of the results has been published in *Nanotechnology*, 2020, 31, 405703.

Swelling behavior, porosity, and wettability of alginate composites

Protein adsorption has a strong correlation with the physicochemical properties of biomaterials. Firstly, swelling experiments were carried out in distilled water at room temperature, and the evaluation of the porosity was performed for alginate composites by using ethanol. Since the TPU-based nanocomposites are without pores, they have no swelling ability. SEM images (Figure S9) also confirmed that the native TPU polymer is not porous and the NPs have no impact on porosity. The porous nature of the alginate can be crucial for absorbing protein, transporting ions [181], analyzing mechanical properties, and cell migration [210]. The swelling ratio analysis revealed that pure alginate featured a swelling of 10%. The embedding of AuNPs induced a steep increase of the swelling ratio up to an Au mass load of 0.1 wt%, while saturation was observed for higher mass loads (Figure 5-16b). On the other hand, the embedment of Fe nanoparticles into alginate leads to a significantly higher swelling up to 50% at a mass load of 0.7 wt%, though the total slope of the curve was lower than in the case of gold (Figure 5-16a). Furthermore, a pronounced decrease in the swelling ratio was discovered for higher Fe mass loads, which could not be observed in the case of Au.

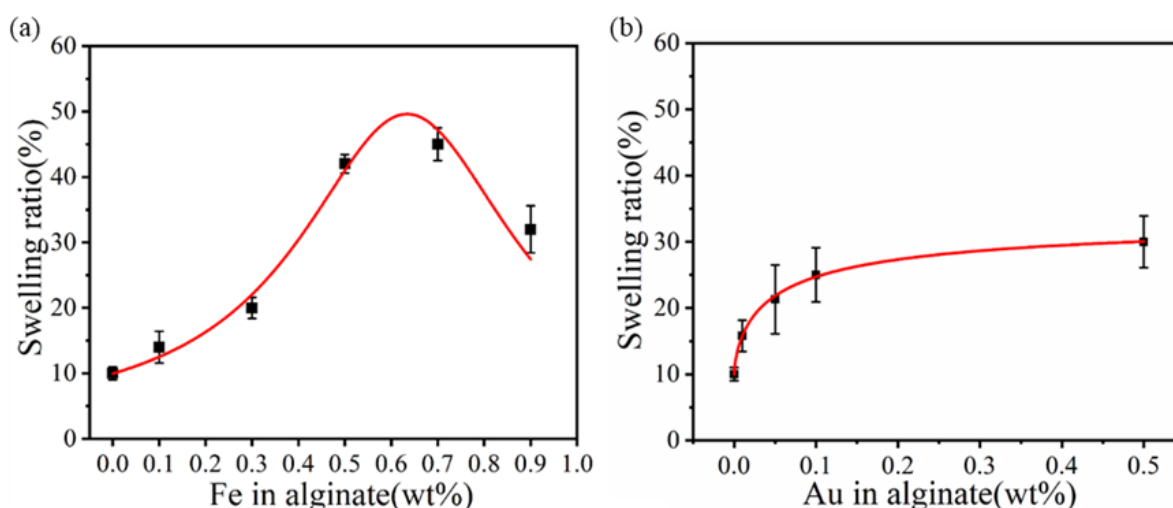


Figure 5-16: Swelling behaviour of alginate hydrogels with different loading amounts of Fe nanoparticles (a) and Au nanoparticles (b).

Although it is a fact that Fe or Au NPs altered the weight of composites, the mass of nanoparticles was negligible in contrast to the alginate weight. The fact that an increasing amount of nanoparticles enhanced the swellability of hydrogel composites is in accordance with previous reports [211, 212]. This could be attributed to the fact that embedded nanoparticles may have caused the enlargement of alginate hydrogel networks [212], which enhances swelling capability. The pronounced difference between the swelling rates for gold and iron could be that iron, due to its lower density, would fill a higher volume of the gel at an equal mass dose. In other words, iron-loaded gels contain a higher number of particles at the same mass load. Additionally, the Fe nanoparticles were reported to possess a significantly higher diameter in comparison to their Au analogs. Another interesting phenomenon is the shrinkage of the gel network at higher iron loads, which could not be observed for gold. The reason could be iron nanoparticles are soluble and release iron ions. At high iron mass loading, these ions could exceed a critical concentration where they interact with the alginate chains and induce further polymerization of the chains. This correlation will be discussed in more detail in conjunction with ion release studies.

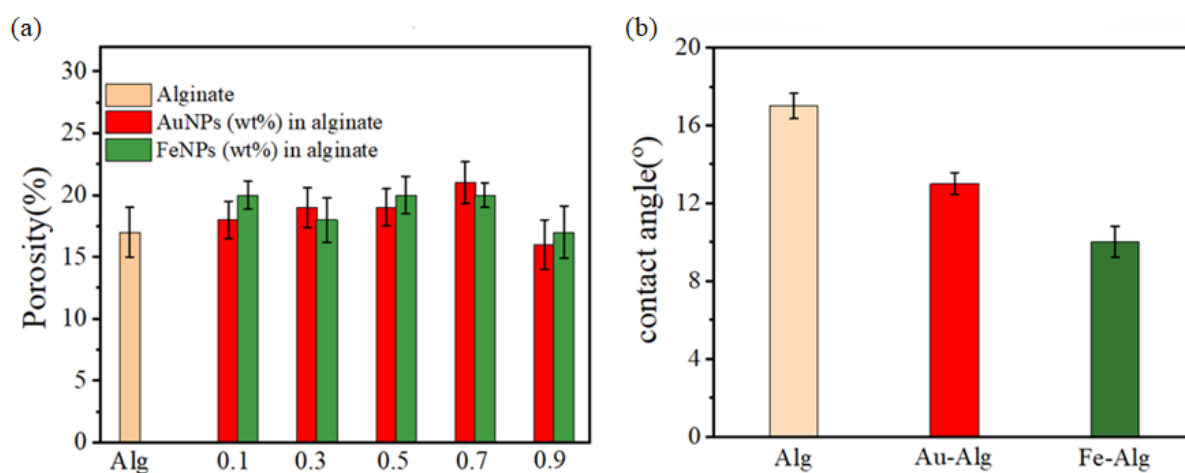


Figure 5-17: Porosity evaluation of different loadings of Au and Fe nanoparticles in alginate (a); and water contact angles of native alginate and nanoparticle-alginate composites (b).

Concerning the polymers' porosities, it was found that the porosities of pure alginate and that of composite did not show any significant variations, both for embedding with Au or Fe nanoparticles up to mass loads of 0.9 wt%, respectively (Figure 5-17a). All samples showed porosities in the range of 17%-23%, which was consistent in the literature [85]. To gain insight into the wettability of alginate nanocomposites, contact angle measurements by the captive bubble method were carried out. An air bubble was attached to the surface of samples as shown

in the insert Figure 5-17b. The angle measured using the captive bubble method is between the air bubble and surface, i.e., θ_{air} , using the Laplace-Young fit. The water contact angle should be recalculated as $180^\circ - \theta_{\text{air}}$. As known a low water angle indicates a more hydrophilic material. The surface of pure alginate and the nanocomposites showed an extremely high degree of hydrophilicity. The contact angle of pure alginate (17°) was reduced from 14° to 7° in the presence of nanoparticles, indicating a slight increase in wettability. The contact angles of different nanoparticle loadings showed no significant differences (Figure S10), probably attributed to the low differences in mass loads used here.

Table 5-2: Calculated pore size of nanoparticle-alginate hydrogels.

Fe-alginate hydrogels						
FeNP conc. (wt%)	0	0.02	0.05	0.09	0.5	1
G' (kPa)	2.8	5.5	4.6	5.9	4.7	5.0
Average pore size (nm)	11.3	9.0	9.6	8.8	9.5	9.3
Au-alginate hydrogels						
AuNP conc. (wt%)	0	0.01	0.02	0.05	0.5	1
G' (kPa)	2.8	3.8	4.2	3.1	3.8	3.6
Average pore size (nm)	11.3	10.2	9.9	10.9	10.2	10.4
0.09 wt% Fe-alginate hydrogels gelled by various CaCl₂ concentration						
CaCl ₂ conc. (mg/mL)	5	10	15	20	25	
G' (kPa)	-	3.1	3.2	5.2	5.9	
Average pore size (nm)	-	10.9	10.8	9.2	8.8	

The calculated pore size of alginate hydrogels was listed in Table 5-2. As equation 12 described, a greater G' value indicated a denser network. Since the concentration of 5 mg/mL CaCl₂ is not sufficient for the complete gelation of solid-like alginate gels, their pore size cannot be

calculated. Not surprisingly, a denser hydrogel network was formed with more calcium ions. The pore size of reference alginate hydrogels was ranging from 8.8 to 11.3 nm. In the presence of embedding nanoparticles, pore size was slightly smaller. The pore size was in the range of the reported alginate hydrogels (5-200 nm) [213]. The surface charge of embedding nanoparticles increases the degree of hydration, contributing to greater storage modulus and smaller calculated pore size. Thus it may explain the swelling ratio curves. Moreover, the pore size of Fe-alginate hydrogels was somewhat smaller than that of Au-alginate, which may due to more FeNPs existing in the network as loading the same weight of Au nanoparticles inside.

Fe ion release kinetics of nanoparticle-alginate hydrogels

Figure 5-18 illustrated the time-dependent Fe ion release from Fe-loaded alginate nanocomposites. Ion releasing curves from a series of different mass loadings of FeNPs in alginate were plotted in Figure S11. The general trend of these curves was similar to other metal ion releasing profiles, which followed the pseudo-first-order equation [12, 214]. The accumulated ion release from Fe nanoparticle composites was obviously higher than the unloaded controls (Figure 5-18a). The release of ions from pure alginate was probably induced by Fe impurities. After an initial increase within the first 10 h, the release profiles entered a plateau. Comparable release kinetics of Fe ions were also found for other nanocomposites in literature [111]. A diffusion-driven mechanism would slow down release in case of higher total ion concentrations in the medium, reducing the relative release under static experimental conditions. Irrespective of the expectations, the highest total amount of Fe ions was released from the alginate samples with lower nanoparticle loadings, such as 0.05 wt% and 0.1 wt% (Figure 5-18a). And the absolute maximum Fe ion concentration clearly decreased with the increasing load of nanoparticles embedded within the alginate matrix, even though high deviations between the individual samples were found (Figure 5-18c). The normalized (to the total mass of loaded Fe) curves of released Fe ions showed a much more pronounced trend, indicating an exponential decrease of the relative ion release with nanoparticle mass load, which saturates below 10% for mass loads > 0.5% (Figure 5-18b and Figure 5-18d).

These findings for the alginate-iron system are in contrast to findings on other release systems previously described in the literature, where the total release typically increased with nanoparticle loading. In contrast, we here find an optimum ion release at low NP loading and a lower total ion release at higher nanoparticle loading. In the following section, we aim to explain this phenomenon by discussing frequently reported effects like ion diffusion and

element solubility, but also solubility of formed metal oxides as well as interactions between the ions and the polymer matrix, which are mostly neglected in the literature.

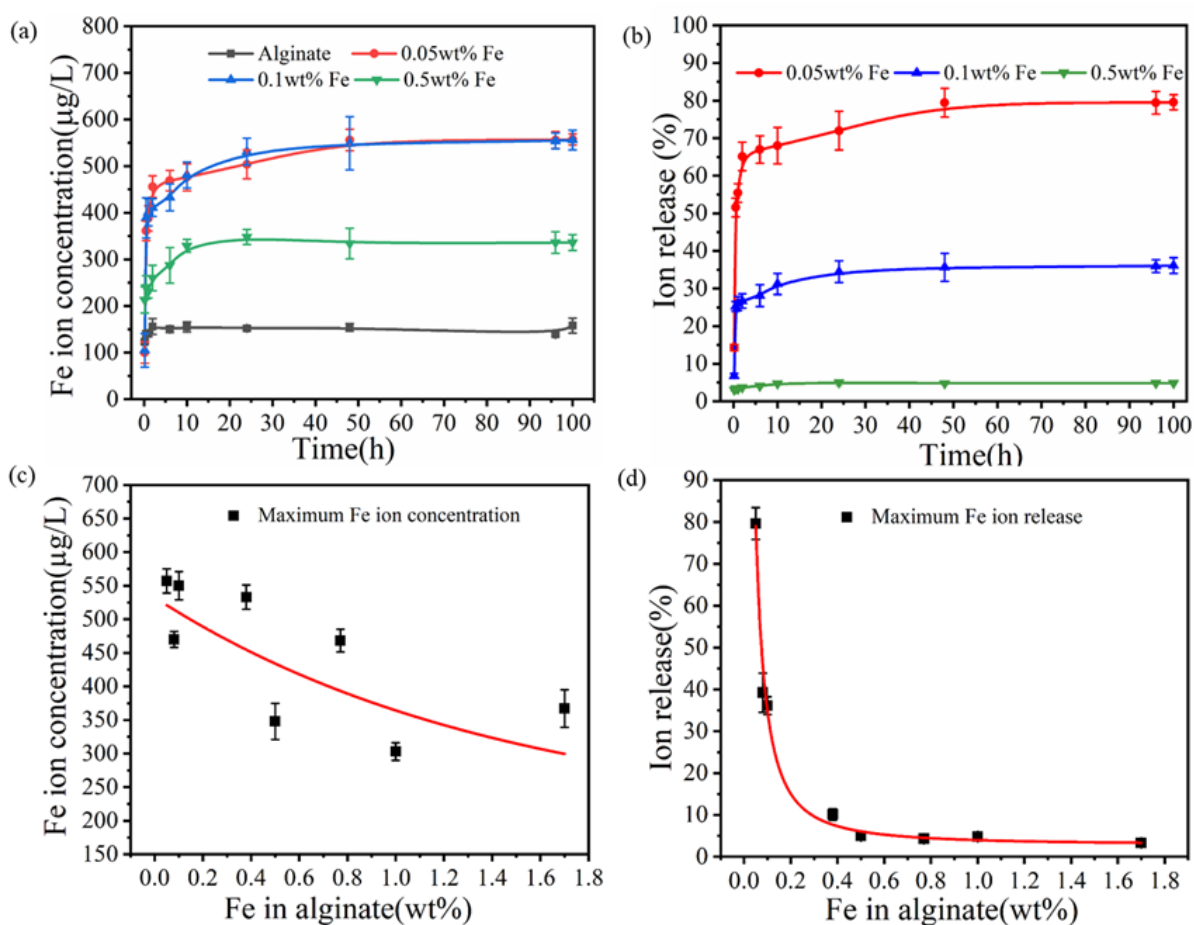


Figure 5-18: Long-term Fe ion release kinetics in the air-saturated buffer: (a) released Fe ion concentration of Fe-alginate composites, (b) released mass percent of different amounts of Fe nanoparticles in alginate, (c) the maximum Fe ion release, and (d) the corresponding ion release percent of Fe-alginate composites.

Our initial hypothesis to explain this counter-intuitive phenomenon was that it may be related to a peculiarity of the alginate gel itself. To further investigate this correlation between the ion release and the loaded nanoparticle mass, control experiments with Zn and Cu nanoparticles in alginate were conducted by following the identical experimental procedure (Figure S12). The obtained results showed that the total concentration of released metal ions increased with the mass of Zn and Cu particles in alginate, while the total concentrations of Zn were much higher than for copper, which is in accordance with the more negative redox potential of Zn. The relative ion release slightly increased for Zn and decreased for Cu, however, the trends were far

less pronounced than in the case of iron. Based on this, we can conclude that the iron-alginate gel system seems to have special release properties, where higher concentrations of particles in the gel seem to inhibit the release of iron ions or particularly pronounced burst release occurs at low mass load.

Figure 5-19 illustrates the individual mechanistic steps involved in the release of ions for Fe compared with Zn. The release of ions from nanoparticle-loaded gels is initially influenced by the diffusion of the solvent into the composite followed by the diffusion of the solvated ions out of the gel. The ions diffuse through channels that consist of the already existing pores of the network structure of the polymer or are migration paths of already released ions and corroded nanoparticles [215]. Diffusion clearly explains the shape of the release curves in all samples as depicted in Figure 5-18. The initial burst release is probably related to the high concentration gradient between the vicinity of the nanoparticle and the outside of the gel as well as the fact that nanoparticles situated close to the gel surface have shorter diffusion paths and therefore induce a faster release. After about 10 h, the release saturates because the concentration gradient, which is the driving force for diffusion, levels, as concentrations inside and outside of the gel reach a steady state under static release conditions.

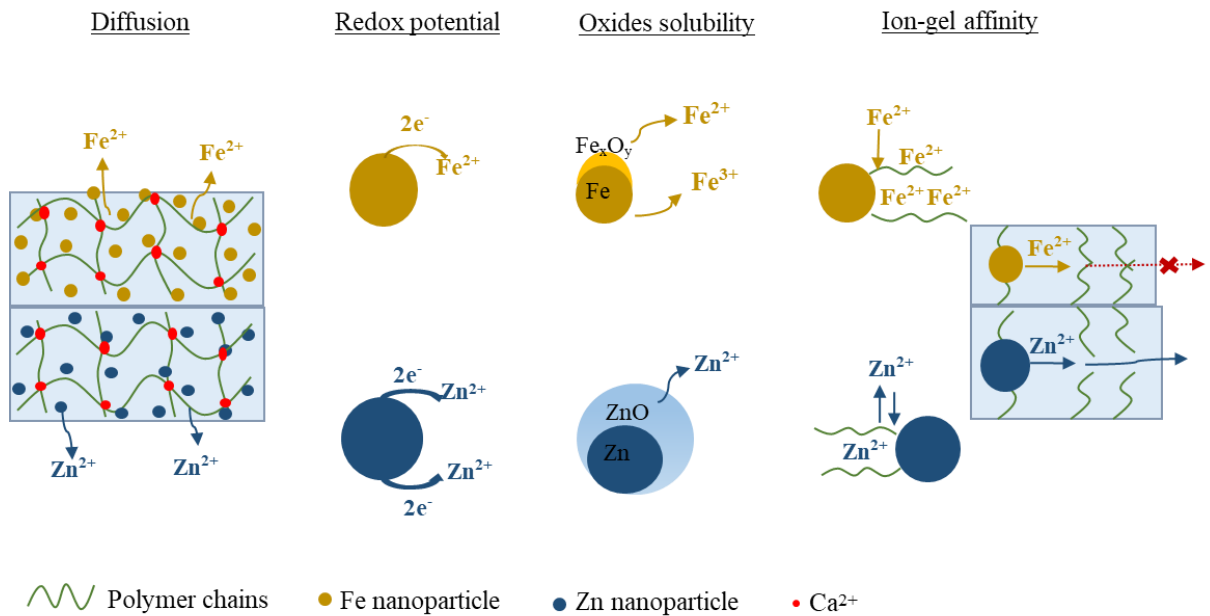


Figure 5-19: Schematic diagram of special Fe ion release behavioural mechanism compared with Zn.

However, as the diffusion coefficients of solvated $\text{Fe}^{2+}/\text{Fe}^{3+}$, Zn^{2+} and $\text{Cu}^+/\text{Cu}^{2+}$ ions are not significantly different (the literature values are shown in Table 5-3), diffusion cannot account for the peculiar behaviour of the iron system, where higher absolute iron mass is released at low particle mass load. The ion release is further influenced by the dissolution of the embedded metal particles. The oxidation ability of metal can be estimated using the electrochemical standard potentials (E°). E° for the oxidative formation of Zn^{2+} , Fe^{2+} and Cu^{2+} from the corresponding metals is -0.762, -0.447 and 0.342V, while the strongest release is expected for the most negative standard redox potential. Based on this we would expect a trend for the highest release rate and final ion concentration $\text{Zn} > \text{Fe} > \text{Cu}$. This trend can be clearly confirmed for higher particle mass loads. For example, at the 1.2 wt% loading of Zn and Cu and 0.5 wt% of Fe, this trend can be observed as the resulting total ion concentration of Zn, Fe and Cu was 550, 300 and 110 $\mu\text{g/L}$ (Figure 5-18 a and Figure S12a). However, the trend is significantly different at lower loads. For example, at 0.3 wt%, the total released mass of iron ions is 4-5 times higher. These findings cannot be explained by the redox potential of the corresponding metal nanoparticles.

Table 5-3: Literature values of ions diffusion coefficients at infinite dilution.

Ion	T(K)	D ($10^{-6} \text{ cm}^2/\text{s}$)	Ref.
Fe^{2+}	293	6.3	[216]
	298	7.2	[217]
Fe^{3+}	293	5.8 ± 0.2	[216]
	298	6.0	[217]
Zn^{2+}	293	6.1	[216]
	298	7.0	[217]
Cu^+	293	6-8	[218]
	298	7.3	[218]
Cu^{2+}	293	5.0	[218]
	298	7.1	[217]

Next to the direct oxidation of the pure metals in an aqueous medium, it is highly likely that the iron nanoparticles, laser-fabricated in aqueous medium are at least partially oxidized. Using picosecond lasers, oxides are frequently obtained by the ablation of elemental targets in liquids,

such as ZnO, CuO, FeO, Fe₃O₄ [219]. The formation of possible Fe₃C species can also not be excluded in case ablation is conducted in organic solvents. In addition, it is known that laser ablation of ignoble metals in an aqueous solution may lead to suboxide nanoparticles, or elemental core- oxide shell nanoparticles [220]. Based on the Pourbaix diagram in aqueous solution at 298K and pH 7.4, oxides like ZnO, Cu₂O, CuO, FeO, Fe₂O₃ and Fe₃O₄ are likely to form. This shows that in the case of several different iron oxides could be formed. However, there are some indications in literature that FeO may be the predominant oxide under these conditions [221].

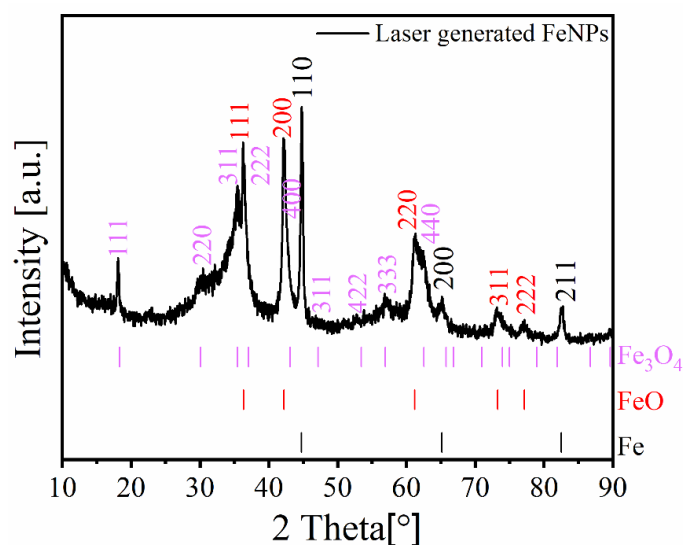
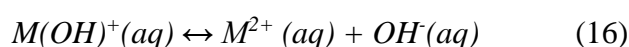
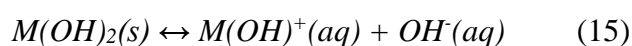


Figure 5-20: XRD pattern of laser-generated FeNPs in DI water.

It is difficult to directly measure FeNPs phase in alginate because the alginate highly affected the determination even at a high nanoparticle amount (Figure S13). Due to the hydrogen bonding among alginate chains, alginate is usually crystalline showing two diffraction peaks at around 13.5° corresponding to the reflection of (110) plane from polyguluronate unit and 22° due to (200) plane from polymannuronate, and a broad peak at 39° indicating the amorphous structure [222]. These characteristic peaks disappeared through laser ablation. Although there is some similar peaks position with pure FeNPs, we still cannot distinguish which kinds of Fe or Fe oxides phases in alginate. Without alginate, Fe phases can be detected as the XRD patterns shown in Figure 5-20. XRD pattern shows that there are peaks of the known structure of Fe₃O₄ crystals (JCPDS No. 74-0748), FeO structure (JCPDS No.73-2144) and Fe⁰ (JCPDS No. 87-0722). For the Fe₃O₄ phase, many characteristic peaks were observed at $2\theta=18.4^\circ, 30^\circ, 35.5^\circ, 37^\circ, 43.2^\circ, 47^\circ, 53.5^\circ, 56.8^\circ, 62.7^\circ$. For the FeO, peaks were at $36.3^\circ, 42.4^\circ, 61.2^\circ, 73.3^\circ$ and 77.4° , while the main peak in the XRD pattern of Fe⁰ appeared at $2\theta=44.7^\circ, 65.2^\circ, \text{ and } 82.4^\circ$.

During the particle dissolution reaction in water, these oxides will initially form hydroxides that can dissolve to form metal ions. As a consequence, the solubility of these oxides may be an important contributing factor to the ion release mechanism [223]. For metal oxides, the following essential reactions occurred in water at pH 7.5, as Mudunkotuwa described for ZnO NPs [223]. Thereto, we compared the solubility product constants K_{sp} of Zn, Cu and Fe hydroxides listed in Table 5-4.



The values reveal that the K_{sp} value of FeO/Fe(OH)₂ is the highest followed by ZnO/Zn(OH)₂, which is considerably higher than CuO/Cu(OH)₂. The solubility constant for the system Fe₃O₄/Fe(OH)₃ cannot be directly compared to the others due to deviating reaction stoichiometry. Based on this we can conclude that the higher solubility of the iron oxides may be a contributing factor to a stronger release of iron ions, however, it does not explain the peculiar particle mass load dependency of the release kinetics.

Table 5-4: Calculated solubility product constant (K_{sp}) for metal oxide nanoparticles in DI water at 25 °C.

	K_{sp}	Ref.
Cu(OH) ₂	4.2×10^{-21}	[224]
Fe(OH) ₂	2.0×10^{-15}	[224]
	4.9×10^{-17}	[217]
Fe(OH) ₃	1.6×10^{-39}	[224]
	2.8×10^{-39}	[217]
Zn(OH) ₂	7.6×10^{-17}	[224]
	3.0×10^{-17}	[217]

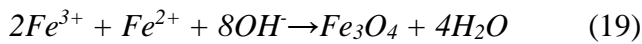
Thereto, one final aspect which needs to be considered concerns the interactions of the metal ions with the alginate matrix. The order of binding affinity of ions for alginate was: Fe²⁺ > Fe³⁺ > Cu²⁺ > Zn²⁺ [225, 226]. Jodra and Mijangos proposed an ion-exchange model between metals

and calcium gelled alginate gels [227]. According to this equilibrium model, the process was described by the next reactions (17) and equation (18) [227]:



$$K_{Ca}^M = \frac{(q_M/C_M)}{(q_{Ca}/C_{Ca})} \quad (18)$$

where K is the corresponding equilibrium constant, q (mol/kg) is the metal mass in alginate, C (mol/L) is the metal concentration. Based on this we can conclude that the strong affinity of the iron ions for the alginate chains would shift the dissolution equilibrium of the FeO to the side of the soluble Fe^{2+} , while furthermore the solubility of the FeO is higher than that of CuO and ZnO. The combination of these two factors may account for the irregular burst release of iron ions at low loadings. However, why is the release inhibited at higher iron mass loads? In this context two factors could contribute. Firstly, high iron ion concentrations may favour the formation of low solubility oxides like Fe_3O_4 according to reaction 19.



Furthermore, Fe ions have the highest affinity for alginate which may further influence the alginate network by inducing additional gelation processes and reducing pore diameters in the gel network. This assumption is backed by the measurements of the swelling rates, which tended to slightly decrease for iron nanoparticle loads exceeding 0.7 wt% (Figure 5-14a). Hence, the higher ion concentration contributes to the decreasing porosity of alginate gels, which will inhibit the release at the higher Fe mass loads [228]. Considering the described factors, it is not the redox potential of the metals and diffusion of metal ions, but most likely the solubility of nano metal oxides and affinity of metal ions for alginate that lead to the special release behaviours of iron ions from alginate gels.

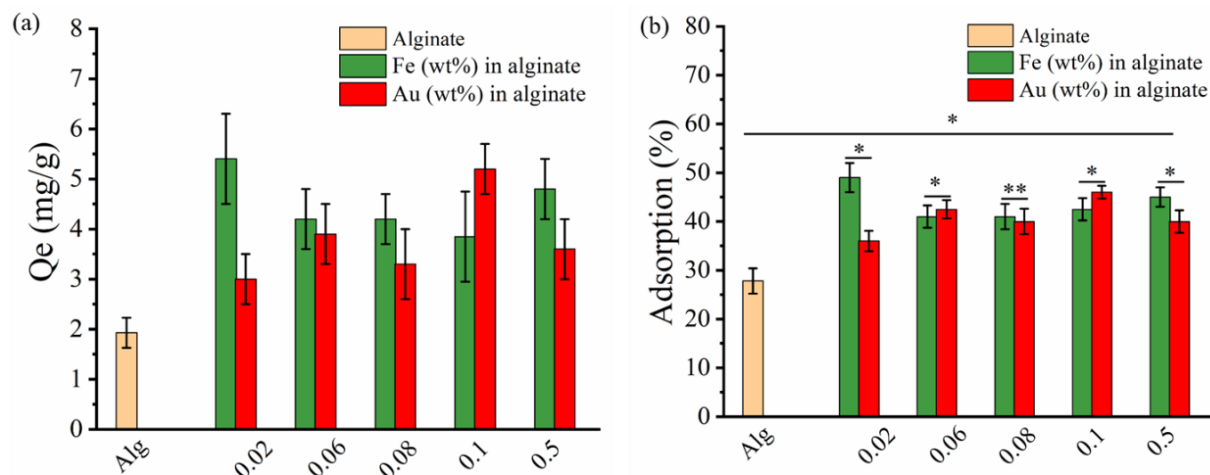


Figure 5-21: Protein adsorption on pure alginate, and corresponding composites as a function of nanoparticle concentration at pH 7.4 and room temperature.

The comparison of the protein adsorption capacity of Au- and Fe-alginate composites as well as of pure alginate is summarized in Figure 5-21. There is a clear trend revealing an elevated protein adsorption capacity compared to pure alginate (1.93 ± 0.3 mg/g). Apparently, minute loadings of the composites with iron (0.02 wt%) have a strong effect on protein adsorption, increasing the protein mass by a factor of 2.8 (5.4 ± 0.9 mg BSA/g composite). Interestingly, this steep increase in protein adsorption occurs in the same concentration regime where highly pronounced ion release is reported. This is in good accordance with cell culture experiments on similar systems where Bläser *et al.* indicated that 0.01wt% Fe-alginate gels strongly favor cell adhesion [12]. For higher Fe nanoparticle loads there is a slight decrease in protein adsorption capacity, however, the values are still higher than the pure alginate control. For the case of Au-alginate composites, there is no steep increase of protein adsorption at low mass load but a constant increase with a local maximum at 5.0 ± 0.5 mg/g at the concentration of 0.1 wt%. It was assumed that the type of embedded nanoparticles (Fe or Au) had no observable impact on protein adsorption. For further clarification and to rule out cross effects from different protein concentrations studied, the relative amount of adsorbed protein was plotted versus the nanoparticle loading in the composites (Figure 5-21b). Nanoparticle-alginate composites adsorbed more BSA than pure alginate, and the adsorption was approximately 1.7 times that of pure alginate. This phenomenon was also found in the collagen I protein adsorption as shown in Figure S14. As a control, collagen I in contrast to BSA, is positively charged at pH 7.4 as indicated in the literature [229]. Our results also showed that the integration of minute amounts of nanoparticles has a universally beneficial effect on protein adsorption, both for albumin and collagen I. This seems to indicate that the net charge of the protein alone is not the dominant factor driving the adsorption process.

The adsorption of proteins on a surface is a complex process, which is affected by the morphology, the ion-exchange, the surface charge, hydrogen bonds, van der Waals interaction and electrostatic interactions [68, 230]. The first step of protein adsorption is a fast direct-attachment to the surface, while the second step is slow and the thickness of the protein layer gradually increases with the increasing amount [68]. Generally, protein preferred hydrophobic surface to hydrophilic ones. However, there is also evidence about protein adsorption on hydrophilic surfaces. In an aqueous environment, the available possibilities for hydrogen

bonding involve the residual amide molecules which form water-amide hydrogen bonds [230]. According to the experimental results, there is protein adherent on the alginate hydrophilic surface. But we still cannot name alginate surface as “protein-adsorbed” or “non-protein adsorbed”. The possible explanation could be that hydrophilic surface sites would attract proteins by electrostatic interactions. Moreover, porous structure of alginate gels provides the channel for protein adsorption. Another important factor is the presence of Au and Fe nanoparticles, which can alter the morphology. Nanoparticles have a high affinity to amine and cysteine groups of proteins, especially for AuNPs. And the increasing ionic strength resulting from the Fe ion release was proved to adsorb larger amounts of protein [230]. Therefore, the hydrophobic or hydrophilic surface was not a significant parameter. The porous structure of the alginate composites and the stronger release of ions play a prominent role in this situation. This demonstrates the high application potential of composites as only minute amounts of NPs in the concentration range; significantly improve protein adsorption known to facilitate cell adhesion and growth.

5.3.3 Iron nanoparticles and fibrin blending promote serum-mediated endothelialization on alginate hydrogels

The physicochemical properties and special ion release profiles from pure alginate hydrogels embedding with iron nanoparticles were clarified in section 5.3.2. Given metal ions could improve protein adsorption, we triple modified alginate gels with Fe-NPs, fibrin, and serum protein coatings (SPCs). Here, we were particularly interested in the synergetic effects of these three modifications and how fibrin blending and NP incorporation alter the physicochemical and mechanical properties of the alginate surface and the resulting endothelium cell behaviours. Part of the results has been published in *Advanced Materials Interfaces*, 2021, 2002015. And the cell experiment was performed by Alena Richter.

Firstly, the surface roughness of hydrogels was determined with AFM as well as the detailed topography was imaged (Figure 5-22). AFM is a powerful technique to observe the topography and understand the mechanics of diverse surfaces as well as biological interactions between different biomolecules, cells, and materials. With the help of special AFM tips for soft materials, we can successfully obtain the surface topography and force-distance curves. In addition, the force-distance curve could provide information such as surface interactions, elastic

determination [231]. Of note, the surface roughness information was read from the AFM images.

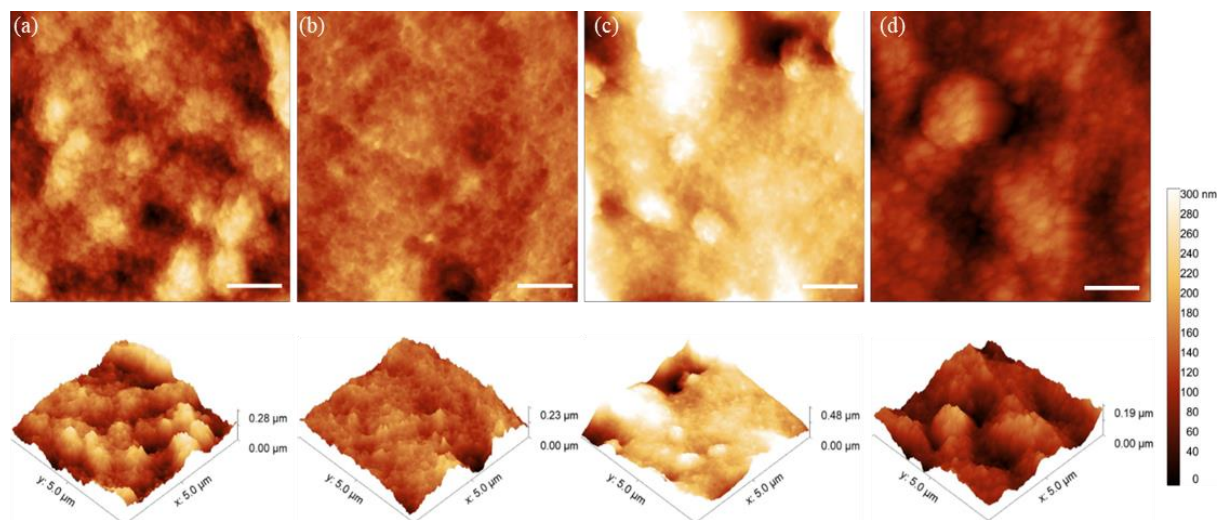


Figure 5-22: AFM (2D and 3D) images of alginate (a), alginate-Fe 200 $\mu\text{g}/\text{mL}$ (b), alginate-fibrin 10 mg/mL (c), and alginate-fibrin-Fe 200 $\mu\text{g}/\text{mL}$ (d). Scale bars are 1 μm .

In table 5-5, it is clear to show the roughness parameters of each sample, which were elucidated in section 4.4. We can conclude that the surface of all gels was bumpy. The sample of Alginate-Fibrin was the roughest ($R_a = 44.1 \text{ nm}$), followed by Alginate gels ($R_a = 38 \text{ nm}$). With the embedment of FeNPs, the roughness of the hydrogel surface decreased, especially in the absence of Fibrin. This finding may be because the capping effect of nanoparticles tends to fill the rough surface of hydrogels.

Table 5-5: Roughness parameters of native alginate, alginate-Fe 200 $\mu\text{g/mL}$, alginate-fibrin 10 mg/mL , and alginate-fibrin 10 mg-Fe 200 $\mu\text{g/mL}$ composites.

Samples	R_a (nm)	R_q (nm)	R_t (nm)
Alg	38.0 ± 0.1	47.3 ± 0.5	269.7 ± 24.9
Alg-FeNPs	19.5 ± 0.3	26.0 ± 0.4	235.2 ± 0.3
Alg-Fibrin	44.1 ± 1.8	64.5 ± 2.2	485.4 ± 9.8
Alg-Fibrin-FeNPs	26.1 ± 0.1	32.0 ± 0.1	192.5 ± 1.7

Stiffness is a term indicating the tendency to return to its original form after being subjected to a force. A stiffer surface can be achieved at a lower strain and obtained a higher elastic modulus [232]. It is known that the stiffness of the hydrogel surface can affect cell motility, differentiation, and proliferation [22, 233]. There are two common methods to indicate the stiffness of hydrogels, including atomic force microscopy [234], or oscillatory shear testing [22, 159, 235]. Comparing force-distance curves of soft sample surfaces can reveal relatively the deformation of soft samples, reflecting the stiffness or elasticity [236]. The slope of the falling linear regime can be fitted to estimate the sensitivity and stiffness of samples [19]. The modulus can be easily calculated using the Sneddon model [237]:

$$F = \frac{E}{1-\nu^2} \frac{2 \tan \alpha}{\pi} \delta^2 \quad (20)$$

F is the force and E is Young's modulus; δ denotes indentation; α and ν is half-angle of tip and Poisson's ratio, respectively.

If there are fillers or embedding particles, the inhomogeneities cannot be appropriately described with the Sneddon model. However, if dividing data into segments, the slope could be obtained from the force F_i and indentation δ_i , which means each segment's stiffness [238]. The steeper slope indicates higher sensitivity, less or no deformation and a stiffer surface, as shown in Figure 5-23. It is suggested a higher stiffness of hydrogel embedded with Fe nanoparticles than pure alginate or alginate-fibrin gels, which was in agreement with the rheological properties in section 5.3.1.

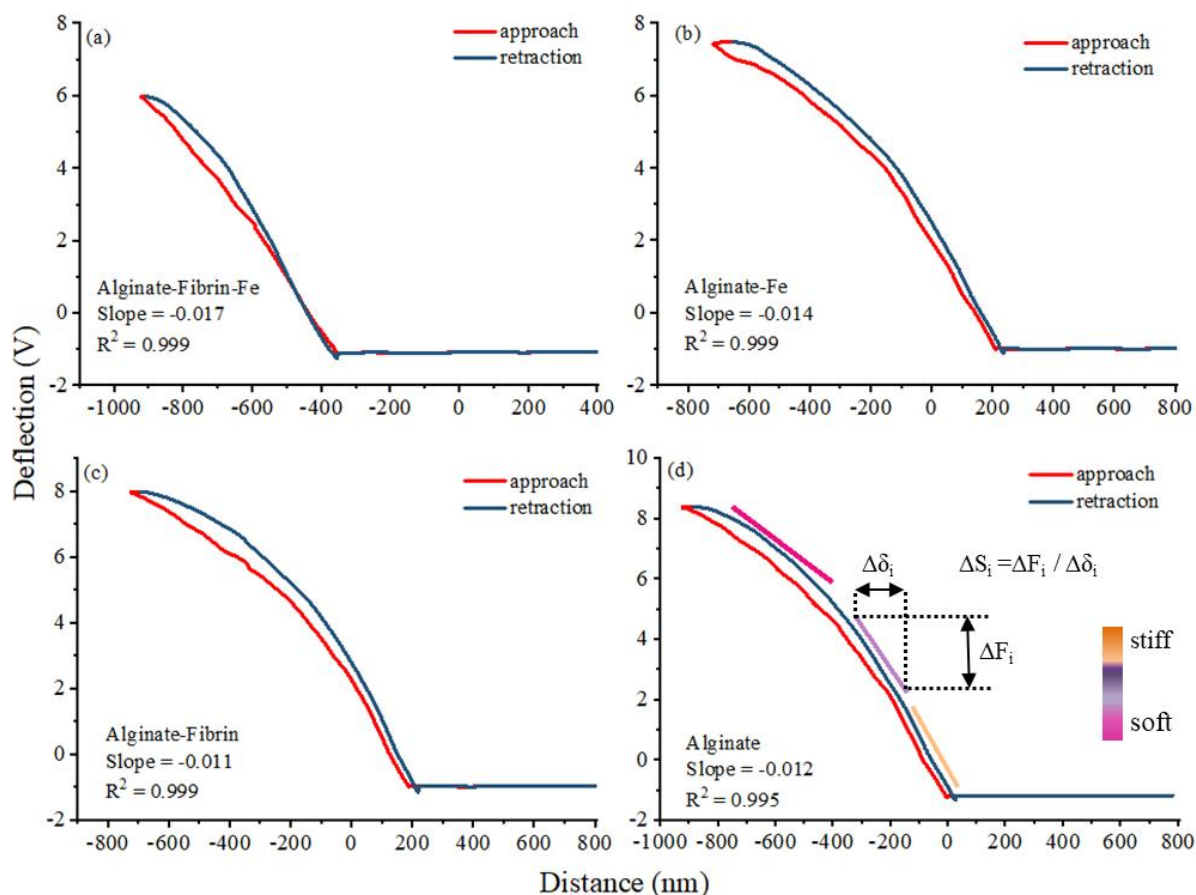


Figure 5-23: Force-distance curves of approach and retraction of alginate-10 mg fibrin-200 $\mu\text{g}/\text{mL}$ Fe (a), alginate-200 $\mu\text{g}/\text{mL}$ Fe (b), alginate-10 mg/mL fibrin (c), and alginate gels (d). The slope ($\text{V}\cdot\text{nm}^{-1}$) in the approach touching regime has been calculated with falling linear regressions.

As alginate blending with fibrin, porosity was still in this range of 17%-23% as above alginate samples while it decreased slightly to 13.4% in the presence of FeNPs (Figure 5-24c). Contact angles (α) of the triple alginate-fibrin-FeNPs hydrogels were also measured with the captive bubble method. As shown in Figure 5-24a,b, it was not surprising that all the hydrogel surfaces were hydrophilic. The contact angles were in the range of 12° - 38° . However, the embedment of Fe nanoparticles and the combination of fibrin in alginate significantly influenced the contact angles. But the effect of these two FeNPs concentrations of 100 and 200 $\mu\text{g}/\text{mL}$ seemed no different. They both decreased the contact angles compared to pure alginate ($*p \leq 0.05$), as reported before. In contrast, the fibrin fibres largely increased the contact angle from 20° of pure alginate to 38° ($**p \leq 0.01$). Van Oss described the hydrophobic surface property of fibrin layers and measured the contact angles of 63.3° - 73.6° [239], indicating blending with fibrin fibres contributed to a more hydrophobic surface. Bialkower *et al.* [240] found that the

hydrophilic cellulose films converted to hydrophobic ones as blending with fibrin. The hydrophobic surface is assumed to be beneficial to protein adsorption. Furthermore, the coating FBS inclined to adhesion on the less hydrophilic surfaces of alginate-fibrin or alginate-fibrin-Fe complex contributed to subsequent cell proliferation.

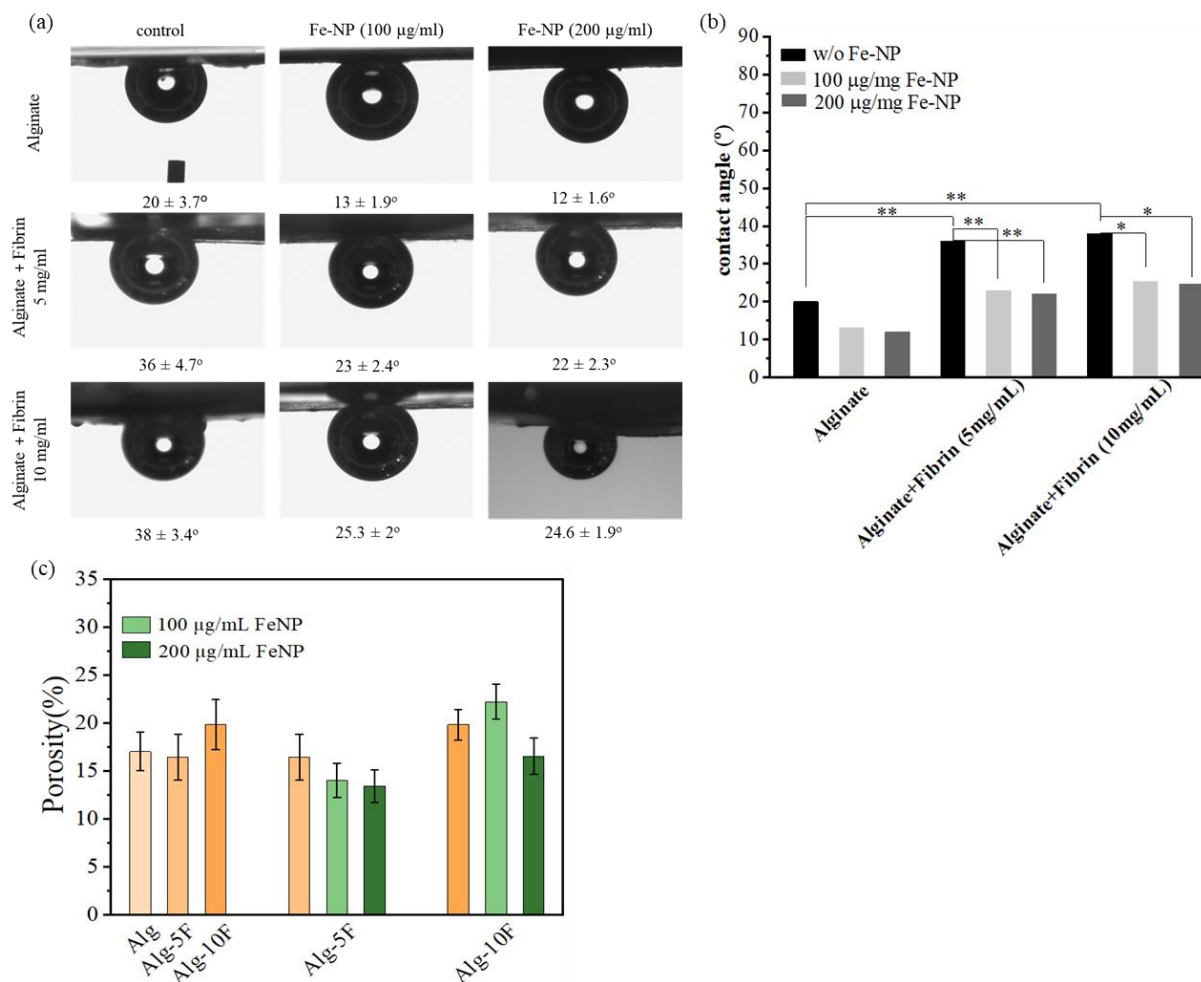


Figure 5-24: (a) Contact angles of air bubble droplets in the water on the surface of biomaterials at room temperature. (b): Bar diagram of summarized contact angles. (c) Porosity of alginate-fibrin hydrogels. Shown are means \pm SEM measured in duplicate and analyzed by 1-way ANOVA and Tukey test (* $p \leq 0.05$ and ** $p \leq 0.01$).

Rheological properties of hydrogel samples were shown in Figure 5-25. It showed that the examined hydrogel samples were only minimally strain-dependent within the testing range (Figure 5-25a). The incorporation of fibrin in alginate had no strong influences on the stiffness and their elastic modulus was around 5.1 kPa (Figure 5-25b). It is worth noting that the embedding Fe nanoparticles enhance the stiffness of both pure alginate and alginate-fibrin matrix. Moreover, the elastic modulus is concentration-dependent. That is to say, high loading

amounts of FeNPs into hydrogels resulted in a slightly stiffer matrix, which was consistent with the force-distance results (Figure 5-23).

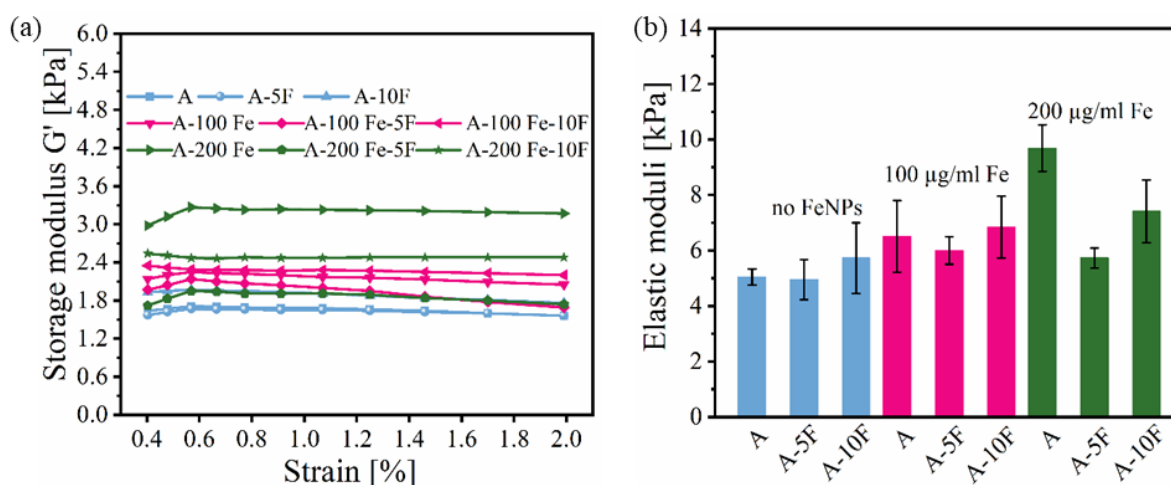


Figure 5-25: Storage moduli G' measured over a decade of oscillation strain in the range of 0.4%-2% (a), and representative elastic modulus E calculated from G' at 1% strain.

To evaluate the impact of these material properties on living cells, EC viability after seeding them onto alginate hydrogels with or without embedded iron nanoparticles in concentrations of 100 $\mu\text{g/mL}$ and 200 $\mu\text{g/mL}$ was assessed after 72 h by WST-8-assays. Only low absorption at a wavelength of 450 nm could be measured on alginate hydrogels (Figure 5-26), which indicates low overall viability. Live/dead staining showed extremely few cells with spherical morphology on pure alginate gels and a slightly increased number of cells with an occasional more physiological shape on the FeNPs embedded gels (Figure 5-27a-c). Nevertheless, high numbers of dead cells indicate insufficient biocompatibility. The blending of alginate hydrogels with fibrin in both concentrations and combination with FeNPs did not result in higher absorption in the viability assay (Figure 5-26). Interestingly, live-dead staining revealed the majority of survived cells were with a physiological spindle-like shape (Figure 5-27d-i).

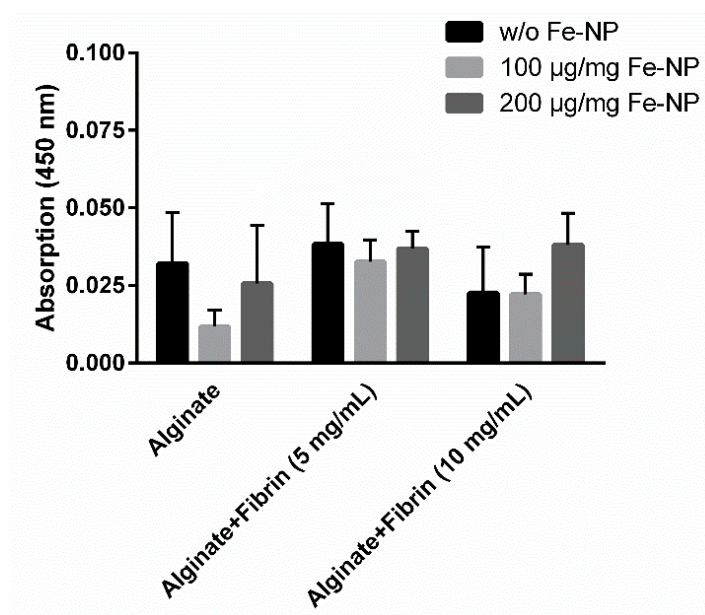


Figure 5-26: Endothelial cell viability on alginate hydrogels blended with 5 or 10 mg/mL fibrin and enriched with 100 or 200 µg/mL iron nanoparticles assessed by WST-8 assay. Shown are means \pm SEM of three independent experiments measured in duplicate and analyzed by 1-way ANOVA and Sidak's post test. No significant differences were calculated.

To test a putative beneficial effect of serum proteins, gels were coated with FBS for 3h prior to endothelial cell seeding. The assessment of WST-8-assays showed that the poor viability of EC seeded on pure alginate gels with or without FeNP was not improved by FBS coating (Figure 5-28a). In the case of alginate-fibrin gels without FeNP, FBS coating did not result in a significant increase in absorption as well. In contrast, the combination of fibrin plus FeNPs in both concentrations resulted in a significant 2.9- and 2.6-fold increase for 5 mg/mL fibrin ($p < 0.01$) and in a 3.0- and 2.4-fold increase for 10 mg/mL fibrin ($p < 0.05$ and < 0.01 ; Figure 5-28b-c).

Live/dead staining of the respective groups confirmed the supporting effect of FBS coating on alginate-fibrin gels enriched with FeNPs (Figure 5-29). The combination of all three components resulted in an almost confluent endothelial layer with physiological cell morphology (Figure 5-29g,h,k,l). The effect was most obvious for the 10 mg/mL fibrin blending enriched with 200 µg/mL FeNPs (Figure 5-29i), suggesting a concentration-dependent influence of fibrin and FeNPs in combination with serum proteins.

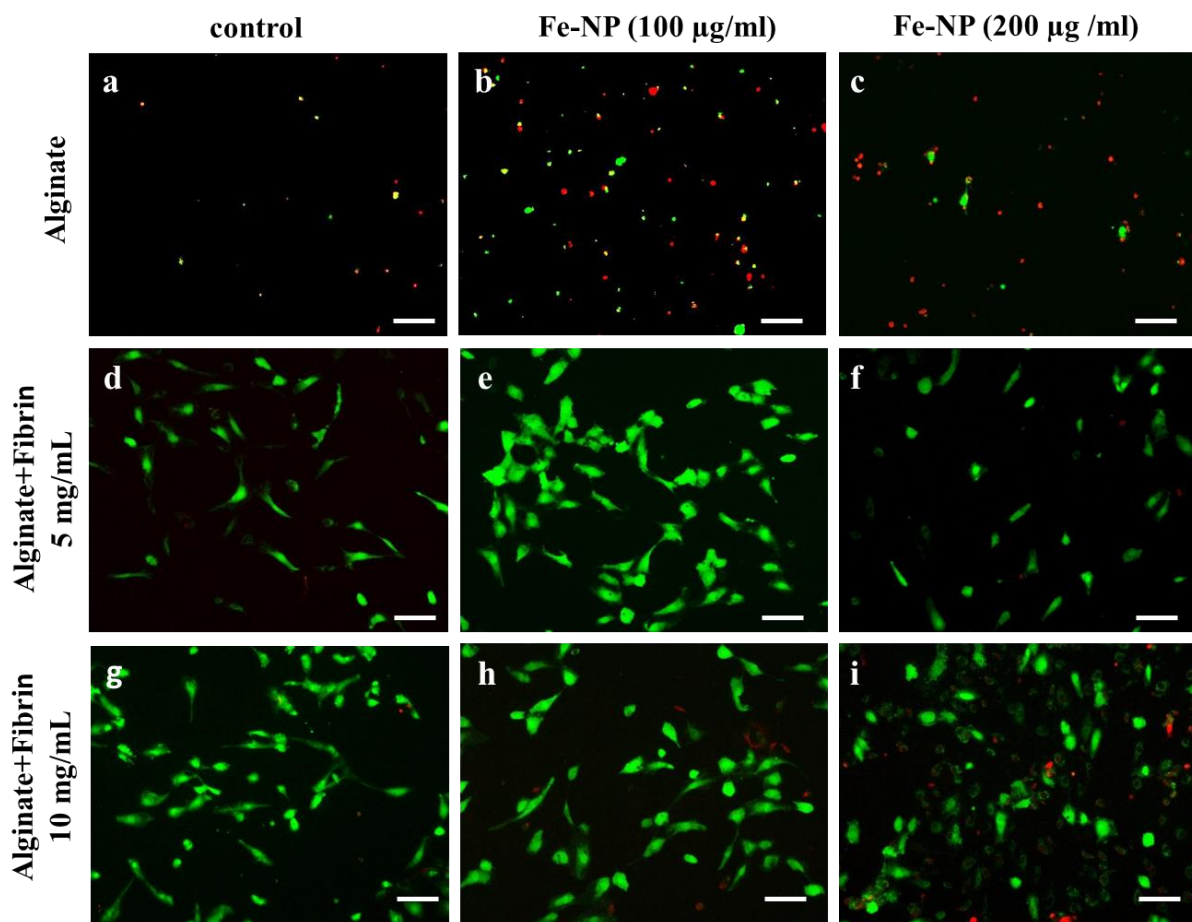


Figure 5-27: Endothelial proliferation and morphology on alginate hydrogels blended with 5 or 10 mg/mL fibrin and enriched with 100 or 200 µg/mL FeNPs assessed by live-dead staining. Shown are typical images of two independently stained gels.

Cell types respond differently to varying degrees of matrix mechanical characteristics stiffness [241]. For example, fibroblasts have been reported to preferentially move towards stiffer substrates [242]. Zhang *et al.* [243] found different responses of endothelial cells to stiff or soft substrates, observing that endothelial-to-mesenchymal transition happened on a stiff matrix while keeping the original phenotype on the soft matrix. In this study, the non-fouling effect became apparent on alginate hydrogels resulting in a high rate of dead HUVEC in live/dead staining and low viability in WST-8-assays. As cellular adhesion is the initial mechanism in the interaction between cells and substrate surfaces, it is essential for subsequent proliferation to a confluent cell layer and vice versa the cause for “Anoikis” (homelessness)-induced apoptosis [244]. In this work, samples with fibrin and FeNPs exhibited a stiffer surface than alginate alone (Figure 5-23).

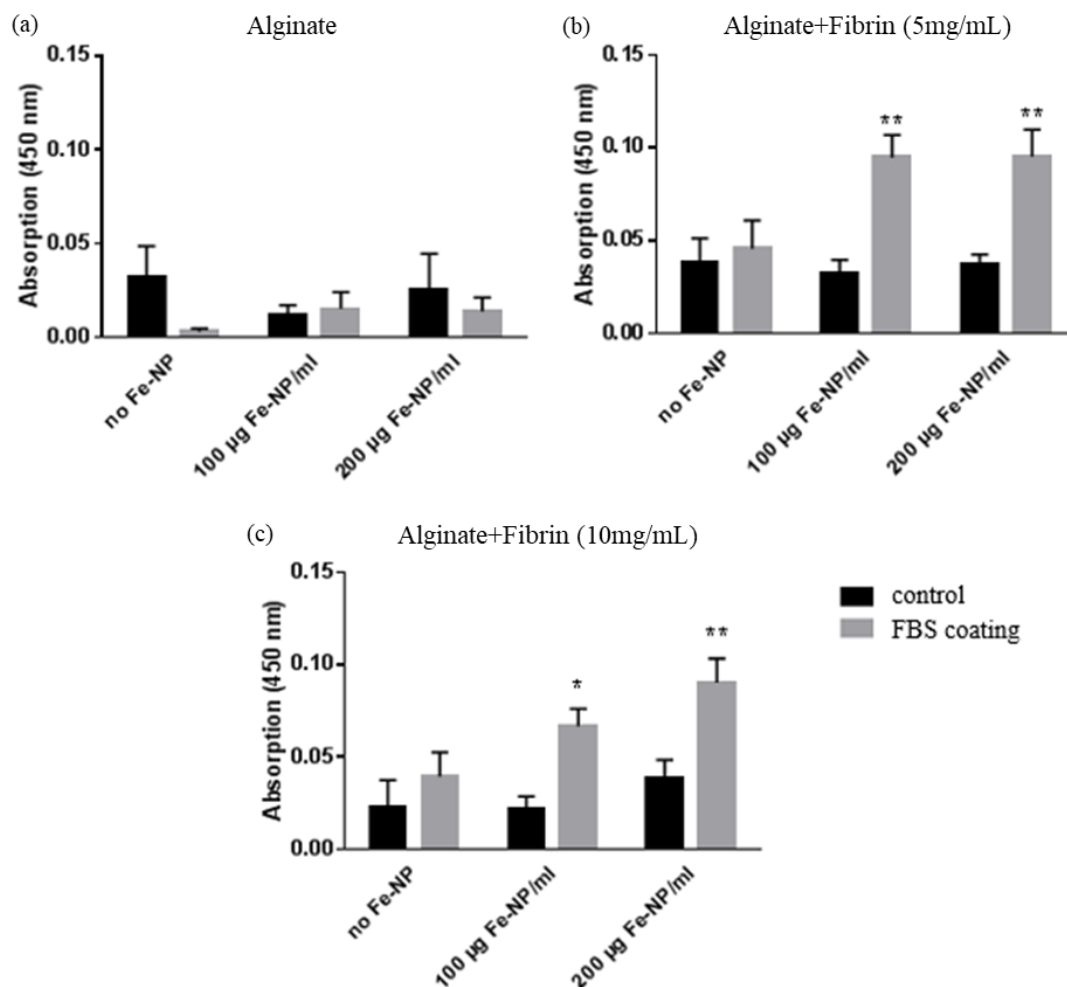


Figure 5-28: Effect of FBS coating on endothelial cell viability on alginate hydrogels blended with 5 or 10 mg/mL fibrin and enriched with 100 or 200 µg/mL FeNPs assessed by WST-8 assay. Shown are means \pm SEM of three independent experiments measured in duplicate and analyzed by 1-way ANOVA and Sidak's post test. * $p \leq 0.05$ and ** $p \leq 0.01$ vs control.

Fibrin exposes RGD peptides [245] favouring integrin clustering and formation of focal adhesions [246, 247] and therefore served as an adhesive molecule in the inherent alginate structure by promoting endothelial cell adhesion, proliferation and migration via integrin receptor $\alpha\beta3$. This effect was visible by live/dead staining depicting a reduced amount of dead endothelial cells and a physiological spindle-like morphology of living cells (Figure 5-27). Besides this biochemical effect, a topographical effect of fibrin fibres is also imaginable since LSCM revealed a considerably rougher surface structure with single visible fibres in alginate-fibrin hydrogels (Figure 5-11 and Figure 5-12). Moreover, AFM results showed that fibrin clearly increased roughness parameters of alginate gels (Table 5-5). The observed reduced wettability of alginate-fibrin gels may have contributed to this effect as well (Figure 5-24b).

Less hydrophilic surfaces enable the development of dehydration forces being essential for protein binding [248]. However, since colorimetric assay did not show enhanced viability (Figure 5-26), the effect of fibrin on endothelial cell adhesion appears to be limited to focal fibrin fibres and does not affect the whole surface structure.

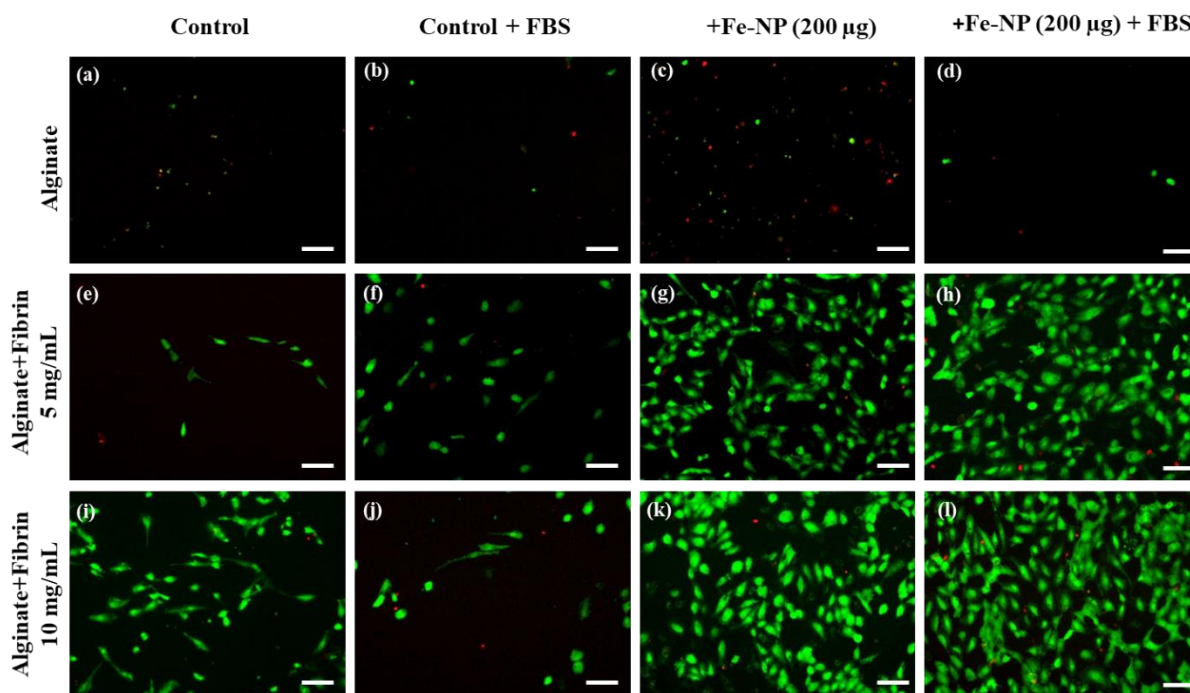


Figure 5-29: Effect of FBS coating on endothelial proliferation and morphology on alginate hydrogels blended with 5 or 10 mg/mL fibrin and enriched with 200 µg/mL iron nanoparticles assessed by live-dead staining. Shown are typical images of two independently stained gels.

It seems that endothelial cell growth prefers stiffer substrates of FeNPs embedding in alginate-fibrin blends. Moreover, on the more rigid matrix, a large number of ECs showed a cobblestone-like shape, and most of the cells displayed an elongated, spindle-shaped morphology on alginate-fibrin gels. With more Fe loadings, cobblestone-like cells were more. Prolong the cultured time at 8 days, this kind of shape transformed into elongated-spindle (Figure S15), which was consistent with the previous study [243]. Additionally, the incorporation of FeNPs as a source for sustained ions release was able to promote cellular compatibility also for endothelial cells displaying a lower proliferative potential [12]. Interestingly, in our study none of these effects became noticeable. FeNPs increased wettability (Figure 5-24a,b) which may have caused the poor attachment and limited survival of endothelial cells on alginate gels filled with FeNPs (Figure 5-26, Figure 5-27a-c).

In triple modification hydrogels, LSCM visualized agglomerating FeNPs along the fibrin fibres (Figure 5-12). Therefore, a direct interaction between iron nanoparticles and fibrin can be supposed. In physiological environments, nanoparticles have been shown to build a protein corona [249]. Interestingly, in our study iron nanoparticles agglomerated on fibrin fibres also seemed to attract serum albumin since LSCM clearly showed that albumin deposition followed the structure of FeNPs-covered fibrin fibres (Figure 5-12). Thus, both alginate modifications and serum protein coating synergize most likely to a triple adhesive complex for endothelial cell adhesion promoting proliferation and viability.

As aforementioned, protein adsorption is the first process in the interaction between cells and a given surface and thus its quantitative and qualitative protein adsorption capacity determines essentially its biocompatibility [61]. The primary interaction between cells and adhesion proteins occurs via integrins being activated by the exposed binding sequences. Integrins are transmembrane receptors to transduce surface characteristics represented by the adsorbed protein profile into basal cellular responses comprising cellular adhesion, morphology, motility, and proliferation [250]. The absence of integrin activation results in cellular apoptosis emphasizing the significance of adequate protein adsorption and following integrin activation [244]. Since increasing protein concentrations in solution are known to accelerate surface protein adsorption [248], the effect of serum protein coating on cellular adhesion seems to be consequential. Though serum proteins were present in lower concentrations in all cell culture experiments (EBM-2 medium contains 2% FBS), obviously a higher concentration was necessary to achieve this effect (Figure 5-27). Extrapolating our result to a clinical scenario, alginate modified by fibrin and FeNPs will encounter sufficiently high serum albumin concentrations after implantation by the bloodstream and thus will provide a promising surface for rapid and stable endothelialization.

5.3.4 Influence of laser-generated Au nanoparticles on the physicochemical properties of collagen gels

To enhance the mechanical property of collagen gels, gelation by chemical crosslinking with EDC/NHS or glutaraldehyde (GTA) was performed at different pHs, ionic strength, embedding AuNPs concentrations. The gelation state was evaluated by Bradford assay and UV-Visible spectroscopy, with an absorbance at 310 nm. A higher absorbance can be related to faster gelation kinetics [251]. Damink *et al.* [30] calculated the primary amine group content of cross

linked and non-cross-linked collagen samples to describe their kinetics. As stated in section 4.5, the reaction of formation of a complex between Bradford dye and protein will cause a shift in the maximum absorbance from 465 nm to 595 nm which is proportional to the concentration of protein present in the sample.

With the calibration lines (Figure S1) and the ungelated proteins, gelation percentages in different conditions can be obtained, as shown in Figure 5-30. It should be mentioned that the collagen gelation at room temperature was not proceeding at an insufficient concentration (< 7 mg/mL), and hence the results were not reported. Figure 5-30a displayed the effects of GTA concentration on collagen gelation at 14 mg/mL collagen and 0.04 wt% loading of AuNPs. At the concentration of 2% GTA, the maximum gelation was around 40%. Damink also demonstrated a slight decrease in gelation when exceeding the concentration of 1 % GTA [30]. When combining GTA with AuNPs, GTA seemed to dominate the gelation process. It can be concluded that Au nanoparticles, in this case, have no positive influences on the gelation process.

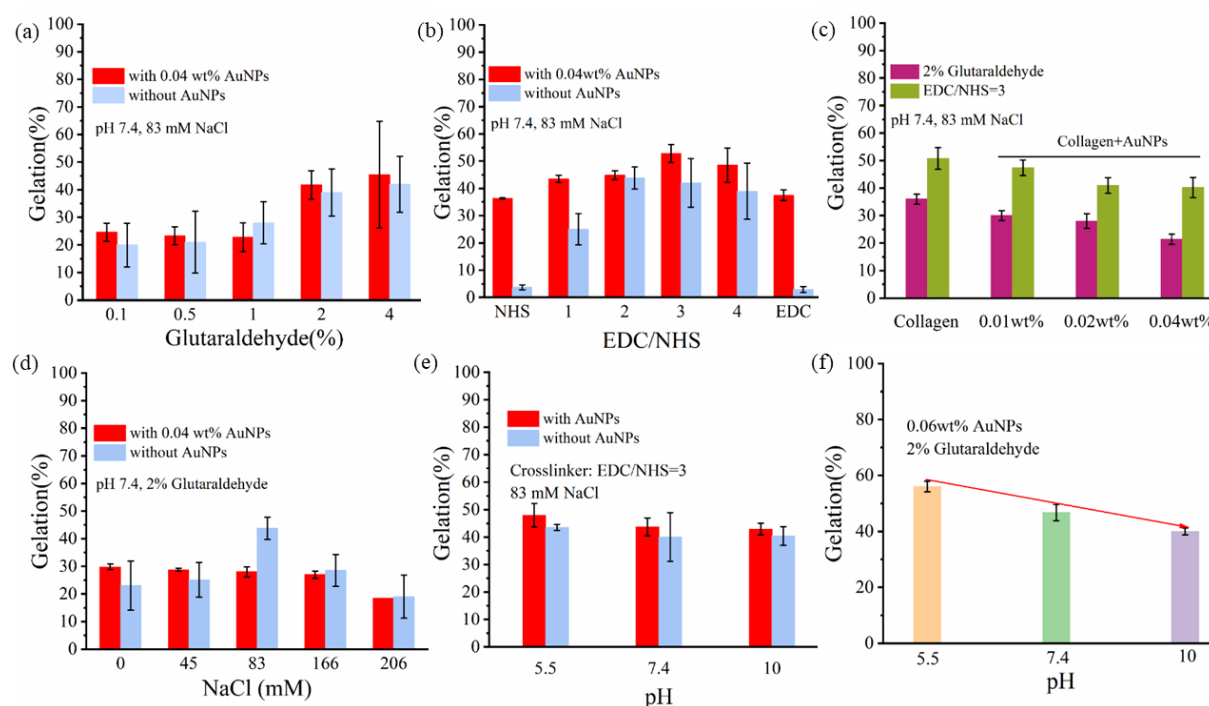


Figure 5-30: Gelation percentage of collagen at different conditions: glutaraldehyde contents (a), EDC/NHS mole ratio (b), Au nanoparticles loadings in collagen (c), ionic strength concentration (d), pH effect on collagen and 0.06 wt% Au-collagen with the crosslinker EDC/NHS (e), and pH effect on 0.06 wt% Au-collagen with the crosslinker 2% glutaraldehyde (f).

1-ethyl-3-(3-dimethylaminopropyl-carbodiimide hydrochloride (EDC) and N-hydroxy succinimide (NHS) are widely used chemicals to crosslink collagen based on the formation of stable esters. Figure 5-30b displayed the gelation efficiency of collagen and Au-collagen composites at various molar ratios of EDC/NHS from 1 to 4. As reported earlier, neither EDC nor NHS alone has a positive effect on gelation. However, combining them with AuNPs may promote the gelation process [98, 252]. One can see that the gelation percentage of collagen increased with increasing molar ratio of EDC/NHS. It reaches its maximum (55%) at an optimum EDC/NHS molar ratio of 3:1.

Duan *et al.* [249] showed that EDC/NHS cross-linked collagen gels had better thermal stability than the gels cross-linked using glutaraldehyde. Further, we compared the results of crosslinking efficiency between 2% GTA and (3:1) EDC/NHS. The results indicated that EDC/NHS presented around 18% higher gelation efficiency than GTA (Figure 5-30c). It is a positive outcome as glutaraldehyde is frequently reported toxic in *in vitro* and *vivo* experiments.

The kinetics of gels as a function of ionic strength has been discussed by other researchers [251, 253]. They demonstrated that collagen's mechanical property and molecular flexibility strongly depended on its ionic strength. Other authors pointed out that the higher the ionic strength, the larger the collagen fibre diameter and faster the self-assembly at lower ionic strengths [254, 255]. But they hold disagreement with the ionic strength effects on the gelation rate. In this situation, we performed the gelation process at different NaCl concentrations. As Figure 5-30d shows, the highest gelation percent at the concentration of 83 mM NaCl was found to be approximately 50% with AuNPs and 42% without AuNPs. However, high ionic strength may prevent the bonding between electrostatically charged amino acid chains [251].

By adjusting the pH of the collagen solution, the gelation percentage remained stable in the presence of EDC/NHS cross linker (Figure 5-30e). But with the addition of 2% GTA, the gelation percentage showed a clear decreasing trend with increasing pH (Figure 5-30f). Diamantides *et al.* [256] also reported the pH-dependent gelation kinetics and observed a more significant polymerization rate of collagen gels cross-linked with glutaraldehyde at a higher pH value [257]. Overall, AuNPs may have no significant influence on collagen gelation with both EDC/NHS and GTA.

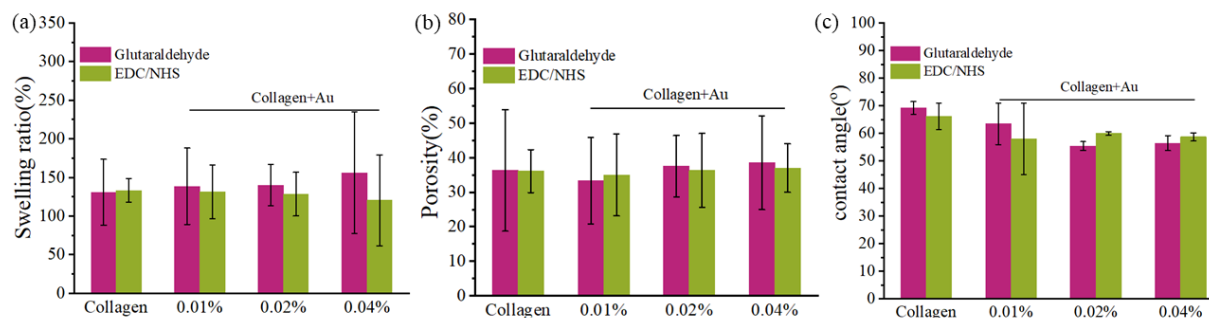


Figure 5-31: Physicochemical properties of collagen and Au-collagen composites gelled by 2% GTA or 3:1 EDC/NHS: swelling ratio (a), porosity (b), contact angles (c).

Figure 5-31a shows the physicochemical properties of AuNPs-collagen composites. As stated in section 3.5, swelling is due to the amount of water content relating to four different water states: free water, associated water, semibound, and bound water, which can be influenced by temperature, pH, ionic strength, etc. [156]. One gram of collagen sponges with a size ranging from 20-200 μm macropores can retain 0.12-0.47 g of water [156]. The collagen hydrogels were lyophilized to obtain the dry weights. The swelling ratios of collagen sponges were in the range of 130%-150%.

Table 5-6: Calculated pore size of collagen hydrogels gelled with cross linker EDC/NHS (3:1) and 2% glutaraldehyde.

Au conc. (wt%)		0	0.01	0.02	0.03
Average pore size (nm)	EDC/NHS (3:1)	16	25	28	20
	2% Glutaraldehyde	18	16	22	23

The porous microstructure is one factor contributing to the swelling process. SEM images confirmed the existence of pores in gelled Au-collagen (Figure S16). The porosity of collagen hydrogels was around 33.3%-38.5% (Figure 5-31b). The 3:1 EDC/NHS and GTA crosslinkers along with the incorporation of AuNPs did not alter the porosity. The calculated pore size of collagen hydrogels was listed in Table 5-6, in the range of 16-28 nm. As shown in Figure 5-31c, the contact angle of pure collagen was around 70° . The obtained average contact angles of collagen+Au (0.01 wt%), collagen+Au (0.02 wt%), and collagen+Au (0.04 wt%) composites were about 60° , 55° , and 54° , respectively. The combination of AuNPs with collagen slightly

enhanced the hydrophilicity of collagen, as Hsieh *et al.* stated [28]. The effect of two different cross-linkers GTA or EDC/NHS on the wettability were not significantly different.

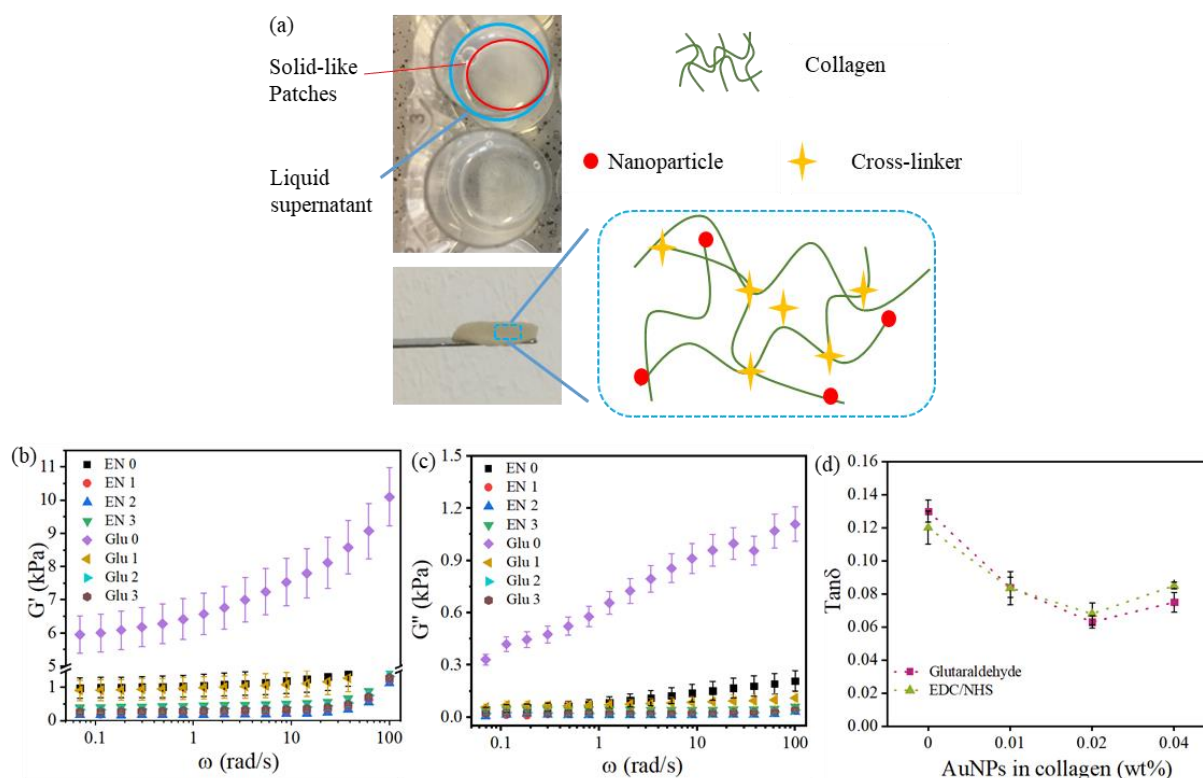


Figure 5-32: Illustration of Au-collagen gels (a), and angular frequency dependent oscillatory shear rheology of collagen and Au-collagen composites gels gelled by 3:1 EDC/NHS and 2% GTA at 20 °C. The number 0, 1, 2, and 3 refers to collagen, 0.01wt% Au-collagen, 0.02 wt% Au-collagen, and 0.04 wt% Au-collagen, respectively. Rheological characterization of collagen hydrogels: Cross-linker effects on the storage modulus G' (b), loss modulus G'' (c) of collagen gels; damping factor $\tan\delta$ (d) of collagen and Au-collagen composites gels at different angular frequencies 10 rad/s and 1% strain.

Rheological measurement is also a way to analyze the gelation process. Holder *et al.* [91] reported the gelation point for typical collagen at approximately 280 s. In this work, the rheological properties of collagen gels were depicted in Figure 5-32a. The results showed that G' and G'' of collagen without embedding AuNPs gelled by GTA were significantly higher than other samples (Figure 5-32b,c). In the case of crosslinker EDC/NHS, G' and G'' of AuNP-collagen composites showed a minor decrease compared to native collagen gels. It could be explained that the AuNPs may enlarge the hydrogel network leading to a loose and weak system. Damping factor $\tan\delta$ (ratio of G''/G'), indicates the gel state. A solid-like materials has a $\tan\delta$

value below the threshold of 1 [128, 157, 164]. As observed in Figure 5-32d, the $\tan\delta$ value was below 0.14, demonstrating a complete gelation process. Moreover, a lower $\tan\delta$ indicates more elastic nature [258]. Due to the interaction between nanoparticles and collagen cross-linked by EDC/NHS and GTA, the mechanical properties of collagen gels could be improved [209].

5.3.5 Physicochemical properties of nanoparticle-TPU composites and their protein adsorption capacity

The results in this part have been published in *Nanotechnology*, 2020, 31, 405703.

As TPU composite films are non-soluble in water, it is easy to study the surface charge under the flowing solutions with varied pH. Corresponding studies with alginate were not possible under these experimental conditions as the alginate gels disintegrated. Figure 5-33a depicts the surface zeta potential of TPU, Fe (0.09 wt%) or Au (0.17 wt%) TPU composite films as a function of pH. The surface charges of films result from bound dissociable groups or adsorbed charge carriers from the environment [259]. In general, materials' isoelectric point (IEP) indicates their electrical properties and application potentials, e.g., cellular adhesion [260]. The TPU control showed positive surface zeta potentials in the pH range of 4.5-8.2 with an IEP at pH 8.2. In particular, at pH 7.4, TPU was positively charged (23 mV), which confirmed the experiments of Yu *et al.* who demonstrated the zeta potential of TPU was 23 mV at pH 7.4 [7]. In contrast, the surface zeta potential for Fe- and Au-TPU was consistently negative at pH above 4.6. And films with nanoparticles were negatively charged between -55 mV and -58 mV, as previously reported for TPU modified with Pt and Au nanoparticles [15]. Laser-generated metal nanoparticles are usually negatively charged [166], which seems to affect the surface of untreated TPU. These nanoparticles have a higher concentration of adsorbed oxygen or ion adsorption.

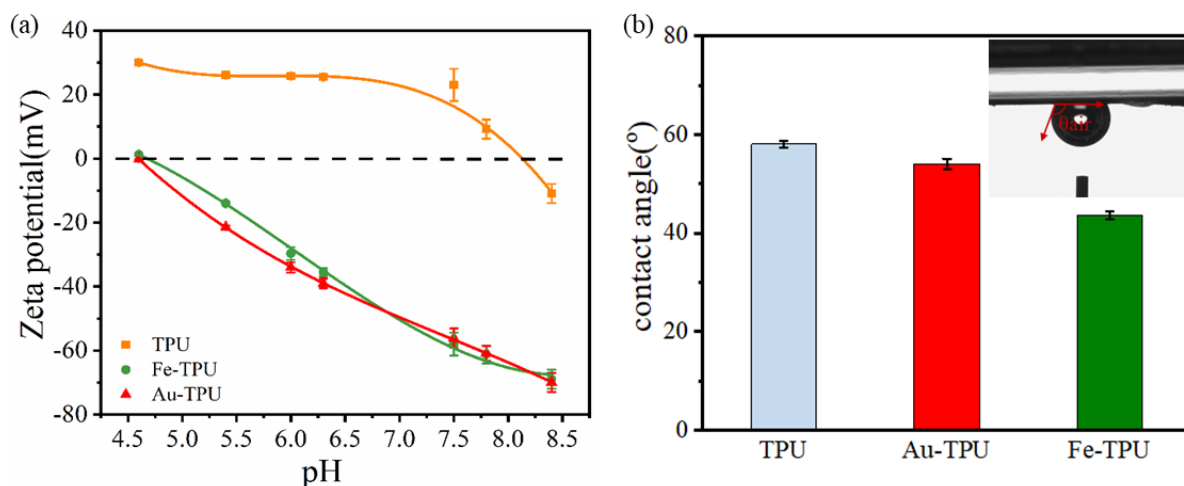


Figure 5-33: (a) Surface zeta potentials of TPU, Fe (0.09 wt%), Au (0.17 wt%) derived from streaming potentials of TPU composite films at the variation with pH are shown. The plots were fitted with a polynomial function. (b) Water contact angle of TPU and nanoparticle-TPU composites.

The wettability of TPU nanocomposites was shown in Figure 5-33b, with a higher contact angle of approximately 43° - 60° , which was in good agreement with previously reported results [15]. The contact angles were approximately 60° for reference TPU and 43° for Fe-TPU composites, indicating that Au and Fe nanoparticles improved the wettability of TPU. The contact angles of different nanoparticle loadings showed no significant differences (Figure S17), probably attributed to the low differences in mass loads used here. These results were in accordance with other findings, where a more hydrophilic surface was obtained through embedding Pt or Au nanoparticles into TPU [15] or surface modification [261]. The observed change of the wettability proved that the incorporated nanoparticles altered the surface properties of the polymers. This finding is in good agreement with the zeta potential measurements, where particles embedded in TPU were shown to reverse the charge and increased the overall net charge of the composites by a factor of >2 .

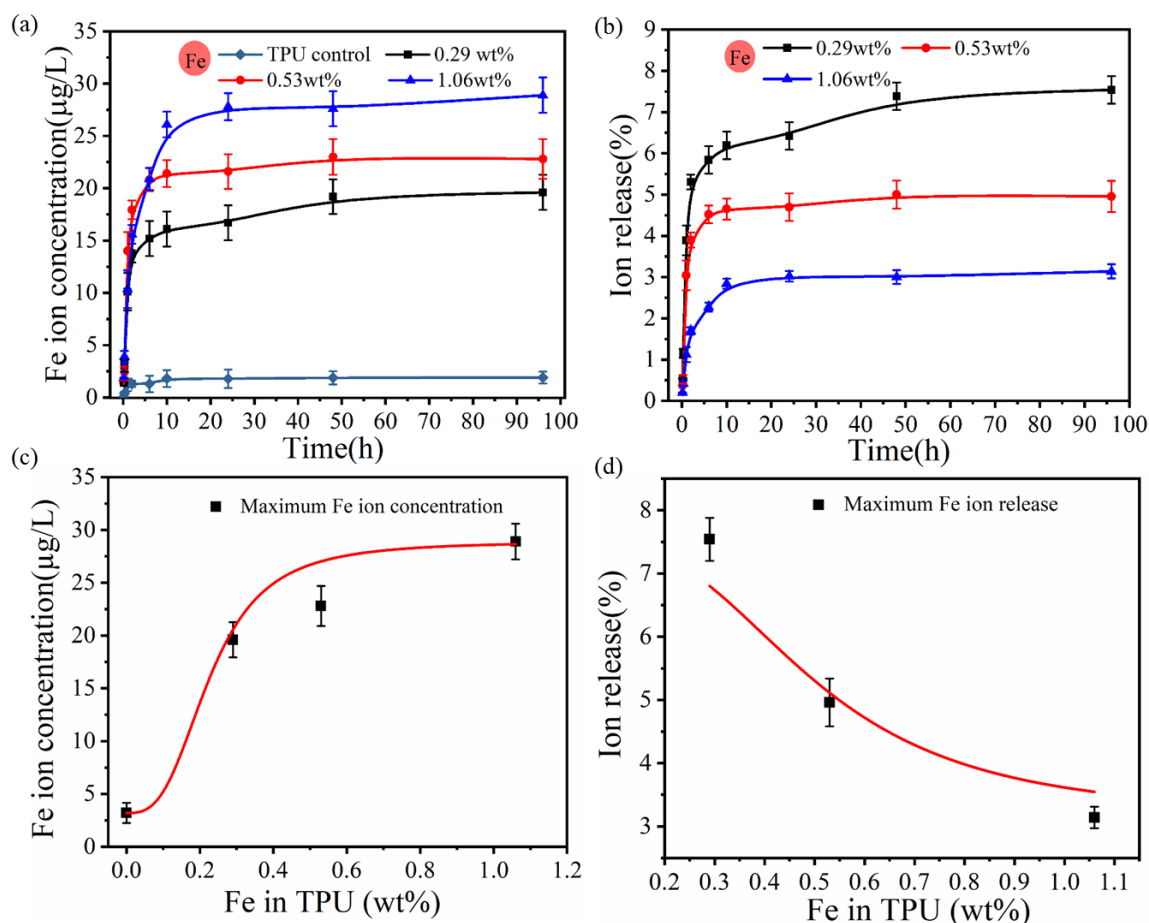


Figure 5-34: Long-term Fe ion release kinetics: (a) released Fe ion concentration of Fe-TPU composites and the TPU control, (b) released mass percent of different amounts of Fe nanoparticles in TPU, (c) the maximum Fe ion release, (d) the corresponding ion release percent of Fe-TPU composites.

The obtained absolute Fe ion concentration in the case of Fe-TPU composites increased with the nanoparticle loading (Figure 5-34a and Figure 5-34c). On the other hand, the ion release in percent was found to decrease with increasing nanoparticle loads (Figure 5-34b and Figure 5-34d). This behaviour is in line with previous findings [111] and expectations, as a more total release of ions is expected at higher particle loadings. On the other hand, a diffusion-driven mechanism would slow down release in case of higher total ion concentrations in the medium, reducing the relative release under static experimental conditions. Compared to the case of alginate matrix, Fe ion releases from TPU were lower, which was attributed to the hydrophobic nature of TPU lowering the water uptake leading to low ions diffusion.

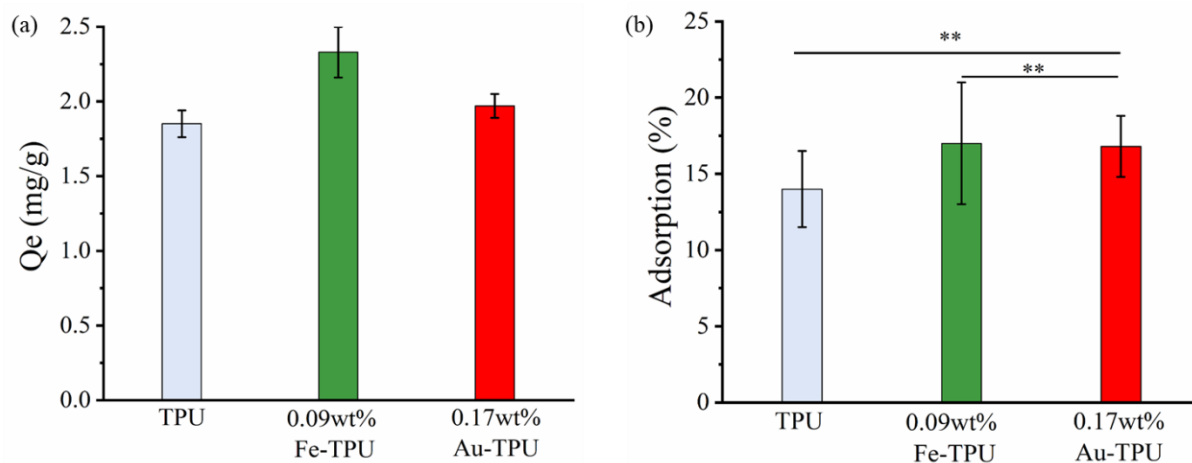


Figure 5-35: Protein adsorption on TPU, and corresponding composites as a function of nanoparticle concentration at pH 7.4 and room temperature. Statistical significance levels were evaluated with a single factor analysis of variance (ANOVA) and significance levels were $p < 0.05$ (*) and $p < 0.01$ (**). (% refers to adsorbed protein vs. deployed protein.)

Protein adsorption on nanoparticle-loaded TPU composites was studied in the same experimental approach with alginate composites. As shown in Figure 5-35a, the adsorption of BSA slightly increased with embedding nanoparticles in TPU compared to the pure TPU films. The maximum Q_e was 2.33 ± 0.17 mg/g in the sample of Fe-TPU composites which was far lower than alginate hydrogels. On the other hand, the type of embedded nanoparticles (Fe or Au) had no observable impact on protein adsorption. For further clarification and to rule out cross effects from different protein concentrations studied, the relative amount of adsorbed protein was plotted versus the nanoparticle loading in the composites (Figure 5-35b). NPs impact on TPU was less pronounced than alginate as shown in Figure 5-21 of section 5.3.2, as indicated by the adsorption rate of Fe-TPU composites at 17%, while the value was 14% for the TPU control. The nonporous nature of TPU may explain this result.

5.4 3D printability of alginate composites

The experiment in this part was performed by Jacqueline Stamm, Andreas Bläser and the results have been published in *Nanotechnology*, 2020, 31, 405703.

The printability of the alginate-nanoparticle composite and its potential applicability as bioink were tested following a novel 3D-bioprinting approach. Using a modular, compact 3D-bioprinter a modification of the previously published methods for FRESH or submerged bioprinting was applied [107, 108, 187, 188]. Briefly, a microextrusion bioprinting process was conducted submerged in calcium-chloride doped gelatin slurry (Figure 5-36a,b). Defined strands of native, iron-, or gold-nanoparticle-laden alginate were printed to form hollow cylinders measuring 7 mm in diameter and up to 13 mm in height (Figure 5-36e). The gelatin slurry did not only support the built-up mechanically but also provided the crosslinker to form a stable gel within seconds after printing. To remove the printed parts, the slurry was heated to 38 °C for 25 minutes (Figure 5-36c,d).

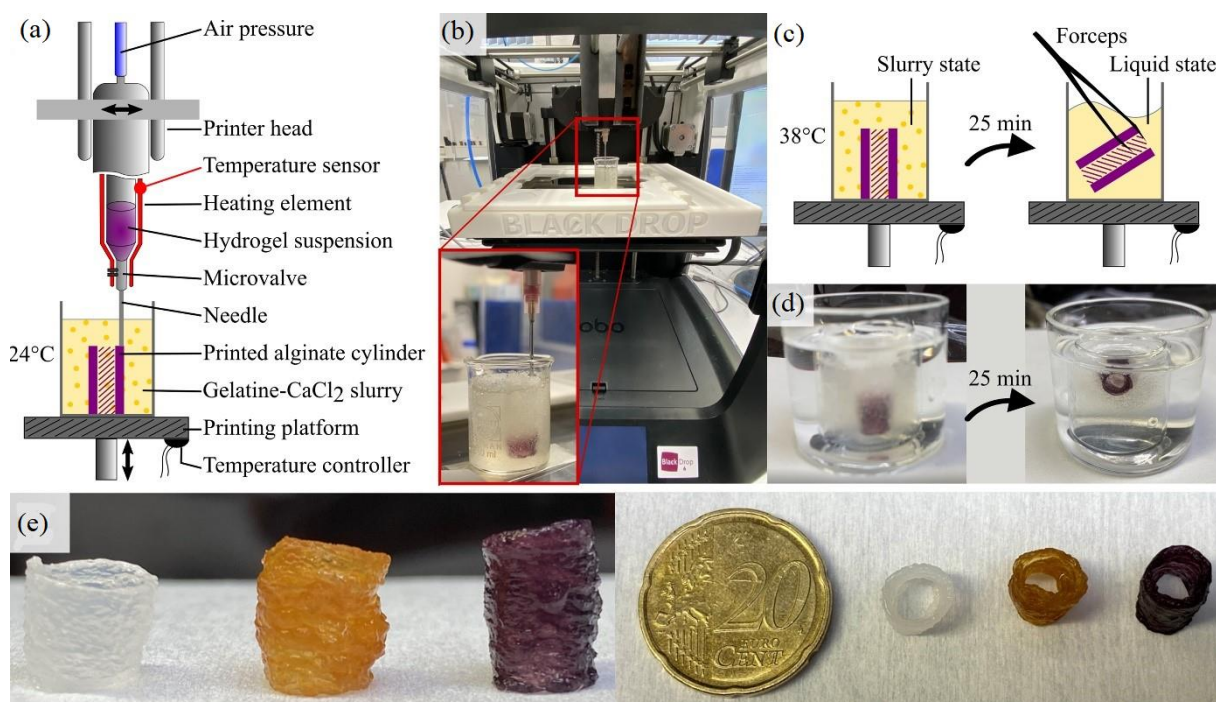


Figure 5-36: Submerged bioprinting of 3D-hydrogel scaffolds made of alginate composite bioinks. The printing process is illustrated schematically (a) as well as in overview and close-up images (b). To stabilize and crosslink the printed alginate constructs, the bioprinting process is conducted submerged in a gelatine- CaCl_2 slurry. After successful printing, the slurry is heated up to 38 °C to melt the gelatin and enable gentle removal of the printed object. The two slurry

states (swollen and melted) are illustrated schematically (c) as well as with recorded images (d). Images of the bioprinted 3D-cylinders (e) are shown in side view (left) as well as in top view (right).

The results of the printing test indicate that the integration of laser-ablated metal nanocomposites does not hamper the process- and printability of alginate hydrogels. Instead, the composite was shown to be an ideal bioink for the submerged fabrication of versatile 3D constructs with relatively high strength that can support its weights during printing. In Figure 5-36e, the coloration of the mesoscopic 3D parts by the nanoparticles is clearly observable.

5.5 Nanoscopic bioglass doped with iron produced by iron slat-sensitized laser fragmentation

The bioactive glass (BG) educts suspension exhibited a negligible light absorption in the visible spectral region (Figure S19a), whereas the Fe-EDTA solution exhibited a pronounced absorption at the laser wavelength (Figure 5-37b). As described in the introduction, there are reports that the ferrous or ferric ions can act as a light-absorbing agent [49, 51, 262], as a consequence, more pronounced fragmentation was expected for BG particles in Fe-EDTA solution.

The flow jet is a frequently used reactor for laser fragmentation of suspensions [137] or colloids [50] and was initially characterized and adapted to BG processing in the presence of Fe ions. Using this setup, the liquid layer was minimized to avoid possible side products by limiting the beam path to the 100 mm focal length [139]. With the power meter, arranged behind the liquid jet, laser power balances can be easily acquired by measuring attenuated laser energies in comparison to a reference beam in air. Results indicate that the laser energy attenuated by the suspension significantly increased with ferrous ions and reached 67%, 1.5 fold higher than the absorbance measured for raw BG suspension in water or EDTA solution (Figure 5-37c). This clearly demonstrates that the light-absorbing properties of iron ion solution could enhance the absorbance during the process of laser fragmentation in liquids (LFL).

The higher viscosity of alginate solution could slow down liquid flow rate compared to water, thus increasing the irradiated pulse number. Waag *et al.* [134] presented a raytracing model to calculate the laser energy density distribution as suspension through the liquid jet and mentioned 13.8% of the jet cross-section cannot be laser irradiated due to refraction effects at the air-jet boundary. The distribution of laser energy in the irradiated colloid can be manipulated using circular to elliptical orifice and elliptical jet can decrease the unilluminated area to a simulation value of 2.8% [50]. Importantly, it should be considered that illuminated fragmented volume is not homogeneous with this setup. Therefore, it is necessary to carry out more than one laser passage to ensure that every particle in the volume is hit. Next to the attenuated laser energy it is also important how many laser pulses are directed at a corresponding volume element, a variable affected by the flow rate and the viscosity of the used media. Hence, we calculated the flow rates as described in section 4.2.2 and the corresponding numbers of pulse/volume element for different BG mass loads and in the presence of alginate (Figure 5-

37d). Our findings revealed a significant reduction of the flow rate with increasing bioglass concentration and especially upon addition of the alginate, which was caused by a change in viscosity in the range of 1.0-2.3 mPa·s (XZ direction), together with a maximum of 79% attenuated laser energy. As a consequence, the number of laser pulses per irradiated volume (XY direction) significantly deviated in the corresponding experimental design, with 330 pulses/volume element for diluted BG dispersions and 470 pulses/volume element in the presence of alginate. However, Au nanoparticles (53 nm) can be reduced to 2.9 - 3.9 nm only with 1 - 4 pulses per volume [263]. This may attribute to the beam diffraction and attenuation of BG particles. In the following paragraphs these deviations in total attenuated laser power, beam illumination and number of pulses/volume elements will be conjointly used to discuss the fragmentation results.

As the ferrous ion solutions play a key role in the laser fragmentation process their pH stability and potential interactions with BG are critically discussed. Fe-EDTA complexes also called “Jacobson solution”, are stable in the acidic pH range of 3.6-5.6 where they show an absorption maximum at 254 nm [264]. Freshly prepared, the pH value of our Fe-EDTA solution was around 2.7 and slightly increased to 3.0 after 12 h of mixing. After the addition of 1 wt% BG powder, pH value sharply increased to 7.0 and was even higher at 9.8 when 20 wt% BG particles were added (Figure S18). Hence, the formation and precipitation of iron oxide can be expected under these conditions and the formation of hydroxide was indicated at the absorbance wavelength of 205 nm in the UV-Vis spectra as shown in Figure S19a [265]. However, alternate reactions may also occur in the presence of BG. It is well known from the literature how 45S5 bioactive glass interacts with water. Here, Si-O-Si bonds are dissociated and transformed into Si-OH or P-O-Si groups, while modifier ions Ca^{2+} or Na^+ are immediately exchanged with H^+ or H_3O^+ from solution (especially Na^+) [266]. Furthermore, it is well known that Na^+ and Ca^{2+} ions can be replaced in the network of silica glass by heavier elements [37]. In this context, Fe-EDTA, which is unstable at this pH may be partially involved in an ion exchange process, probably further emphasized by the fact that Ca^{2+} has a high affinity towards EDTA compared to Fe ions at pH values of more than 7.0 [267]. We expect that Fe-doped bioactive glass can be obtained through these reactions and we also expect a more pronounced ion-exchange upon laser irradiation, as verified in the consecutive paragraphs.

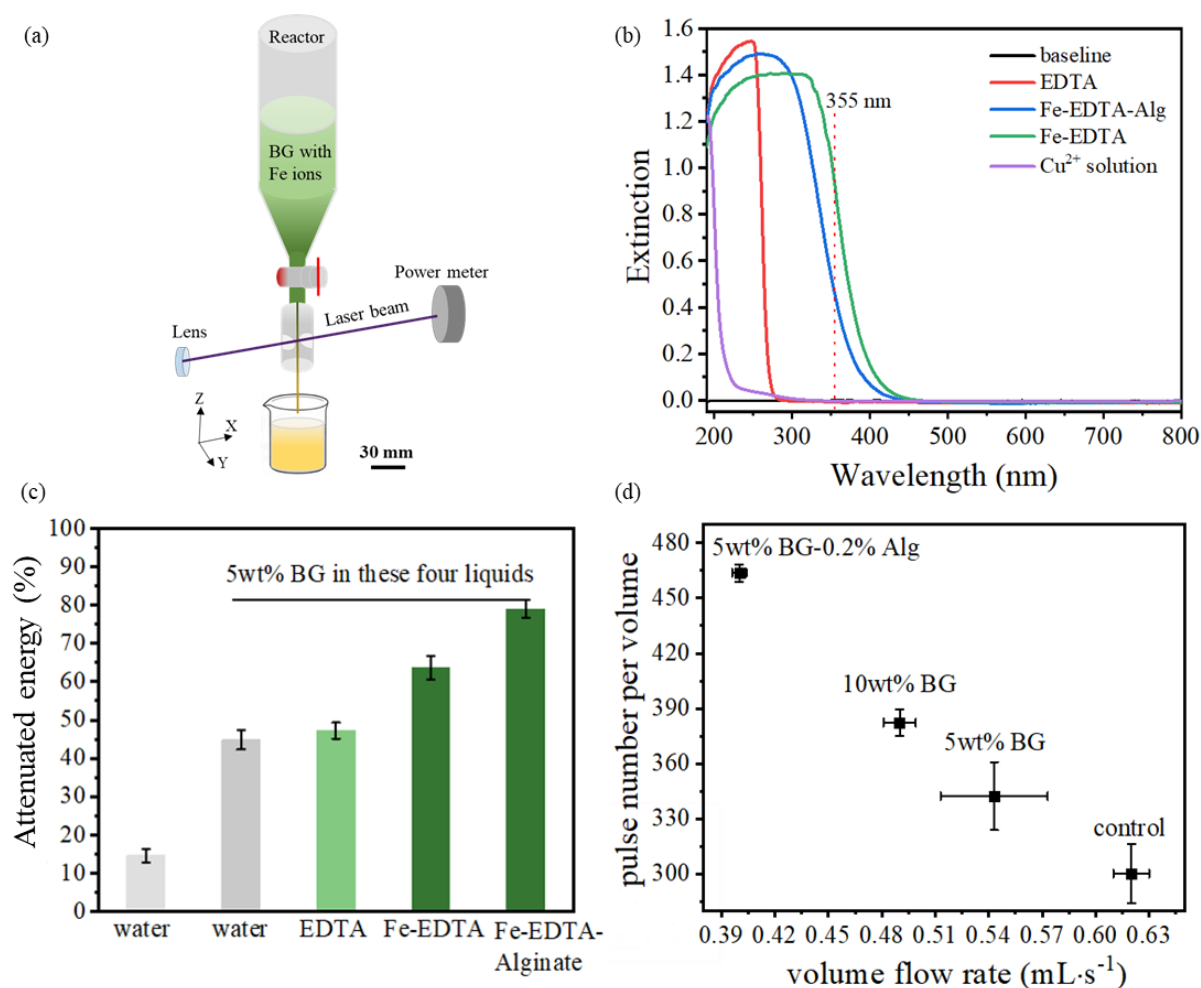


Figure 5-37: Illustration of the laser fragmentation setup including a reactor with a valve to control the liquid flow and laser beam focused onto the liquid jet; (b) UV-vis spectra of EDTA, Fe-EDTA solution, and liquid after laser fragmentation; (c) Attenuated laser power energy of BG suspension with or without ferrous ions; (d) Volumetric flow rate and calculated pulses per volume in the picosecond laser-irradiated samples. Fe-EDTA solution without bioglass powder was taken as control. Alg is abbreviation for Alginate.

The average particle size of raw BG powder is in the range of 3.5–4 μm , as shown in DLS-analyzed number-weighted size distribution (Figure S19b). However, there are much smaller or bigger particles in the SEM images, in a wide range of 200 nm–11 μm (Figure 5-38a). As shown in Figure S19c, bimodal particle size distributions were plotted with peaks at 2.0 μm and 6.3 μm .

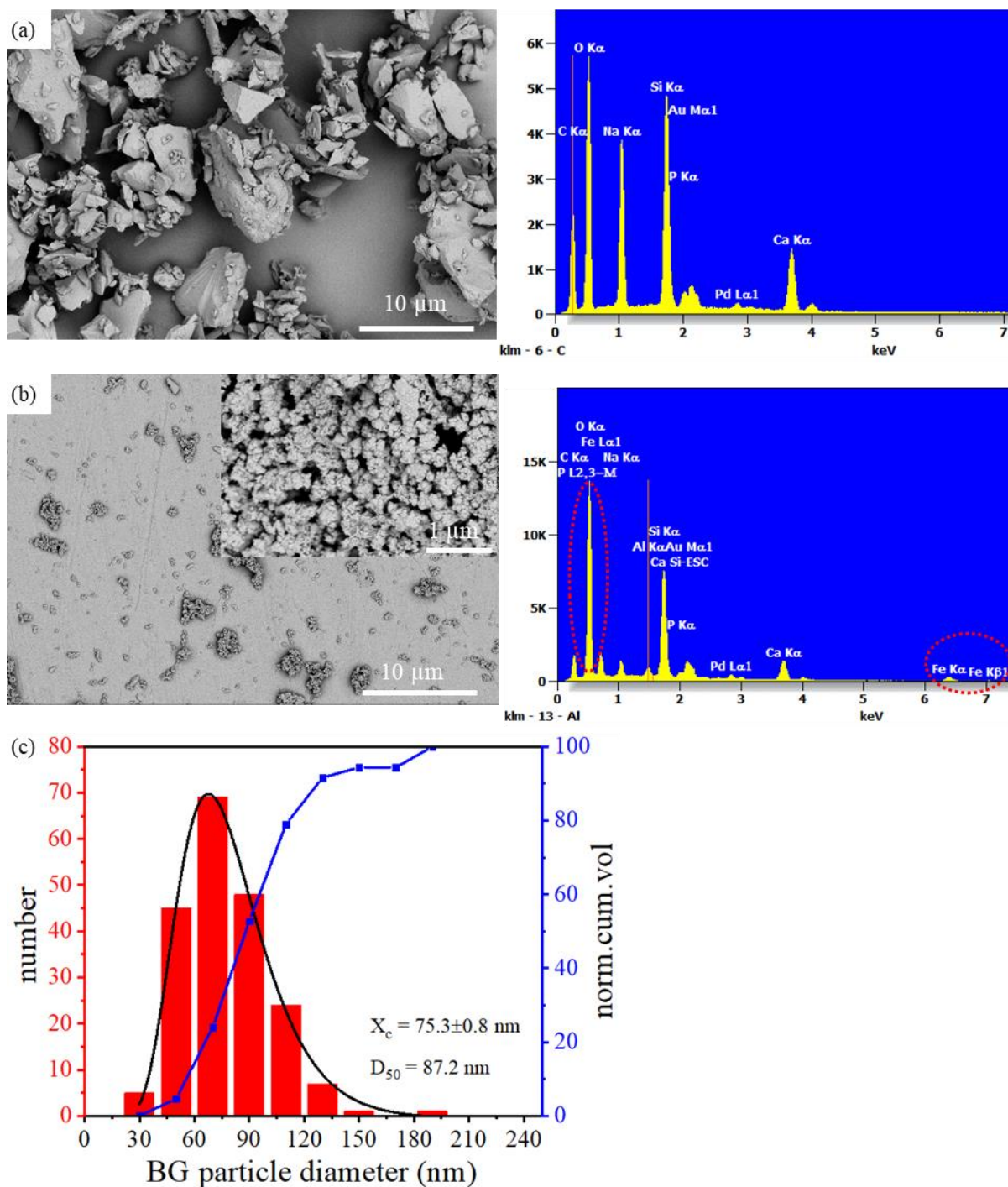


Figure 5-38: SEM images and EDX spectra of raw BG (a), separated particles centrifuged at 537 g for 5min from BG dispersed in Fe-EDTA solution (b) via laser fragmentation, (c) size distribution of laser processed BG particles.

To further confirm the size reduction due to the laser-irradiated, the educts were centrifuged in the same way and a small fraction of particles was obtained (Figure S19a). ADC results in Figure S20a indicated small particles at around 87 nm in the raw BG after centrifugation at 134 g for 5 min but in low mass intensity. It should be noted that with increased centrifugal force,

the small particle concentration was below the detectable threshold. As expected, the particle size was significantly reduced via laser fragmentation after 30 passages in a flow-through jet reactor, and a pronounced change in morphology could be observed. While large particles dominated the unirradiated samples, the irradiated structure exhibits a sponge-like morphology with aggregates (insert SEM image of Figure 5-38b), composed of smaller particles in a size range of 30-190 nm (Figure 5-38c).

Analytical disc centrifugation (ADC) confirmed these results and showed BG nanoparticles, with mass-, surface- and number-weighted hydrodynamic size distributions of 28 nm, 27 nm, and 26 nm, respectively (Figure 5-39a). The reduced particle size was further evaluated using TEM and the results displayed a particle size range of 20-50 nm (Figure 5-39b insert TEM image). Similar size-reduction phenomena also occurred in laser fragmentation experiments of alginate-Fe-EDTA solutions (Figure S20b). Thus, we confirm a significant size reduction of raw bioglass through laser fragmentation at a laser wavelength of 355 nm.

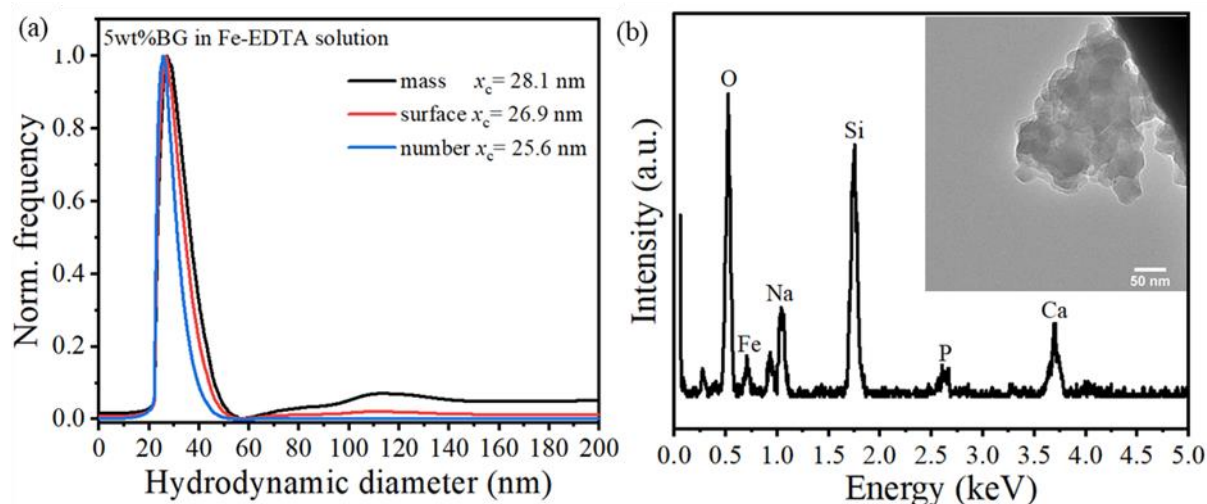


Figure 5-39: Analytical disc centrifugation (ADC) analysis (a), EDX spectra (b) of bioactive glass particles laser-irradiated in Fe-EDTA solution (insert TEM image) washed before analysis.

The elemental composition of the bioglass before and after fragmentation was further investigated by EDX and XRF. The typical 45S5 bioglass formulation has 45 wt% SiO_2 -24.5 wt% Na_2O -24.5 wt% CaO -6 wt% P_2O_5 , which is based on the unit of $[\text{SiO}_4]$ tetrahedron forming a network via $-\text{Si}-\text{O}-\text{Si}-$ bridging oxygen bonds where sodium and calcium disrupt as modifiers crating non-bridging oxygen bonds [133]. The chemical composition containing Si, Ca, P, Na, O of raw bioglass powder was measured and is depicted in Figure 5-38a and S21a.

Here we found a good correlation between the nominal and the measured compositions as compared to the values listed in Table S1. The products after laser irradiation in the presence of Fe-EDTA were found to be doped with Fe ions as the marks in Figure 5-38b, as well as in Figure 5-39b and Figure S21b.

Figure 5-40 shows the individual element variations of exemplary samples as weight and atom concentration based on EDX analysis. The irradiated samples were found to be significantly depleted in Na and Ca concentration, with a 5.6-14 and 1.7-1.9 fold loss in atomic composition, respectively. However, they were enriched with iron up to 25 wt%. Based on these findings, we may conclude that Fe ions replace the network modifier ions (Na, Ca) during laser-irradiation process. The ratio of Ca/P slightly decreased in the laser-irradiated samples from 8.6 to 11.5; however, it is still far higher than the proportional component in hydroxyapatite (Ca/P = 1.67) [133]. Even though we observe a very pronounced increase in iron loading, based on the current experimental design, we cannot differentiate whether the iron was incorporated by laser irradiation or chemically introduced as previously discussed. Thereto, we analyzed a control sample where raw bioglass was just mixed with Fe-EDTA (without irradiation) and consecutively washed similar to the irradiated sample. These samples also exhibited a significant iron doping up to 3 at. % and 11 wt.%. However, it was around 50% lower than that of the irradiated sample. Based on this, we may conclude that both chemical and laser irradiation contributed to the observed Fe doping in the BG particles.

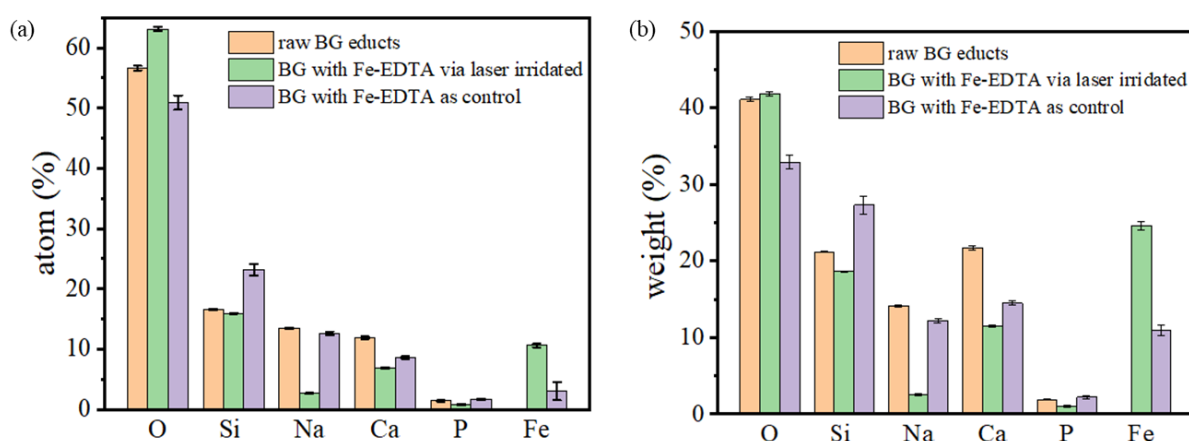


Figure 5-40: Energy-dispersive X-ray spectroscopy (EDX) analysis showing the atomic (a) and weight (b) concentration for each element present in BG educts, BG directly mixing with Fe ions solution.

We further analyzed the crystallinity of the BG particles by XRD in order to probe whether the predominantly amorphous BG structure would be affected by the laser treatment and the presence of the high amounts of iron. In literature, magnetite phases (Fe_3O_4), maghemite ($\gamma\text{-Fe}_2\text{O}_3$) in addition to FeO phase are frequently found in calcium phosphate particles doped with iron [49, 51]. Furthermore, there are two commonly reported crystalline phases, $\text{Na}_6\text{Ca}_3\text{Si}_6\text{O}_{18}$ and $\text{Na}_2\text{Ca}_4(\text{PO}_4)_2\text{SiO}_4$, frequently found in raw 45S5 bioglass during sintering or heat-treatment [268, 269]. The measured XRD diffractograms of 45S5 BG before and after laser treatment is dominated by a broad band at 32° , while no potential reflexes associated to common crystalline phases were observable (Figure 5-41a). Based on these findings it may be concluded that the BG retained its amorphous structure following laser irradiation.

The FTIR spectra of raw and laser-irradiated BG powders are presented in Figure 5-41b. The bioglass educts exhibit peaks at 1000 cm^{-1} and 908 cm^{-1} , which could be corresponding to the groups of Si-O-Si or PO_4^{3-} , and vibration of Si-O nonbonding oxygen (NBO), respectively [270]. The peak at 1440 cm^{-1} can be assigned to symmetric stretching vibration of P-O [43]. It should be noted that the peak intensity at 1000 cm^{-1} was stronger and the peak at 908 cm^{-1} was shifted to 874 cm^{-1} in the laser processed BG-Fe-EDTA. The new peak at 1646 cm^{-1} may be attributed to the replacement of phosphorous with another ion, like Fe [43].

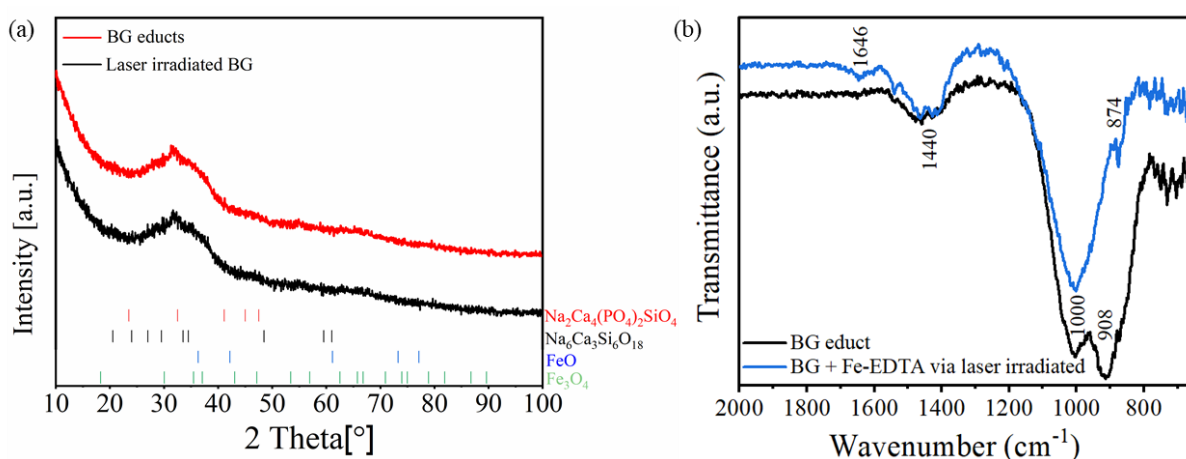


Figure 5-41: XRD spectra showing four crystalline phases from literature as cited above (a) and FTIR spectra (b) of BG educts powder and BG in Fe-EDTA solution processed via laser fragmentation. Samples were washed before analysis.

The scaling up of nanoscopic bioglass productivity is still a challenge. In previous experiments we could verify that laser fragmentation in liquid can reduce BG particle size and incorporate foreign elements like iron, however, the yield of bioglass particles smaller than $1\ \mu\text{m}$ is equally

important for potential applicability. Therefore, BG particles after laser fragmentation were separated at different centrifugation parameters and the particle size of the obtained supernatant was measured using DLS (Figure S22). Based on these findings it may be concluded that centrifugation at 34 g for 5 min resulted in a quantitative separation of particles smaller than 1 μm . Supernatant and pellets obtained under these conditions were consecutively used for gravimetric yield evaluation.

In an initial approach, we evaluated the yield of small particles ($< 1 \mu\text{m}$) in correlation with the number of passages Figure S23. We found a steep increase of the fragmentation yield within the first 10 passages and saturation after the 30th passage at a yield of 5%. Therefore, 30 passages were used in all fragmentation experiments unless otherwise stated. It should be noted that the yield value is 0.04% without adding Fe ions as light-absorbing agent. Cu^{2+} was taken as light-absorbing agent control, one can see no significant absorption peak at 355 nm and the resulting yield is around 0.036%, which is not enhanced much compared to the raw educt in water (Figure 5-37b). As mentioned above, this low yield was due to the inefficient absorption of laser energy. The efficiency was however improved in the presence of Fe ions due to the iron ions' absorption capability as Figure 5-37c shown. Hence, laser energy absorbing ions are a prerequisite for successful fragmentation. Furthermore, as Figure 5-42 reveals, the yield enhancement of small BG particles after laser fragmentation was around 8%. It should be mentioned that the weight of final BG products was subtracted from the initial gravimetric weight of alginate. The results may be attributed to the 79% increase in laser energy absorption (Figure 5-37c). Another factor is the increased number of pulses per volume resulting from the decreased volume flow rate (Figure 5-37d). As BG particles downsized from micrometers to 50 nm, the increased surface area ($44 \text{ m}^2/\text{g}$) of the samples would lead to a high reactivity of glass surface and accelerate their interaction with tissue [136]. The yield of BG nanoparticles is measurable and the obtained products can be considered as a promising material for bone tissue engineering.

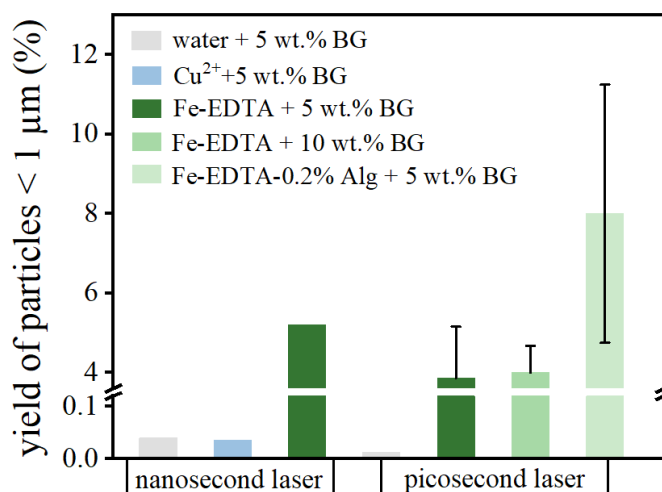


Figure 5-42: Yield of bioactive glass particles smaller than 1 μm in water, Cu^{2+} solution controls and Fe-EDTA solution as light-absorbing agent processed by nanosecond or picosecond laser.

In a final experimental series, we compared the influence of different lasers with ps and ns pulse durations on the yield of particles smaller than 1 μm . Figure 5-42 compares the yield of picosecond (4%) and nanosecond laser sources (5%). The used laser parameters are listed in Table 4-4. The nanosecond laser is with high power at moderate repetition rates and has high laser fluence. Further, laser fluence of nanosecond laser is around 9 times higher than that of the picosecond laser. Given all these information, we suppose the high fluence of nanosecond laser contributed to a slightly higher yield.

Even though the size reduction of BG microparticles can be achieved with both pico- and nanosecond laser, the mechanism could be different. SEM images of the fragmentation products reveal (Figure 5-43b) that the morphology of BG particles produced by picosecond laser is dominated by irregularly shaped particles. On the other hand, when nanosecond lasers were used (detailed information was shown in Table 4-4), most morphology was similar. However, some melting of the edges occurred, as shown by the red-circle markings in Figure 5-43. In both cases, the particles were highly aggregated, which is a frequently found phenomenon for BG [8, 136].

As described previously, the size reduction during LFL is a complex process and well understood for metal particles, though under explored for low-density amorphous structures like BG. Based on previous findings for metal particles, fragmentation is believed to be either the consequence of photothermal evaporation or Coulomb explosion, which depends on the pulse duration (τ_p), laser energy density and electron-phonon coupling time (τ_{e-p}) [271]. In case

of $\tau_p \gg \tau_{e-p}$, it is mainly heating and melting, while at $\tau_p \approx \tau_{e-p}$, it is partial evaporation and fragmentation, and for $\tau_p \ll \tau_{e-p}$, Coulomb explosion is predicted to be the dominant mechanism. However, there is no reported τ_{e-p} value of 45S5 bioglass. Here a thermomechanical shockwave induced mechanism is conceivable (Figure 5-43a). It would start with local heating of the BG particles, particularly in the vicinity of adsorbed ion precursors. This would initiate a thermally-induced shockwave, which can propagate into the solid particle and would be reflected at the corresponding particle edges. The result would be a mechanically-induced particle fragmentation of the brittle BG particles. Similar processes may also occur in the case of nanosecond pulses, however, the higher optical penetration depth and the longer lifetime of the laser pulse may initiate the observed melting artifacts.

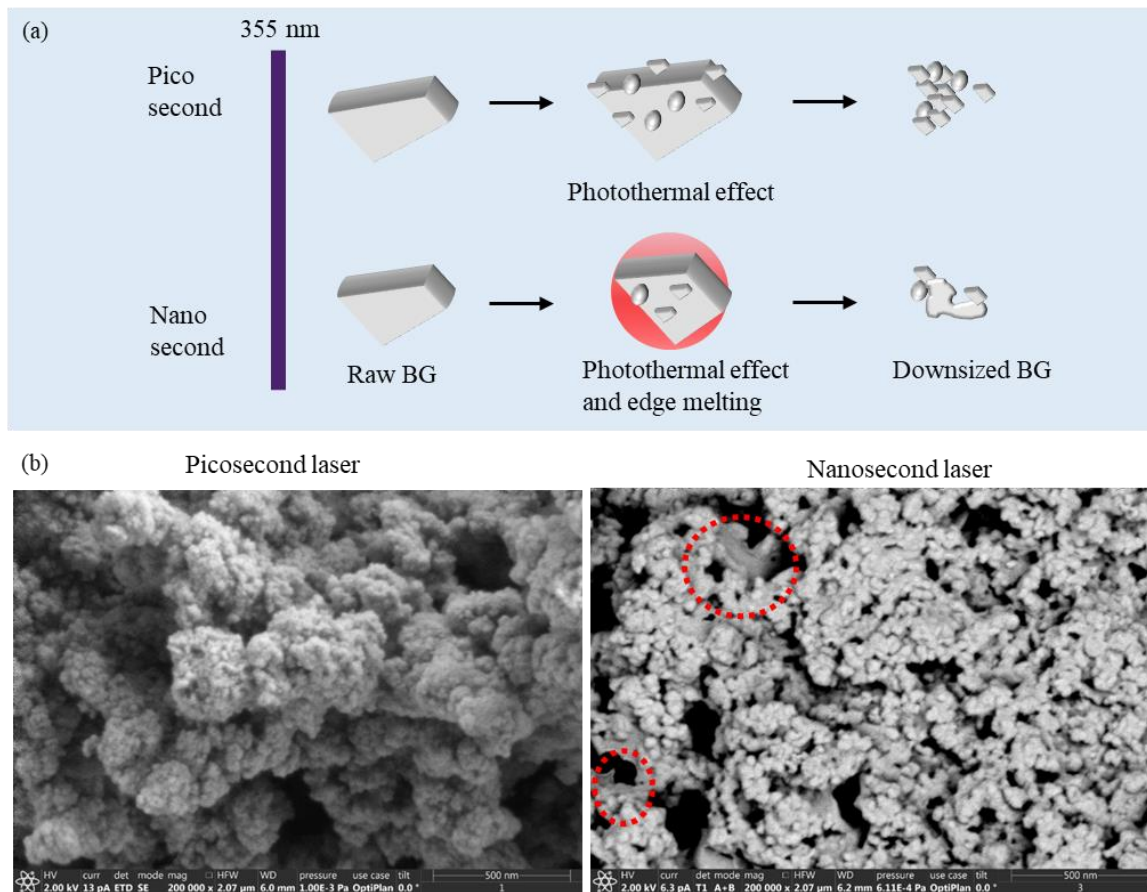


Figure 5-43: (a) Proposed mechanism of nanosized bioglass fragmented by pico or nanosecond laser; (b) SEM images of bioactive glasses produced by pico- or nanosecond laser.

In vitro dissolution is vital to investigate the therapeutic ion release from bioglass and predict their bioactive responses since metal ion release could trigger osteogenic gene expression [39, 272]. A number of factors such as bioglass type, dissolution medium, particle size would

influence dissolution. Sepulveda *et al.* [273] compared 45S5 and 58S bioglass with fine (5-20 μm), medium (90-300 μm), coarse sizes (90-710 μm) in different culture medium and not surprisingly the highest dissolution rate was found in fine powders. Arango-Ospina *et al.* [274] investigated the dissolution process of ICIE 16 bioglass in simulated body fluids or Tris solutions under static or dynamic conditions. In both the media, there was similar ion dissolution and pH increase. With increasingly doped boron amounts in the bioglass, they obtained a faster dissolution rate in all media.

Consequently, we analyzed the dissolution of Ca^{2+} ions from unprocessed and laser-processed bioglass samples and observed a steep increase in pH for all the samples, more pronounced for the raw bioglass in contrast to the irradiated sample which is partially substituted with iron (Figure 5-44a). In the unprocessed BG educts pH increased to 7.85, while the pH for the laser-irradiated suspensions remained below 7.5 after 144 hours.

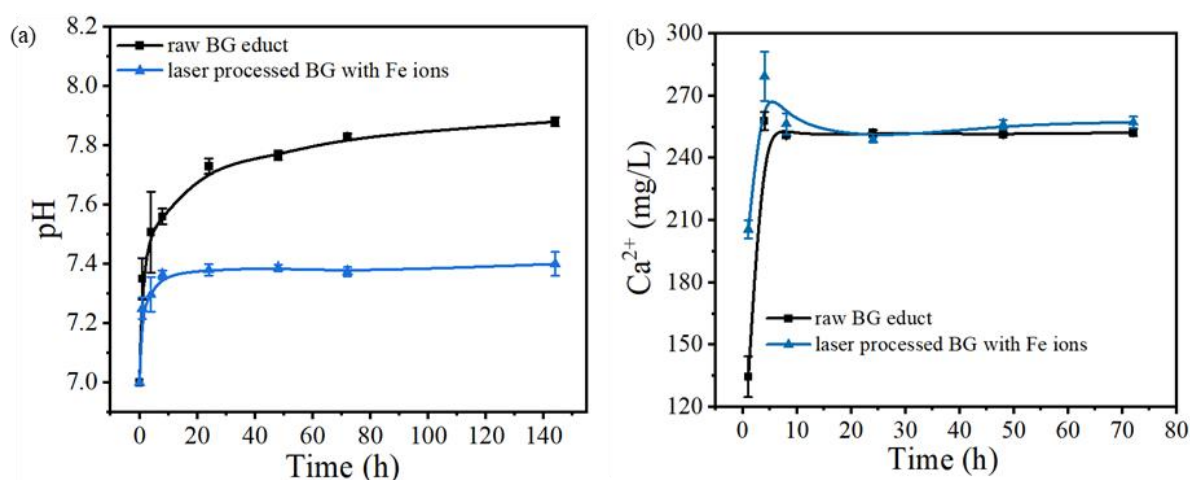


Figure 5-44: Ca^{2+} ion dissolution profiles of various bioglass powders (45 mg) in 30 mL of 50 mM Tris-HCl buffer as a function of incubation time at 37°C under static conditions.

During the normal dissolution process of BG in aqueous media, Ca^{2+} , Na^+ ions are exchanged with H_3O^+ protons from the buffer. For this reason, the pH increases, especially during the first few hours. The acidic conditions in the case of laser-fabricated BG spiked with Fe addition and could be attributed to the fact that there are significantly less sodium ions present in this sample (Figure 5-40) and hence the replacement reaction with H_3O^+ is less pronounced. It is well known from literature that this reaction is dominated by Na^+ and not Ca^{2+} [275]. This kind of sodium “pre-wash” may enhance *in vitro* biocompatibility, considering sodium not being necessary for glass bioactivity [276]. Another reason might be the parallel release of iron ions

from the laser-processed hydrogel, which would make the aqueous medium more acidic, as specified previously. Of note, the released Ca^{2+} concentration is relative. The Ca^{2+} release kinetics, on the other hand, showed a burst release after 1 h (first point in Figure 5-44b), which is slightly more pronounced in the laser-irradiated sample while both samples reach a similar saturation concentration after 10 h. This stronger Ca^{2+} burst release in the laser-irradiated sample may be attributed to the higher surface area and hence the higher solubility of the BG particles due to smaller particle sizes. This effect seems to be dominant as a quicker release in a diffusion-based mechanism would be expected for the unprocessed sample, as it possesses a higher calcium content according to Figure 5-40.

6 Summary

Designing of tissue engineering scaffolds for different organs is intricate, and the interaction with trigger factors and cells makes it more complicated. Nanoparticle-polymer composites hold great potentials in application of scaffold development, due to their biodegradation, biocompatibility, easy processing, and fabrication. Laser-based synthesis has already been proven to be a versatile technique in nanotechnology. This work was mainly focused on the systematic design, fabrication, and characterization of Au, Fe, bioactive glass nanoparticles, and Au/FeNPs -TPU, collagen, alginate polymer composites. This work tried to contribute to a better understanding of their relationship between nanoparticle effects and physicochemical and mechanical properties of polymers. In particular, the triple network of alginate-fibrin, FeNPs, and serum protein coatings were investigated for endothelialization.

In this thesis, firstly nanoparticles' power-specific productivity in various polymer solutions was evaluated (chapter 5.1). It turns out that this technique enables to produce a measurable level of NPs. The highest laser-specific productivity of AuNPs and FeNPs obtained in the alginate solution were around 12 mg/h·W and 5.8 mg/h·W, respectively. Compared to FeNPs, the productivity of laser-ablated AuNPs was higher due to the high density and efficient light-absorption of the Au target. Low NPs productivity was usually found in organic solvents that could generate gases such as CH₄ and CO₂ and these bubbles could shield the incoming laser beam. Apart from solvents, the viscosity and turbidity of polymer solutions also play a key role in NP productivity rather than density. The high viscosity and turbidity of liquids usually lower the laser efficiency. Importantly, polymers have a minor degradation level during the laser ablation process, as the results of FTIR displayed. The obtained AuNPs had no adverse effects on the gelation of collagen molecules (chapter 5.3.4).

In addition, polymer chains induced a size quenching effect that was observed (chapter 5.2.1). The average AuNP and FeNP sizes obtained in water was 6.3 nm and 10.6 nm, respectively. While in organic solvents like THF and acetic acid, there were larger particles (> 60 nm) obtained. In the presence of polymer molecules, AuNP and FeNP sizes were reduced to 3.3 nm and 8 nm, respectively. Fe oxides particles with a dominated dipolar coupling arrangements were also found in the liquid of acetic acid. The XRD patterns demonstrated the existence of a certain amount of Fe oxides.

The dispersion of particles in the polymer matrix is associated with the properties of composites. Accordingly, we utilized laser scanning confocal microscopy to characterize the particles in the polymer matrices and demonstrated that they were well-distributed, although agglomerations were frequently found. We have further developed this method to measure the co-localization of FeNPs and TRITC-labeled serum proteins at separate and typical channels. And it turned out that there was an overlay of the detected signals from FeNPs and FBS proteins on the matrix and fibrin fibres (chapter 5.2.2).

Moreover, the embedding of nanoparticles was found to affect the rheological properties of alginate and alginate-fibrin hydrogels (chapter 5.3.1). The highest elastic modulus of 12.4 kPa was achieved in the sample of 0.09 wt% FeNP loadings in alginate samples cross linked with 25 mg/mL CaCl₂ solution. Such high strength could support the own weights of laser generated nanoparticle-alginate composites during 3D printing (chapter 5.4). Furthermore, nanoparticles have influences on the physicochemical properties such as wettability, surface charge, porosity, and roughness of composites as well (chapter 5.3.2 and 5.3.3). The surface of TPU was modified with nanoparticles and it became more negatively charged and hydrophilic. And the total ion release concentration from Fe-TPU composites was proportional to the NP mass loading (chapter 5.3.5).

Interestingly, specific Fe ion release kinetics that had a higher relative and total release of Fe ions were detected at a relatively low mass loading of Fe nanoparticles, specifically in the alginate polymer (chapter 5.3.2). This peculiar behaviour is probably attributed to the high affinity of the released Fe ions towards the alginate network in contrast to its Zn and Cu analog. It constitutes a finding highly relevant for the understanding of ion release processes of nanocomposites and could significantly improve the design of medically relevant ion release systems where less is more and low loadings can lead to higher impact. As these biologically relevant nanocomposites are quite effective at low loadings far below 0.1 wt% (e.g. as low as 1000 ppm for Fe-alginate), laser ablation in liquid can be efficiently used for large-scale production of these materials. Hence, we further studied the triple modification of alginate hydrogels with FeNPs, fibrin, and FBS coatings (chapter 5.3.3). It was demonstrated that the synergistic effect of fibrin, Fe-NPs, and serum proteins contributed to a confluent endothelialization and displayed a promising material for stent coating.

Finally, we have successfully downsized and Fe doped 45S5 bioactive glass from micrometers (3.5 -11 μm) to below 50 nm by applying laser fragmentation method using Fe ions as light-

absorbing agent (chapter 5.5). 45S5 bioactive glass acts as an attractive biomaterial in bone regeneration. Nanosized particles with a large surface area ($44 \text{ m}^2/\text{g}$) could enhance and support the healing process of bone defects (chapter 3.3). The mechanism of laser-irradiated nanoscopic bioglass depended on the laser duration: thermally-induced shock wave was dominated when using picosecond laser and its thermal effects and melting that dominated with nanosecond laser. This fabrication process is simple, rapid, and incorporates metallic ions into the bioglass composition in one step. The laser processed 45S5 glass sample shows a rapid Ca^{2+} dissolution in the pH range of 7.0-7.4, indicating faster apatite formation. Apatite is an essential constituent for bone regeneration.

In conclusion, a series of experiments has been performed to provide a fundamental understanding on the behaviours of nanocomposites. This work demonstrates that the laser ablation method is a promising strategy to produce metal nanoparticle polymer (alginate hydrogel, collagen and thermoplastic polyurethane) composites with efficient productivity, while laser fragmentation is powerful to downsize the BG particles. Metal nanoparticles can alter the physicochemical and mechanical properties of composites. Moreover, nanoparticle-alginate composites are capable of being 3D printable educts for biological applications. A potential application for the triple network of FeNPs, fibrin, FBS in alginate is in the stent coatings. With promising results, the presently prepared composites reveal a great potential for applications in tissue engineering and bioactive ion delivery, where a controlled release of metal ions could induce beneficial effects on the cellular response.

7 Outlook

Despite the remarkable progress made in this work, further scaling up of NP productivity in polymer solution remains a challenge. Notably, neither increasing the laser power nor the scanning speed is ideal for a higher productivity and it is costly. However, NP productivities were found higher in the pure solvents such as water and THF. Therefore, we could firstly produce NPs in pure solvents and then mix them with various polymers to obtain composites. Thus, the particle stability, distribution, and effects on the properties of the final composites are to be further investigated.

Regarding the production of nanoscopic bioglass in much higher productivity, manipulation of the laser energy profile, and other types of jet geometries, for example, flat jet, might be an option. Another drawback in this part work is the lack of experiments on angiogenic and osteogenic properties of BG. However, the initial step of *in vitro* cell viabilities was conducted, as illustrated in Figure S25. This result underlines that even higher particle content does not have a toxic impact on cell viability. Overall, all samples have high viability of over 80% compared to the control.

With the scope of our presented work, we hypothesized that the Fe ion release played a key role in the protein adsorption process and the following biological response. But there is no direct proof. Therefore, to characterize the interaction between metal ions and proteins is a tricky problem. Although the fragment transformation method can be used to predict the metal ion-binding sites of proteins [277], its accuracy needs improving. Recently researchers utilized atomic force microscopy and standalone software AFMech Suite to describe the interface bonding between bacteria and supporting surface of poly(N-isopropylamide) (PNIPAM) hydrogels [278]. This technique has a scope to investigate the bonding between ions and proteins or cells.

8 References

- [1] A. Z. Unal, J. L. West. Synthetic ECM: Bioactive synthetic hydrogels for 3D tissue engineering. *Bioconjugate Chem.* **2020**, 31 (10), 2253-2271.
- [2] R. Silva, R. Singh, B. Sarker, D. G. Papageorgiou, J. A. Juhasz-Bortuzzo, J. A. Roether, I. Cicha, J. Kaschta, D. W. Schubert, K. Chrissafis, R. Detsch, A. R. Boccaccini. Hydrogel matrices based on elastin and alginate for tissue engineering applications. *Int. J. Biol. Macromol.* **2018**, 114, 614-625.
- [3] A. Doderò, S. Scarfi, M. Pozzolini, S. Vicini, M. Alloisio, M. Castellano. Alginate-based electrospun membranes containing ZnO nanoparticles as potential wound healing patches: biological, mechanical, and physicochemical characterization. *ACS Appl. Mater. Interfaces* **2020**, 12 (3), 3371-3381.
- [4] F. Olate-Moya, L. Arens, M. Wilhelm, M. A. Mateos-Timoneda, E. Engel, H. Palza. Chondroinductive alginate-based hydrogels having graphene oxide for 3D printed scaffold fabrication. *ACS Appl. Mater. Interfaces* **2020**, 12 (4), 4343-4357.
- [5] R. Michel, R. Auzély-Velty. Hydrogel-colloid composite bioinks for targeted tissue-printing. *Biomacromolecules* **2020**, 21 (8), 2949-2965.
- [6] M. Silva, F. N. Ferreira, N. M. Alves, M. C. Paiva. Biodegradable polymer nanocomposites for ligament/tendon tissue engineering. *J. Nanobiotechnology* **2020**, 18 (1), 33.
- [7] D. G. Yu, W. C. Lin, C. H. Lin, Y. H. Yeh, M. C. Yang. Construction of antithrombogenic polyelectrolyte multilayer on thermoplastic polyurethane via layer-by-layer self-assembly technique. *J. Biomed. Mater. Res. B. Appl. Biomater.* **2007**, 83 (1), 105-113.
- [8] N. Pajares-Chamorro, X. Chatzistavrou. Bioactive glass nanoparticles for tissue regeneration. *ACS Omega* **2020**, 5 (22), 12716-12726.
- [9] T. Y. Hosida, A. C. B. Delbem, L. A. Morais, J. C.S. Moraes, C. Duque, J. A. S. Souza, D. Pedrini. Ion release, antimicrobial and physio-mechanical properties of glass ionomer cement containing micro or nanosized hexametaphosphate, and their effect on enamel demineralization. *Clin. Oral Invest.* **2019**, 23 (5), 2345-2354.
- [10] K. Brändle, T. C. Bergmann, A. Raic, Y. Li, N. Million, C. Rehbock, S. Barcikowski, C. Lee-Thedieck. Iron nanoparticle composite hydrogels for studying effects of iron ion release on red blood cell *in vitro* production. *ACS Appl. Bio Mater.* **2020**, 3 (8), 4766-4778.
- [11] K. C. Huang, S. H. Ehrman. Synthesis of iron nanoparticles via chemical reduction with palladium ion seeds. *Langmuir* **2007**, 23 (3), 1419-1426.
- [12] A. Blaeser, N. Million, D. F. D. Campos, L. Gamrad, M. Köpf, C. Rehbock, M. Nachev, B. Sures, S. Barcikowski, H. Fischer. Laser-based *in situ* embedding of metal nanoparticles into bioextruded alginate hydrogel tubes enhances human endothelial cell adhesion. *Nano Res.* **2016**, 9 (11), 3407-3427.

- [13] N. Million. Lasergenerierte funktionale Nanopartikel-Polymer-Komposite als Ionenfreisetzungssysteme für medizinische Anwendungen. Doctoral thesis, Universität Duisburg-Essen, **2017**.
- [14] P. Wagener, G. Brandes, A. Schwenke, S. Barcikowski. Impact of *in situ* polymer coating on particle dispersion into solid laser-generated nanocomposites. *Phys. Chem. Chem. Phys.* **2011**, 13 (11), 5120-5126.
- [15] C. Hess, A. Schwenke, P. Wagener, S. Franzka, C. Laszlo Sajti, M. Pflaum, B. Wiegmann, A. Haverich, S. Barcikowski. Dose-dependent surface endothelialization and biocompatibility of polyurethane noble metal nanocomposites. *J. Biomed. Mater. Res. A.* **2014**, 102 (6), 1909-1920.
- [16] D. Zhang, B. Gökce. Perspective of laser-prototyping nanoparticle-polymer composites. *Appl. Surf. Sci.* **2017**, 392, 991-1003.
- [17] E. Maurer, S. Barcikowski, B. Gökce. Process chain for the fabrication of nanoparticle polymer composites by laser ablation synthesis. *Chem. Eng. & Technol.* **2017**, 40(9), 1535-1543.
- [18] R. S. Ambekar, B. Kandasubramanian. Progress in the advancement of porous biopolymer scaffold: Tissue engineering application. *Ind. Eng. Chem. Res.* **2019**, 58 (16), 6163-6194.
- [19] J. W. Goss, C. B. Volle. Using atomic force microscopy to illuminate the biophysical properties of microbes. *ACS Appl. Bio Mater.* **2020**, 3 (1), 143-155.
- [20] T. Kochane, S. Budriene, S. Miasojedovas, N. Ryskevici, A. Straksys, S. Maciulyte, A. Ramanaviciene. Polyurethane-gold and polyurethane-silver nanoparticles conjugates for efficient immobilization of maltogenase. *Colloids Surf. A Physicochem. Eng. Asp.* **2017**, 532, 436-443.
- [21] X. He, Y. Ding, W. Xie, *et al.* Rubidium-containing calcium alginate hydrogel for antibacterial and diabetic skin wound healing applications. *ACS Biomater. Sci. Eng.* **2019**, 5 (9), 4726-4738.
- [22] W. Su, L. Ma, Y. Ran, X. Ma, Z. Yi, G. Chen, X. Chen, X. Li. Alginate-assisted mineralization of collagen by collagen reconstitution and calcium phosphate formation. *ACS Biomater. Sci. Eng.* **2020**, 6 (6), 3275-3286.
- [23] M. Morra, C. Cassineli. Non-fouling properties of polysaccharide-coated surfaces, Journal of biomaterials science. *J. Biomater. Sci. Polym. Ed.* **1999**, 10 (10), 1107-1124.
- [24] J. A. Rowley, G. Madlambayan, D. J. Mooney. Alginate hydrogels as synthetic extracellular matrix materials. *Biomaterials* **1999**, 20 (1), 45-53.
- [25] G. A. Junter, P. Thebault, L. Lebrun. Polysaccharide-based antibiofilm surfaces. *Acta Biomater.* **2016**, 30, 13-25.
- [26] C. E. Vorwald, T. Gonzalez-Fernandez, S. Joshee, P. Sikorski, J. K. Leach. Tunable fibrin-alginate interpenetrating network hydrogels to support cell spreading and network formation. *Acta Biomater.* **2020**, 108, 142-152.

- [27] A. Dewle, N. Pathak, P. Rakshasmare, A. Srivastava. Multifarious fabrication approaches of producing aligned collagen scaffolds for tissue engineering applications. *ACS Biomater. Sci. Eng.* **2020**, 6 (2), 779-797.
- [28] S. C. Hsieh, H. J. Chen, S. H. Hsu, *et al.* Prominent vascularization capacity of mesenchymal stem cells in collagen-gold nanocomposites. *ACS Appl. Mater. Interfaces* **2016**, 8 (42), 28982-29000.
- [29] M. Jafari-Sabet, H. Nasiri, R. Ataee. The effect of cross-linking agents and collagen concentrations on properties of collagen scaffolds. *J. Arch. Mil. Med.* **2016**, 4 (4), e42367.
- [30] L. H. H. Olde Damink, P. J. Dijkstra, M. J. A. Van Luyn, P. B. Van Wachem, P. Nieuwenhuis, J. Feijen. Glutaraldehyde as a crosslinking agent for collagen-based biomaterials. *J. Mater. Sci. Mater. Med.* **1995**, 6, 460-472.
- [31] U. Daood, Z. Akram, J. P. Matinlinna, A. S. Fawzy. Dentine collagen cross-linking using tiopronin-protected Au/EDC nanoparticles formulations. *Dent. Mater.* **2019**, 35 (7), 1017-1030.
- [32] M. Vedhanayagam, M. Nidhin, N. Duraipandy, *et al.* Role of nanoparticle size in self-assemble processes of collagen for tissue engineering application. *Int. J. Biol. Macromol.* **2017**, 99, 655-664.
- [33] A. Negahi Shirazi, A. Fathi, F. G. Suarez, Y. Wang, P. K. Maitz, F. Dehghani, A novel strategy for softening gelatin-bioactive-glass hybrids. *ACS Appl. Mater. Interfaces* **2016**, 8 (3) 1676-1686.
- [34] M. L. Dittler, I. Unalan, A. Grünwald, A. M. Beltrán, C. A. Grillo, R. Destch, M. C. Gonzalez, A. R. Boccaccini. Bioactive glass (45S5)-based 3D scaffolds coated with magnesium and zinc-loaded hydroxyapatite nanoparticles for tissue engineering applications. *Colloids Surf. B.* **2019**, 182, 110346.
- [35] K. Zheng, A. R. Boccaccini. Sol-gel processing of bioactive glass nanoparticles: A review. *Adv. Colloid Interface Sci.* **2017**, 249, 363-373.
- [36] A. S. Verma, A. Singh, D. Kumar, A. K. Dubey. Electro-mechanical and polarization-induced antibacterial response of 45S5 bioglass-sodium potassium niobate piezoelectric ceramic composites. *ACS Biomater. Sci. Eng.* **2020**, 6 (5), 3055-3069.
- [37] Y. Xiang, J. Du. Effect of strontium substitution on the structure of 45S5 bioglasses. *Chem. Mater.* **2011**, 23 (11), 2703-2717.
- [38] L. Weng, S. K. Boda, M. J. Teusink, F. D. Shuler, X. Li, J. Xie. Binary doping of strontium and copper enhancing osteogenesis and angiogenesis of bioactive glass nanofibers while suppressing osteoclast activity. *ACS Appl. Mater. Interfaces* **2017**, 9 (29), 24484-24496.
- [39] V. Mouriño, R. Vidotto, J. P. Cattalini, A. R. Boccaccini. Enhancing biological activity of bioactive glass scaffolds by inorganic ion delivery for bone tissue engineering. *Curr. Opin. Biomed. Eng.* **2019**, 10, 23-34.
- [40] A. M. Brokesh, A. K. Gaharwar. Inorganic biomaterials for regenerative medicine. *ACS Appl. Mater. Interfaces* **2020**, 12 (5), 5319-5344.

- [41] Y. Qi, H. Qi, Y. He, W. Lin, P. Li, L. Qin, Y. Hu, L. Chen, Q. Liu, H. Sun, Q. Liu, G. Zhang, S. Cui, J. Hu, L. Yu, D. Zhang, J. Ding. Strategy of metal-polymer composite stent To accelerate biodegradation of iron-based biomaterials. *ACS Appl. Mater. Interfaces* **2018**, 10 (1), 182-192.
- [42] J. V. Rau, M. Curcio, M. G. Raucchi, K. Barbaro, I. Fasolino, R. Teghil, L. Ambrosio, A. De Bonis, A.R. Boccaccini. Cu-releasing bioactive glass coatings and their *in vitro* properties. *ACS Appl. Mater. Interfaces* **2019**, 11 (6), 5812-5820.
- [43] A. Łapa, M. Cresswell, I. Campbell, P. Jackson, W.H. Goldmann, R. Detsch, A.R. Boccaccini. Gallium- and cerium-doped phosphate glasses with antibacterial properties for medical applications. *Adv. Eng. Mater.* **2020**, 22 (9), 1901577.
- [44] A. A. R. de Oliveira, D. A. de Souza, L. L. S. Dias, S. M. de Carvalho, H. S. Mansur, M. de Magalhães Pereira. Synthesis, characterization and cytocompatibility of spherical bioactive glass nanoparticles for potential hard tissue engineering applications. *Biomed. Mater.* **2013**, 8 (2), 025011.
- [45] P. Saravanapavan, J. R. Jones, R. S. Pryce, L. L. Hench. Bioactivity of gel-glass powders in the CaO-SiO₂ system: a comparison with ternary (CaO-P₂O₅-SiO₂) and quaternary glasses (SiO₂-CaO-P₂O₅-Na₂O). *J. Biomed. Mater. Res. A.* **2003**, 66 (1), 110-119.
- [46] A. Lukowiak, J. Lao, J. Lacroix, J. M. Nedelec. Bioactive glass nanoparticles obtained through sol-gel chemistry. *Chem. Commun.* **2013**, 49 (59), 6620-6622.
- [47] Q. Z. Chen, G. A. Thouas. Fabrication and characterization of sol-gel derived 45S5 bioglass-ceramic scaffolds. *Acta Biomater.* **2011**, 7 (10), 3616-3626.
- [48] M. Sadat-Shojai, M. T. Khorasani, E. Dinpanah-Khoshdargi, A. Jamshidi. Synthesis methods for nanosized hydroxyapatite with diverse structures. *Acta Biomater.* **2013**, 9 (8), 7591-7621.
- [49] M. Nakamura, A. Oyane, I. Sakamaki, Y. Ishikawa, Y. Shimizu, K. Kawaguchi. Laser-assisted one-pot fabrication of calcium phosphate-based submicrospheres with internally crystallized magnetite nanoparticles through chemical precipitation. *Phys. Chem. Chem. Phys.* **2015**, 17 (14), 8836-8842.
- [50] S. Siebeneicher, F. Waag, M. Escobar Castillo, V. V. Shvartsman, D. C. Lupascu, B. Gökce. Laser fragmentation synthesis of colloidal bismuth ferrite particles. *Nanomaterials* **2020**, 10 (2), 359.
- [51] M. Nakamura, A. Oyane. Structural analysis of calcium phosphate-based submicrospheres with internally-crystallized iron oxide nanoparticles fabricated by a laser-assisted precipitation process. *Materials* **2019**, 12 (24), 4234.
- [52] L. Gaffney, E. A. Wrona, D. O. Freytes. Potential synergistic effects of stem cells and extracellular matrix scaffolds. *ACS Biomater. Sci. Eng.* **2018**, 4 (4), 1208-1222.

- [53] A. de Mel, G. Jell, M. M. Stevens, A. M. Seifalian. Biofunctionalization of biomaterials for accelerated *in situ* endothelialization: A Review. *Biomacromolecules* **2008**, 9 (11), 2969-2979.
- [54] L. N. Woodard, M. A. Grunlan. Hydrolytic degradation and erosion of polyester biomaterials. *ACS Macro. Lett.* **2018**, 7 (8), 976-982.
- [55] H. Sánchez-Morán, A. Ahmadi, B. Vogler, K. H. Roh. Oxime cross-linked alginate hydrogels with tunable stress relaxation. *Biomacromolecules* **2019**, 20 (12), 4419-4429.
- [56] R. K. Saini, L. P. Bagri, A. K. Bajpai. Nano-silver hydroxyapatite based antibacterial 3D scaffolds of gelatin/alginate/poly (vinyl alcohol) for bone tissue engineering applications. *Colloid Surf. B.* **2019**, 177, 211-218.
- [57] M. Jaymand. Chemically modified natural polymer-based theranostic nanomedicines: are they the golden gate toward a de Novo clinical approach against cancer? *ACS Biomater.Sci. Eng.* **2020**, 6 (1), 134-166.
- [58] P. Sobhanian, M. Khorram, S. S. Hashemi, A. Mohammadi. Development of nanofibrous collagen-grafted poly (vinyl alcohol)/gelatin/alginate scaffolds as potential skin substitute. *Int. J. Biol. Macromol.* **2019**, 130, 977-987.
- [59] R. A. Latour. Fundamental principles of the thermodynamics and kinetics of protein adsorption to material surfaces. *Colloids Surf. B.* **2020**, 191, 110992.
- [60] S. Höhn, S. Virtanen, A. R. Boccaccini. Protein adsorption on magnesium and its alloys: A review. *Appl. Surf. Sci.* **2019**, 464, 212-219.
- [61] C. J. Wilson, R. E. Clegg, D. I. Leavesley, M. J. Percy. Mediation of biomaterial-cell interactions by adsorbed proteins: a review. *Tissue Eng.* **2005**, 11 (1-2), 1-18.
- [62] R. M. Visalakshan, M. N. MacGregor, S. Sasidharan, *et al.* Biomaterial surface hydrophobicity-mediated serum protein adsorption and immune responses. *ACS Appl. Mater. Interfaces* **2019**, 11 (31), 27615-27623.
- [63] F. Rusmini, Z. Zhong, J. Feijen. Protein immobilization strategies for protein biochips. *Biomacromolecules* **2007**, 8 (6), 1775-1789.
- [64] K. Zhao, T. Chen, B. Lin, W. Cui, B. Kan, N. Yang, X. Zhou, X. Zhang, J. Wei. Adsorption and recognition of protein molecular imprinted calcium alginate/polyacrylamide hydrogel film with good regeneration performance and high toughness. *React. Funct. Polym.* **2015**, 87, 7-14.
- [65] N. E. Angar, D. Aliouche. An enhanced immobilization of BSA biomolecule on anionic hydrogels: Swelling and adsorption modeling. *Chem. Pap.* **2017**, 71 (8), 1389-1397.
- [66] Y. Yang, S. Knust, S. Schwiderek, Q. Qin, Q. Yun, G. Grundmeier, A. Keller. Protein adsorption at nanorough titanium oxide surfaces: The importance of surface statistical parameters beyond surface roughness. *Nanomaterials.* **2021**, 11 (2), 357.
- [67] A. M. Rahmatika, Y. Toyoda, T. T. Nguyen, Y. Goi, T. Kitamura, Y. Morita, K. Kume, T. Ogi. Cellulose nanofiber and magnetic nanoparticles as building blocks constructing biomass-

based porous structured particles and their protein adsorption performance. *ACS Sustain. Chem. Eng.* **2020**, 8 (50), 18686-18695.

[68] K. Nakanishi, T. Sakiyama, K. Imamura. On the adsorption of proteins on solid surfaces, a common but very complicated phenomenon. *J. Biosci. Bioeng.* **2001**, 91 (3), 233-244.

[69] H. M. Yang, J. Y. Teoh, G. H. Yim, Y. Park, Y. G. Kim, J. Kim, D. Yoo. Label-Free analysis of multivalent protein binding using bioresponsive nanogels and surface plasmon resonance (SPR). *ACS Appl. Mater. Interfaces* **2020**, 12 (5), 5413-5419.

[70] A. Hasan, S. K. Pattanayek, L. M. Pandey. Effect of functional groups of self-assembled monolayers on protein adsorption and initial cell adhesion. *ACS Biomater. Sci. Eng.* **2018**, 4 (9) 3224-3233.

[71] J. S. Pober, W. C. Sessa. Evolving functions of endothelial cells in inflammation. *Nat. Rev. Immunol.* **2007**, 7 (10), 803-815.

[72] I. Kocherova, A. Bryja, P. Mozdziak, *et al.* Human umbilical vein endothelial cells (HUVECs) co-culture with osteogenic cells: From molecular communication to engineering prevascularised bone grafts. *J. Clin. Med.* **2019**, 8 (10), 1602.

[73] H. Y. Mi, X. Jing, J. A. Thomsom, L. S. Turng. Promoting endothelial cell affinity and antithrombogenicity of polytetrafluoroethylene (PTFE) by mussel-inspired modification and RGD/heparin grafting. *J. Mater. Chem. B.* **2018**, 6 (21), 3475-3485.

[74] W. Chen, B. Tian, J. Liang, S. Yu, Y. Zhou, S. Li. Matrix stiffness regulates the interactions between endothelial cells and monocytes. *Biomaterials* **2019**, 221, 119362.

[75] H. He, Z. Zou, B. Wang, G. Xu, C. Z. Chen, X. Qin, C. Yu, J. Zhang. Copper oxide nanoparticles induce oxidative DNA damage and cell death via copper ion-mediated P38 MAPK activation in vascular endothelial cells. *Int. J. Nanomedicine* **2020**, 15, 3291-3302.

[76] T. Mehrabi, A. S. Mesgar, Z. Mohammadi. Bioactive glasses: A promising therapeutic ion release strategy for enhancing wound healing. *ACS Biomater. Sci. Eng.* **2020**, 6 (10), 5399-5430.

[77] X. Wu, Y. Tan, H. Mao, M. Zhang. Toxic effects of iron oxide nanoparticles on human umbilical vein endothelial cells. *Int. J. Nanomed.* **2010**, 5, 385-399.

[78] S. Tenzer, D. Docter, S. Rosfa, *et al.* Nanoparticle size is a critical physicochemical determinant of the human blood plasma corona: A comprehensive quantitative proteomic analysis. *ACS Nano* **2011**, 5 (9), 7155-7167.

[79] M. Fathi-Achachelouei, H. Knopf-Marques, C. E. Ribeiro da Silva, J. Barthès, E. Bat, A. Tezcaner, N. E. Vrana. Use of nanoparticles in tissue engineering and regenerative medicine. *Front. Bioeng. Biotechnol.* **2019**, 7 (113), 1-22.

[80] H. Tan, K. G. Marra. Injectable, biodegradable hydrogels for tissue engineering applications. *Materials* **2010**, 3 (3), 1746-1767.

- [81] X. Li, S. Chen, B. Zhang, M. Li, K. Diao, Z. Zhang, J. Li, Y. Xu, X. Wang, H. Chen. *In situ* injectable nano-composite hydrogel composed of curcumin, N,O-carboxymethyl chitosan and oxidized alginate for wound healing application. *Int. J. Pharm.* **2012**, 437 (1), 110-119.
- [82] S. J. Hooper, S. L. Percival, K. E. Hill, D. W. Thomas, A. J. Hayes, D. W. Williams. The visualisation and speed of kill of wound isolates on a silver alginate dressing. *Int. Wound J.* **2012**, 9 (6), 633-642.
- [83] A. C. Jen, M. C. Wake, A. G. Mikos. Review: Hydrogels for cell immobilization. *Biotechnol. Bioeng.* **1996**, 50 (4), 357-364.
- [84] A. J. Putnam, D. J. Mooney. Tissue engineering using synthetic extracellular matrices. *Nat. Med.* **1996**, 2, 824.
- [85] S. R. Moxon, N. J. Corbett, K. Fisher, G. Potjewyd, M. Domingos, N. Hooper. Blended alginate/collagen hydrogels promote neurogenesis and neuronal maturation. *Mat. Sci. Eng. C, Mater.* **2019**, 104, 109904.
- [86] R. D. Horniblow, M. Dowle, T. H. Iqbal, G. O. Latunde-Dada, R. E. Palmer, Z. Pikramenou, C. Tselepis. Alginate-iron speciation and its effect on *in vitro* cellular iron metabolism. *PLoS One* **2015**, 10 (9), e0138240.
- [87] A. Roth, F. Murschel, P. L. Latreille, V. A. Martinez, B. Liberelle, X. Banquy, G. De Crescenzo. Coiled coil affinity-based systems for the controlled release of biofunctionalized gold nanoparticles from alginate hydrogels. *Biomacromolecules* **2019**, 20 (5), 1926-1936.
- [88] A. Letzel, S. Reich, T. dos S. Rolo, A. Kanitz, J. Hoppius, A. Rack, M. P. Olbinado, A. Ostendorf, B. Gökce, A. Plech, S. Barcikowski. Time and mechanism of nanoparticle functionalization by macromolecular ligands during pulsed laser ablation in liquids. *Langmuir* **2019**, 35 (8), 3038-3047.
- [89] D. Zhang, B. Gokce, S. Barcikowski. Laser synthesis and processing of colloids: fundamentals and applications. *Chem. Rev.* **2017**, 117 (5), 3990-4103.
- [90] F. M. Shaikh, A. Callanan, E. G. Kavanagh, P. E. Burke, P. A. Grace, T. M. McGloughlin. Fibrin: a natural biodegradable scaffold in vascular tissue engineering. *Cells Tissues Organs.* **2008**, 188 (4), 333-346.
- [91] A. J. Holder, N. Badiei, K. Hawkins, C. Wright, P. R. Williams, D. J. Curtis. Control of collagen gel mechanical properties through manipulation of gelation conditions near the sol-gel transition. *Soft Matter.* **2018**, 14 (4), 574-580.
- [92] M. N. Kirichenko, L. L. Chaikov, S. V. Krivokhizha, A. S. Kirichenko, N. A. Bulychev, M. A. Kazaryan. Effect of iron oxide nanoparticles on fibrin gel formation and its fractal dimension. *J. Chem. Phys.* **2019**, 150 (15), 155103.
- [93] K. Wang, K. Albert, G. Mosser, B. Haye, A. Percot, C. Paris, C. Peccate, L. Trichet, T. Coradin. Self-assembly/condensation interplay in nano-to-microfibrillar silicified fibrin hydrogels. *Int. J. Biol. Macromol.* **2020**, 164, 1422-1431.

- [94] B. Hoyer, A. Bernhardt, A. Lode, S. Heinemann, J. Sewing, M. Klinger, H. Notbohm, M. Gelinsky. Jellyfish collagen scaffolds for cartilage tissue engineering. *Acta Biomater.* **2014**, 10 (2), 883-92.
- [95] M. JoséFonseca, M. Asunción Alsina, F. Reig. Coating liposomes with collagen (Mr 50 000) increases uptake into liver. *Biochim. Biophys. Acta. Biomembr.* **1996**, 1279 (2), 259-265.
- [96] M. Maeda, S. Tani, A. Sano, K. Fujioka. Microstructure and release characteristics of the minipellet, a collagen-based drug delivery system for controlled release of protein drugs. *J. Control. Release* **1999**, 62 (3), 313-324.
- [97] W. Friess. Collagen biomaterial for drug delivery. *Eur. J. Pharm. Biopharm.* **1998**, 45, 113-136.
- [98] L. Castaneda, J. Valle, N. Yang, S. Pluskat, K. Slowinska. Collagen cross-linking with Au nanoparticles. *Biomacromolecules* **2008**, 9 (12), 3383-3388.
- [99] R. Xing, T. Jiao, L. Yan, G. Ma, L. Liu, L. Dai, J. Li, H. Möhwald, X. Yan. Colloidal gold-collagen protein core-shell nanoconjugate: One-step biomimetic synthesis, layer-by-layer assembled film, and controlled cell growth. *ACS Appl. Mater. Interfaces* **2015**, 7 (44), 24733-24740.
- [100] W. L. Medical urethanes, part 2: Versatility offers a myriad possibilities. *Urethanes Technol.* **2005**, 22 (2), 34-37.
- [101] A. Burke, N. Hasirci. Polyurethanes in biomedical applications. *Adv. Exp. Med. Biol.* **2004**, 83-101.
- [102] Q.Z Chen, S.L. Liang, G.A. Thouas. Elastomeric biomaterials for tissue engineering. *Prog. Polym. Sci.* **2013**, 38 (3-4), 584-671.
- [103] F. Pouladzadeh, A. A. Katbab, N. Haghighipour, E. Kashi. Carbon nanotube loaded electrospun scaffolds based on thermoplastic urethane (TPU) with enhanced proliferation and neural differentiation of rat mesenchymal stem cells: The role of state of electrical conductivity. *Eur. Polym. J.* **2018**, 105, 286-296.
- [104] N. Kasoju, R.R. Bhonde, U. Bora. Fabrication of a novel micro-nano fibrous nonwoven scaffold with *Antheraea assama* silk fibroin for use in tissue engineering. *Mater. Lett.* **2009**, 63 (28), 2466-2469.
- [105] I. Nelson, S. E. Naleway. Intrinsic and extrinsic control of freeze casting. *J. Mater. Res. Technol.* **2019**, 8 (2), 2372-2385.
- [106] F. Pati, J. Gantelius, H.A. Svahn. 3D Bioprinting of Tissue/Organ Models. *Angew. Chem. Int. Ed.* **2016**, 55 (15), 4650-4665.
- [107] A. Lee, A. R. Hudson, D. J. Shiwarski, J. W. Tashman, T. J. Hinton, S. Yerneni, J. M. Bliley, P. G. Campbell, A. W. Feinberg. 3D bioprinting of collagen to rebuild components of the human heart. *Science.* **2019**, 365 (6452), 482.

- [108] A. Blaeser, D. F. Duarte Campos, U. Puster, W. Richtering, M. M. Stevens, H. Fischer. Controlling shear stress in 3D bioprinting is a key factor to balance printing resolution and stem cell integrity. *Adv. Healthc. Mater.* **2016**, 5 (3), 326-333.
- [109] P. C. Liu, H. Z. Shen, Y. Zhi, J. W. Si, J. Shi, L. H. Guo, S. G. Shen, 3D bioprinting and *in vitro* study of bilayered membranous construct with human cells-laden alginate/gelatin composite hydrogels. *Colloid Surf. B.* **2019**, 181, 1026-1034.
- [110] M. Patel, H. J. Lee, S. Son, H. Kim, J. Kim, B. Jeong. Iron ion-releasing polypeptide thermogel for neuronal differentiation of mesenchymal stem cells. *Biomacromolecules* **2020**, 21 (1), 143-151.
- [111] E. A. Abou Neel, I. Ahmed, J. J. Blaker, A. Bismarck, A. R. Boccaccini, M. P. Lewis, S. N. Nazhat, J. C. Knowles. Effect of iron on the surface, degradation and ion release properties of phosphate-based glass fibres. *Acta Biomater.* **2005**, 1 (5), 553-563.
- [112] S. W. Koo, K. A. Casper, K. B. Otto, A. K. Gira, R. A. Swerlick. Iron chelators inhibit VCAM-1 expression in human dermal microvascular endothelial cells. *J. Invest. Dermatol.* **2003**, 120 (5), 871-879.
- [113] A. Hahn, T. Stöver, G. Paasche, M. Löbler, K. Sternberg, H. Rohm, S. Barcikowski. Therapeutic window for bioactive nanocomposites fabricated by laser ablation in polymer-doped organic liquids. *Adv. Eng. Mater.* **2010**, 12 (5), 156-162.
- [114] F. Baino, S. Hamzehlou, S. Kargozar. Bioactive glasses: Where are we and where are we going? *J. Funct. Biomater.* **2018**, 9 (1), 25.
- [115] A. B. Katsnelson, I. L. Privalova, B. V. Gurvich, *et al.* Comparative *in vivo* assessment of some adverse bioeffects of equidimensional gold and silver nanoparticles and the attenuation of nanosilver's effects with a complex of innocuous bioprotectors. *Int. J. Mol. Sci.* **2013**, 14 (2), 2449-2483.
- [116] T. Junaid, X. Wu, H. Thanukrishnan, R. Venkataramanan. Chapter 30 - Therapeutic Drug Monitoring in: D. Thomas (Ed.), *Clinical Pharmacy Education, Practice and Research*, Elsevier **2019**, 425-436.
- [117] E. D. R. Gurny, N. A. Peppas. Modelling of sustained release of water- soluble drugs from porous, hydrophobic polymers. *Biomaterials* **1981**, 3, 6.
- [118] R. W. Korsemeyer, R. Gurny, E. M. Doelker, P. Buri, N. A. Peppas. Mechanism of solute release from porous hydrophilic polymers. *Int. J. Pharm.* **1983**, 15, 25.
- [119] A. Hahn, G. Brandes, P. Wagener, S. Barcikowski. Metal ion release kinetics from nanoparticle silicone composites. *J. Control Release* **2011**, 154 (2), 164-170.
- [120] J. Krstić, J. Spasojević, A. Radosavljević, A. Perić-Grujić, M. Đurić, Z. Kačarević-Popović, S. Popović. *In vitro* silver ion release kinetics from nanosilver/poly(vinyl alcohol) hydrogels synthesized by gamma irradiation. *J. Appl. Polym. Sci.* **2014**, 131 (11), 40321-40335.
- [121] J. Y. Liu, R. H. Hurt. Ion release kinetics and particle persistence in aqueous nano-silver. *Environ. Sci. Technol.* **2010**, 44, 6.

- [122] R. S. T. Aydin, M. Pulat. 5-Fluorouracil encapsulated chitosan nanoparticles for pH-stimulated drug delivery: Evaluation of controlled release kinetics. *J. Nanomater.* **2012**, 10, 1-10.
- [123] C. M. Ho, S. K. W. Yau, C. N. Lok, M. H. So, C. M. Che. Oxidative dissolution of silver nanoparticles by biologically relevant oxidants: A kinetic and mechanistic study. *Chem. An Asian J.* **2010**, 5 (2), 285-293.
- [124] J. Liu, D. A. Sonshine, S. Shervani, R. H. Hurt. Controlled release of biologically active silver from nanosilver surfaces. *ACS Nano* **2010**, 4 (11), 6903-6913.
- [125] S. Pandav, J. Naik. Preparation and *in vitro* evaluation of ethylcellulose and polymethacrylate resins loaded microparticles containing hydrophilic drug. *J. Pharm.* **2014**, 2014, 904036.
- [126] S. L. P. K. Mandapalli, S. Chawla, R. Janupally, D. Sriram, V. V. K. Venuganti. Polymer-gold nanoparticle composite films for topical application: Evaluation of physical properties and antibacterial activity. *Polym. Compos.* **2015**, 38 (12), 2829-2840.
- [127] I. Machida-Sano, Y. Matsuda, H. Namiki. *In vitro* adhesion of human dermal fibroblasts on iron cross-linked alginate films. *Biomed. Mater.* **2009**, 4 (2), 025008.
- [128] H. Li, S. Liu, L. Lin. Rheological study on 3D printability of alginate hydrogel and effect of graphene oxide. *Int. J. Bioprinting.* **2016**, 2 (2), 54-66.
- [129] C. Ding, M. Zhang, G. Li. Rheological properties of collagen/hydroxypropyl methylcellulose (COL/HPMC) blended solutions. *J. Appl. Polym. Sci.* **2014**, 131 (7), 40042.
- [130] A. G. Esfahani, M. Soleimanzade, C. E. Campiglio, A. Federici, L. Altomare, L. Draghi, A. R. Boccaccini, L. De Nardo. Hierarchical microchannel architecture in chitosan/bioactive glass scaffolds via electrophoretic deposition positive-replica. *J. Biomed. Mater. Res. A.* **2019**, 107(7), 1455-1465.
- [131] J. A. Juhasz, S. M. Best. Bioactive ceramics: processing, structures and properties. *J. Mater. Sci.* **2012**, 47 (2), 610-624.
- [132] K. A. Egol, A. Nauth, M. Lee, H. C. Pape, J. T. Watson, J. J. Borrelli. Bone grafting: sourcing, timing, strategies, and alternatives. *J. Orthop. Trauma.* **2015**, 29, 10-14.
- [133] E. Fiume, J. Barberi, E. Verné, F. Baino. Bioactive glasses: From parent 45S5 composition to scaffold-assisted tissue-healing therapies. *J. Funct. Biomater.* **2018**, 9 (1), 24.
- [134] J. Venkatesan, I. Bhatnagar, P. Manivasagan, K.H. Kang, S.K. Kim. Alginate composites for bone tissue engineering: a review. *Int. J. Biol. Macromol.* **2015**, 72, 269-281.
- [135] L. L. Hench, R. J. Splinter, W. C. Allen, T. K. Greenlee. Bonding mechanisms at the interface of ceramic prosthetic materials. *J. Biomed. Mater. Res.* **1971**, 5 (6), 117-141.
- [136] M. Mačković, A. Hoppe, R. Detsch, D. Mohn, W. J. Stark, E. Spiecker, A. R. Boccaccini. Bioactive glass (type 45S5) nanoparticles: *in vitro* reactivity on nanoscale and biocompatibility. *J. Nanoparticle Res.* **2012**, 14 (7), 966.

- [137] F. Waag, B. Gökce, C. Kalapu, G. Bendt, S. Salamon, J. Landers, U. Hagemann, M. Heidelmann, S. Schulz, H. Wende, N. Hartmann, M. Behrens, S. Barcikowski. Adjusting the catalytic properties of cobalt ferrite nanoparticles by pulsed laser fragmentation in water with defined energy dose. *Sci. Rep.* **2017**, 7 (1), 13161.
- [138] T. Schmitz, U. Wiedwald, C. Dubs, B. Gökce. Ultrasmall yttrium iron garnet nanoparticles with high coercivity at low temperature synthesized by laser ablation and fragmentation of pressed powders. *Chemphyschem.* **2017**, 18 (9), 1125-1132.
- [139] M. Lau, S. Barcikowski. Quantification of mass-specific laser energy input converted into particle properties during picosecond pulsed laser fragmentation of zinc oxide and boron carbide in liquids. *Appl. Surf. Sci.* **2015**, 348, 22-29.
- [140] K. Charipar, H. Kim, A. Piqué, N. Charipar. ZnO nanoparticle/graphene hybrid photodetectors via laser fragmentation in liquid. *Nanomaterials* **2020**, 10 (9), 1648.
- [141] G. Compagnini, A. A. Scalisi, O. Puglisi. Ablation of noble metals in liquids: a method to obtain nanoparticles in a thin polymeric film. *Phys. Chem. Chem. Phys.* **2002**, 4 (12), 2787-2791.
- [142] J. Xiao, P. Liu, C. X. Wang, G. W. Yang. External field-assisted laser ablation in liquid: An efficient strategy for nanocrystal synthesis and nanostructure assembly. *Prog. Mater. Sci.* **2017**, 87, 140-220.
- [143] M. E. Povarnitsyn, T. E. Itina, P. R. Levashov, K. V. Khishchenko. Mechanisms of nanoparticle formation by ultra-short laser ablation of metals in liquid environment. *Phys. Chem. Chem. Phys.* **2013**, 9 (15), 3018-3114.
- [144] M. R. Kalus, N. Barsch, R. Streubel, E. Gokce, S. Barcikowski, B. Gokce. How persistent microbubbles shield nanoparticle productivity in laser synthesis of colloids - quantification of their volume, dwell dynamics, and gas composition. *Phys. Chem. Chem. Phys.* **2017**, 19 (10), 7112-7123.
- [145] C. Y. Shih, C. P. Wu, M. V. Shugaev, L. V. Zhigilei. Atomistic modeling of nanoparticle generation in short pulse laser ablation of thin metal films in water. *J. Colloid Interface Sci.* **2017**, 489, 3-17.
- [146] Y. Orooji, B. Jaleh, F. Homayouni, P. Fakhri, M. Kashfi, M. J. Torkamany, A. A. Yousefi. Laser ablation-assisted synthesis of Poly (Vinylidene Fluoride)/Au nanocomposites: crystalline phase and micromechanical finite element analysis. *Polymers* **2020**, 12 (11), 2630.
- [147] N. Million, V. Coger, P. Wilke, C. Rehbock, P. M. Vogt, A. Pich, S. Barcikowski. Water-based, surfactant-free cytocompatible nanoparticle-microgel-composite biomaterials - rational design by laser synthesis, processing into fiber pads and impact on cell proliferation, *BioNanoMaterials.* **2017**, 18 (3-4), 20170004.
- [148] R. Onsi, K. Easawi, S. Abdallah, S. Negm, H. Talaat. Preparation of silver nanoparticles dispersed in almond oil using laser ablation technique. *IOP Conf. Ser.: Mater. Sci. Eng.* **2020**, 762, 012005.

- [149] N. G. Semaltianos, G. Karczewski. Laser synthesis of magnetic nanoparticles in liquids and application in the fabrication of polymer-nanoparticle composites. *ACS Appl. Nano Mater.* **2021**, 4 (7), 6407-6440.
- [150] A. Schwenke, H. Dalüge, R. Kiyan, C. L. Sajti, B. N. Chichkov. Non-agglomerated gold-PMMA nanocomposites by *in situ*-stabilized laser ablation in liquid monomer for optical applications. *Appl. Phys. A* **2013**, 111 (2), 451-457.
- [151] T. X. Phuoc. Complete green synthesis of gold nanoparticles using laser ablation in deionized water containing chitosan and starch. *J. Mater. Sci. Nanotechnol.* **2014**, 2 (2), 1-7.
- [152] F. Redaelli, M. Sorbona, F. Rossi. 10-Synthesis and processing of hydrogels for medical applications, in: G. Perale, J. Hilborn (Eds.), *Bioresorbable Polymers for Biomedical Applications*. Woodhead Publishing **2017**, 205-228.
- [153] M. Mulder. Membrane separation/phase inversion membranes, in: I.D. Wilson (Ed.), *encyclopedia of separation science*. Academic Press, Oxford, **2000**, 3331-3346.
- [154] C. Kojima, Y. Narita, Y. Nakajima, N. Morimoto, T. Yoshikawa, N. Takahashi, A. Handa, T. Waku, N. Tanaka. Modulation of cell adhesion and differentiation on collagen gels by the addition of the ovalbumin secretory signal peptide. *ACS Biomater. Sci. Eng.* **2019**, 5 (11), 5698-5704.
- [155] L. Wu, H. Shao, Z. Fang, Y. Zhao, C. Y. Cao, Q. Li. Mechanism and effects of polyphenol derivatives for modifying collagen. *ACS Biomater. Sci. Eng.* **2019**, 5 (9), 4272-4284.
- [156] V. M. Gun'ko, I. N. Savina, S. V. Mikhalovsky. Properties of water bound in hydrogels. *Gels* **2017**, 3 (4), 37.
- [157] E. A. Appel, M. W. Tibbitt, M. J. Webber, B. A. Mattix, O. Veiseh, R. Langer. Self-assembled hydrogels utilizing polymer–nanoparticle interactions. *Nat. Commun.* **2015**, 6, 6295.
- [158] C. Yan, D. J. Pochan. Rheological properties of peptide-based hydrogels for biomedical and other applications. *Chem. Soc. Rev.* **2010**, 39 (9), 3528-3540.
- [159] T. R. Cox, C. D. Madsen. Relative stiffness measurements of cell-embedded hydrogels by shear rheology *in vitro*. *Bioprotocol* **2017**, 7 (1), e2101.
- [160] S. Unterman, L.F. Charles, S. E. Strecker, D. Kramarenko, D. Pivovarchik, E.R. Edelman, N. Artzi. Hydrogel nanocomposites with independently tunable rheology and mechanics. *ACS Nano* **2017**, 11 (3), 2598-2610.
- [161] A. Shakeel, H. Mahmood, U. Farooq, Z. Ullah, S. Yasin, T. Iqbal, C. Chassagne, M. Moniruzzaman. Rheology of pure ionic liquids and their complex fluids: A review. *ACS Sustain. Chem. Eng.* **2019**, 7 (16), 13586-13626.
- [162] O. Nechyporchuk, M. N. Belgacem, F. Pignon. Current progress in rheology of cellulose nanofibril suspensions. *Biomacromolecules* **2016**, 17 (7), 2311-2320.
- [163] R. Bai, B. Chen, J. Yang, Z. Suo. Tearing a hydrogel of complex rheology. *J. Mech. Phys. Solids* **2019**, 125, 749-761.

- [164] T. G. Mezger. The Rheology Handbook: For user of rotational and oscillatory rheometers. Vincentz Network GmbH, Hannover, Germany, **2006**.
- [165] M. Kim, H. Y. Song, W. J. Choi, K. Hyun. Evaluation of the degree of dispersion of polymer nanocomposites (PNCs) using nonlinear rheological properties by FT-Rheology. *Macromolecules* **2019**, 52 (22), 8604-8616.
- [166] C. Streich. Laser-synthesized bioconjugated noble metal nanoparticles - rational design and efficacy against pathological protein aggregation. Institut für Technische Chemie I, Dotocral thesis, Universität Duisburg-Essen, **2017**.
- [167] C. C. Miller, J. Walker. The Stokes-Einstein law for diffusion in solution. Proceedings of the Royal Society of London. Series A, Containing Papers of a Mathematical and Physical Character **1924**, 106 (740), 724-749.
- [168] A. A. Steiner, H. van Winden. Recipe for ferric salts of ethylenediaminetetraacetic acid. *Plant Physiol.* **1970**, 46 (6), 862.
- [169] M. Lau. Laser fragmentation and melting of particles, Faculty of Chemistry. Dotocral thesis, University of Duisburg-Essen, **2016**.
- [170] S. K. Jawad, S. M. Hameed, S. A. Hussain. Liquid ion exchange application for micro amount separation and determination of Ca(II) and Mg(II) as anions species with EDTA. *Orient J. Chem.* **2017**, 33 (5), 2421-2429.
- [171] M. M. Bradford. A rapid and sensitive method for the quantitation of microgram quantities of protein utilizing the principle of protein-dye binding. *Anal. Biochem.* **1976**, 72, 248-254.
- [172] M. Zammarano, P. H. Maupin, L. P. Sung, J. W. Gilman, E. D. McCarthy, Y. S. Kim, D. M. Fox. Revealing the interface in polymer nanocomposites. *ACS Nano* **2011**, 5 (4), 3391-3399.
- [173] W. Guan, S. Wang, C. Lu, B. Z. Tang. Fluorescence microscopy as an alternative to electron microscopy for microscale dispersion evaluation of organic-inorganic composites. *Nat. Commun.* **2016**, 7 (1), 11811.
- [174] A. V. F. T. Züchner, A. Hartschuh and A. J. Meixner. A novel approach to detect and characterize the scattering patterns of single Au nanoparticles using confocal microscopy. *J. Microsc.* **2008**, 229 (2), 337-343.
- [175] P. S. Klein S, Taylor U, Rath D, Barcikowski S. Quantitative visualization of colloidal and intracellular gold nanoparticles by confocal microscopy. *J. Biomed. Opt.* **2010**, 15 (3), 036015.
- [176] S. Mugesh, R. Arun, K. Arunkumar, M. Murugan. Synthesis of biogenic copper nanoparticles embedded in graphene oxide-chitosan composite and its anti-bacterial and cytotoxic activities. *J. Nanosci. Nanotechnol.* **2019**, 19 (5), 2625-2632.
- [177] A. Knoester, G. J. Brakenhoff. Applications of confocal microscopy in industrial solid materials: some examples and a first evaluation. *J. Microsc.* **1990**, 157 (1), 105-113.

- [178] M. Ilčíková, M. Danko, M. Doroshenko, A. Best, M. Mrlík, K. Csomorová, M. Šlouf, D. Chorvát, K. Koynov, J. Mosnáček. Visualization of carbon nanotubes dispersion in composite by using confocal laser scanning microscopy. *Eur. Polym. J.* **2016**, 79, 187-197.
- [179] J. Torrent-Burgués, F. Sanz. AFM in mode peak force applied to the study of un-worn contact lenses. *Colloids Surf. B.* **2014**, 121, 388-394.
- [180] N. Lin, J. Huang, P. R. Chang, L. Feng, J. Yu. Effect of polysaccharide nanocrystals on structure, properties, and drug release kinetics of alginate-based microspheres. *Colloids Surf. B.* **2011**, 85 (2), 270-279.
- [181] O. Catanzano, A. Soriente, A. La Gatta, M. Cammarota, G. Ricci, I. Fasolino, C. Schiraldi, L. Ambrosio, M. Malinconico, P. Laurienzo, M.G. Raucci, G. Gomez d' Ayala. Macroporous alginate foams crosslinked with strontium for bone tissue engineering. *Carbohydr. Polym.* **2018**, 202, 72-83.
- [182] N. Adrus, M. Ulbricht. Rheological studies on PNIPAAm hydrogel synthesis via *in situ* polymerization and on resulting viscoelastic properties. *React. Funct. Polym.* **2013**, 73 (1), 141-148.
- [183] J. Wang, V. M. Ugaz. Using *in situ* rheology to characterize the microstructure in photopolymerized polyacrylamide gels for DNA electrophoresis. *Electrophoresis* **2006**, 27 (17), 3349-3358.
- [184] P. Sherovski, G. Stojkovic, N. Ristovska. Development, validation and application of first derivative spectroscopy ratio method for estimation of Bradford assay. *Anal. Biochem.* **2018**, 558, 35-40.
- [185] Y. Cheng, H. Wei, R. Sun, Z. Tian, X. Zheng. Rapid method for protein quantitation by Bradford assay after elimination of the interference of polysorbate 80. *Anal. Biochem.* **2016**, 494, 37-39.
- [186] M. Bergaoui, C. Aguir, M. Khalfaoui, E. Enciso, L. Duclaux, L. Reinert, J. L. G. Fierro, New insights in the adsorption of bovine serum albumin onto carbon nanoparticles derived from organic resin: Experimental and theoretical studies. *Microporous Mesoporous Mater.* **2017**, 241, 418-428.
- [187] D. F. Duarte Campos, A. Blaeser, M. Weber, J. Jäkel, S. Neuss, W. Jahnen-Dechent, H. Fischer. Three-dimensional printing of stem cell-laden hydrogels submerged in a hydrophobic high-density fluid. *Biofabrication* **2012**, 5 (1), 015003.
- [188] A. Blaeser, D. F. Duarte Campos, M. Weber, S. Neuss, B. Theek, H. Fischer, W. Jahnen-Dechen. Biofabrication under fluorocarbon: A novel freeform fabrication technique to generate high aspect ratio tissue-engineered constructs. *BioResearch Open Access* **2013**, 2 (5), 374-384.
- [189] S. Lau, D. Eicke, M. Carvalho Oliveira, B. Wiegmann, C. Schrimpf, A. Haverich, R. Blasczyk, M. Wilhelmi, C. Figueiredo, U. Boer. Low immunogenic endothelial cells maintain morphological and functional properties required for vascular tissue engineering. *Tissue Eng. Part A* **2018**, 24 (5-6), 432-447.

- [190] S. Kohsakowski, F. Seiser, J. P. Wiederrecht, S. Reichenberger, T. Vinnay, S. Barcikowski, G. Marzun. Effective size separation of laser-generated, surfactant-free nanoparticles by continuous centrifugation. *Nanotechnology* **2019**, 31 (9), 095603.
- [191] R. Streubel, G. Bendt, B. Gokce. Pilot-scale synthesis of metal nanoparticles by high-speed pulsed laser ablation in liquids. *Nanotechnology* **2016**, 27 (20), 205602.
- [192] S. Dittrich, R. Streubel, C. McDonnell, H. P. Huber, S. Barcikowski, B. Gökce. Comparison of the productivity and ablation efficiency of different laser classes for laser ablation of gold in water and air. *Appl. Phys. A* **2019**, 125 (6), 432.
- [193] F. Waag, R. Streubel, B. Gökce, S. Barcikowski. Synthesis of gold, platinum, and gold-platinum alloy nanoparticle colloids with high-power megahertz-repetition-rate lasers: the importance of the beam guidance method. *Appl. Nanosci.* **2021**, 11, 1303-1312.
- [194] N. G. Semaltianos. Nanoparticles by laser ablation of bulk target materials in liquids. in: M. Aliofkhazraei (Ed.), Handbook of Nanoparticles, *Springer International Publishing*, **2015**, 1-22.
- [195] A. S. Raut, D.S . Kalonia. Pharmaceutical perspective on opalescence and liquid–liquid phase separation in protein solutions. *Mol. Pharm.* **2016**, 13 (5), 1431-1444.
- [196] W. S. M. Werner, K. Glantschnig, C. Ambrosch-Draxl. Optical constants and inelastic electron-scattering data for 17 elemental metals. *J. Phys. Chem. Ref. Data* **2009**, 38 (4), 1013-1092.
- [197] N. Sasithorn, L. Martinová. Fabrication of silk nanofibres with needle and roller electrospinning methods. *J. Nanomater.* **2014**, 2014, 947315.
- [198] V. Singh, K. Kumari. Some physicochemical measurements of chitosan/starch polymers in acetic acid-water mixtures. *Macromol. Symp.* **2012**, 320 (1), 81-86.
- [199] V. Amendola, P. Riello, M. Meneghetti. Magnetic nanoparticles of iron carbide, iron oxide, iron@iron oxide, and metal iron synthesized by laser ablation in organic solvents. *J. Phys. Chem. C* **2011**, 115 (12), 5140-5146.
- [200] T. Hoang, K. Ramadass, T. T. Loc, T. T. Mai, L. D. Giang, V. V. Thang, T. M. Tuan, N. T. Chinh. Novel drug delivery system based on ginsenoside Rb1 loaded to chitosan/alginate nanocomposite films. *J. Nanosci. Nanotechnol.* **2019**, 19 (6), 3293-3300.
- [201] R. Noreen, M. Moenner, Y. Hwu, C. Petibois. FTIR spectro-imaging of collagens for characterization and grading of gliomas. *Biotechnol. Adv.* **2012**, 30 (6), 1432-1446.
- [202] A. Orza, O. Soritau, L. Olenic, M. Diudea, A. Florea, D. Rus Ciuca, C. Mihiu, D. Casciano, A. S. Biris. Electrically conductive gold-coated collagen nanofibers for placental-derived mesenchymal stem cells enhanced differentiation and proliferation. *ACS Nano* **2011**, 5(6), 4490-4503.
- [203] S. Saha, A. Pal, S. Kundu, S. Basu, T. Pal. Photochemical green synthesis of calcium-alginate-stabilized Ag and Au nanoparticles and their catalytic application to 4-Nitrophenol reduction. *Langmuir* **2010**, 26 (4), 2885-2893.

- [204] V. Amendola, S. Polizzi, M. Meneghetti. Laser ablation synthesis of gold nanoparticles in organic solvents. *J. Phys. Chem. B* **2006**, 110 (14), 7232-7237.
- [205] D. M. Lentz, A. M. Rhoades, R. A. Pyles, K. W. Haider, M. S. Angelone, R. C. Hedden, Combinatorial study of a gold nanoparticle infusion process in a polymer film. *J. Nanoparticle Res.* **2011**, 13 (10), 4795-4808.
- [206] H. Yao, Y. Ishikawa. Finite size effect on magneto-optical responses of chemically modified Fe₃O₄ nanoparticles studied by MCD spectroscopy. *J. Phys. Chem. C* **2015**, 119 (23), 13224-13230.
- [207] M. Kalyva, G. Bertoni, A. Milionis, R. Cingolani, A. Athanassiou. Tuning of the characteristics of Au nanoparticles produced by solid target laser ablation into water by changing the irradiation parameters. *Microsc. Res. Tech.* **2010**, 73 (10), 937-943.
- [208] N. T. K. Thanh, N. Maclean, S. Mahiddine. Mechanisms of nucleation and growth of nanoparticles in solution. *Chem. Rev.* **2014**, 114 (15), 7610-7630.
- [209] C. Dannert, B. T. Stokke, R. S. Dias. Nanoparticle-hydrogel composites: From molecular interactions to macroscopic behavior. *Polymers* **2019**, 11 (2), 275.
- [210] T. Fischer, A. Hayn, C. T. Mierke. Fast and reliable advanced two-step pore-size analysis of biomimetic 3D extracellular matrix scaffolds. *Sci. Rep.* **2019**, 9 (1), 8352.
- [211] V. Thomas, M. Namdeo, Y. Murali Mohan, S. K. Bajpai, M. Bajpai. Review on polymer, hydrogel and microgel metal nanocomposites: A facile nanotechnological approach. *J. Macromol. Sci. Part A* **2007**, 45 (1), 107-119.
- [212] E. M. Ahmed, F. S. Aggor. Swelling kinetic study and characterization of crosslinked hydrogels containing silver nanoparticles. *J. Appl. Polym. Sci.* **2010**, 117 (4), 2168-2174.
- [213] A. Sergeeva, A. S. Vikulina, D. Volodkin. Porous alginate scaffolds assembled using vaterite CaCO₃ crystals. *Micromachines (Basel)* **2019**, 10(6), 357.
- [214] E. N. Sowa-Söhle, A. Schwenke, P. Wagener, A. Weiss, H. Wiegel, C. L. Sajti, A. Haverich, S. Barcikowski, A. Loos. Antimicrobial efficacy, cytotoxicity, and ion release of mixed metal (Ag, Cu, Zn, Mg) nanoparticle polymer composite implant material. *BioNanoMaterials* **2013**, 14 (3-4), 217-227.
- [215] D. X. Zhang, C. Yoshikawa, N. G. Welch, P. Pasic, H. Thissen, N. H. Voelcker. Spatially controlled surface modification of porous silicon for sustained drug delivery applications. *Sci. Rep.* **2019**, 9 (1), 1367.
- [216] I. Rodushkin, A. Stenberg, H. Andrén, D. Malinovsky, D.C. Baxter. Isotopic fractionation during diffusion of transition metal ions in solution. *Anal. Chem.* **2004**, 76 (7), 2148-2151.
- [217] W. M. Haynes. CRC Handbook of Chemistry and Physics., 93 ed., CRC press **2012-2013**.
- [218] E. Stricker, Z. Adler, J. Wainright, R. Savinell. Diffusion coefficients of cuprous and cupric ions in electrolytes with high concentrations of bromide ions. *J. Chem. Eng. Data* **2019**, 64 (3), 1095-1100.

- [219] D. Zhang, Z. Ma, M. Spasova, A.E. Yelsukova, S. Lu, M. Farle, U. Wiedwald, B. Gökce. Formation mechanism of laser-synthesized iron-manganese alloy nanoparticles, manganese oxide nanosheets and nanofibers. *Part. Part. Syst. Charact.* **2017**, 34 (3), 1600225.
- [220] V. Amendola, D. Amans, Y. Ishikawa, N. Koshizaki, S. Scirè, G. Compagnini, S. Reichenberger, S. Barcikowski. Room-temperature laser synthesis in liquid of oxide, metal-oxide core-shells, and doped oxide nanoparticles. *Chem. Eur. J.* **2020**, 26 (42), 9206-9242.
- [221] A. De Bonis, T. Lovaglio, A. Galasso, A. Santagata, R. Teghil. Iron and iron oxide nanoparticles obtained by ultra-short laser ablation in liquid. *Appl. Surf. Sci.* **2015**, 353, 433-438.
- [222] P. Sundarrajan, P. Eswaran, A. Marimuthu, L. B. Subhadra, P. Kannaiyan. One pot synthesis and characterization of alginate stabilized semiconductor nanoparticles. *Bull. Korean Chem. Soc.* **2012**, 33 (10), 3218-3224.
- [223] I. A. Mudunkotuwa, T. Rupasinghe, C. M. Wu, V. H. Grassian. Dissolution of ZnO nanoparticles at circumneutral pH: A study of size effects in the presence and absence of citric acid. *Langmuir* **2012**, 28 (1), 396-403.
- [224] M. M. Benjamin. Water Chemistry, 1st ed., McGraw-HillCompanies, New York, **2002**.
- [225] Y. K. Y Idota, T. Kato, K. Yano, H. Arakawa, C. Miyajima, F. Kasahara, and T. Ogihara. Relationship between physical parameters of various metal ions and binding affinity for alginate. *Biol. Pharm. Bull* **2016**, 39 (11), 1893-1896.
- [226] Y. L. Lai, M. Thirumavalavan, J. F. Lee. Effective adsorption of heavy metal ions (Cu^{2+} , Pb^{2+} , Zn^{2+}) from aqueous solution by immobilization of adsorbents on Ca-alginate beads. *Toxicol. Environ. Chem.* **2010**, 92 (4), 697-705.
- [227] Y. Jodra, F. Mijangos. Ion exchange selectivities of calcium alginate gels for heavy metals. *Water Sci. Technol.* **2001**, 43 (2), 237-244.
- [228] T. S. Pathak, J. H. Yun, J. Lee, K. J. Paeng. Effect of calcium ion (cross-linker) concentration on porosity, surface morphology and thermal behavior of calcium alginates prepared from algae (*Undaria pinnatifida*). *Carbohydr. Polym.* **2010**, 81 (3), 633-639.
- [229] A. L. Andrade, J. M. F. Ferreira, R. Z. Domingues. Zeta potential measurement in bioactive collagen. *Mater.s Res.* **2004**, 7 (4), 631-634.
- [230] W. Norde. Adsorption of proteins from solution at the solid-liquid interface. *Adv. Colloid Interface Sci.* **1986**, 25, 267-340.
- [231] C. A. Amo, R. Garcia. Fundamental high-speed limits in single-molecule, single-cell, and nanoscale force spectroscopies. *ACS Nano* **2016**, 10 (7), 7117-7124.
- [232] H. Z. D Lee, and S. J Ryu. Elastic modulus measurement of hydrogels. M.I.H. Mondal (Ed.), *Springer International Publishing AG* **2018**.
- [233] S. Tan, J. Y . Fang, Z. Yang, M. E. Nimni, B. Han. The synergetic effect of hydrogel stiffness and growth factor on osteogenic differentiation. *Biomaterials* **2014**, 35 (20), 5294-5306.

- [234] C. Abadías, C. Serés, J. Torrent-Burgués. AFM in peak force mode applied to worn siloxane-hydrogel contact lenses. *Colloids Surf. B.* **2015**, 128, 61-66.
- [235] R. Kocen, M. Gasik, A. Gantar, S. Novak. Viscoelastic behaviour of hydrogel-based composites for tissue engineering under mechanical load. *Biomed. Mater.* **2017**, 12 (2), 025004.
- [236] A. L. Weisenhorn, M. Khorsandi, S. Kasas, V. Gotzos, H. J. Butt. Deformation and height anomaly of soft surfaces studied with an AFM. *Nanotechnology* **1993**, 4 (2), 106-113.
- [237] H. L. Cebull, J. M. Stukel, R. Willits. Developing AFM techniques for testing PEG hydrogels. *Honors Research Projects* **2017**, 447.
- [238] S. Janel, M. Popoff, N. Barois, E. Werkmeister, S. Divoux, F. Perez, F. Lafont. Stiffness tomography of eukaryotic intracellular compartments by atomic force microscopy. *Nanoscale* **2019**, 11 (21), 10320-10328.
- [239] C. J. van Oss. Surface properties of fibrinogen and fibrin. *J. Protein Chem.* **1990**, 9 (4), 487-491.
- [240] M. Bialkower, H. McLiesh, C. A. Manderson, R. F. Tabor, G. Garnier. Rapid paper diagnostic for plasma fibrinogen concentration. *Analyst* **2019**, 144 (16), 4848-4857.
- [241] P. C. Georges, P. A. Janmey. Cell type-specific response to growth on soft materials. *J. Appl. Physiol.* **2005**, 98 (4), 1547-1553.
- [242] D. E. Discher, P. Janmey, Y. L. Wang. Tissue cells feel and respond to the stiffness of their substrate. *Science* **2005**, 310 (5751), 1139-1143.
- [243] H. Zhang, H. Chang, L. M. Wang, K. F. Ren, M. C. L. Martins, M. R. A. Barbosa, J. Ji. Effect of polyelectrolyte film stiffness on endothelial cells during endothelial-to-mesenchymal transition. *Biomacromolecules* **2015**, 16 (11), 3584-3593.
- [244] S. M. Frisch, H. Francis. Disruption of epithelial cell-matrix interactions induces apoptosis. *J. Cell Bio.* **1994**, 124 (4), 619-626.
- [245] A. Henschen. On the structure of functional sites in fibrinogen. *Thromb. Res. Suppl.* **1983**, 5, 27-39.
- [246] S. Yakovlev, I. Mikhailenko, G. Tsurupa, A. M. Belkin, L. Medved. Polymerisation of fibrin alphaC-domains promotes endothelial cell migration and proliferation. *Thromb. Haemost.* **2014**, 112 (6), 1244-1251.
- [247] A. M. Belkin, G. Tsurupa, E. Zemskov, Y. Veklich, J. W. Weisel, L. Medved. Transglutaminase-mediated oligomerization of the fibrin(ogen) alphaC domains promotes integrin-dependent cell adhesion and signaling. *Blood* **2005**, 105 (9), 3561-3568.
- [248] M. Holmberg, X. Hou. Competitive protein adsorption-multilayer adsorption and surface induced protein aggregation. *Langmuir* **2009**, 25 (4), 2081-2089.
- [249] T. Cedervall, I. Lynch, S. Lindman, T. Berggard, E. Thulin, H. Nilsson, K. A. Dawson, S. Linse. Understanding the nanoparticle-protein corona using methods to quantify exchange rates and affinities of proteins for nanoparticles. *PNAS* **2007**, 104 (7), 2050-2055.

- [250] J. D. Humphries, M. R. Chastney, J. A. Askari, M. J. Humphries. Signal transduction via integrin adhesion complexes. *Curr. Opin. Cell Biol.* **2019**, 56, 14-21.
- [251] M. Achilli, D. Mantovani. Tailoring mechanical properties of collagen-based scaffolds for vascular tissue engineering: The effects of pH, temperature and ionic strength on gelation. *Polymers* **2010**, 2 (4), 664-680.
- [252] S. H. Hsu, H. J. Yen, C. L. Tsai. The response of articular chondrocytes to type II collagen-Au nanocomposites. *Artif. Organs* **2007**, 31 (12), 854-868.
- [253] N. Rezaei, A. Lyons, N. R. Forde. Nano-mechanical studies of collagen: The influence of ionic strength, pH and collagen sources on molecular flexibility. *Biophys. J.* **2017**, 112 (3, Supplement 1), 488a.
- [254] B. A. Roeder, K. Kokini, J. E. Sturgis, J. P. Robinson, S. L. Voytik-Harbin. Tensile mechanical properties of three-dimensional type I collagen extracellular matrices with varied microstructure. *J. Biomecha. Eng.* **2002**, 124 (2), 214-222.
- [255] G. C. Wood, M. K. Keech. The formation of fibrils from collagen solutions. 1. The effect of experimental conditions: kinetic and electron-microscope studies. *Biochem. J.* **1960**, 75 (3), 588-598.
- [256] N. Diamantides, L. Wang, T. Pruiksma, J. Siemiatkoski, C. Dugopolski, S. Shortkroff, S. Kennedy, L. J. Bonassar. Correlating rheological properties and printability of collagen bioinks: the effects of riboflavin photocrosslinking and pH. *Biofabrication* **2017**, 9 (3), 034102.
- [257] K. E. Rasmussen, J. Albrechtsen. Glutaraldehyde. The influence of pH, temperature, and buffering on the polymerization rate. *Histochemistry* **1974**, 38 (1), 19-26.
- [258] K. K. Moncal, V. Ozbolat, P. Datta, D.N. Heo, I.T. Ozbolat. Thermally-controlled extrusion-based bioprinting of collagen. *J. Mater. Sci.: Mater. Med.* **2019**, 30 (5), 55.
- [259] J. Schurz, G. Erk, W. Schempp, V. Ribitsch. Zeta potential as an analytical tool for graft copolymers and for polymer surfaces. *J. Macromol. Sci.: Part A Chem.* **1990**, 27 (13-14), 1673-1692.
- [260] M. F. Cuddy, A. R. Poda, L. N. Brantley. Determination of isoelectric points and the role of pH for common quartz crystal microbalance sensors. *ACS Appl. Mater. Interfaces* **2013**, 5 (9), 3514-3518.
- [261] S. Chng, M. G. Moloney, L. Y. L. Wu. Photochromic materials by postpolymerisation surface modification. *ACS Omega* **2018**, 3 (11), 15554-15565.
- [262] M. Nakamura, A. Oyane, Y. Shimizu, S. Miyata, A. Saeki, H. Miyaji. Physicochemical fabrication of antibacterial calcium phosphate submicrospheres with dispersed silver nanoparticles via coprecipitation and photoreduction under laser irradiation. *Acta Biomater.* **2016**, 46, 299-307.
- [263] A. R. Ziefuß, S. Barcikowski, C. Rehbock. Synergism between specific Halide anions and pH effects during nanosecond laser fragmentation of ligand-free gold nanoparticles. *Langmuir* **2019**, 35 (20), 6630-6639.

- [264] S. Ahmad, G. S. Rao. EDTA: An alternative spectrophotometric reagent for iron estimation. *J. Anal. Toxicol.* **1997**, 21 (2), 172-173.
- [265] M. Torras, C. Moya, G. A. Pasquevich, A. Roig. Accurate iron quantification in colloids and nanocomposites by a simple UV-Vis protocol. *Microchim. Acta* **2020**, 187 (9), 488.
- [266] S. K. Nandi, A. Mahato, B. Kundu, P. Mukherjee. Doped bioactive glass materials in bone regeneration. *Adv. Tech. Bone Regeneration* **2016**, 275-289.
- [267] S. Corsello, A. Fulgenzi, D. Vietti, M. E. Ferrero. The usefulness of chelation therapy for the remission of symptoms caused by previous treatment with mercury-containing pharmaceuticals: a case report. *Cases J.* **2009**, 2 (199), 1757-1626.
- [268] E. A. Aguilar-Reyes, C. A. León-Patiño, E. Villicaña-Molina, V. I. Macías-Andrés, L. P. Lefebvre. Processing and *in vitro* bioactivity of high-strength 45S5 glass-ceramic scaffolds for bone regeneration. *Ceram. Int.* **2017**, 43 (9), 6868-6875.
- [269] A. Baranowska, M. Leśniak, M. Kochanowicz, J. Żmojda, P. Miluski, D. Dorosz. Crystallization kinetics and structural properties of the 45S5 bioactive glass and glass-ceramic fiber doped with Eu^{3+} . *Materials* **2020**, 13 (6), 1281.
- [270] B. Marelli, C. E. Ghezzi, J. E. Barralet, A. R. Boccaccini, S. N. Nazhat. Three-dimensional mineralization of dense nanofibrillar collagen-bioglass hybrid scaffolds. *Biomacromolecules* **2010**, 11 (6), 1470-1479.
- [271] N. G. Semaltianos. Nanoparticles by laser ablation. *Crit. Rev. Solid State Mater. Sci.* **2010**, 35 (2), 105-124.
- [272] L. Souza, J. H. Lopes, D. Encarnação, I. O. Mazali, R. A. Martin, J. A. Camilli, C. A. Bertran. Comprehensive *in vitro* and *in vivo* studies of novel melt-derived Nb-substituted 45S5 bioglass reveal its enhanced bioactive properties for bone healing. *Sci. Rep.* **2018**, 8 (1), 12808.
- [273] P. Sepulveda, J. R. Jones, L. L. Hench. *In vitro* dissolution of melt-derived 45S5 and sol-gel derived 58S bioactive glasses. *J. Biomed. Mater. Res.* **2002**, 61 (2), 301-311.
- [274] M. Arango-Ospina, L. Hupa, A. R. Boccaccini. Bioactivity and dissolution behavior of boron-containing bioactive glasses under static and dynamic conditions in different media. *Biomed. Glas.* **2019**, 5 (1), 124-139.
- [275] K. E. Wallace, R. G. Hill, J. T. Pembroke, C. J. Brown, P. V. Brown. Influence of sodium oxide content on bioactive glass properties. *J. Mater. Sci.: Mater. Med.* **1999**, 10, 697-701.
- [276] X. Chen, D. S. Brauer, R. M. Wilson, R. V. Law, R. G. Hill, N. Karpukhina. Sodium is not essential for high bioactivity of glasses. *Int. J. Appl. Glass Sci.* **2017**, 8 (4), 428-437.
- [277] S. Barber-Zucker, B. Shaanan, R. Zarivach. Transition metal binding selectivity in proteins and its correlation with the phylogenomic classification of the cation diffusion facilitator protein family. *Sci Rep.* **2017**, 7, 16381.
- [278] M. Galluzzi, S. L. Tang, C. S. Biswas, J. L. Zhao, S. G. Chen, F. J. Stadler. Atomic force microscopy methodology and AFMech Suite software for nanomechanics on heterogeneous soft materials. *Nat. Commun.* **2018**, 9, 3584.

[279] C. Rehbock, V. Merk, L. Gamrad, R. Streubel, S. Barcikowski. Size control of laser-fabricated surfactant-free gold nanoparticles with highly diluted electrolytes and their subsequent bioconjugation. *Phys. Chem. Chem. Phys.* **2013**, 15 (9), 3057-3067.

9 Appendix

9.1 Supporting information

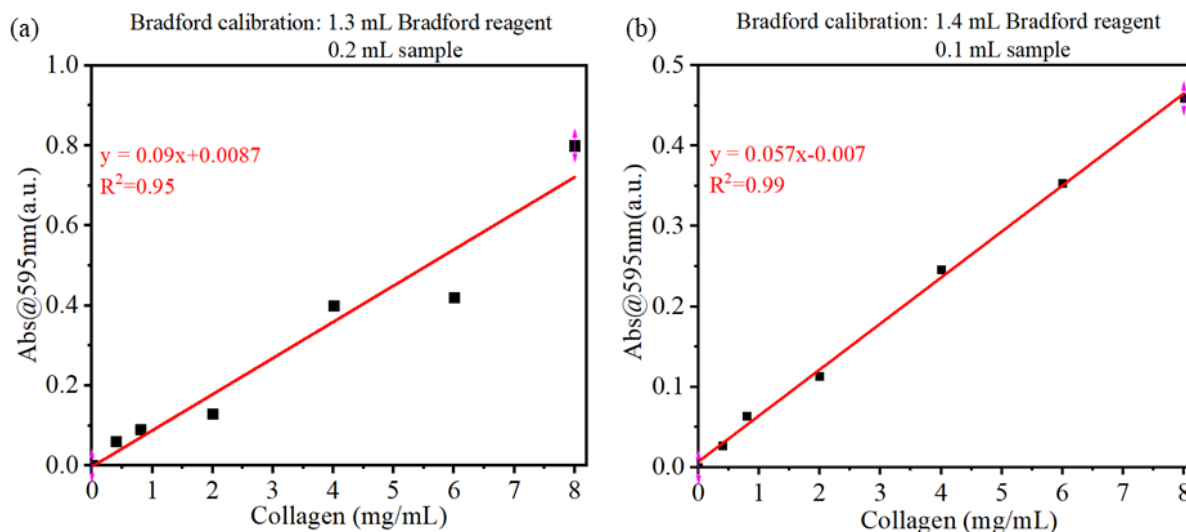


Figure S1: Calibration line of Bradford assay to determine unknown collagen concentration. (a) Bradford reagent and collagen are 1.3 mL and 0.2 mL. (b) Bradford reagent and collagen are 1.4 mL and 0.1 mL.

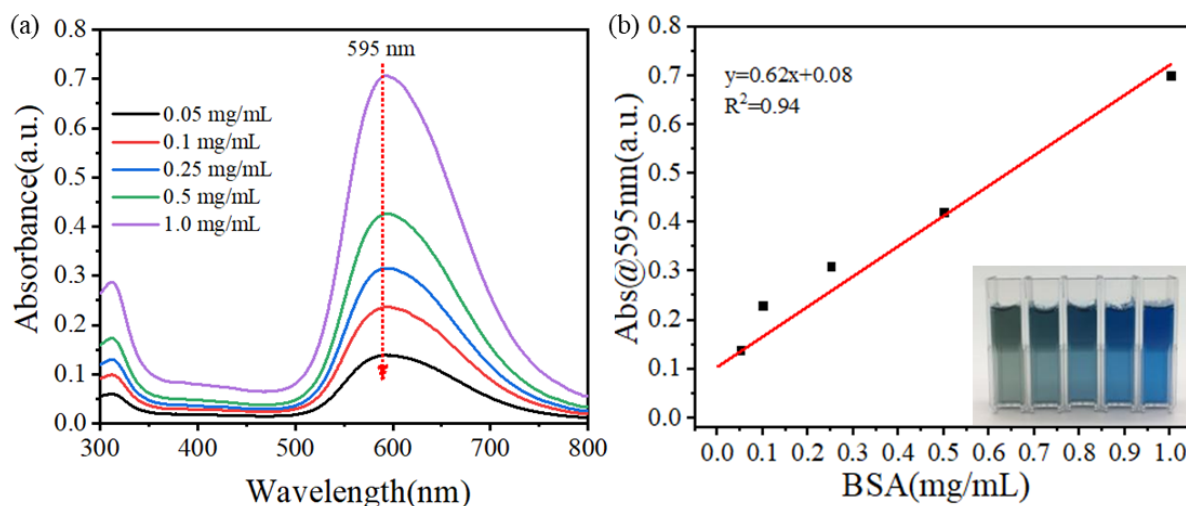


Figure S2: Calibration curves (b) for standard BSA protein plotted from the absorbance at 595 nm of UV-Vis spectra (a). This calibration line is to calculate the unknown protein concentrations.

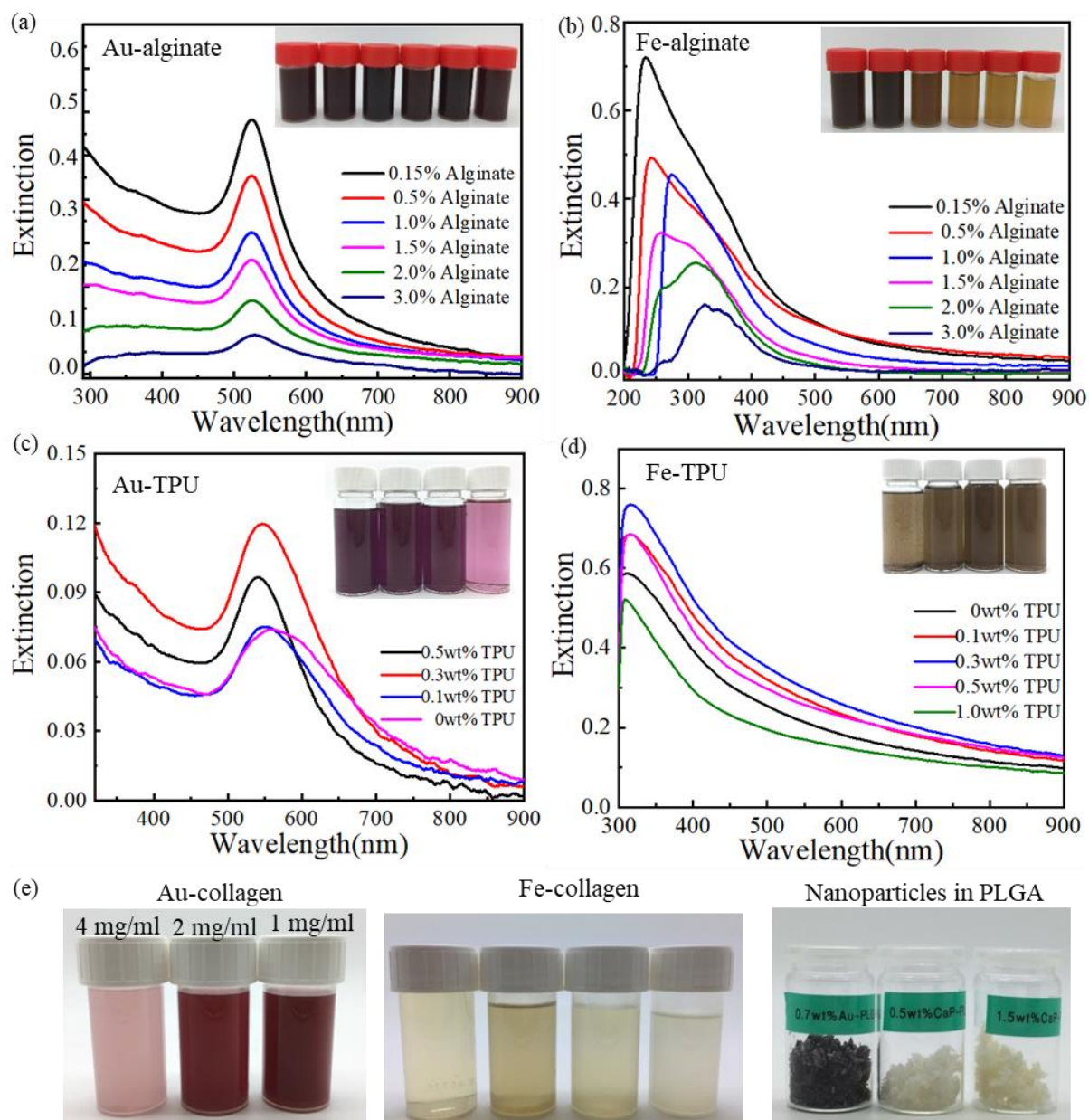


Figure S3: (a-d) UV-Vis spectra of nanoparticle-alginate, nanoparticle-TPU composites solutions; (e) Digital photographs of laser-ablated nanoparticles in collagen and PLGA polymers.

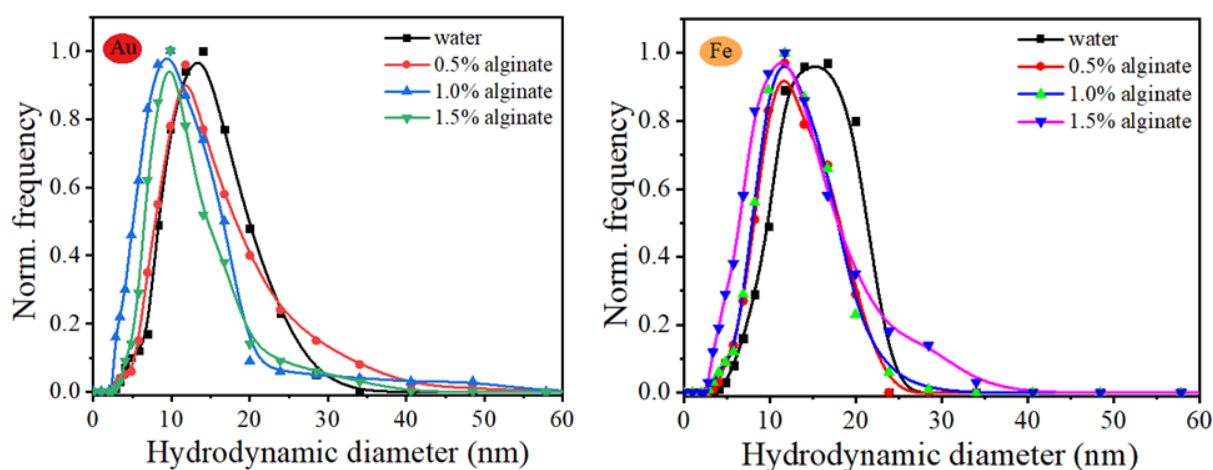


Figure S4: Dynamic light scattering (DLS) analysis of laser-generated Au and Fe in the various alginate solutions. The calculated surface-distributed particle size was summarized.

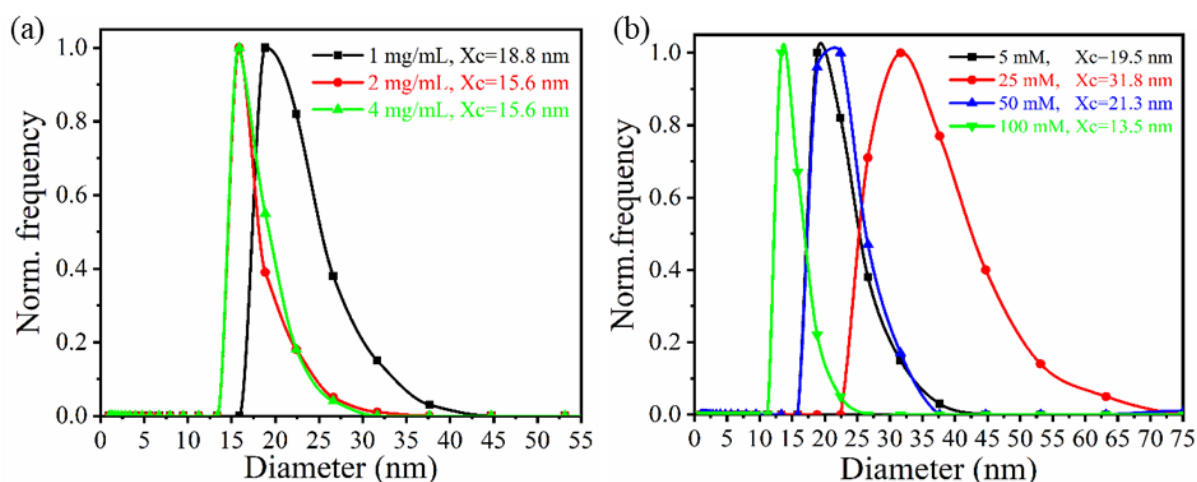


Figure S5: Dynamic light scattering (DLS) analysis of Au collagen composites generated as the variation of collagen amounts (a) and acetic acid concentrations (b). Number-weighted distributions was used here.

Characterization of Au/Fe nanoparticles in collagen solutions

SPR peak of different solutions is constant at 526 nm in varying acetic acid concentrations (Figure S6c). Primary-particle-index (PPI) was firstly proposed by Rehbock *et al.* and defined as the ratio of interband absorption at $\lambda = 380$ nm and the scattering signal of aggregates, agglomerates and larger particles at $\lambda = 800$ nm to quantify the degree of aggregation of the NPs [279]. The PPI is by far largest at 100 mM acetic acid (about 10). In the range of pH 5-10, the PPI value increased with the increasing pH contributing to the decreased aggregation and enhanced stability of the examined Au colloids [279]. When collagen concentrations went

higher which affected UV-Vis spectra and PPI value is not suitable to evaluate particles' stability any longer.

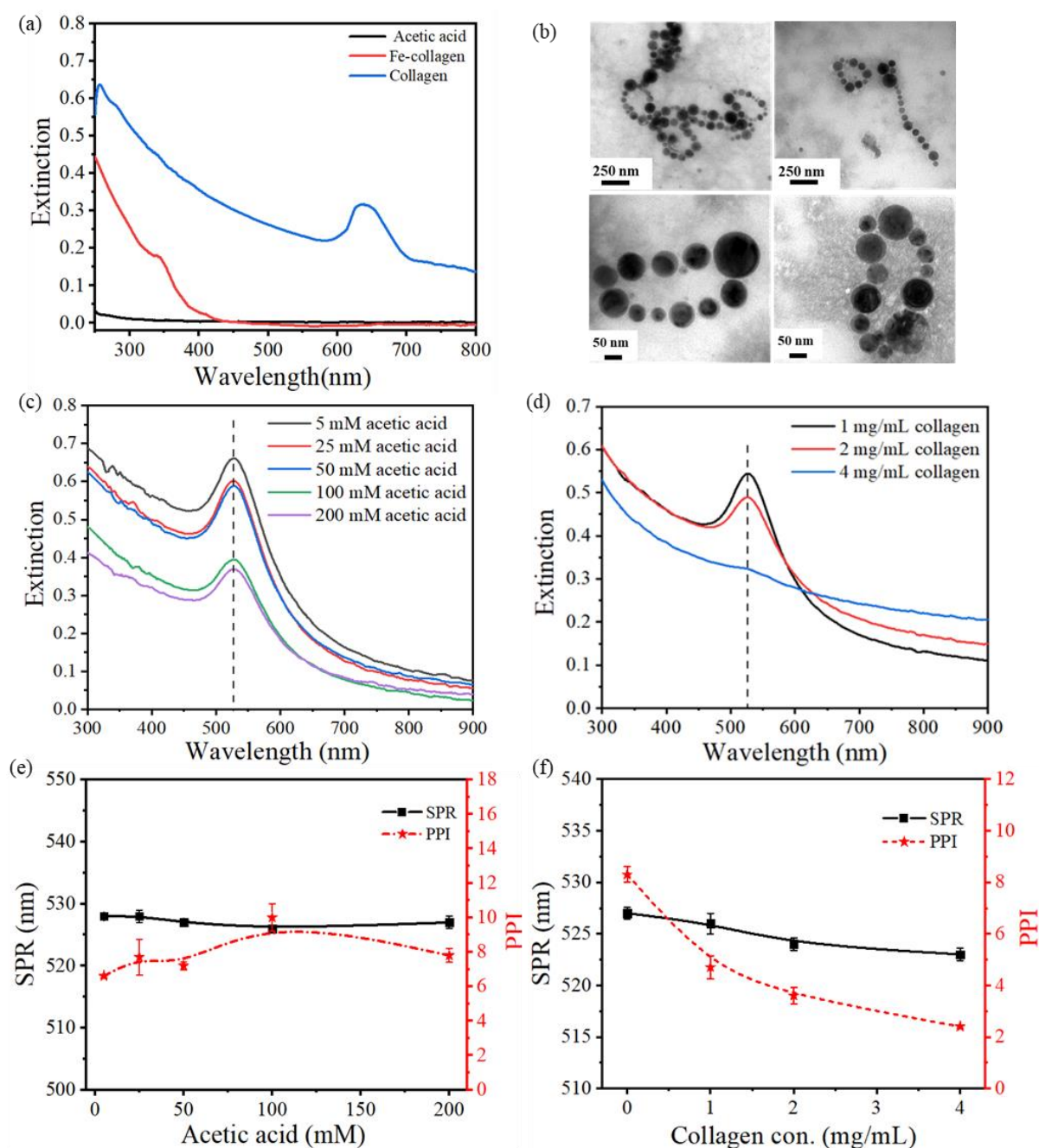


Figure S6: (a) UV-Vis spectra of Fe-collagen composites, (b) representative TEM images of FeNPs laser generated in collagen solutions; UV-Vis spectra of Au-collagen composite solutions as a function of acetic acid (c) and collagen concentration(d); Primary particle index (PPI), maximum SPR peaks as a function of acetic acid (e) and collagen concentration (f).

Confocal images of Au/Fe nanoparticles in collagen gels

Similar to the alginate hydrogels, there are also AuNP agglomerates in collagen composites. The detectable Fe signals are weaker compared to AuNPs. Moreover, in the fluorescence mode, AuNPs can be also observed as shown by circles in Figure S7c. However, it is impossible to measure FeNPs in fluorescence mode. This may not only due to the surface plasmon resonance of AuNPs but also the weak Fe signals.

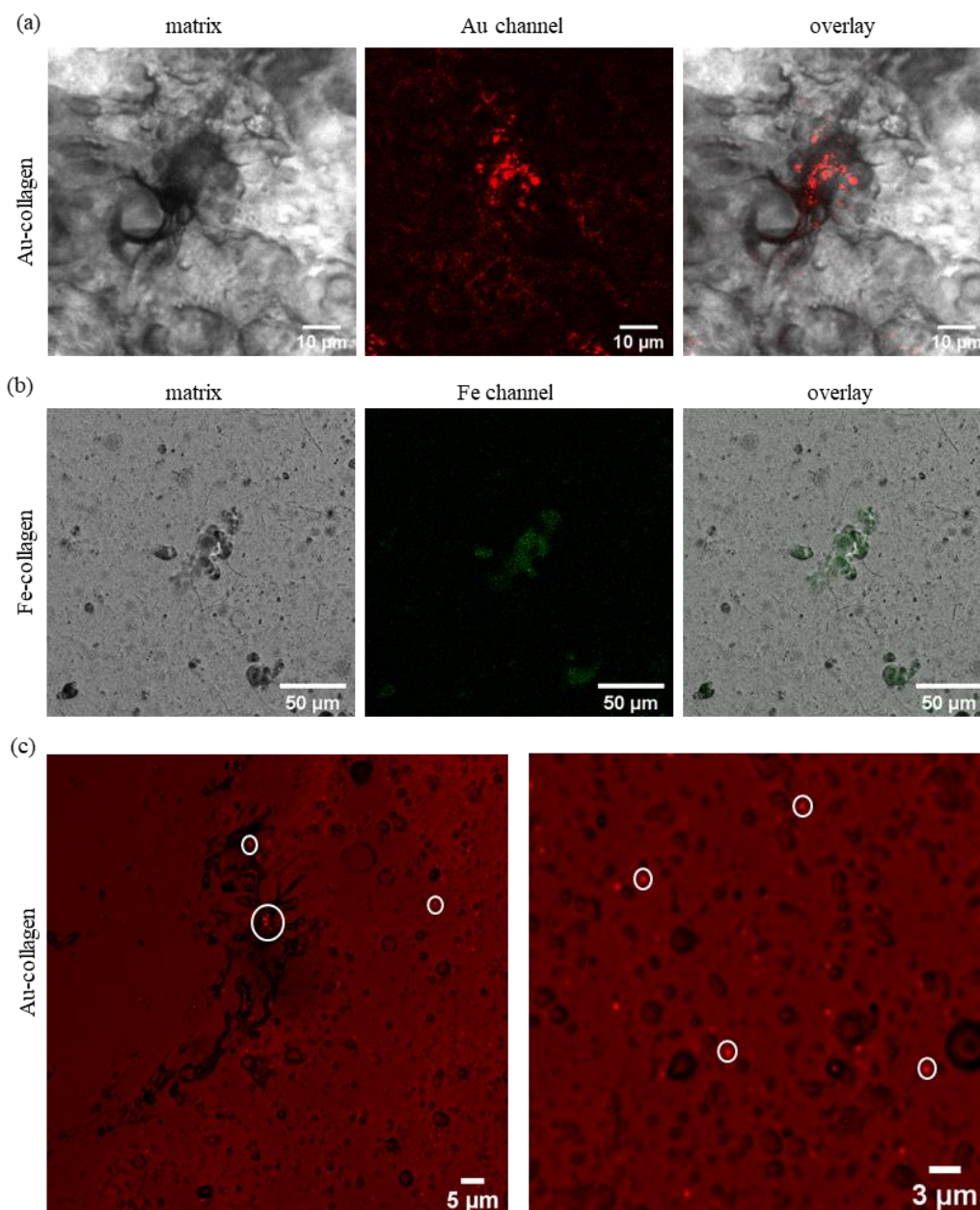


Figure S7: Confocal microscopy images of gelled Au-collagen (a), Fe-collagen composite gels (b) measured in reflection mode, and observed Au-collagen gels in fluorescence mode (c).

Damping factor ($\tan\delta$) of Au/Fe nanoparticles alginate hydrogels

Samples in Figure S8a, b were cross-linked with 25 mg/mL CaCl_2 solution. It seemed that the embedding of Au or FeNPs significantly affected the damping factor of pure alginate but not their quantity. In contrast, this value climbed up with increasing Ca^{2+} concentration. It is predicted that the concentrations of cross linkers have influences on the printing quality, more than that of nanoparticle loadings in alginate [128].

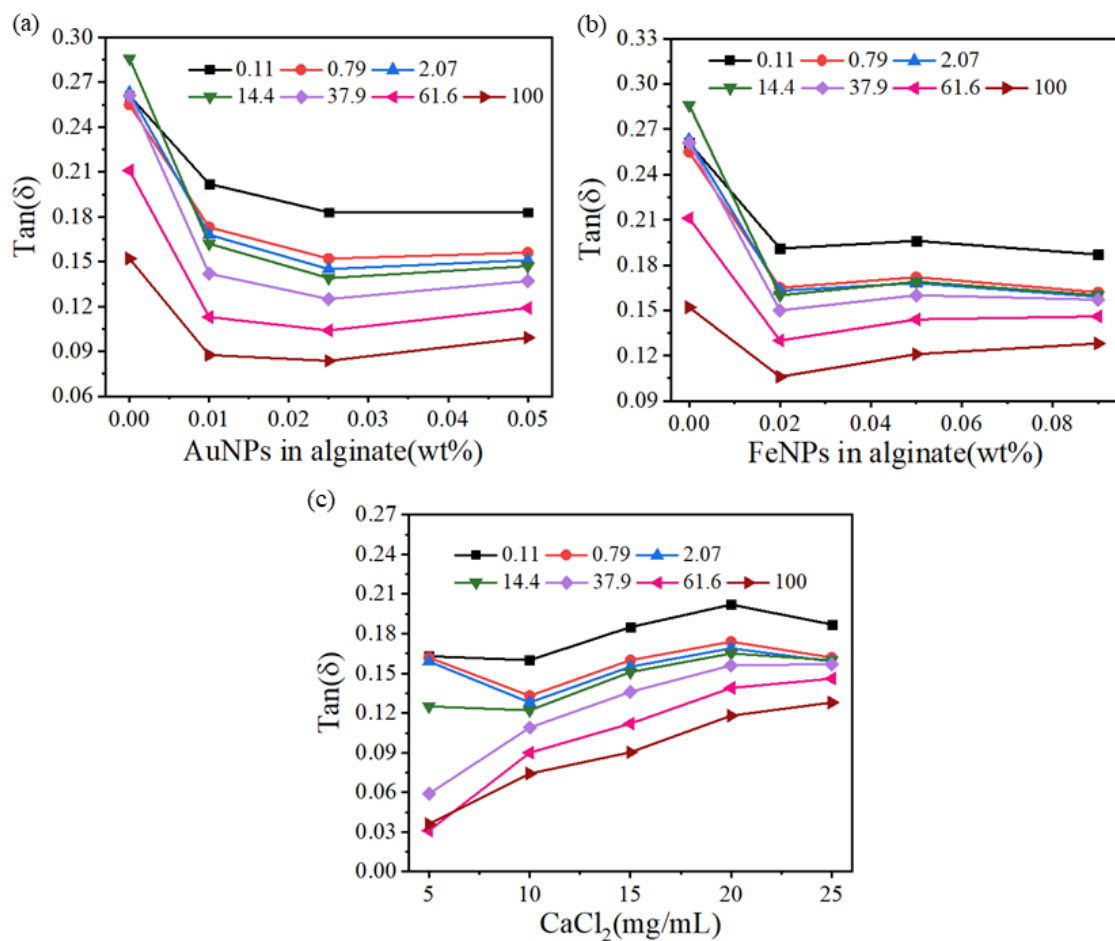


Figure S8: Dependence of $\tan\delta$ of alginate, Au-alginate (a), Fe-alginate (b), and Fe-alginate cross-link with various CaCl_2 solutions (c) at different angular frequencies in rad/s.

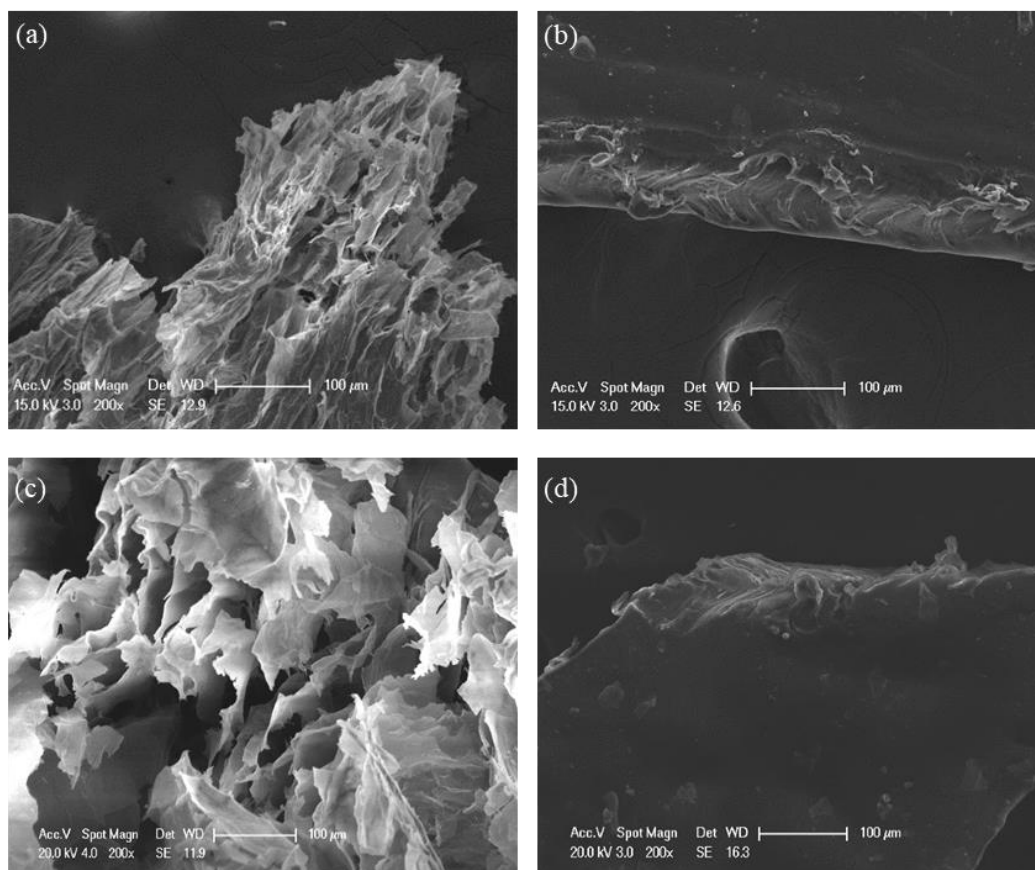


Figure S9: SEM images of alginate (a), TPU (b), Fe-alginate (c), and Fe-TPU (d). The microstructure of samples was characterized by scanning electron microscopy.

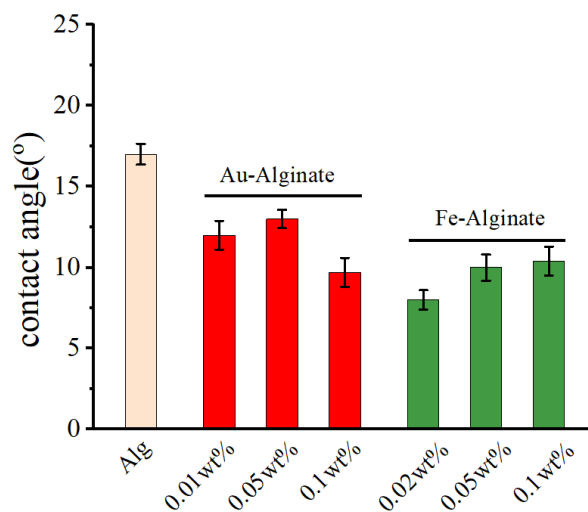


Figure S10: Water contact angles of different loadings of Au and Fe nanoparticles in alginate.

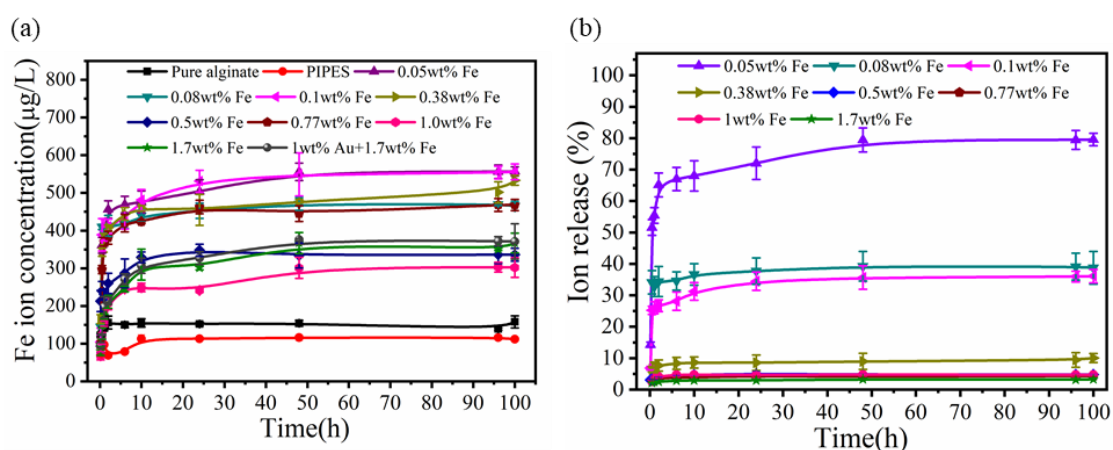


Figure S11: Long-term Fe ion release kinetics in the air-saturated buffer: (a) released Fe ion concentration of Fe-alginate composites and the controls, (b) released mass percent of different Fe nanoparticles amount in alginate.

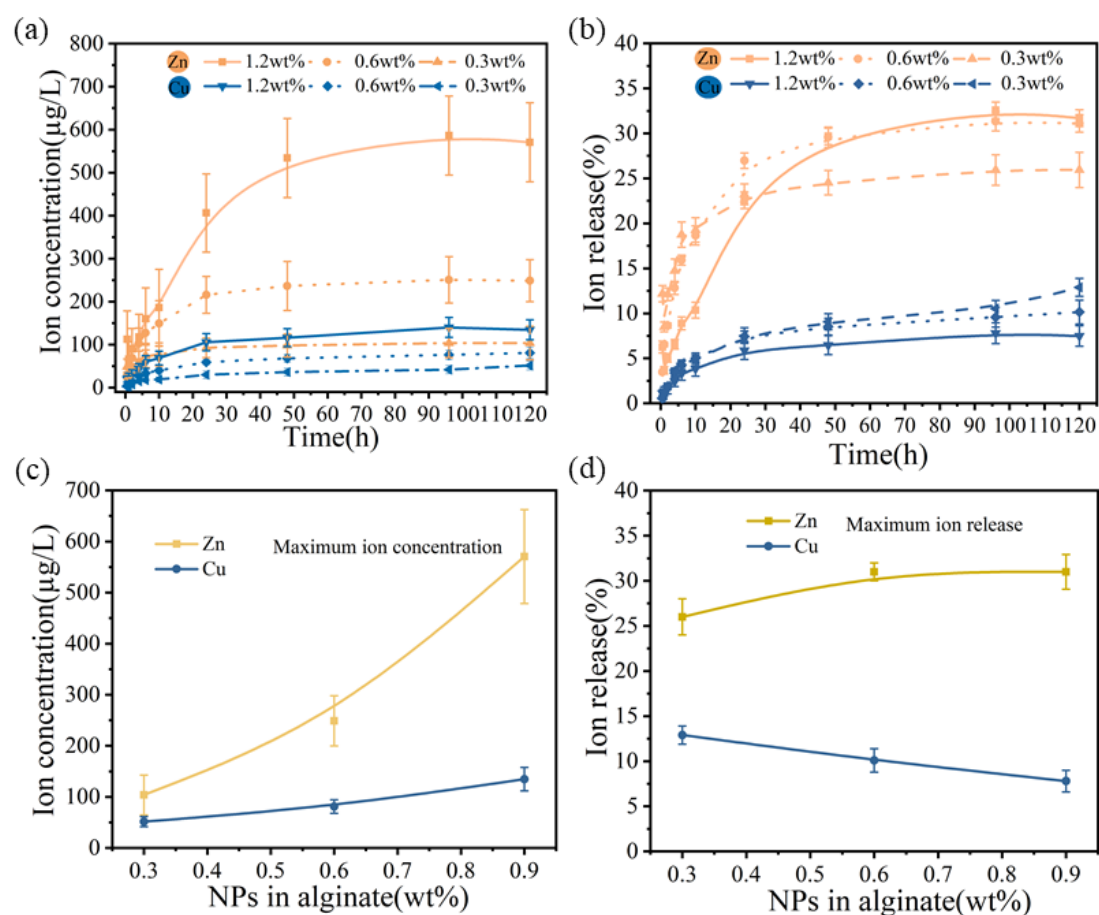


Figure S12: Long-term ion release kinetics in the air-saturated buffer: (a) released Zn and Cu ion concentration of nanoparticle-alginate composite, (b) ions released percent of different nanoparticles amount in alginate, (c) maximum ion concentration, and (d) maximum ion released percent of different nanoparticles amount in 1.5% m/v alginate.

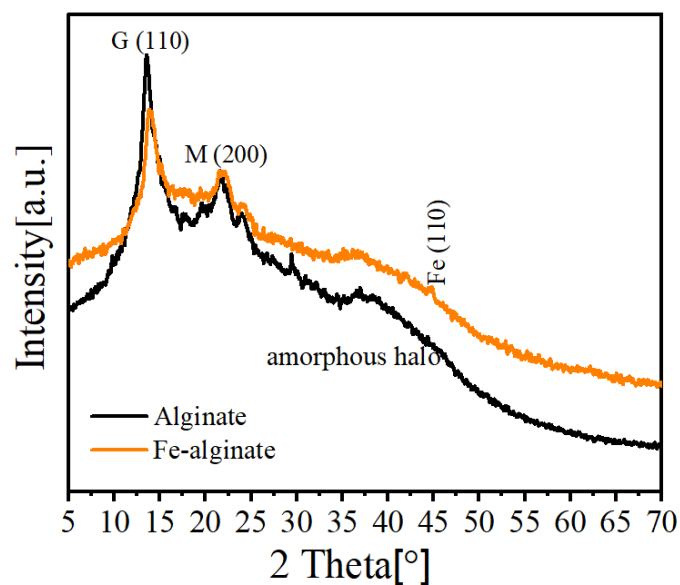


Figure S13: XRD patterns of alginate and 22.8wt% Fe-alginate.

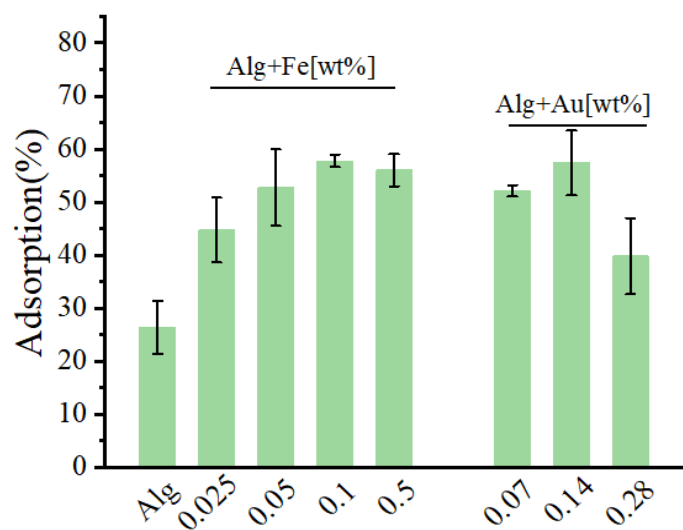


Figure S14: Collagen I protein adsorption percentage on the nanoparticle-alginate gels.

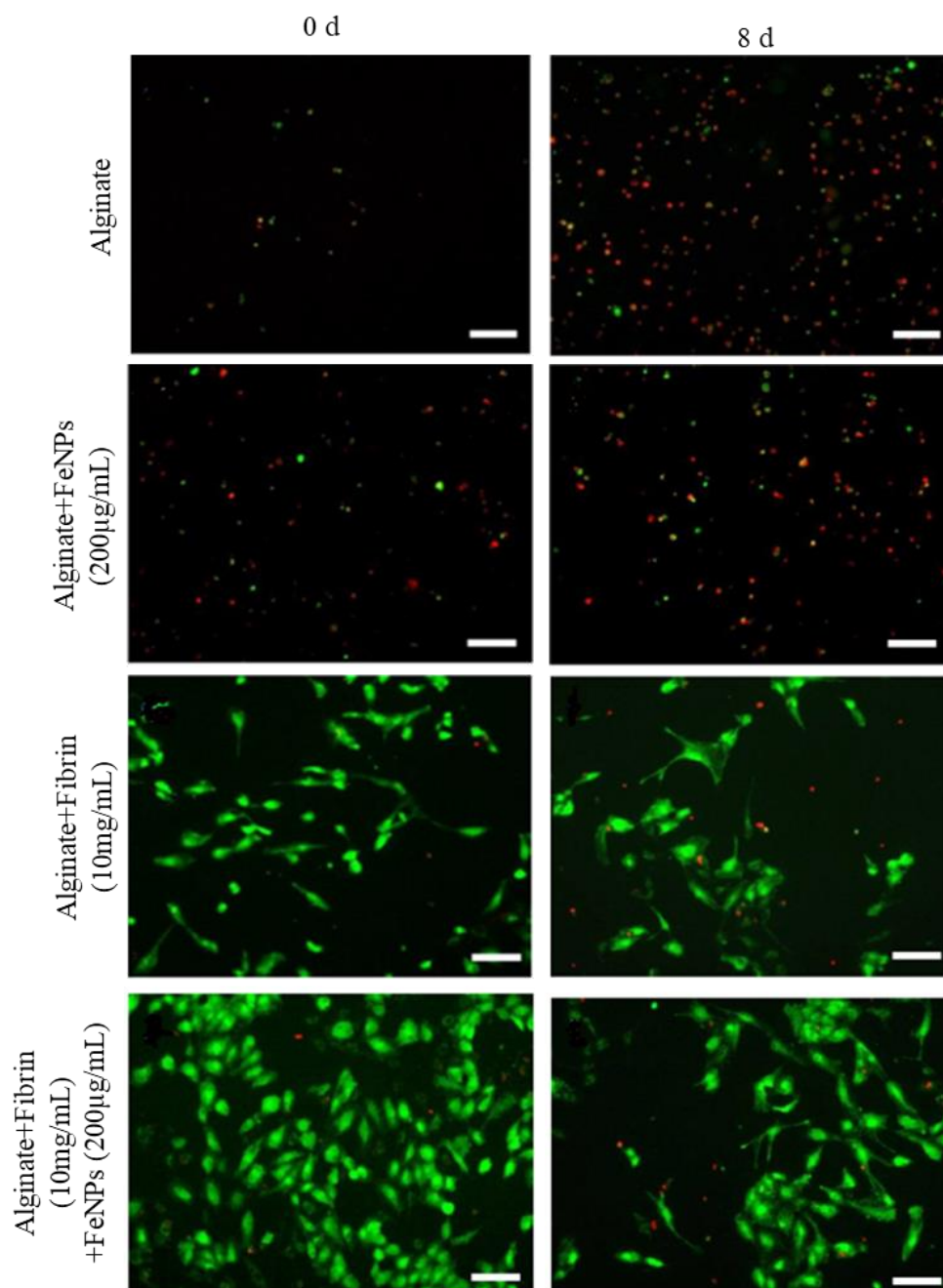


Figure S15: Typical images of endothelial cell proliferation and morphology on various alginate hydrogel films after storage for 8 days assessed by live-dead staining. Scale bars are 100 μ m.

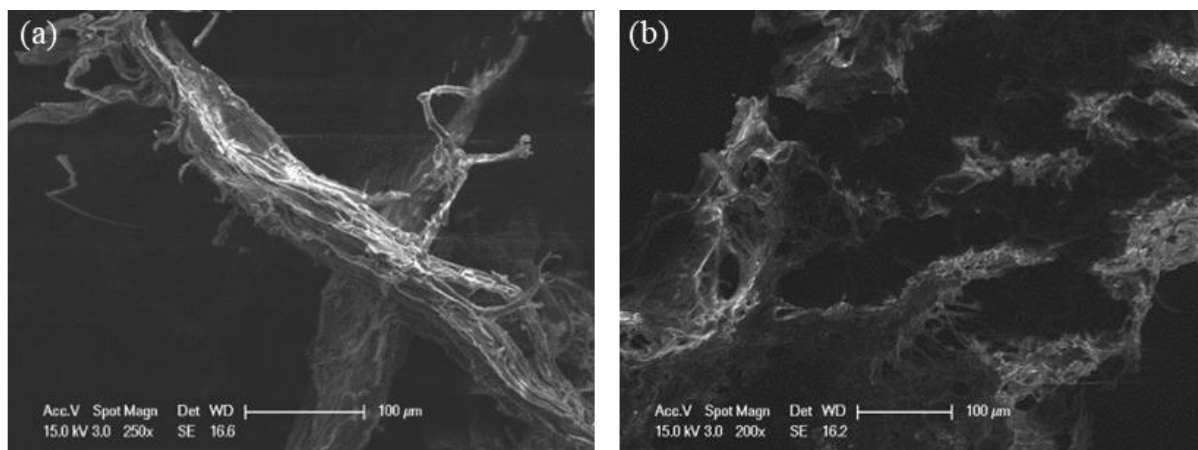


Figure S16: SEM images of raw collagen (a) and grafted Au-collagen composites (b).

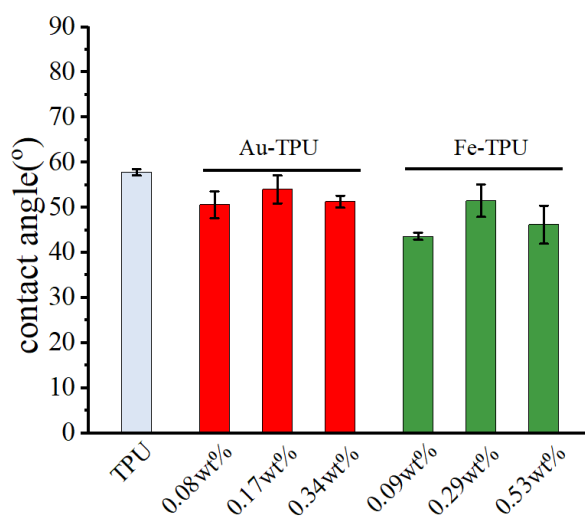


Figure S17: Water contact angles of different loadings of Au and Fe nanoparticles in TPU.

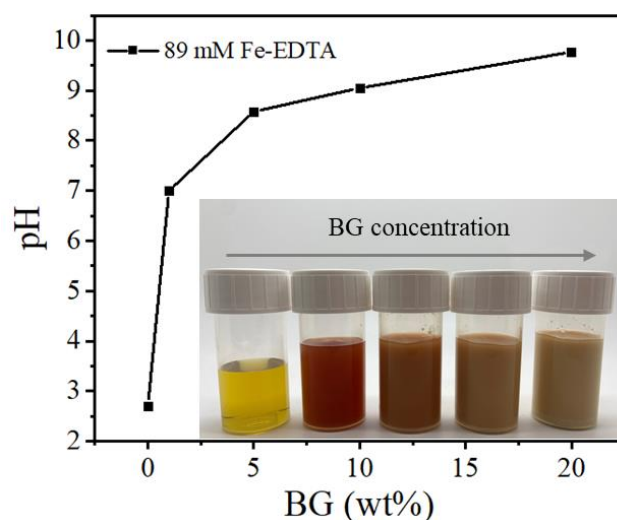


Figure S18: pH values of the as-prepared reaction mixtures with respect to bioactive glass concentration.

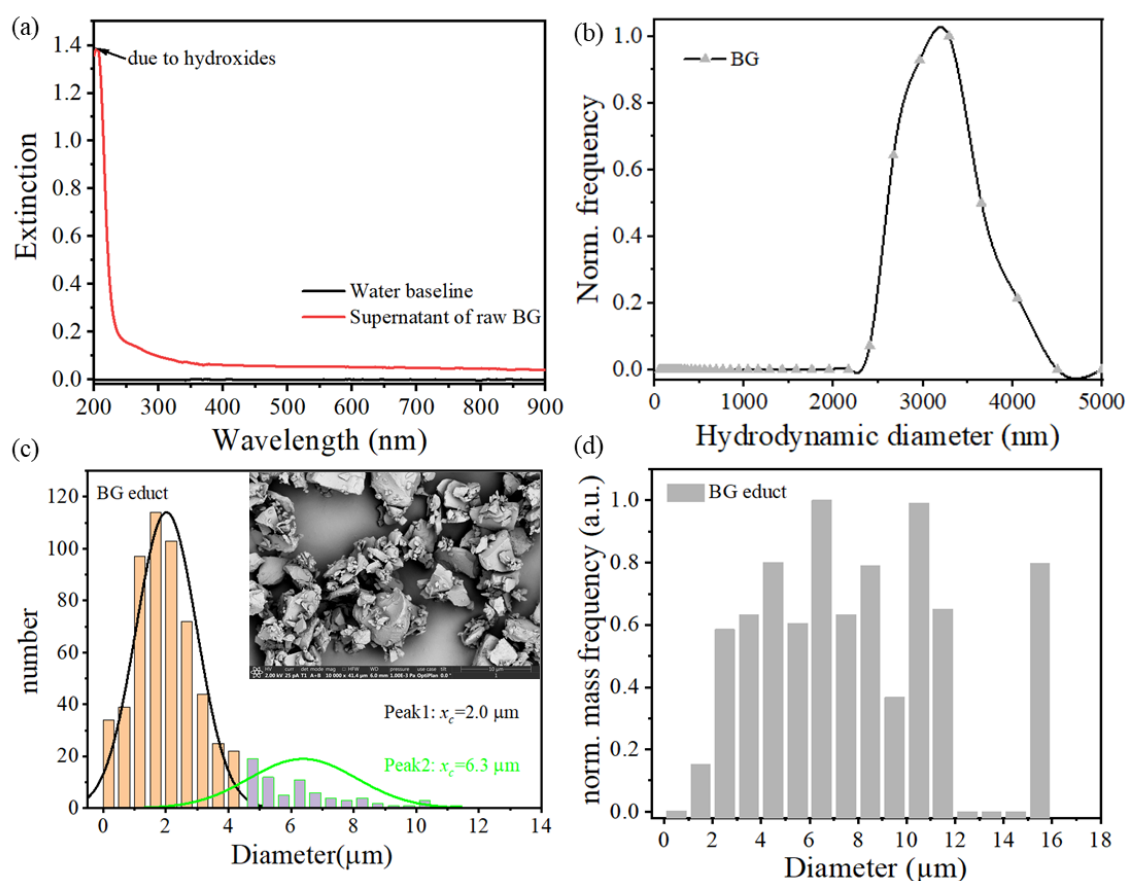


Figure S19: (a) UV-Vis spectra of raw BG supernatant centrifuged at 4000 rpm for 5 min; (b) Number- size distribution of raw bioglass detected by dynamic light scattering (DLS). Number- (c) and mass- (d) size distribution of BG educts measured from SEM images. Spherical BG particles were assumed in this case.

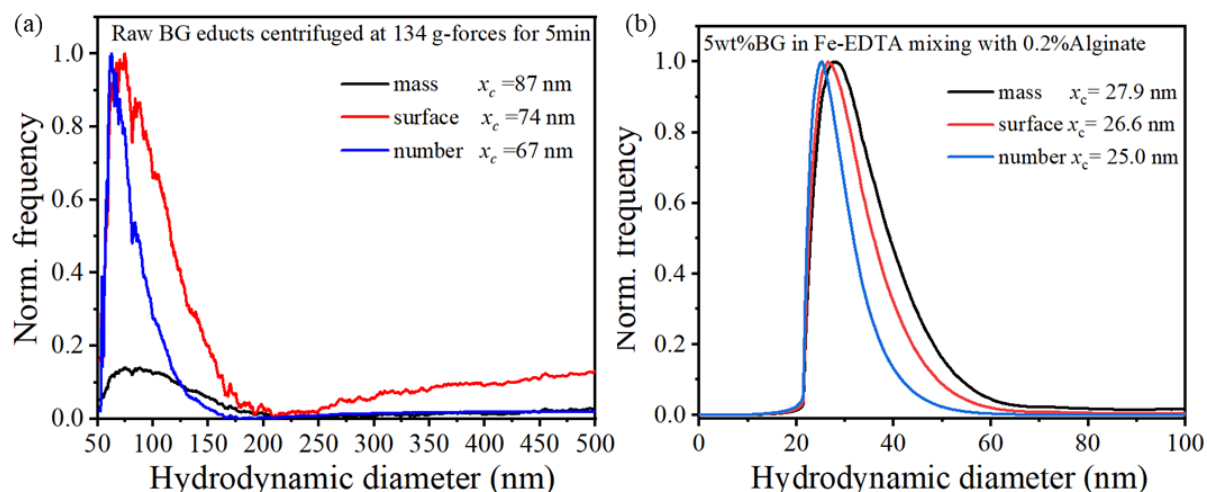


Figure S20: ADC resulted size distribution of raw BG educts (a) and laser irradiated bioactive glass particles in Fe-EDTA solution mixing with 0.2% alginate (b).

Table S1 Energy-dispersive X-ray spectroscopy (EDX) analysis showing the value of weight and atomic concentration for each element present in samples. We compared Fe contents in the sample of BG with Fe ions solution via laser irradiation and the control was directly mixing with Fe ions solution.

Element	BG educts		Laser irradiated BG		unirradiated control	
	Wt. (%)	At (%)	Wt. (%)	At (%)	Wt. (%)	At (%)
O	41.1±0.3	56.6±0.4	41.8±0.3	63.1±0.4	32.9±0.9	50.9±1.2
Na	14.1±0.1	13.5±0.1	2.5±0.1	2.7±0.1	12.2±0.3	12.6±0.3
Si	21.2±0.1	16.6±0.1	18.6±0.1	15.9±0.1	27.3±1.2	23.2±1.0
P	1.9±0.1	1.4±0.1	1.0±0.1	0.8±0.1	2.2±0.2	1.7±0.1
Ca	21.7±0.3	11.9±0.2	11.5±0.2	6.9±0.1	14.5±0.3	8.6±0.2
Fe	-	-	24.6±0.6	10.6±0.3	11.0±0.7	3.0±1.5

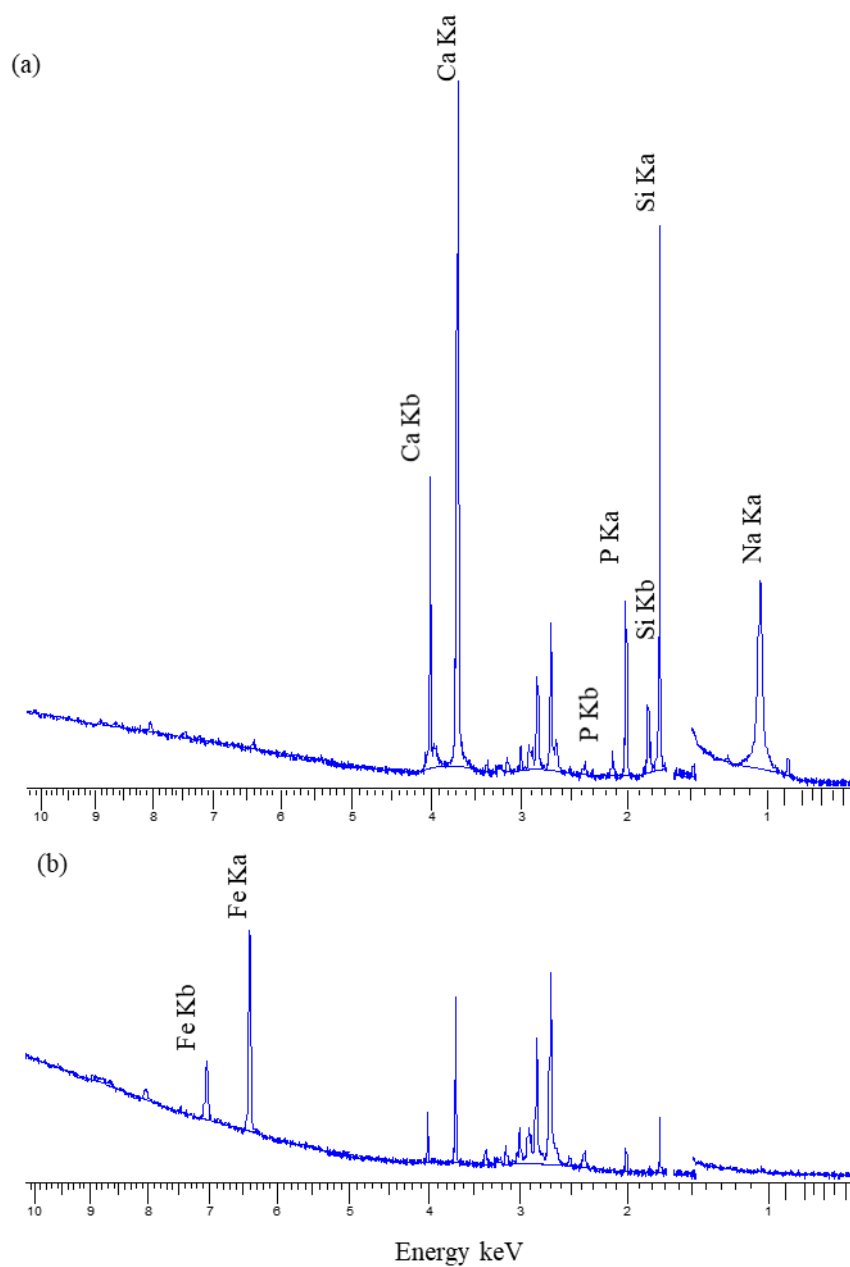


Figure S21: X-ray fluorescence (XRF) spectrum of raw bioglass powder (a) and laser fragmentation bioglass dispersed in iron ions solution after washing (b).

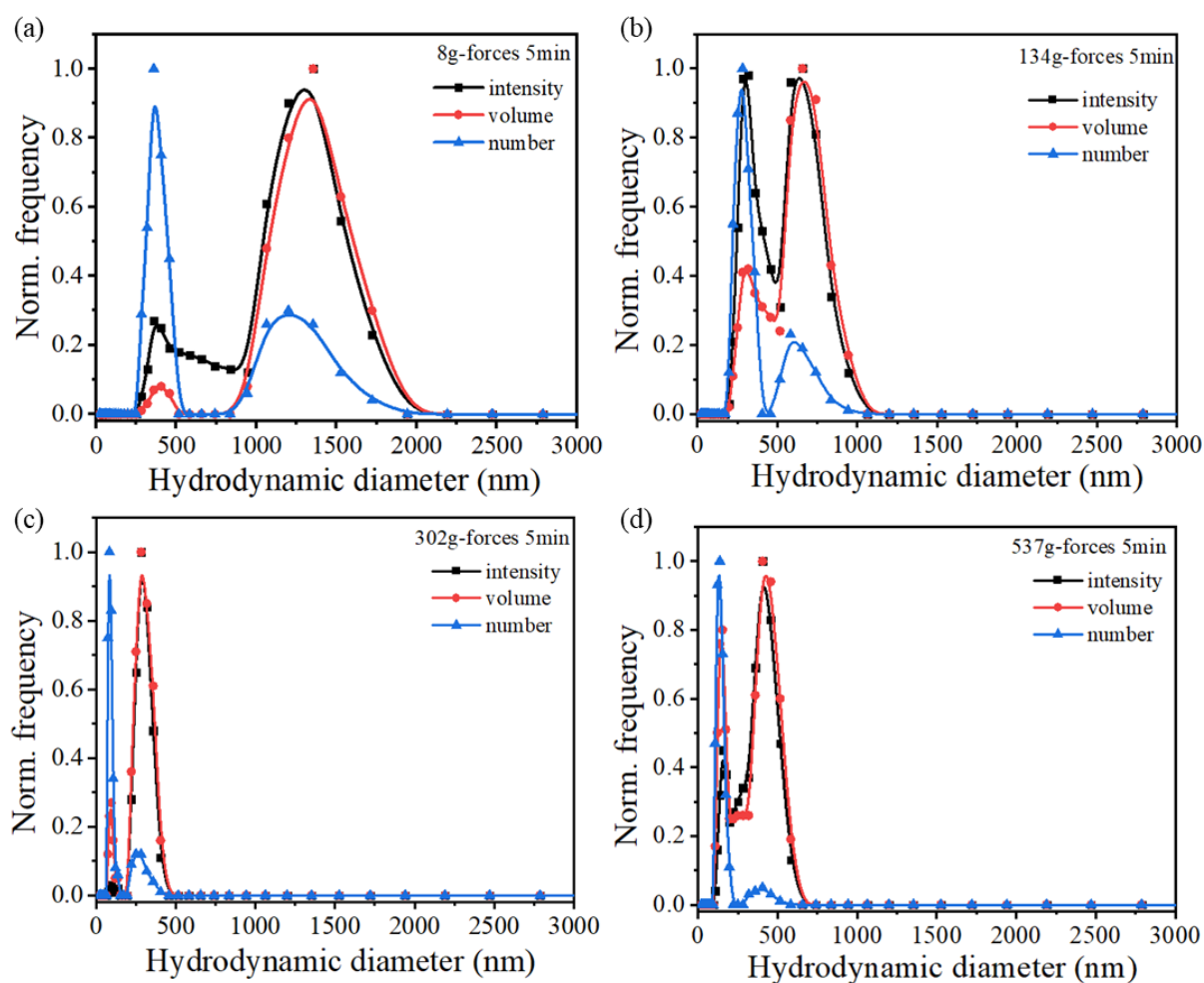


Figure S22: DLS analyzed the hydrodynamic diameter of BG particles at different centrifuged speed.

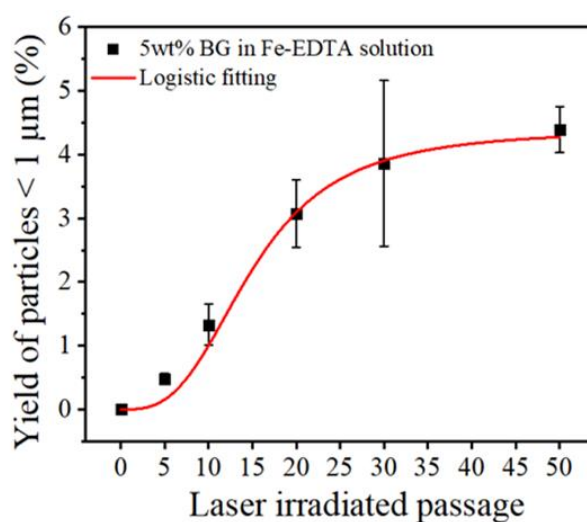


Figure S23: Yield of BG particles smaller than 1 μm in the condition of different laser irradiated passages.

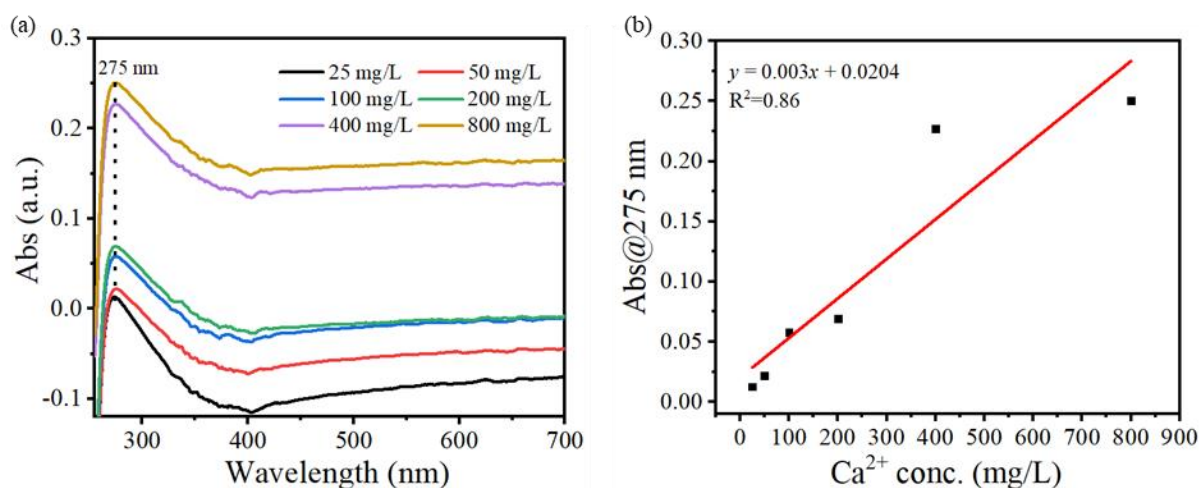


Figure S24: Calibration line for determining the Ca²⁺ ion release from bioglass powders.

In vitro biocompatibility

In vitro characterization of cell-loaded hydrogels was performed to determine the biocompatibility of the incorporated BG particles. For cell culture studies MG-63 osteoblast-like cells (Sigma-Aldrich, Germany) as an adequate model for bone cells were used. DMEM culture medium (Dulbecco's modified Eagle's medium, Gibco Germany) was supplemented with 10% (w/v) fetal bovine serum and 1% (w/v) penicillin-streptomycin. The cells and cell samples were incubated at cell culture conditions (37°C, 5% CO₂, humidified conditions). The cell density was set to 1×10^6 cells/ml hydrogel. 100 μ l of the cell-loaded hydrogel compositions was pipetted into each 48-well and cross-linked with 0.1 M CaCl₂ for 10 min. As a control pure (particle-free) alginate 1.5% (w/v) was prepared. All samples were covered with the culture medium and incubated for up to 7 days. Culture medium was changed every two days.

To assess the viability of cells, live staining was performed with Calcein AM after 1 and 7 days of cultivation, and nuclei were visualized by blue nucleic acid stain, DAPI. The images of Calcein-DAPI stained cells were taken by fluorescence microscope (Axio Scope A.1, Carl Zeiss Microimaging GmbH, Germany). Fluorescence images were used for cell counting, which was performed using ImageJ software. Statistical analysis of cell viability was accomplished by one-way analysis of variance (ANOVA, Bonferroni's test).

In Figure S25a, fluorescence microscope images of Calcein/DAPI staining of MG-63 osteoblast like cells incorporated in different hydrogel compositions are shown. The cell viability

percentage of investigated samples are visible (Figure S25b). Slightly higher cell viability for samples 4, 6 and 7 for day 1 could be observed. However, the results are not significantly different. Thus, an increase of particles concentration from 0.1% (w/v) to 0.5% (w/v) seems not to change the cell viability. This result underlines that even a higher particle content does not have a negative impact on cell viability and seems not to have a toxic influence. Overall, all samples have high viability of over 80% compared to the pure alginate 1.5% (w/v) control sample.

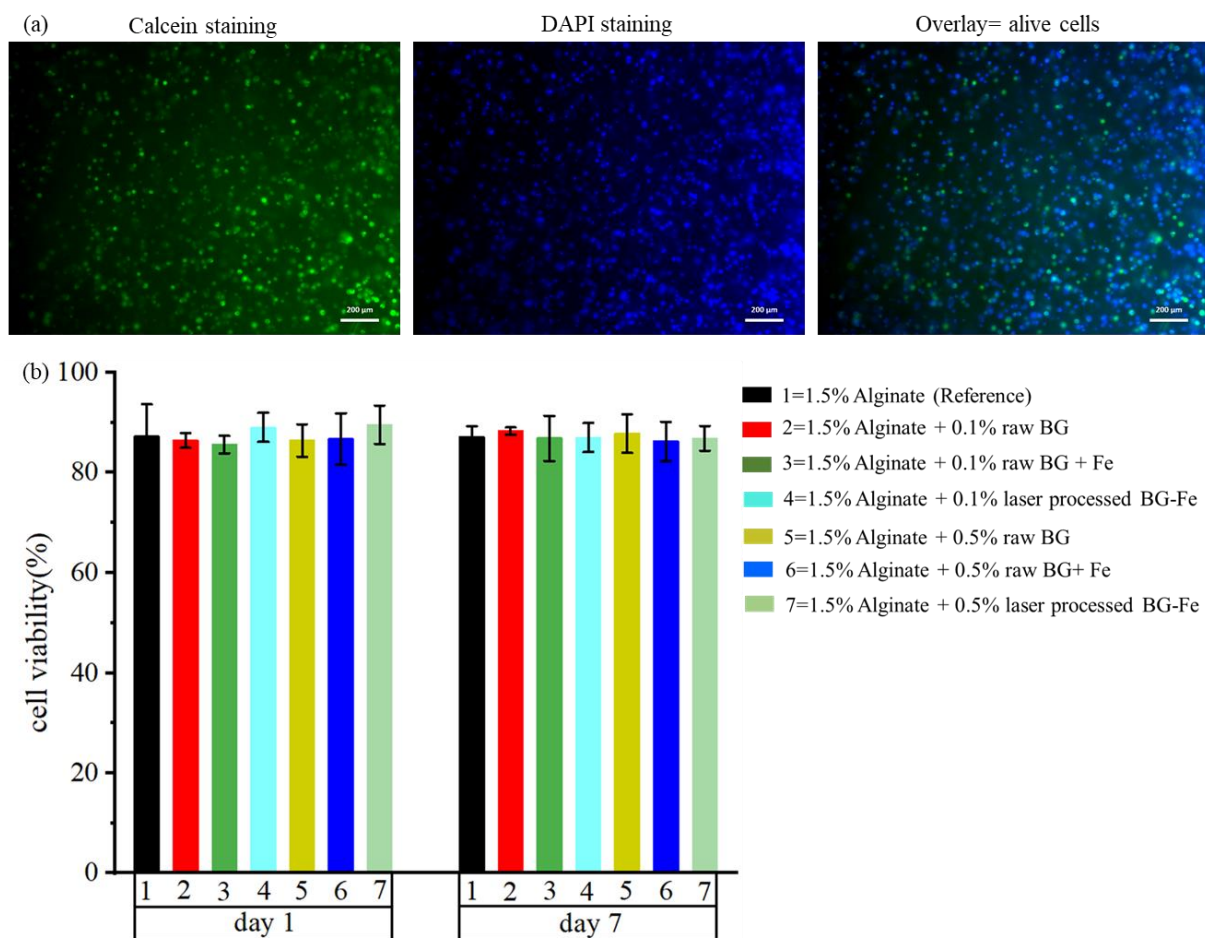


Figure S25: Cell viability percentage on the investigated samples. For all samples, n=9 technical replicates were prepared. The results are calculated as mean values \pm standard deviation. No statistically significant difference was found by one-way analysis of variance (ANOVA). This experiment was carried out by coworker Faina Bider, Institute of Biomaterials, Department of Materials Science and Engineering, University of Erlangen-Nuremberg. Supervisor: Prof. Dr. Aldo R. Boccaccini

9.2 List of abbreviations and physical variables

List of abbreviations

AIS	aggregation-induced scattering
ADC	analytical disc centrifugation
AFM	atomic force microscopy
AuNPs	gold nanoparticles
BG	bioactive glass
BSA	bovine serum albumin
CBB	Coomassie brilliant blue G-250 dye
Conc.	concentration
DLS	dynamical light scattering
EC	endothelial cells
ECM	extracellular matrix
EDC	1-ethyl-3-(3-dimethyl aminopropyl) carbodiimide
EDTA	Ethylenediaminetetraacetic acid
EDX	energy-dispersive X-ray spectroscopy
FBS	fetal bovine serum
FeNPs	iron nanoparticles
FTIR	Fourier-transform infrared
G	α -L-gulonate
GTA	glutaraldehyde
HAP	hydroxyapatite
HUVEC	human umbilical cord vein endothelial cells
ICP-MS	inductively coupled plasma mass spectrometry
IEP	isoelectric point
LAL	laser ablation in liquids
LFL	laser fragmentation in liquids
LSCM	laser scanning confocal microscopy
M	β -D-mannuronate
MSCs	mesenchymal stem cells
NHS	N-hydroxysuccinimide
NP	nanoparticle
PA	polyalanine

PBS	phosphate-buffered saline
PDI	polydispersity index
PGA	polyglycolic acid
PIPES	piperazin-N,N'-bis(2- ethansulfonsäure)
PLGA	poly(lactic-co-glycolic acid)
PMT	photomultiplier tube
PPI	primary-particle-index
PTFE	polytetrafluoroethylene
rpm	revolution(s) per minute
SEM	scanning electron microscopy
SPC	serum protein coating
SPR	surface plasmon resonance
TE	tissue engineering
TEM	transmission electron microscopy
THF	tetrahydrofuran
TLD	transmittance light detector
TPU	thermoplastic polyurethane
TRITC	tetramethylrhodamine
UV-Vis	ultraviolet visible
XRD	X-ray diffraction

Physical parameters used in this thesis

Symbol	Description	Unit
δ	indentation	
ε	strain	
θ	angle	°
σ	stress	Pa
λ	wavelength	m
C	concentration	mg/mL, mol/L
D	pore size	m
E	elastic modulus	Pa
F	force	N
G'	storage modulus	Pa
G''	loss modulus	Pa
K_{sp}	solubility product constant	
N_A	Avogadro number	$6.02 \times 10^{23} \text{ mol}^{-1}$
ρ	density	g/cm^3
p	significance levels	
P	porosity	
q	metal mass in alginate	mol/kg
Q_e	adsorption capacity	mg/g

Symbol	Description	Unit
R	gas constant	
S	swelling ratio	
R_a	mean roughness	m
R_q	root mean square roughness	m
$\tan\delta$	loss or damping factor	
R_t	maximum peak to valley height	m
T	temperature in Kelvin	K
ν	Poisson's ratio	
V	volume	m ³
W	weight	kg
w^2	standard deviation	
ω	angular frequency	rad/s
x_c	average particle diameter	m

9.3 List of Authored and Co-authored Publications

Peer-Reviewed Publications

(1) Richter A.*, **Li Y.Y.***, Rehbock C., Barcikowski S., Haverich A., Wilhelmi M., Böer U. Triple Modification of Alginate Hydrogels by Fibrin Blending, Iron Nanoparticle Embedding, and Serum Protein-Coating Synergistically Promotes Strong Endothelialization. *Adv.Mater. Interfaces* 2021, 2002015. (*co-first author)

(2) **Li Y. Y.**, Rehbock C., Nachev M., Stamm J., Sures B., Blaeser A., Barcikowski S. Matrix-specific mechanism of Fe Ion release from laser-generated 3D-printable nanoparticle-polymer composites and their protein adsorption properties. *Nanotechnology*, 2020, 31, 405703

(3) Brändle K., Bergmann T.C., Raic A., **Li Y.Y**, Million N., Rehbock C., Barcikowski S., Lee-Thedieck C. Iron Nanoparticle Composite Hydrogels for Studying Effects of Iron Ion Release on Red Blood Cell *In Vitro* Production. *ACS Appl. Bio Mater.* 2020, 3, 4766–4778

Oral Presentations (*presenting author)

(1) **Li Y Y***, Rehbock C, Nachev M, Stamm J, Sures B, Blaeser A and Barcikowski S. Matrix-specific mechanism of Fe Ion release from laser-generated 3D-printable nanoparticle-polymer composites and their protein adsorption properties. CENIDE Conference 2020, March 2020, Bergisch Gladbach

Poster Presentations (*presenting author)

(1) **Li Y Y***, Rehbock C and Barcikowski S. Nanoscopic bioglass produced by laser fragmentation using Fe ions as lightabsorbing agents. 9th NRW Nano Conference, April 2021, (Online conference)

(2) **Li Y Y***, Rehbock C, Nachev M, Sures B and Barcikowski S. Ion release from nanoparticle-polymer composites and their ion release protein adsorption properties. ESB 2019 (30th Conference of the European Society for Biomaterials), September 2019, Dresden

(3) **Li Y Y***, Rehbock C, Lee-Thedieck C and Barcikowski S. Design of iron and gold nanoparticle-hydrogel composites and their absorption capacity with BSA. MSE 2018 (Materials Science and Engineering), September 2018, Darmstadt

9.4 Curriculum Vitae

The curriculum vitae is not included in the online version for data protection reasons.

9.5 Declarations

Experimental contribution:

1. TEM measurements in section 5.2.1 were carried out by Jurij Jakobi, UDE, Essen.
2. SEM measurements in section 8.1 and section 5.5 were performed by Vaijayanthi Ramesh and Dr. Kateryna Loza, respectively, UDE, Essen.
3. AFM measurements in section 5.3.3 were conducted by Marcus Hildebrandt, UDE, Essen.

Publication contribution:

(1) **Yaya Li**, Christoph Rehbock, Milen Nachev, Jacqueline Stamm, Bernd Sures, Andreas Blaeser and Stephan Barcikowski. Matrix-specific mechanism of Fe Ion release from laser-generated 3D-printable nanoparticle-polymer composites and their protein adsorption properties. *Nanotechnology*, 2020, 31, 405703

The authors gave the following contributions: The experimental design was from SB, YL and CR. Experiments were conducted by YL. Ion release measurements were carried out under the help of MN. 3D printing of alginate composites was performed by JS and AB. Data analysis and interpretation were performed by YL, CR, MN, JS, BS, AB and SB. The first draft was written by YL under the guidance of CR and SB. All authors revised the manuscript. Figure 5-1, Figure 5-6, Figure 5-7, Figure 5-10, section 5.3.2 and 5.3.5 in this thesis came from this publication.

(2) Katharina Brändle, Timna C. Bergmann, Annamarija Raic, **Yaya Li**, Nina Million, Christoph Rehbock, Stephan Barcikowski and Cornelia Lee-Thedieck. Iron nanoparticle composite hydrogels for studying effects of iron ion release on red blood cell *in vitro* production. *ACS Appl. Bio Mater.* 2020, 3, 4766–4778

The authors gave the following contributions: The experimental design was from KB, TB and CT. Experiments were conducted by KB, CTB, YL and NM. Data analysis and interpretation were performed by KB, TB, AR, YL, NM, CR, SB and CT. The first draft was written by KB under the guidance of CT. All authors revised the manuscript.

(3) Alena Richter, **Yaya Li**, Christoph Rehbock, Stephan Barcikowski, Axel Haverich, Mathias Wilhelmi, Ulrike Böer. Triple modification of alginate hydrogels by fibrin blending, iron nanoparticle embedding, and serum protein-coating synergistically promotes strong endothelialization. *Adv. Mater. Interfaces*, 2021, 2002015.

The authors gave the following contributions: The experimental design was from AR, YL CR and UB. Hydrogel preparation, characterization (Figure 5-22, Figure 5-23, Figure 5-24, Figure 5-25 in section 5.3.3) and related data analysis were carried out by YL while cell experiments (Figure 5-26, Figure 5-27, Figure 5-28, Figure 5-29, Figure S15 in section 5.3.3) were conducted and interpreted by AR. Data analysis and interpretation were performed by AR, YL, CR, SB, AH, MW and UB. The first draft was written by AR and YL under the guidance of UB and CR. All authors revised the manuscript. Figure 5-11b, Figure 5-12, Figure 5-13 based on YL's work shown in section 5.2.2 and results in section 5.3.3 has been published in this paper.

The following student works have been completed under my co-supervision:

Lars Philipp Pötters, Bachelor thesis, July 2019-October 2019, “Der Einfluss von lasergenerierten Goldnanopartikeln auf die physikalischen und chemischen Eigenschaften von Kollagen-Gelen”, part of the results in section 5.3.4 were from his thesis.

Shijie Zhou, Mater thesis, November 2020-April 2021, “ Downsize 45S5 glass particles via laser irradiation using metal (Fe, Cu) ions as light-absorbing agents ”, results related to nanosecond laser in Figure 5-42a were taken from his thesis.

I hereby declare that I am the sole author of this thesis and that I have not used any sources other than those listed in the bibliography and identified them as references. All figures have been created exclusively for this work and do not violate any copyright provision. The results used in this thesis have been partly published in peer-reviewed papers as well as in the bachelor thesis of the supervised student. I have received financial support from the China Scholarship Council during my doctoral study, only to an extent that is commensurate with good scholarly practice and permitted by the laws on examinations.

I further declare that I have neither successfully nor unsuccessfully participated in any other doctoral program. Consequently, I have not submitted and will not submit this work in this form or any similar form to any other institution.

I am aware that making any false declarations in this statement can cause me to be excluded from the doctoral proceedings or, at a later date, result in termination of the proceedings or revocation of an already awarded doctoral title.

9.6 Acknowledgment

I appreciate that the China Scholarship Council for the financial support to my doctoral study at the University of Duisburg-Essen. I am grateful to my Ph.D. supervisor Prof. Dr.-Ing. Stephan Barcikowski for providing me this interesting and challenging research topic, great scientific supervision with many stimulating discussions, and a seemingly unlimited number of ideas. I would like to thank him for enabling me to attend numerous conferences to present many of our research results. Similar gratitude goes to my tutor Dr. Christoph Rehbock. They both have taught me many things, but nothing was more precious than their enthusiasm to push the boundaries of knowledge and attitude towards science and research. I guess I will be benefited my whole life. My further thanks go to Prof. Dr. Cornelia Lee-Thedieck for being the second reviewer of this dissertation.

In this dissertation, numerous measurements would not have been possible without help from colleagues and collaborations from other working groups. Dr. Carmen Streich helped me a lot during my initial days in Germany and shared her expertise in the experiments. It was Dr. Friedrich Waag who provided fruitful discussions. I thank Jurij Jakobi for the TEM measurements. Florian de Kock for the XRD measurements, and René Streubel for the laser set up. I would like to thank the group of Prof. Dr. Mathias Ulbricht for the possibility of carrying out surface zeta potential and contact angle measurements. I would like to thank Dr. Milen Nachev for the help in ion release measurement with the device ICP-MS. I appreciate that Dr. Marcus Hildebrandt for conducting the AFM measurements. I thank the Imaging Center of the University Hospital Essen (IMCES) for laser scanning confocal microscopy measurements.

It is a great working atmosphere in TC I group, not only during working but also the off-work activities outside the laboratory: joint lunch breaks at the Falafelbude and in front of the ice cream parlor, Currywurst and Werewolf evenings, cycling in the wild, swing golf, bowling, cinema visits, fire pincer punch evenings, visits to the Christmas market, and the Christmas parties. They made me feel warm like a family.

I furthermore must thank my parents and lovely friends for always having open ears and helping hands and providing sufficient distraction after work. They are always open-minded to listen and support me in difficult times. These were the most memorable years I have had. While challenging, it was undoubtedly exciting.